



ELSEVIER

Contents lists available at SciVerse ScienceDirect

Physics Reports

journal homepage: www.elsevier.com/locate/physrep

Growth and self-organization of SiGe nanostructures

J.-N. Aqua ^{a,*}, I. Berbezier ^{b,*}, L. Favre ^b, T. Frisch ^c, A. Ronda ^b^a Institut des Nanosciences de Paris, Université Pierre et Marie Curie Paris 6 and CNRS UMR 7588, 4 place Jussieu, 75252 Paris, France^b Institut Matériaux Microélectronique Nanoscience de Provence, Aix-Marseille Université, UMR CNRS 6242, 13997 Marseille, France^c Institut Non Linéaire de Nice, Université de Nice Sophia Antipolis, UMR CNRS 6618, 1361 routes des Lucioles, 06560 Valbonne, France

ARTICLE INFO

Article history:

Accepted 5 September 2012

Available online xxxx

editor: G.E.W. Bauer

ABSTRACT

Many recent advances in microelectronics would not have been possible without the development of strain induced nanodevices and bandgap engineering, in particular concerning the common SiGe system. In this context, a huge amount of literature has been devoted to the growth and self-organization of strained nanostructures. However, even if an overall picture has been drawn out, the confrontation between theories and experiments is still, under various aspects, not fully satisfactory. The objective of this review is to present a state-of-the-art of theoretical concepts and experimental results on the spontaneous formation and self-organization of SiGe quantum dots on silicon substrates. The goal is to give a comprehensive overview of the main experimental results on the growth and long time evolution of these dots together with their morphological, structural and compositional properties. We also aim at describing the basis of the commonly used thermodynamic and kinetic models and their recent refinements. The review covers the thermodynamic theory for different levels of elastic strain, but focuses also on the growth dynamics of SiGe quantum dots in several experimental circumstances. The strain driven kinetically promoted instability, which is the main form of instability encountered in the epitaxy of SiGe nanostructures at low strain, is described. Recent developments on its continuum description based on a non-linear analysis particularly useful for studying self-organization and coarsening are described together with other theoretical frameworks. The kinetic evolution of the elastic relaxation, island morphology and film composition are also extensively addressed. Theoretical issues concerning the formation of ordered island arrays on a pre-patterned substrate, which is governed both by equilibrium ordering and kinetically-controlled ordering, are also reported in connection with the experimental results for the fabrication technology of ordered arrays of SiGe quantum dots.

© 2012 Elsevier B.V. All rights reserved.

Contents

1. Introduction.....	2
2. Morphological, structural and compositional evolution	5
2.1. Evolution and relaxation	5
2.1.1. Kinetic phase diagram	5
2.1.2. Wetting layer growth	7
2.1.3. Morphological instability	7
2.1.4. Prepyramids	10
2.1.5. 2D/3D transition	13
2.1.6. Hut islands	13

* Corresponding authors.

E-mail addresses: aqua@insp.jussieu.fr (J.-N. Aqua), isabelle.berbezier@im2np.fr (I. Berbezier).

2.1.7.	Hut islands and vicinal substrates	19
2.1.8.	Dome islands	23
2.2.	Composition	30
2.2.1.	Bidimensional layer	31
2.2.2.	Pyramid and dome islands	32
2.2.3.	Multilayers and superlattices	40
2.2.4.	Surfactant	44
3.	Formation mechanisms	45
3.1.	Low strain regime	45
3.1.1.	Basics of the Asaro-Tiller-Grinfeld instability	45
3.1.2.	ATG instability with wetting and anisotropy	47
3.1.3.	Isotropic islands	50
3.2.	High strain regime	52
3.2.1.	Submonolayer aggregation	52
3.2.2.	2D–3D transition	54
3.3.	Hut pyramids	57
3.3.1.	Stabilization of the (105) facet	57
3.3.2.	Hut growth dynamics	59
3.4.	Coexistence of pyramids and domes	61
3.5.	Composition evolution	63
3.5.1.	Continuum model	64
3.5.2.	Instability and pre-pyramids	64
3.5.3.	Simulations and numerical results	67
3.6.	Microscopic processes	69
3.6.1.	Defect diffusion	69
3.6.2.	Incorporation in surface steps	70
3.6.3.	Mobility differences	73
3.7.	Coarsening	77
3.7.1.	Initial mound coarsening	77
3.7.2.	Pyramid coarsening	77
3.7.3.	Energetic pathways	81
3.7.4.	Pyramid to dome transition	83
4.	Substrate design and self-organization	83
4.1.	Lithographic patterning	85
4.1.1.	Simulations	86
4.1.2.	Conventional lithography	91
4.1.3.	e-beam lithography	92
4.1.4.	Focused ion beam	94
4.2.	Substrate designed by instabilities	96
4.2.1.	Instability driven patterning on Si(001)	96
4.2.2.	Periodic patterns on Si(111) and Si(113)	97
4.2.3.	Self-organization on spontaneously formed periodic surfaces	99
4.2.4.	Periodic patterns on planar surfaces	102
4.2.5.	Surfactant effect	105
4.2.6.	ATG instability	107
4.3.	Strain inhomogeneities	109
4.4.	Impurities	111
4.4.1.	Surfactant effect	112
4.4.2.	C quantum fortresses	113
4.4.3.	Di-block copolymer	115
4.5.	Exotic substrates	115
5.	Conclusion	119
	References	121

1. Introduction

The manipulation and observation of matter at the atomic level has led to a quantitative revolution in the so-called domain of nanotechnology. Miniaturized electronic and optical devices useful for large-scale memory storage, efficient lasers or electroluminescent diodes with unusual spectrum, photovoltaic structures with higher efficiency, etc., are now commonly manufactured. The constant scale reduction opens the path to the production of quantum nanostructures with unprecedented properties. We focus here on the production of quantum dots made of silicon and germanium which draw attention both as model systems and for their application in the electronic industry mainly based on silicon (Si) systems [1–7]. An example of paramount importance is the metal oxide semiconductor field effect transistor device (MOSFET) which,

Nomenclature

List of symbols

CVD	chemical vapor deposition
FEM	finite element method
FIB	focused ion beam
GIXRD	grazing incidence X-ray diffraction
GISAXS	grazing incidence small angle X-ray scattering
KMC	kinetic Monte-Carlo
LPE	liquid phase epitaxy
MBE	molecular beam epitaxy
MC	Monte-Carlo
ML	monolayer
QD	quantum dot
SK	Stranski-Krastanov
UHV	ultra-high vacuum
WL	wetting layer

since its first experimental demonstration more than fifty years ago, has become a driver for the microelectronic industry. Even if its operating mode remained almost identical, the scaling down of its physical dimensions following the so-called Moore's law has produced an exponential development of the microelectronic industry with a huge gain of integration coming from a density of transistors doubling every 18 months. This progress was associated to a significant improvement of the transistor characteristics due to a significant control of the fabrication processes. While the advanced technology of integration engineering is driven by commercial dynamic random access memory (DRAM) and non volatile semiconductor memory (NVSM) circuitry, basic physical questions (spanning the entire range from basic materials issues to device concepts, and especially epitaxial processes) remain key issues as regards band gap engineering [8].

Challenges related to the making of future devices concern the memory technologies, the information processing and logic devices. In the first category, the new technology is expected to provide the best memory features compatible with the CMOS technology and to be produced with a process flow scalable beyond the 25 nm gate length (which corresponds to a 22 nm node). In the second category, to sustain the scaling of CMOS logic technology beyond 16 nm, the strained silicon MOSFET channel is expected to be replaced by an alternate material offering higher carrier velocity and mobility. Additional challenges concern the reduction in leakage currents and power dissipation by introducing new materials into the MOSFET, while simultaneously minimizing the statistical fluctuations of the dopant concentration in the channel. At the material scale, the most difficult challenge is to deliver such new materials with a precise control of the properties at the nanometer scale, which requires basic research on materials synthesis, modeling and nano-characterization.

In the present time, we begin to observe the degradation of the electrical features with the pursuit of the scaling down of devices below 25 nm. Even if future technological progresses may still lead to improved performances, alternative routes to CMOS technology should definitely be developed for sizes approaching 15 nm, mostly because of the problems related to the self-heating due to power dissipation in logic circuits and to the scaling down of the storage capacitors in DRAM cells [9]. Materials foreseen for such alternatives include strained germanium (Ge), SiGe or III-V compound semiconductors, quantum dots and wires, carbon nanotubes, graphene, etc. It is interesting to note that the advanced research in SiGe and III-V devices is converging simultaneously towards quantum dots (QD) and quantum wires (QW) based systems. While it would be premature to conclude that future information processing will be based on quantum computing, it is certain that the smallest devices will be affected by quantum confinement and other quantum effects such as decoherence, see e.g. [10,11]. It is consequently a key issue to clarify whether self-assembling of SiGe QDs could create sufficiently dense arrays of QDs with an improved control and reliability of their properties.

Quantum dots may result from lithography techniques such as focused ion beam, photolithography or selective chemical etching. An alternative and less intrusive technique is the self-organization of quantum dots. Self-ordering may arise in metallic, semi-conducting and molecular materials [12] but we focus here on the self-organization resulting in heteroepitaxy during molecular beam epitaxy (MBE) or chemical vapor deposition (CVD). The possibility to grow Ge islands on Si which remain coherent [13] and display different kinetically controlled shapes [14], opened the way for a huge effort to understand, control and use such self-organized islands. In the heteroepitaxy of SiGe systems, QDs arise as one route for relaxing the elastic strain after completion of a wetting layer as depicted by the Stranski-Krastanov (SK) mode, see e.g. [15–17]. Indeed, the small 4% difference between the Si and Ge lattice parameters allows for an heteroepitaxy which may remain coherent when a Ge or $\text{Si}_{1-x}\text{Ge}_x$ film deposited on a Si substrate [13]. However, the latter difference in lattice parameters enforces a significant biaxial misfit strain parallel to the film/substrate interface which can be partially relaxed by a morphological evolution in the perpendicular direction. We restrict our attention to dislocation free crystals more

amenable to applications in optics or electronics, and thence to a deposited film thickness below the critical Matthews length [18] in order to maintain a coherent epitaxy [15].

The deposition of SiGe on Si may be basically described as a classic Stranski-Krastanov process where the formation of quantum dots is governed by the competition between kinetics and thermodynamics [1]. Self-organization of QDs proceeds through the classical stages of nucleation or continuous process and subsequent growth of islands during coarsening (Ostwald ripening or other diffusive mechanisms). However, the growth of SiGe films involves in fact more complex mechanisms not accounted for in the simplified SK growth scheme. The SiGe deposition proceeds first by a layer by layer mode characterized by a fast increase in the monolayer (ML) step density and the formation of dimer vacancies that order in a $(2 \times N)$ reconstruction. After roughening of the initial surface, 3D islands arise on top of a wetting layer and grow thanks to a mass transfer driven by surface diffusion. They may result either from the nucleation of 3D nuclei for a large enough strain or from a nucleationless morphological instability, where a quasi periodic array of islands display sidewalls which continuously increase their slopes. As coverage keeps on increasing, a variety of metastable morphologies occur such as square-base or rectangular-base (hut) pyramids which are kinetic path for the formation of larger dome islands, [14] which finally undergo a transition towards very large $\sim 1 \mu\text{m}$ dislocated islands (superdomes) [19]. In this scheme of growth, the origin of the initial stage of roughening is still under debate (kinetic or stress driven instabilities). In addition, the transition from huts to domes was matter of controversy as regards a possible first order transition as opposed to an anomalous coarsening. An extra relevant parameter not included in the basic SK description is the surface anisotropy. Experiments on different substrate orientations exhibit different growth modes and morphologies depending on the substrate orientation, e.g. (001) or (111). In particular, metastable strained morphologies can be completely inhibited on specific orientations. Moreover, heteroepitaxy involves different materials and alloying also comes into play as one route to relieve strain. It enforces concentration inhomogeneities in islands which in turn alter the growth mode and impact the QDs properties. It is therefore of crucial importance to determine the balance between the basic driving forces of nucleation and growth of QDs in order to predict and understand their self-organization and improve their physical properties at the nanometer scale.

The typical characteristics of the QDs needed to achieve new devices have to be examined in order to develop appropriate self-organization processes. Quantum nano-structures are characterized by the fact that one of their size is smaller than the electronic de Broglie wavelength (quantum wires, wells and dots) depending on the number of dimensions (respectively 1, 2 and 3) in which charge carriers are confined [6]. The characteristic length scale of a quantum dot is typically in the range of 1–10 nm. When matter is confined at this nanometer scale, the dot properties are dominated by new physics which originates either from geometric effects or from quantum phenomena. The reduction of the number of atoms when the surface to volume ratio is large enough, may change the crystal stable structure and the reactive properties of the surface. Quantum effects become dominant on the de Broglie wavelength λ_B which depends on the carrier effective mass m_{eff} and on the temperature T as $\lambda = h/\sqrt{m_{\text{eff}}k_B T}$ where k_B is the Boltzmann constant. Quantization is thence important when the typical dot size d is typically smaller than λ_B . Given the effective mass of the charge carrier in Ge, $m_{\text{eff}} = 0.55m_e$, with the electron mass m_e , the maximum dot diameter d_{max} for observing size quantization is approximately 7 nm. Note that the dot size dispersion modifies the energy of confinement and widens the density of states of carriers and should be limited to at most 20%, as a too large inhomogeneity may inhibit the use of QD in many electronic applications. Similarly, the bottleneck of QD fabrication for optoelectronic applications is the non resonant energy spectrum of QD ensembles which arises even when the dots are located in an apparently perfectly ordered array but result from slight size, shape and composition differences.

More generally, the following requirements must be fulfilled in order to make QDs useful for devices operating at room temperature: (i) QDs should have a sufficiently small size to obtain deep enough localized states; (ii) QD ensembles should display a good uniformity and a high volume filling factor; (iii) the system should remain coherent without defects such as dislocations. These conditions are usually hard to achieve experimentally and a lot of attention have been devoted to the elaboration of suitable QDs. The preparation of self-assembled QDs is one of the rapidly emerging fields which can meet these requirements, spanning applied physics and electronic engineering. Many ways have been explored to organize regular ensembles of QDs using spontaneous or forced self-organization on natural [7,20–22] or artificially pre-structured [23–25] substrates. Spontaneous self-organization processes are limited by the resulting dot size distribution [26]. Most of the growth processes are dedicated to optimize the growth conditions, substrate orientations and layer sequences, etc., to achieve a higher degree of lateral ordering and lower size dispersion. Forced alignment on pre-patterned substrates may be used to define preferential nucleation centers by appropriate pre-patterning of the substrate. This approach allows an absolute positioning of the quantum dots with respect to the pattern structure, which is required by device fabrication, but which can only be applied to nanometric size patterns at the expense of long time processing. Hence, the challenge which is still to be faced is the manufacturing of dense and homogeneous arrays of ultra-small QDs on large scale (typically on a wafer size). The aim of this review is to give a state-of-the-art of the self-organization of quantum dots in the paradigmatic SiGe systems, dealing with the individual basic mechanisms at work during growth and the competition between them. We put emphasis both on the theory and experiments, and on the comparison between them, leading to the open questions still to be faced to get a comprehensive understanding of the dot growth. We underline the difference between instabilities and nucleation which both lead to quantum dots, and discuss their dynamics and modelization. We also analyze different ways probed to control the dots self-organization, by designing either the substrate morphology or its physical and chemical properties.

The review is organized as follows. In Section 2, the experimental facts concerning island formation in SiGe systems are introduced in connection with the structural, morphological and compositional evolution. The review focuses first on the evolution of samples at different levels of elastic relaxation, spanning from a flat bi-dimensional layer, to an undulated layer produced by growth instability, to hut and dome islands and superdomes. Critical review is given of the various (sometimes contradictory) experimental data reported on the structures, morphologies and compositions at different levels of relaxation. In Section 3, the mechanisms at the origin of island formation are presented and theoretical issues are discussed. We review first the morphological instability at work in the low strain regime, reminiscent of the Asaro-Tiller-Grinfeld instability, and especially its long-time dynamics free of singularity. We then discuss the island nucleation operating at larger strain together with shape coexistence resulting from both regimes. We pay attention to the island coarsening and discuss in which condition it may be suppressed. We also review how alloying results from the growth process and in turn influences the growth dynamics both from mesoscopic and microscopic points of view. Concentration inhomogeneities play an important role in the confinement potential of the electrons and on the structure of the electronic band and are therefore important to understand both for fundamental reasons but also for technological applications. In Section 4, the self-organization on functionalized substrates (bottom-up approach) is considered both theoretically and experimentally. In this last section, we review the self-organization of QDs on functionalized substrates following the bottom-up approach. The functionalization using either naturally formed self-assembled patterns or nanotechnological patterning process is described. The ordering of Ge islands on nano-patterned template layers is analyzed and the efficiency of various driving forces is deduced. Various patterning processes are reviewed which aim to modify (i) the surface morphology with patterns fabricated by technological tools; (ii) the surface energy, using kinetic and stress driven instabilities (which have the advantage of natural formation on large scales in a unique process) as well as instability induced by ion beam sputtering; (iii) the surface stress with for instance the creation of regular dislocation networks; (iv) the surface chemistry with various chemical impurities (gold, carbon, oxides ...).

2. Morphological, structural and compositional evolution

2.1. Evolution and relaxation

Strain relaxation is the common driving force for the different routes leading to the formation of quantum dots in SiGe systems. Strain may be partially relaxed by surface reconstruction, intermixing, morphological instability, island formation, shape transition, dislocation introduction, etc. We discuss in this first part the different morphological evolutions in connection with the associated strain relaxation while we focus in next part on the relaxation induced by compositional relaxation. We will also discuss the relaxation state of quantum dots at different stages of their evolution. Formation and glide of misfit dislocations may also serve as a possible way for inelastic strain relaxation but it happens for high enough strain and/or large enough film heights above the Matthews critical height [18]. We restrict our attention to the elastic regime where dislocation free dots are produced which are best suitable for application. The incremental strain relaxation happening during the different stages of the coherent morphological evolution is sketched in Fig. 1, exemplified in Fig. 2 and discussed in the following. The knowledge of strain distribution within quantum dots is crucial for the understanding of electronic and optical properties. Strain impacts significantly the electronic band structure and strain maps can be valuable for the design of efficient devices, see e.g. [27].

2.1.1. Kinetic phase diagram

It is commonly reported that $\text{Si}_{1-x}\text{Ge}_x$ quantum dot self-assembly proceeds through the initial stage of roughening followed by the nucleation and/or growth of islands as a model example of the classic Stranski-Krastanov process [30,16]. At low misfit, islands nucleate at specific sites of a periodic corrugation induced by a stress-driven instability. Finally a last sequence of island coarsening (Ostwald ripening or other diffusive mechanism) [31] leads to large isolated islands. However, while island formation is commonly described by a widely used SK growth scheme, complex mechanisms based on competitive effect of kinetics and thermodynamics take place during the epitaxy of $\text{Si}_{1-x}\text{Ge}_x$ on Si(001). The aim of this section is to follow the morphological evolution of $\text{Si}_{1-x}\text{Ge}_x$ deposits on Si. We present a comprehensive description of the different growth modes of $\text{Si}_{1-x}\text{Ge}_x$ films with x varying from 0 to 1 on Si(001) and Si(111). The results are presented in kinetic morphological growth diagrams, see Fig. 3, of as-grown samples as a function of the deposited film height h and misfit $m = \delta a/a$, where the difference of the film and substrate lattice parameters δa is related to the film composition x and to the film lattice parameter a . Such diagrams have been extrapolated from systematic investigations of as-grown $\text{Si}_{1-x}\text{Ge}_x$ surfaces that develop for a growth temperature $T = 550^\circ\text{C}$, see [7]. A medium growth temperature is chosen in order to avoid dislocation nucleation which occurs at higher temperature [32]. Different growth regimes are distinguished on Si(001) and (111) which correspond to different levels of relaxation. The latter can be monitored e.g. by the measurement of the (220) peak diffraction of the grazing incidence X-ray diffraction (GIXRD) spectrum [7]. Every growth regime is characteristic of as-grown sample but may also be associated to specific steady states observed after long-term annealing of as-grown samples.

The regimes observed on Si(001) correspond first to (i) the 2D layer-by-layer growth of a wetting layer associated with a change in the surface reconstruction, regime I in Fig. 3. Then, depending on the value of the misfit, one may

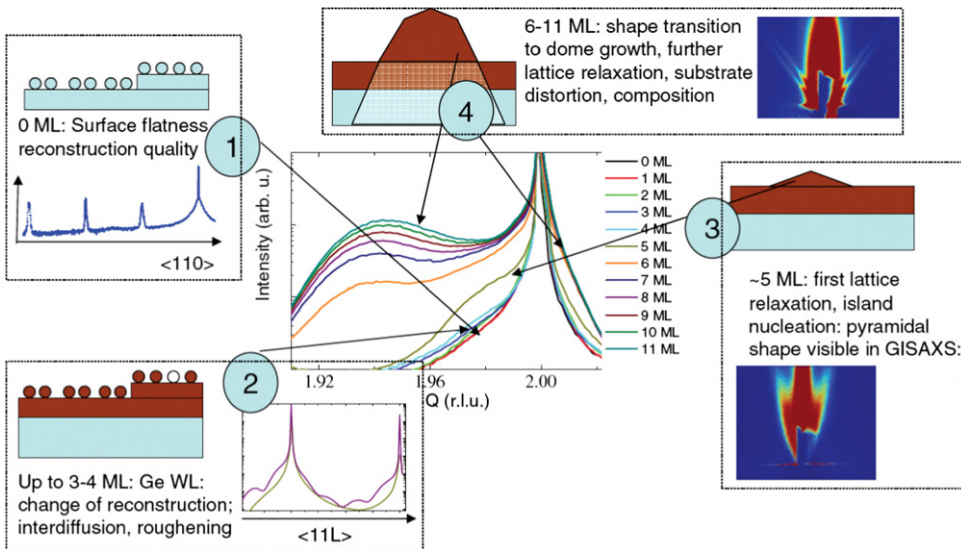


Fig. 1. Summary of all relevant growth stages of Ge on Si(001) as observed by X-ray diffraction. As an example, the intensity in the vicinity of the Si (220) Bragg peak is plotted for 0–11 ML of Ge deposition. For 0–4 ML the focus of interest lies in the evolution of the surface reconstruction. After island nucleation, the combination of GISAXS and GID attributes an island shape to a certain degree of relaxation.
Source: from [28].

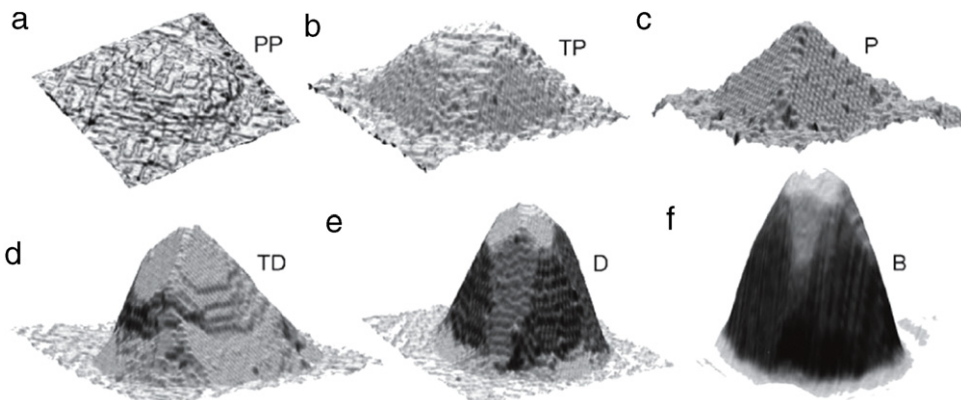


Fig. 2. Scanning tunneling microscopy (a)–(e) and AFM (f) images of representative islands illustrating the morphological evolution of coherent SiGe islands on Si(001). Islands are prepyramids [PP, (a)], truncated pyramids [TP, (b)], pyramids [P, (c)], islands with shape intermediate between pyramids and domes [TD, (d)], domes [D, (e)], superdomes or barns [B, (f)]. Images were obtained on several samples grown under different conditions.
Source: from [29].

either find a nucleationless evolution when the surface continuously and smoothly transform into islands at low misfit, or an abrupt 2D/3D transition associated with island nucleation at large misfit. In the low misfit case ($x \lesssim 0.5$) after a critical thickness which corresponds to the completion of the wetting layer, the formation of islands does not involve nucleation, but rather proceeds via a precursor array of shallow stepped mounds (prepyramids) on the surface that result from the morphological instability of a strained film [33,34]. In this case, the surface displays (ii) a surface corrugation corresponding to a morphological instability with a well-defined wavelength and which, after some ripening, transforms into (iii) prepyramids with rounded shapes and no noticeable facets, separated by a wetting layer. These prepyramids undergo some coarsening while they increase their aspect ratio until they reach a side angle of 11.3° corresponding to (105) facets. As the deposited height increases from this stage, the surface is characterized by (iv) square-base huts pyramids with four (105) facets, associated with a 15%–20% elastic relaxation, regime II in Fig. 3, followed by (v) a bimodal distribution of so-called hut and dome islands with 20% and 50% relaxation respectively in regime III. Finally, for larger h (vi) a bimodal size distribution is found including domes and superdomes with 50% and 80% relaxation in regime IV. When the misfit is large enough ($x \gtrsim 0.5$) the stages (ii) and (iii) are hidden by the sudden 2D–3D transition for a given critical thickness when, after small embryo nuclei have arisen, the surface promptly transforms into huts and domes [stage (iv)] after completion of the wetting layer [14,1,19,4]. It was shown more recently in a precise range of parameters [35] that micrometer long nanowires

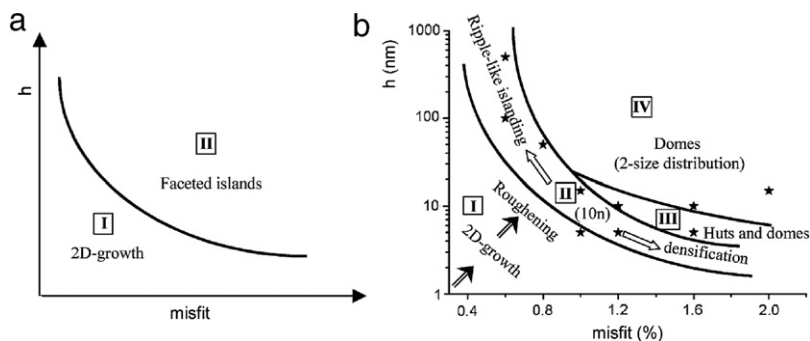


Fig. 3. Kinetic phase diagram (at $T = 550$ °C) representing the main growth regimes of $\text{Si}_{1-x}\text{Ge}_x$ layers as a function of the deposited thickness h and misfit m on (a) Si(111) and (b) Si(001).

Source: from [2].

with a height of only 3 unit cells can arise for a deposited thickness just below the critical thickness for the formation of three-dimensional islands.

On Si(111), only two growth regimes can be distinguished: 2D layer-by-layer growth at low (h, m) and classical Stranski-Krastanov growth at high (h, m). The latter case consists of dislocated islands that present extended facets oriented along (113) and (111) [2]. The transition between 2D growth of atomically flat layers and nucleation of 3D islands is very abrupt. Roughening processes such as growth instabilities and dislocation-free coherently strained islands were never observed on this substrate orientation. The very different morphological evolutions observed on Si(111) and Si(001) appeal for consideration of anisotropy on the growth dynamics.

2.1.2. Wetting layer growth

The first stage of growth corresponds to the formation of a flat wetting layer where the compressive strain may be relaxed [7] either by intermixing, creation of dimer vacancy lines or kinks and additional steps [37,38]. Intermixing [39,40] may lead to Ge present throughout the top four layers as seen in the following. The first stage is characterized by a layer by layer growth accompanied by a gradual increase in the surface roughness for increasing (h, m). In particular, it was shown that the roughness primarily consists of dimer vacancies [36], kinks and additional steps [37,38] that are assumed to allow strain-relief [41,42,33,43]. Further strain relaxation arises from dimer vacancy ordering [44,36,45,46] which modifies the original (2×1) reconstruction of Si and form a ($2 \times N$) reconstruction [28], see [1] for a review. Indeed, lateral relaxation of the last reconstructed layer is allowed by periodic arrangement of vacancies of complete dimers in the dimer rows [44]. For every N -th dimer, trenches of missing dimers allow for a partial reduction of strain by lateral relaxation of Ge near the trenches. A new periodicity is built up along the dimer lines and the original (2×1) reconstruction is converted into a ($2 \times N$) reconstruction which can further evolve into a ($M \times N$) reconstruction [36,47,42,31,1,48,49]. If trench formation minimizes the elastic energy, it is nevertheless compensated by the cost of the trench formation energy. The balance between the two determines the periodicity N of the reconstruction which may depend on the SiGe stoichiometry and strain [1]. In close connection with the change of surface reconstruction, the step geometry is also modified in the first stages of growth. Indeed, the ($2 \times N$) reconstruction introduces new Vacancy Site (VS) kinks along the S_A steps, with lower energy as compared to the normal dimer vacancies because of difference in local bonding, see Fig. 4 and [36]. The originally straight S_A steps of Si then roughen as the Ge coverage increases while the initially rough S_B steps become increasingly straight [7]. The reversal of the step roughness by the Ge adsorption is well evidenced on STM images of Fig. 5 [36]. It was shown that the development of the ($2 \times N$) reconstruction produces the variations of the step morphology since it introduces a new type of kink along the S_A steps and confines the meandering of the S_B steps. For the two types of steps, the step energy decreases monotonically as the Ge concentration increases. First because the strength of a Ge–Ge bond or Si–Ge bond is weaker than that of a Si–Si bond, an overall smaller step energy is expected as Si–Si bonds are replaced by Ge–Ge bonds. Second, at higher Ge coverage, the surface is more strongly strained and the elastic energy released by the creation of a step is larger, reducing also the step energy.

2.1.3. Morphological instability

For low enough strain, $x \lesssim 0.5$, a morphological instability [53,51,54–56,15,57,33,58] develops as a nucleationless process [33] which is reminiscent of the Asaro-Tiller-Grinfeld (ATG) instability [59,60] characterized by a spatial order on the surface with a typical wavelength, see next Section for its theoretical description [51]. The nucleationless evolution proceeds by the growth of mounds mostly along their height, which is accompanied by a continuous increase in the mound slope and step density (Fig. 6) [50]. Besides Si/Ge systems, the ATG instability was experimentally evidenced on mechanically stressed ^4He surfaces in Balibar group [61,62] following the observation of the modulation of a strained film [63]. It was also identified in polymerized polydiacetylene films deposited on their monomer substrate which induces a uniaxial stress [64]. Note that dewetting films or directional solidification under stress [65,66] may also involve this instability.

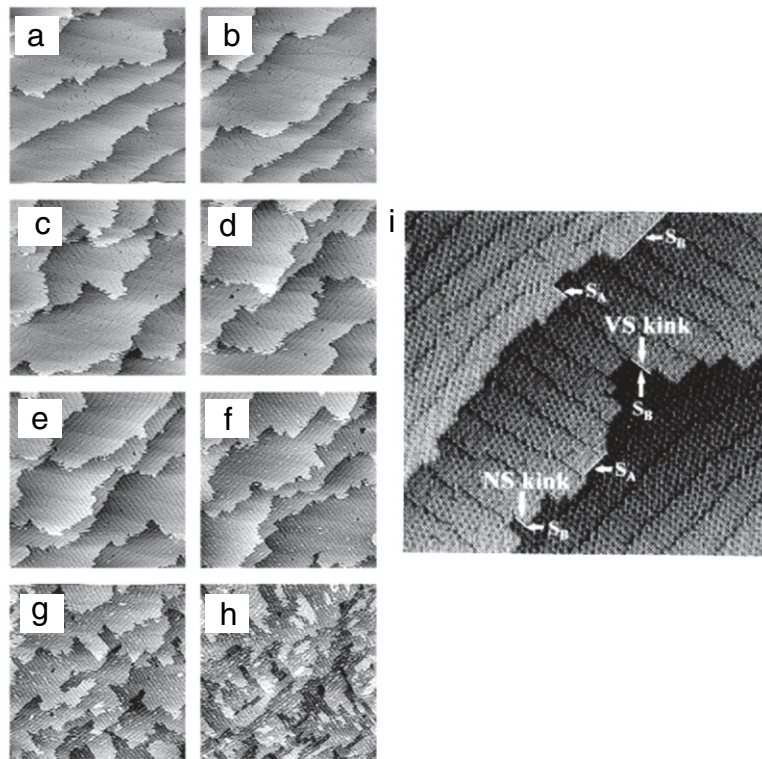


Fig. 4. STM images of the wetting layer during the growth of Ge on Si(001) and the evolution of the $(2 \times N)$ surface reconstruction (image area: $1600 \times 1600 \text{ \AA}^2$, $T = 575 \text{ K}$, Ge coverages: 0, 0.33, 0.62, 0.92, 1.26, 1.58, 1.82, and 2.11 ML in (a)–(h), respectively). The distance between the trenches of the $(2 \times N)$ reconstruction decreases with coverage. The orientation of the trenches rotates by 90° on neighboring terraces. (i) Shows atomically resolved structures of steps, kinks, dimer-vacancy lines and dimer rows perpendicular to these lines. Vacancy-site (VS) and normal-site (NS) kinks are shown along the S_A step.

Source: from [36].

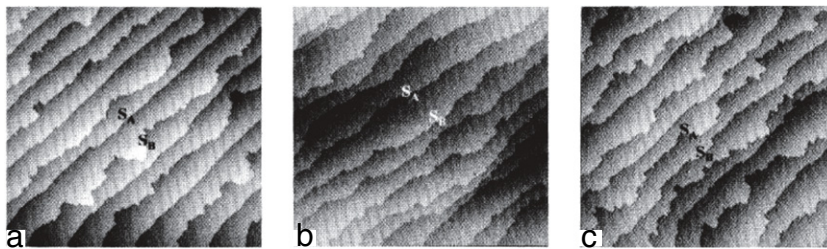


Fig. 5. STM image of vicinal Si(001) surface 0.3° miscut towards [110]. (a) clean surface; (b) Ge coverage $\sim 0.8 \text{ ML}$; (c) Ge coverage $\sim 1.6 \text{ ML}$.
Source: from [36].

The ATG instability was first evidenced in semiconductor epitaxy in InGaAs systems [69] and then in SiGe ones [51,53,15], see Figs. 7 and 8. As seen in the following, its basic theoretical description enforces a wavelength inversely proportional to the Young modulus and misfit square which was first roughly verified [51]. However, a better description is obtained when considering also alloying effect in the theory in order to find a suitable fit of the wavelength as a function of the film composition x (Fig. 9) [33,67]. Moreover, this instability is noticeably function of the system anisotropy: it arises on a Si(001) substrate (Fig. 8) but is inhibited on Si(111) even after long time annealing, pointing out the high stiffness of the latter orientation, see Fig. 12. Conversely, the (001) orientation is characterized by a low stiffness and its experimental properties may be explained by considering that it is a stable but not a facet orientation [34]. This conclusion is corroborated by the atomic-scale roughness visible on SiGe morphologies, see Fig. 11 [34], which is consistent with the hypothesis of thermally rough SiGe films on Si(001) and a vanishing or even negative step energy under strain. Indeed, atomistic calculations [68] show that under a compressive strain, the line energy of a step on Si(001) becomes negative. The latter energy λ_0 is defined as usual by writing the projected surface energy of a vicinal surface as

$$\gamma = \gamma_0 + \frac{\lambda_0}{a_t} |\tan \theta| + 2 \frac{\lambda_d}{a_t} |\tan \theta|^3, \quad (1)$$

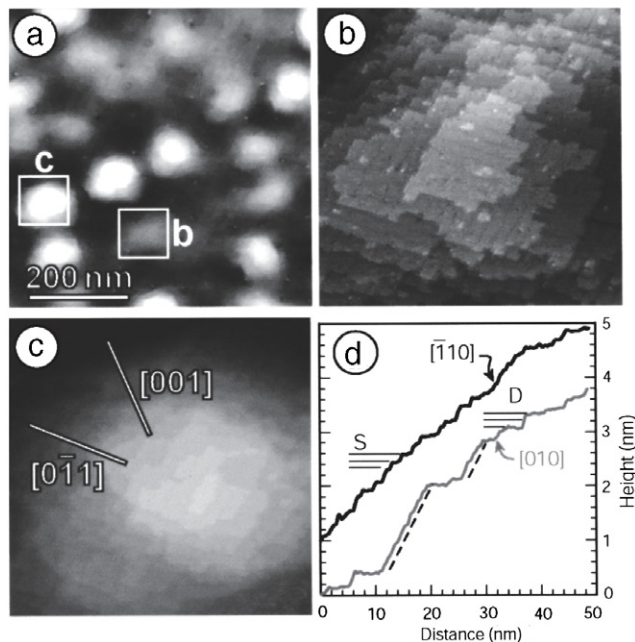


Fig. 6. (a) STM image of 40 ML $\text{Si}_{0.75}\text{Ge}_{0.25}$ grown on $\text{Si}(001)$ at 650°C . Mounds at an early and a later stage of their height evolution are labeled “b” and “c” respectively. (b) Closeup image of the shallow mound marked in (a), consisting of a stack of (001) terraces bounded by atomic steps. (c) Closeup image of the tall mound marked in (a), with lines indicating [001] and [011] directions in the substrate plane. (d) Surface profiles along the [001]/[011] lines in (c). “S”: single steps; “D”: double step; dashed lines: {105} facets.

Source: from [50].

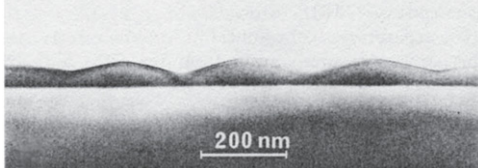


Fig. 7. Cross-sectional TEM images, viewed along a (100) direction, from a 40 nm-thick $\text{Si}_{1-x}\text{Ge}_x$ with $x = 0.21$ layer grown at 750°C .

Source: from [51].

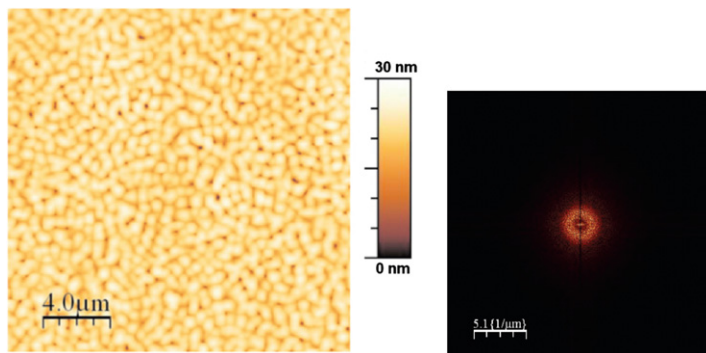


Fig. 8. (left) AFM top-view image of a 130 nm-thick as-grown $\text{Si}_{0.85}\text{Ge}_{0.15}$ layer on a $\text{Si}(001)$ substrate and (right) its Fourier transform.

Source: from [52].

where θ is the angle of the surface with respect to the substrate, while λ_d characterizes step interactions. The atomistic results lead to a negative line energy $\lambda_0 \sim -150 \text{ meV}/a_t$ for a 2% compression where a_t is the terrace width $a_t = 3.84 \text{ \AA}$, see Fig. 10 [68]. This estimate was corroborated by a linear elasticity analysis by computing the interaction between the step strain field and the uniform strain in the film [70]. This property precisely allows the nucleationless evolution of these films where a continuous deformation of an unfaceted surface starts on a nominal substrate.

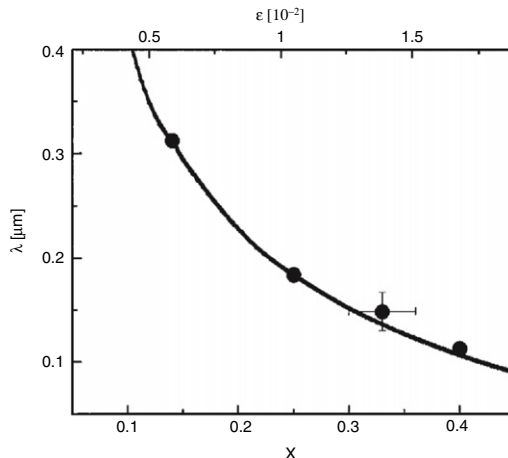


Fig. 9. Dependence of the wavelength λ of the initial cell pattern on Ge concentration, x , of the alloy film. Points denote values measured from LEEM images. The line is a calculation according to the model of Ref. [67], using a dimensionless growth rate $v = 10^{-3}$ and solute expansion coefficient $\eta^* = 0.5$. Source: from [33].

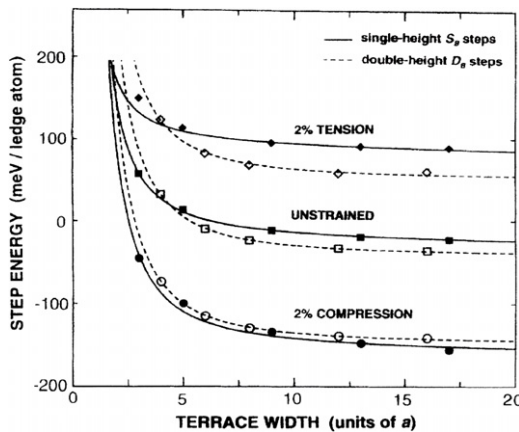


Fig. 10. Step energy per ledge atom versus terrace width for S_B steps (solid lines) and D_B steps (dashed lines) on a Si(001) surface under three different conditions of strain. The terrace width is in units of $a = a_0/\sqrt{2} = 3.94 \text{ \AA}$. The absolute step energy values are not accurate but the relative shifts due to strain are.

Source: from [68].

A remarkable feature is that the instability may occur for a small level of relaxation even if the latter is the driving force of the dynamics. Using convergent beam electron diffraction (CBED) and GIXRD, it was found that undulated layers of SiGe are almost fully strained with no measurable lateral elastic relaxation [56]. This conclusion is corroborated by strain analysis. If one considers theoretically the morphology given by the instability of a $\text{Si}_{0.75}\text{Ge}_{0.25}$ film on Si, see below, one finds that when the surface amplitude measured by the peak to peak difference is already 2 nm, the in-plane strain relaxation measured by $\epsilon_{\parallel} = \epsilon_{xx} + \epsilon_{yy}$ is quite small, see Fig. 13, and deviations from the full bi-axial strain (which is equal in this calculation to -0.021 for $x = 0.25$) are of order of $\Delta\epsilon_{\parallel} = 0.06\%$.

In the classical scheme of growth, the driving force of the instability at low misfit was discussed in [71] since kinetic instabilities and equilibrium processes may also come into play. Different mechanisms, island formation and step flow, were identified in [71] at low and high temperature. Some effects which may be accounted to describe the morphological instability are: (i) the anisotropic sticking or anisotropic diffusion of adatoms [72]; and (ii) different S_A and S_B steps advance rates in transient growth mode between 2D nucleation and step flow (leading to the formation of D_B double steps responsible of step bunching) [73].

2.1.4. Prepyramids

After its initial exponential growth, the fate of the ATG instability depends on the physical parameters. In ${}^4\text{He}$ films together as in thick SiGe films (nonetheless below the Matthews length characterizing dislocation introduction in a flat geometry), experiments reveal that the surface corrugation keeps growing until misfit dislocations and cracks arise on the surface which are spatially correlated with the instability [75,51,54,15,62]. Contrarily to the thick film case, another

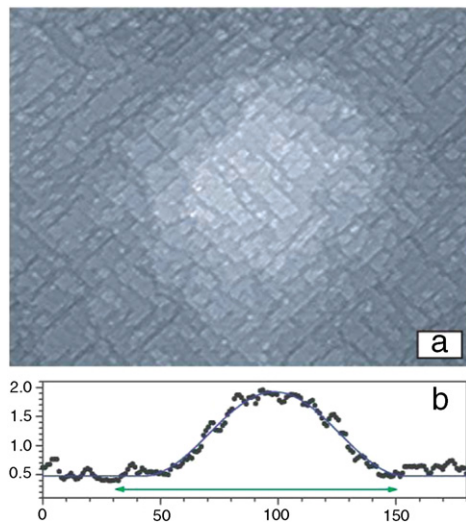


Fig. 11. (a) STM image ($114 \times 75 \text{ nm}^2$) of a small island obtained by depositing $\text{Si}_{0.5}\text{Ge}_{0.5}$ on $\text{Si}(001)$. (b) Line scan through island (dots) and cosine fit (line). Scan extends beyond the STM image, and a double arrow indicates the range of the image. Scale is in nm.
Source: from [34].

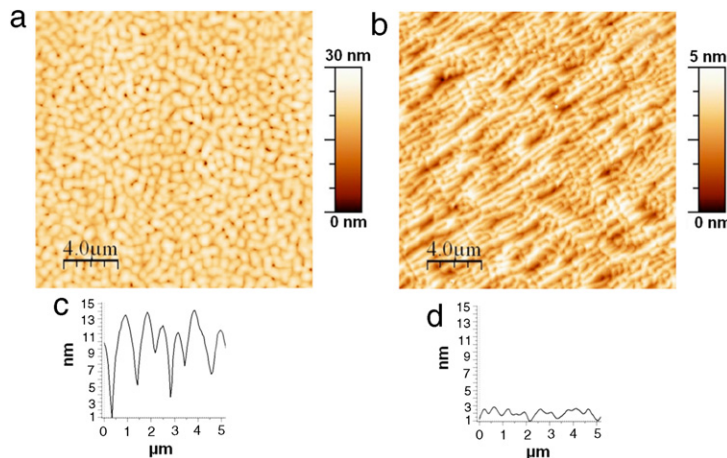


Fig. 12. (Color online) AFM top-view images of 130 nm-thick as-grown $\text{Si}_{0.85}\text{Ge}_{0.15}$ layers (a) on (001) Si substrate and (b) on (111) Si substrate; side views are shaped in (c) and (d) respectively.

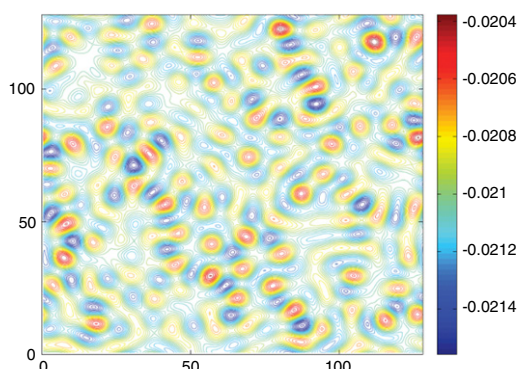


Fig. 13. (Color online) Strain map $\epsilon_{\parallel} = \epsilon_{xx} + \epsilon_{yy}$ on the surface with the film reference state based on a continuum calculation. The system corresponds to the initial stage of the ATG instability of a $\text{Si}_{0.7}\text{Ge}_{0.3}$ film with a peak to peak amplitude of 2 nm and a homogeneous composition. Note the negligible strain relaxation as opposed to the results in the late stage of the instability (see Fig. 28).

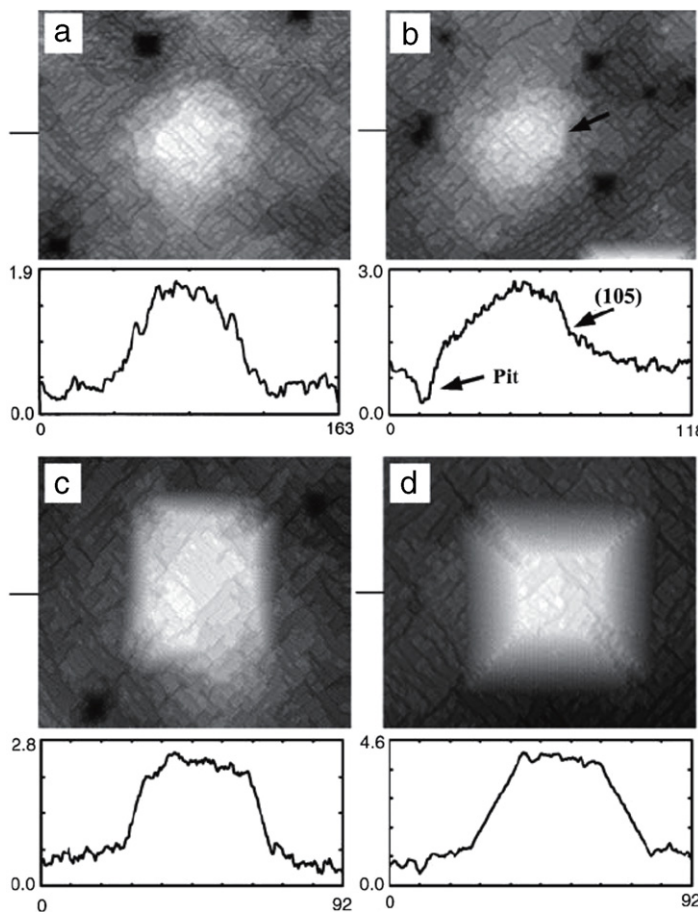


Fig. 14. STM images of precursors of {105} faceted pyramids at different stages of their evolution. Scale: (a) 163 nm × 132 nm (b) 118 nm × 95 nm (c) 92 nm × 80 nm (d) 92 nm × 80 nm. Every image is accompanied by a line scan taken along the [100] direction in correspondence with the black segment at the left side of the image (lengths are expressed in nm). Gray-scale according to height. Image sides are aligned along the [100] and [010] directions. The black arrow in (b) points at a small (105) facet.

Source: from [74].

scenario occurs in thin films where wetting interactions come into play. In this case, the development of the ATG instability in experiments leads to growing mounds which form islands separated by a wetting layer, see Fig. 14 [57,33,58]. These mounds called prepyramids have rounded shapes and undergo some coarsening until faceted islands arise as discussed in the following [19,2,76,74,50]. This evolution allows for a barrierless island formation [34] as wetting layer prevents the instability to deepen into the substrate.

As a consequence, regime II on Si(001) in Fig. 3(b) is characterized by ripple-like islands that exhibit a broad distribution in size and in shape either at low h or low m . The striking feature of these ripple-like islands is their side orientation along (100) directions. Furthermore, at increasing thickness, they elongate in chains or in square patterns still oriented along [100] and [010] (Fig. 15). They present very small aspect ratios (height H over width L , $H/L \sim 0.03$), small side angles below 11.3° and no extended facets on their sides (various (10n) orientations were measured). Such undulations are nearly fully strained since no noticeable relaxation is found by GIXRD (in agreement with previous measurements obtained by convergent beam electron diffraction (CBED)).

The strain map resulting from a given surface shape may be computed by different means (see Ref. [4] for a detailed review): (i) atomistic calculation where one minimizes the total energy which may be computed as the sum of pair or triplet potentials, or nearest-neighbor interactions with Stillinger–Weber or Tersoff potential for SiGe; (ii) finite element method (FEM) for solving the partial differential equations of the mechanical equilibrium, where a good choice of the elastic constants C_{jk} can lead to a good comparison with the elastic properties of nanoscale islands, see Fig. 17 [77,78]; (iii) analytical resolution of the Lamé equations, which can be done exactly in two dimensions, see e.g. [79] or, with a wide domain of validity for SiGe dots, within the small-slope approximation when elasticity is solved thanks to series in the film slope which is assumed to be small.

The general findings for a given shape and a homogeneous concentration field may be exemplified by the solution of the elasticity equations solved numerically using the boundary integral method in two-dimensions [80] as depicted in Fig. 16.

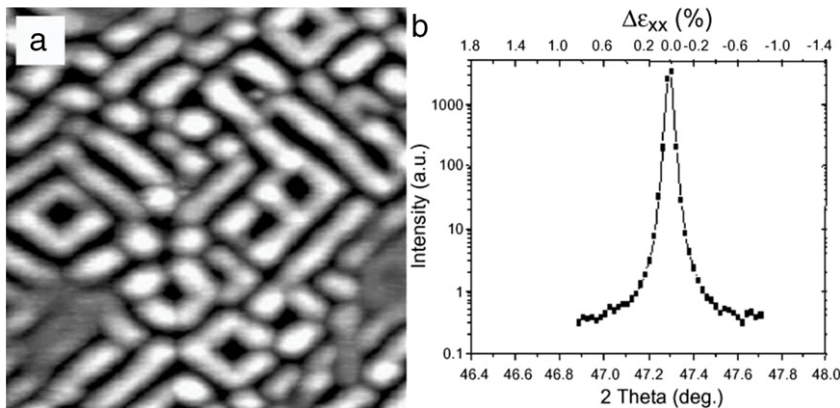


Fig. 15. AFM image ($5 \times 5 \mu\text{m}^2$) of ripple-like islands elongated along (100) and (010) directions, regime II, for $\text{Si}_{0.85}\text{Ge}_{0.15}$ ($m \sim 0.6\%$, $h = 100 \text{ nm}$) with [110] horizontal; (b) 2θ GIXRD spectrum which shows the very sharp peak of $\text{Si}_{1-x}\text{Ge}_x$ layer fully coherent with the Si substrate.

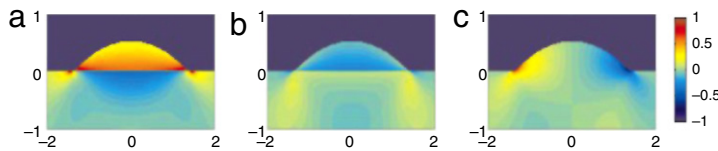


Fig. 16. (Color online) Strains of equilibrium islands, scaled relative to the strain for a planar film (a) ϵ_{xx} , (b) ϵ_{zz} and (c) ϵ_{xz} . (Note the change of strain sign as compared with forthcoming results due to the choice of a reference where the substrate is uniformly stressed at infinity.)
Source: from [80].

The main properties are the following: (i) stress relaxation occurs mainly at the island peak, where the misfit stress may even vanish; (ii) stress is mainly concentrated in the island and in the substrate near the island edge; (iii) stress relaxation in the island is conjugate with the deformation of the substrate which is proportional with an opposite sign to the film relaxation; (iv) stress decay in the substrate in the vertical direction within a few island heights. These results corroborate the solution of the elastic field obtained by finite element minimization as sketched in Fig. 17.

2.1.5. 2D/3D transition

Contrarily to the smooth and continuous evolution observed in the low strain regime, islands appear in high strained films by a sudden and disordered mechanism. In the high strain regime, $0.5 \leq x \leq 1$, islands arise from a 3D nucleation process [81,82]. Quantitative estimate of fluctuations [49] indicate that large thermal fluctuations involving many atoms, are required. When the film thickness exceeds 3 ML for Ge on Si(001) [13,14], 2 bilayers (BL) on Si(111) [83] and 8 ML for tensile Si on Ge(001) [84], a 2D–3D transition occurs where 2D nuclei promptly transform into islands [85–88]. These islands again enable strain relaxation and result from the competition between strain relaxation and the stabilizing surface energy [16].

As regards Ge on Si(001), 2D islands first evolve into small 3D prepyramid embryo [89,82,1,74,90] which act as subcritical nuclei for subsequent nucleation and result from thermal fluctuations. These embryo can nucleate near surface defects such as pits, step edges or irregularities on the surface reconstruction [91,1]. Thermal fluctuations at 575 K produce small nuclei with up to 270 atoms that are subcritical and shrink, while large enough nuclei grow and display shallow unfaceted mound shapes. The prepyramids are only present for a narrow range of Ge coverages [89] before (105) facets appear (Fig. 18).

2.1.6. Hut islands

In the low strain regime, prepyramids undergo some coarsening where the smallest ones disappear to the benefit of larger ones. As a consequence they increase their aspect ratio and display steeper side angles until they reach 11.3° corresponding to (105) facets (as measured by AFM and HRTEM cross-section), see Figs. 14 and 19 [76,74]. The (105) facet is particular to strained SiGe systems as it is not an equilibrium orientation but is stabilized by the surface reconstruction under stress [92–96], see Section 3.3.1. These islands are usually called huts because they adopt a pyramidal shape with four (105) facets and a base oriented along [100] directions [14] and do not display (001) facets on their top, see the TEM cross-section in Fig. 20. Their shape evolves towards elongated rectangular base islands for increasing h (Fig. 21(a)) and towards highly dense square based islands for increasing m (Fig. 21(b)) while their strain relaxation remain constant and low (Fig. 22). The coexistence of both square and rectangular shapes may result from the growth dynamics which can prevent the thermodynamically stable square shape [97] or from energetic effects for large enough clusters [98]. Note that on a Si(111) substrate, Ge islands develop tetrahedron like shapes bounded by (113) facets [83,99,1], while islands grown by liquid phase epitaxy (LPE) display

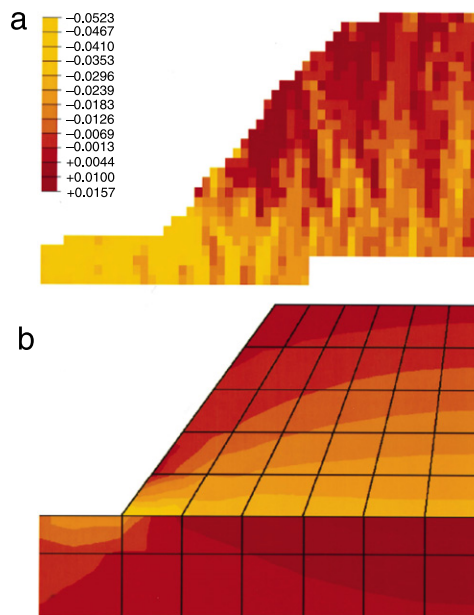


Fig. 17. (Color online) (a) Strain, ϵ_{xx} measured from a high resolution TEM image. The colors are proportional to the strain, dark red is $+1.6\%$, light yellow is -5.2% . (b) The strain, ϵ_{xx} calculated by FEM. The scale is the same as in (a). The apparent discrepancy at the interface is caused by the different reference lattices used in the two methods. In the HRTEM-based measure, the strain is calculated relative to the selected reference lattice close to the top of the island, whereas in the FEM-based calculation, the strain on either side of the interface of the dot and the substrate is calculated relative to the bulk lattice parameters.

Source: from [77].

truncated pyramidal shapes with {111} side facets and a (001) top facet, see Fig. 23 [78], presumably {115} facets [100], and may also align along chains on the elastically soft <100> directions [101].

On the contrary, in the high strain regime, real-time STM observations of the nucleation of (105) islands [102] shows that the formation of hut islands is preceded by the nucleation of subcritical nuclei and not gradual faceting of prepyramids as observed in the low strain regime, see Figs. 18 and 24. The latter nuclei consist of two adjacent truncated tetrahedral pyramids, which, upon unification, form a tiny square-based pyramidal critical nucleus, see Fig. 24 [90]. Their subsequent growth was shown to occur from their base where new material arrives, see Fig. 25 [103]. The nuclei of the square and rectangular hut pyramids were also observed and found to have different structures. In rectangular huts, the formation of the second atomic layer results in a rearrangement of its first layer. On the contrary, the square hut pyramid grows without transitions and the structure of its vertex reflects the structure of the nucleus, see Fig. 26 [104].

The onset of hut islands corresponds to an elastic relaxation which may be experimentally evidenced either by its mean global effect or more precisely by local strain maps [28]. As regards the global characterization, the use of X-rays proved to be valuable either using GIXRD or grazing incidence small angle X-ray scattering (GISAXS), see Ref. [28] for a recent summary. Probing the vicinity of the Bragg peak around the (220) direction, the GIXRD analysis reveals a local maximum associated with a partial lattice relaxation due to island formation. The general trend corresponds a compressed island lying on a substrate under tensile stress.

The first hut pyramids arising from the surface initial corrugation are still not significantly relaxed, see Fig. 29(b). The diffraction pattern of the initial hut islands display a sharp peak associated with the silicon substrate, centered on the mean of a Gaussian curve associated with islands, which display no measurable relaxation. However, after 18 h annealing of a 50 Å thick $\text{Si}_{0.75}\text{Ge}_{0.25}$ film, see Fig. 29, small hut islands are replaced by large isolated hut islands which display a larger relaxation. The GIXRD analysis [105] shows that $\Delta\epsilon_{xx} = 0.244\%$, see Fig. 29(c), which corresponds to a relative elastic relaxation of 25% of the initial strain and is attributed to the pyramidal shape. Applied to a $\text{Si}_{0.7}\text{Ge}_{0.3}$ film, this technique shows that hut islands are associated to a 16% relaxation [106]. No further evolution of the morphology nor of the relaxation occurs during the following 46 h annealing [2] so that one can conclude that the steady state morphology in this range of parameters consists of (105) hut islands, see Section 3.7 for a discussion of coarsening.

In-situ analysis of the global stress can also be achieved thanks to the measure of the bending of the film-substrate system [107]. Indeed, the film/substrate system can be designed as a cantilever free to be bend when the mismatch stress increases during the film deposition. Monitoring this effect by looking at the deflection of a laser beam leads to a real-time measure of stress relaxation. The onset of pyramids is betrayed by a change of slope of the stress-thickness versus thickness plot, and leads to an estimate of the global stress relaxation of the order of 20% for a $\text{Si}_{0.8}\text{Ge}_{0.2}$ film on Si.

Beside the mean stress relaxation, strain maps are also important to characterize further the island properties. As the composition evolves rather abruptly at the island/substrate interface, the strain changes its sign from positive (tensile) to

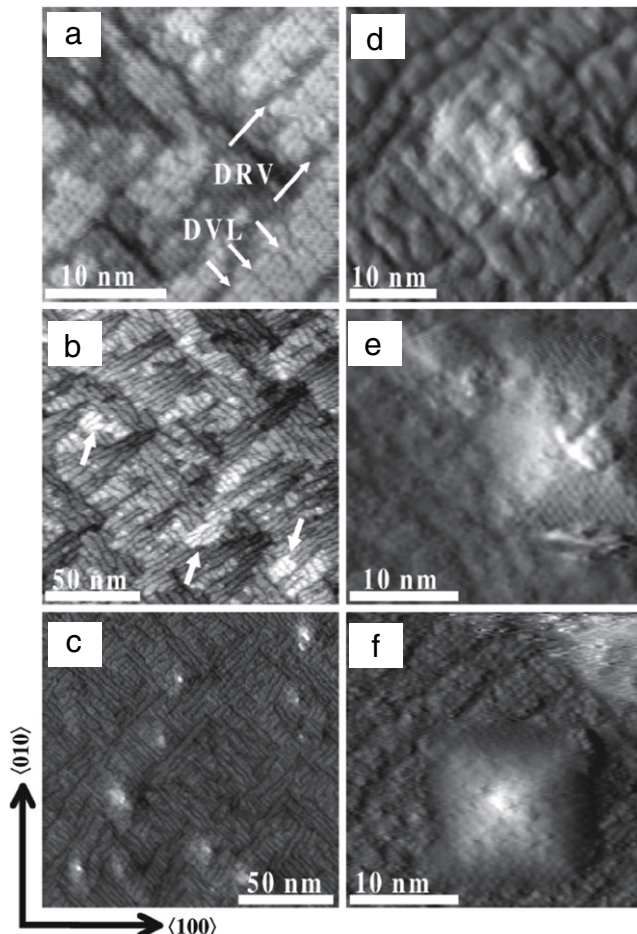


Fig. 18. STM images showing the evolution of Ge grown on Si(001) : (a), (b) 2D wetting layer at $\theta_{Ge} = 2.8$ and 2.9 ML, respectively, (c) 3D prepyramid islands at $\theta_{Ge} = 3.55$ ML, (d) initial prepyramid island at $\theta_{Ge} = 3.55$ ML, (e)(001)-truncated $\{105\}$ -faceted pyramid at $\theta_{Ge} = 3.85$ ML, and (f) completely formed $\{105\}$ -faceted pyramid at $\theta_{Ge} = 4.0$ ML. DVL and DRV are dimer vacancy lines and dimer row vacancies, respectively. 2D islands in (b) are labeled with arrows. The images are partially differentiated to enhance the details and they appear side lit from the lower left corner.
Source: from [89].

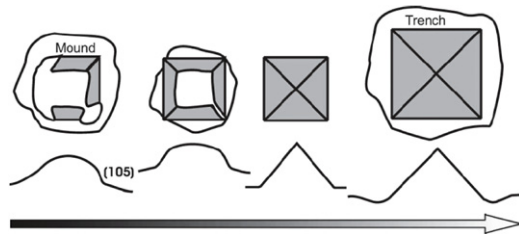


Fig. 19. Schematic representation of the prepyramid to pyramid evolution: plan (up) and side (down) view. In the plan view, shaded areas represent $\{105\}$ facets.
Source: from [74].

negative (compressive), see Fig. 27 for a general sketch and Fig. 28 for an estimate of the lateral strain relaxation from simulations. In the following, we write z the coordinate along the growth direction perpendicular to the substrate plane characterized by the 2D vector \mathbf{r} . A first result was obtained for Ge islands on Si [109] matching X-ray diffraction (XRD) profiles around Bragg peaks with different calculations assuming different laws for the effective lattice parameter as a function of the height in the film. This method allows to scan partially averaged strain relaxation and the best fit is obtained for a quadratic dependence in the island $a_{eff}(z) = a_{bottom} + (a_{top} - a_{bottom})(z/h)^2$. At the Ge/Si interface, the Ge clusters are almost fully strained with a misfit of only 0.5% compared to Si. On the other hand, the strain at the island apex is almost fully relaxed and the atomic spacing is close to the natural Ge lattice spacing with a 4.2% misfit. A similar approach

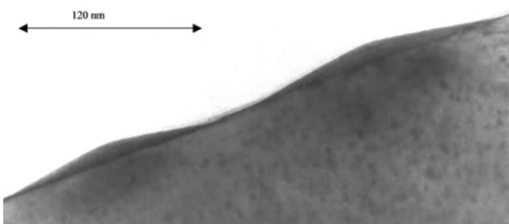


Fig. 20. TEM cross-section of huts obtained for a 5 nm thick $\text{Si}_{0.7}\text{Ge}_{0.3}$ film ($m = 1.2\%$).

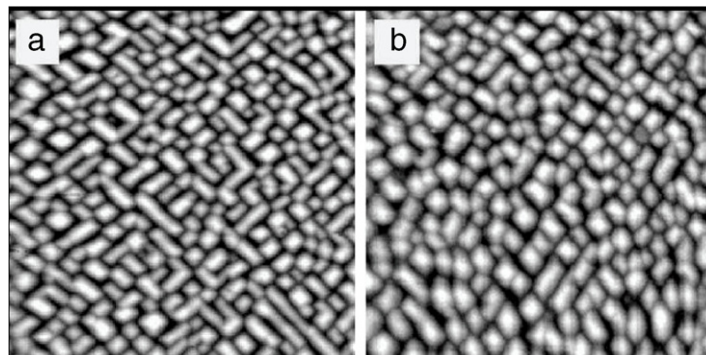


Fig. 21. AFM image of $\text{Si}_{1-x}\text{Ge}_x$ surfaces obtained in regime II, for the following deposits: (a) $x = 0.3$ ($m \sim 1.2\%$), $h = 10 \text{ nm}$ and (b) $x = 0.38$ ($m \sim 1.6\%$), $h = 5 \text{ nm}$. Scan size is $2 \mu\text{m}$.

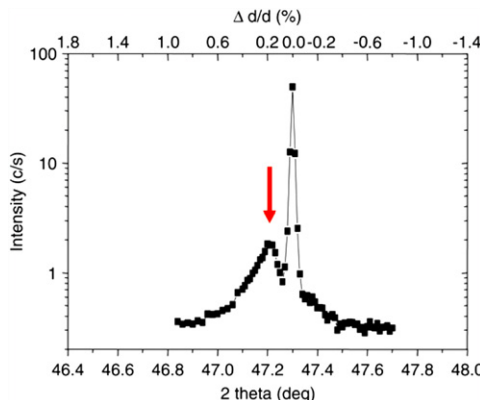


Fig. 22. GIXRD spectrum of the sample. It shows a small lateral relaxation of the deposit.
Source: from [7].

augmented by the account of the composition in the islands leads to similar but less pronounced results, see Fig. 30 [108]. In this approach, both in-plane and perpendicular lattice parameters are measured by measuring reciprocal space maps with a positive component of the momentum transfer along the growth direction. Fig. 30 shows the calculated reciprocal space maps with the best fitting Ge distribution which is assumed to depend only on z (with a maximum content of $x = 1$ at the top of the island, and $x = 0.5$ at its base). Even at the island top, the elastic relaxation is only about 50% in contrast to, e.g., InAs islands on GaAs, which have a higher lattice mismatch and a higher aspect ratio [110]. Raman scattering spectra also prove to be a powerful tool for analyzing strain maps and provide quantitative results regarding average composition and both the $\epsilon_{||}$ and ϵ_{zz} strain components [111]. The results are displayed in Fig. 31 and show significant strain relaxation within the core of the islands, with a rather low global strain relaxation of the order of 18%.

The previous analyses reveal global trends for the local strain but through an average process performed on different islands. The usually large diffracted beam is produced by different islands which display size and shape inhomogeneity resulting in a smearing of the diffraction pattern. Scanning of individual islands allow to circumvent this drawback but requires analysis of weaker signals. This can be achieved using focused X-ray beams [112–114] which compensate for the smaller diffraction given by a single nanostructure. One example for a single SiGe island grown in liquid phase epitaxy [113] shows that the top of a truncated pyramid is fully relaxed. In this approach, the Ge concentration profile is adapted to reach

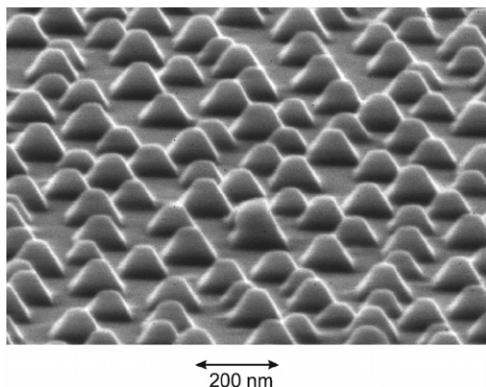


Fig. 23. Scanning electron micrograph of a $\text{Si}_{0.75}\text{Ge}_{0.25}/\text{Si}(001)$ layer. The sample consists of coherently strained truncated pyramids exhibiting {111} side facets and a (001) top facet. The island base width and height are about 135 and 80 nm, respectively, with a narrow size distribution.
Source: from [78].

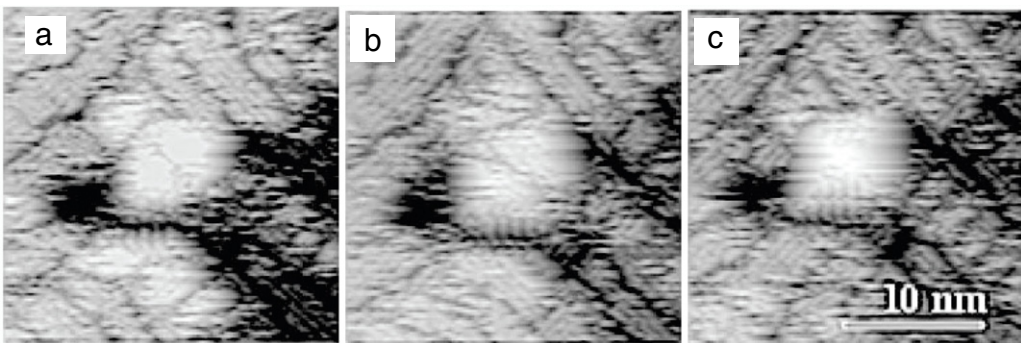


Fig. 24. Nucleation of a {105}-pyramidal hut at 420 °C. Under proper contrast conditions the {105} faceting shows already at the most initial stages, such as in (a) and (b) still in the split configuration, as well as in the full pyramid in (c).
Source: from [90].

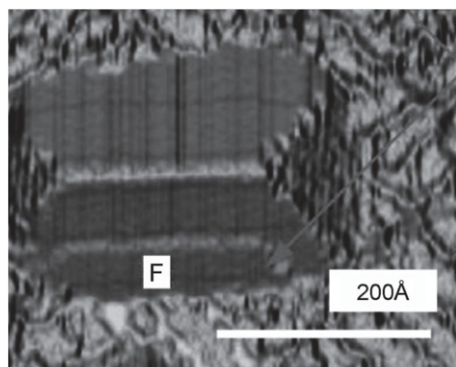


Fig. 25. STM image of a hut pyramid observed during CVD growth. An incomplete hut cluster facet is marked by an "F". The new nucleated material covers the bottom of the hut cluster facet.
Source: from [103].

a close match between measurements and simulations. The average strain along the beam direction projected onto the film/substrate interface, see Fig. 32, can be computed for these islands and is displayed in Fig. 33. The main trends follow the expected ones: the strain is maximum at the central part of the island and lower at the bottom, especially at the lower corners [114].

Finally, another technique leading to individual scanning is the transmission electron microscopy phase imaging method [115]. This method consists in retrieving the diffraction phase from a focus series of plane view images and provides insights on the full strain $\epsilon = \epsilon_{\parallel} + \epsilon_{zz}$ and composition fields integrated along the beam direction with the resolution of atomic columns. Applied to SiGe hut pyramids, it reveals that the integrated strain along the vertical direction displays a

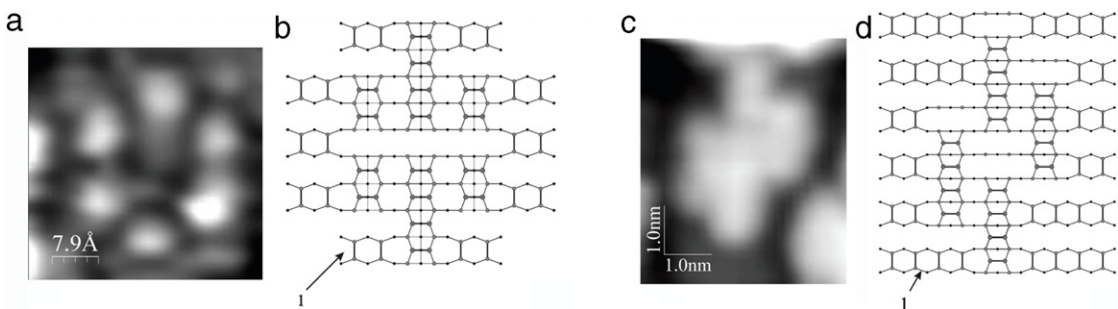


Fig. 26. Nuclei of Ge hut clusters: (a) and (c) STM empty-state images and [(b) and (d)] atomic structures of the (a) and (b) pyramid and [(c) and (d)] wedge nuclei, symbol 1 is WL.
Source: from [104].

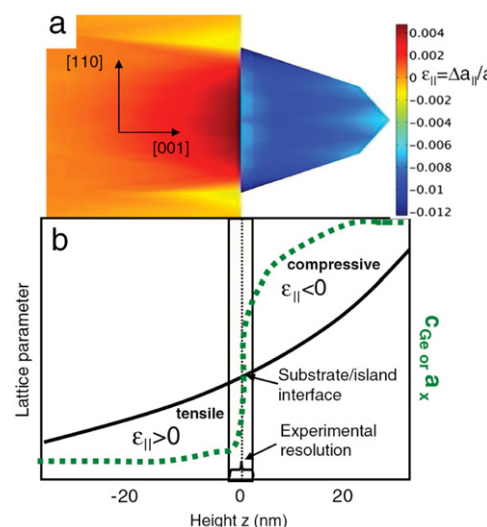


Fig. 27. (a) Simulation of the strain inside a SiGe island on Si(001) (note that the shape is not to scale). (b) Sketch of the mean evolution of the lattice parameter (full line) and the Ge content or the equilibrium lattice parameter a_x (dashed line) as a function of height inside the substrate and the island. The experimental resolution is indicated as a shaded bar.
Source: from [28].

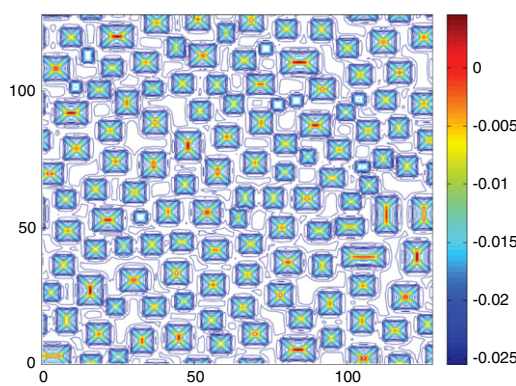


Fig. 28. (Color online) Strain map $\epsilon_{xx} + \epsilon_{yy}$ on the surface in the final stage of the evolution initially depicted in Fig. 13.

compressive maximum at the vertical of the island apex, see Fig. 34 [116]. This trend which may at first glance seem to contradict the general one, can in fact be rationalized by integrating the total strain ϵ in the growth direction.

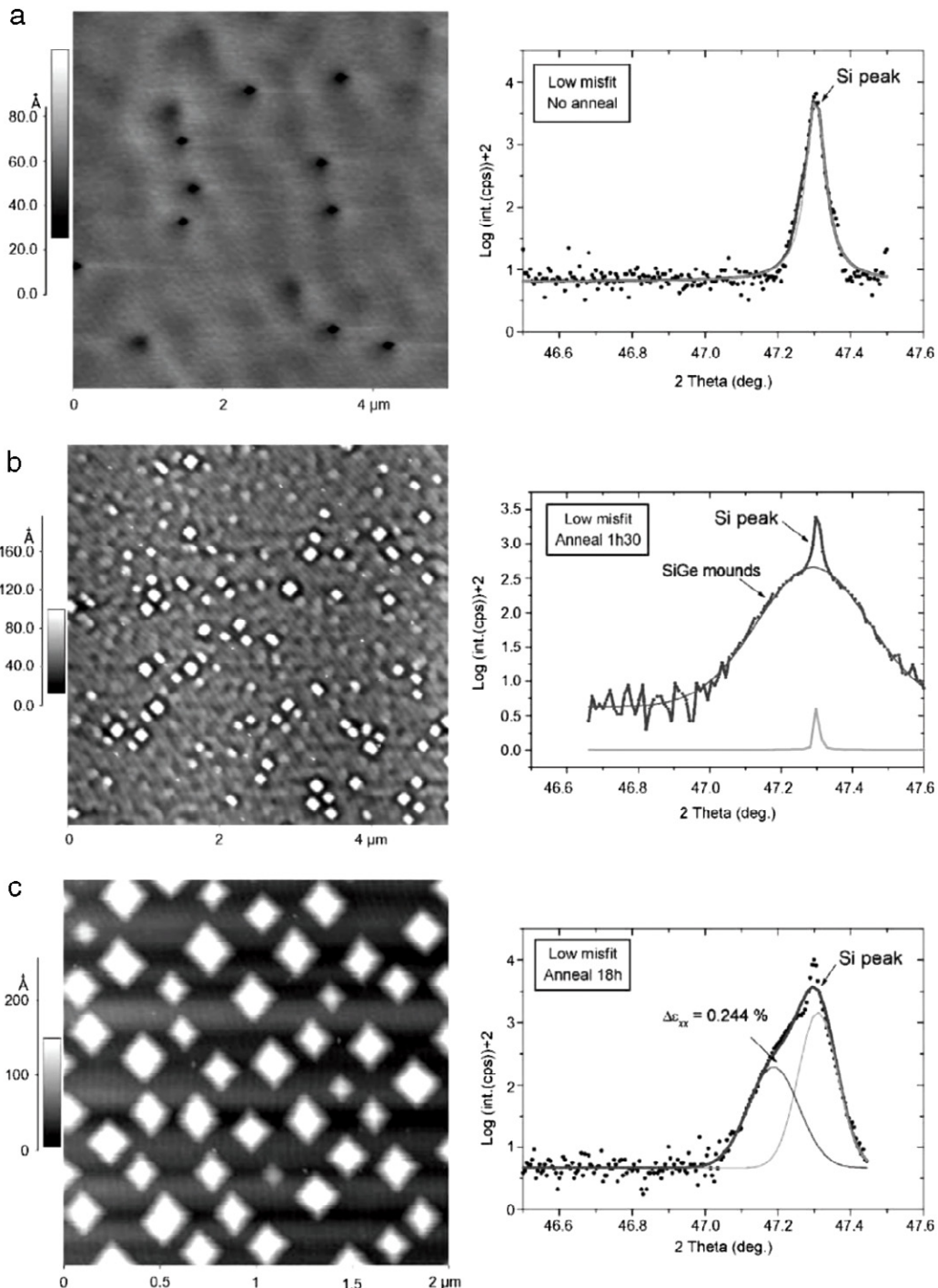


Fig. 29. Evolution of the morphology (AFM images on the left) and of the stress relaxation (GIXRD spectra on the right) of a $\text{Si}_{0.75}\text{Ge}_{0.25}$ layer ($m = 1\%$) 50 Å thick during an annealing at 550 °C: (a) as-grown; (b) 1.5 h anneal; (c) 18 h anneal. In the AFM images the [110] direction is horizontal.

2.1.7. Hut islands and vicinal substrates

The influence of the atomic steps of a vicinal substrate on hut islands [117,7] was systematically investigated by considering $\text{Si}_{1-x}\text{Ge}_x$ films on Si with orientations near (001) in regime II. Misorientation angles were varied from 1° to 10° off in the [110] direction [106,2]. Hut islands that are still visible on the 1° off substrate (Fig. 35(a)) transform in triangular based islands on a 4° off substrate (Fig. 35(b)). At 6° off they display very anisotropic shapes with their length elongated perpendicularly to the step edges (Fig. 35(c)). On the 10° off substrate, islands transform in wires with an anisotropic

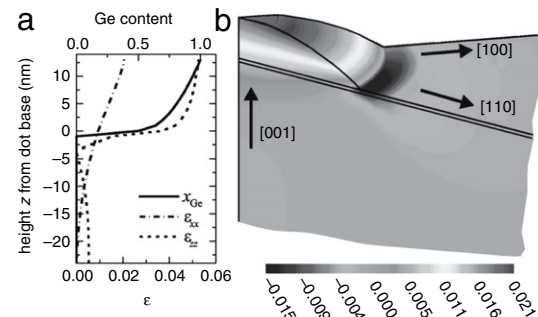


Fig. 30. (a) Ge distribution and variation of strain components ϵ_{xx} and ϵ_{zz} along the growth direction, and (b) ϵ_{xx} strain distribution in the SiGe island. The elastic strain relaxation in the islands reaches a maximum of only about 50% at the island top (with the Si reference state).
Source: from [108].

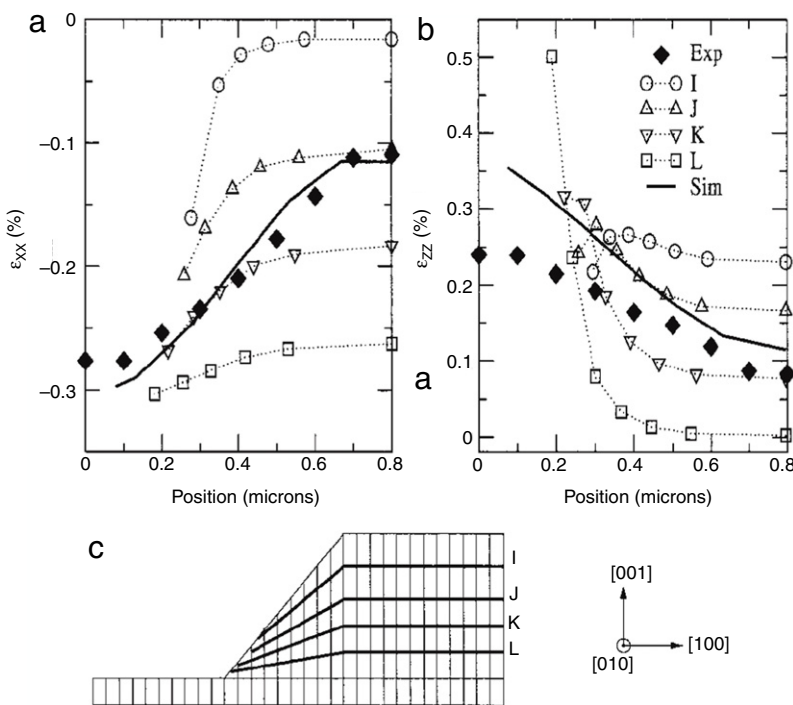


Fig. 31. Experimental strain (filled diamond) calculated on a square island vs spatial position: (a) ϵ_{xx} , and (b) ϵ_{zz} . I, J, K, and L represent strain profiles calculated at different levels in the island; see (c). Solid lines are simulated profiles including the convolution by the Raman probing volume. (Note that the horizontal coordinate starts from 0 at the island edge while it ends at the island center and the Ge reference state is used.)
Source: from [111].

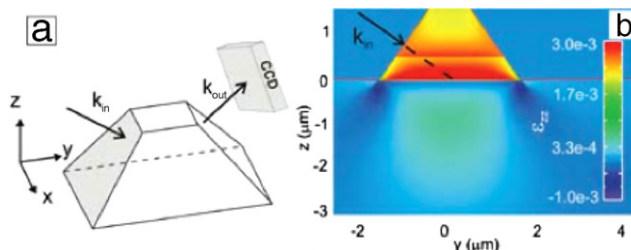


Fig. 32. (Color online) (a) Scattering geometry of the experiment. (b) FEM calculation of the ϵ_{zz} strain tensor component. The SiGe island has a square base of $3.2 \mu\text{m}$ length and a height of $1.6 \mu\text{m}$. In the calculation a 4.6% Ge concentration in the lower third and 5.3% in the upper two-thirds of the island.
Source: from [114].

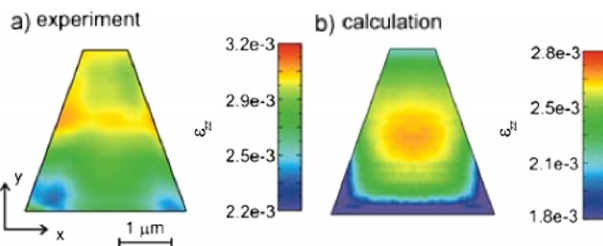


Fig. 33. (Color online) (a) ϵ_{zz} strain tensor component projected onto the beam direction extracted from the measured diffraction patterns. Only the scanned region corresponding to the front facet is shown. (b) Average ϵ_{zz} projected along the incoming beam through the SiGe island from a 3D FEM calculation.

Source: from [114].

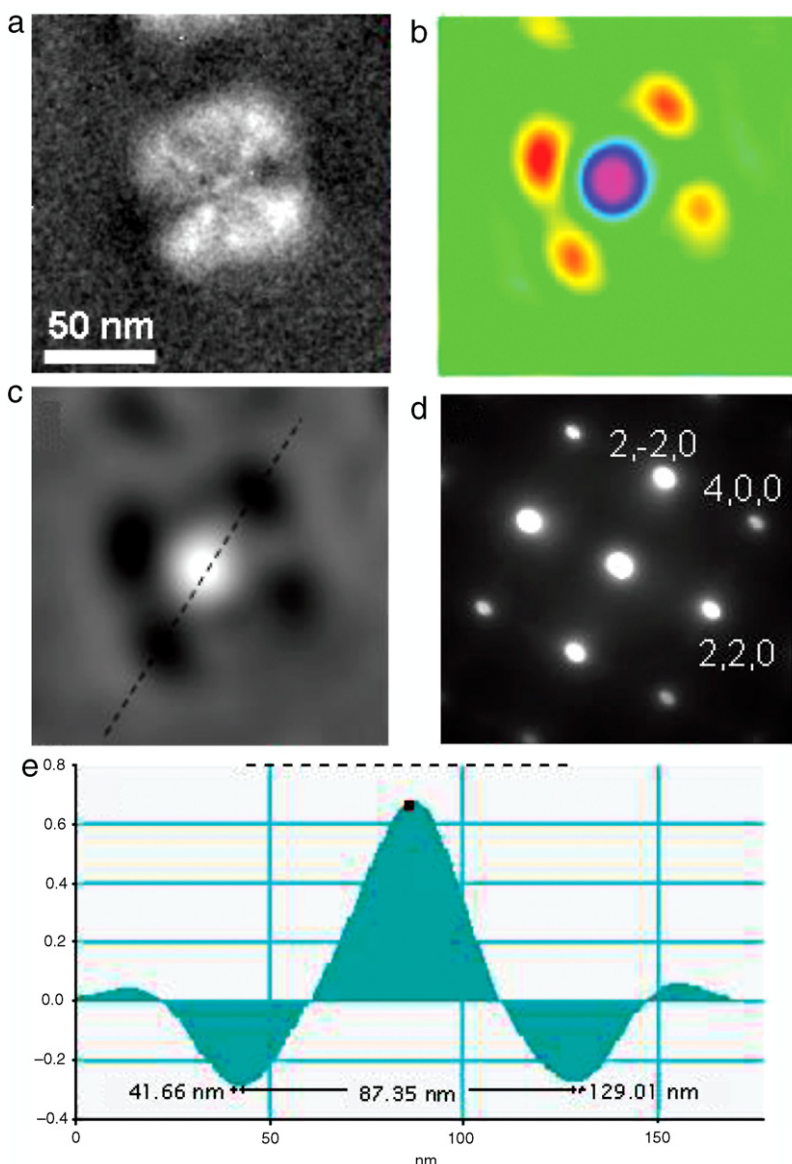


Fig. 34. (Color online) Phase map analysis of a hut pyramid. (a) TEM high magnification image of the nanostructure. (b) and (c) phase images of (a). The diffraction pattern in (d) indicates the direction of the line crossing the negative phase lobes is a $[1 -1 0]$ direction. (e) Displays the profile taken along this direction (phase in radian).

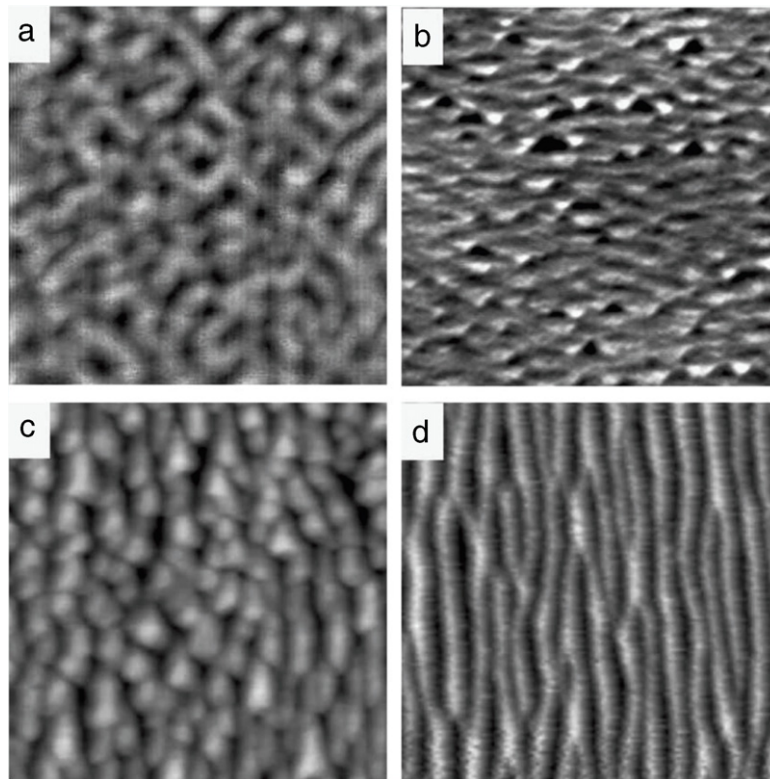


Fig. 35. Morphological evolution of Si_{0.7}Ge_{0.3} islands with $h = 10$ nm deposited on misoriented substrates with a miscut angle of: (a) 1°; (b) 4°; (c) 6°; (d) 10°. AFM images are $2 \times 2 \mu\text{m}^2$ with [110] direction (step edges) horizontal.

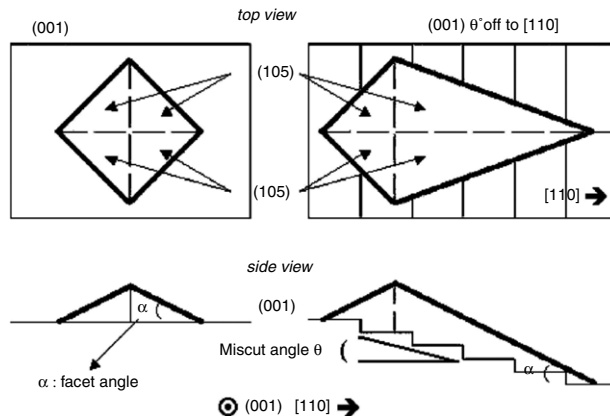


Fig. 36. Schematic representation of islands lying on a misoriented surface.

coefficient ratio of 10 which are elongated perpendicularly to the step edges. This elongation perpendicularly to the step edges only reflects the reduction of the angle between the substrate orientation and the (105) facets as schematized in Fig. 36. These elongated shapes which preserve the stabilizing (105) orientation are produced for Ge on vicinal Si(001) [118] in coherence with the same shapes produced at the end of the ATG instability on such substrates [105]. In fact, the side walls of all the islands observed on orientations close to (001) (with pyramidal, triangular or wire shapes) consist of (105) facets which are still ruling the island shapes. During long-term annealing, the wire shaped islands formed on a 10° off substrate (Fig. 37(a)) undergo the same transition than the hut islands produced on nominal (001) and merge into large isolated triangular islands with extended (113) and (111) facets (Fig. 37(b) and (c)).

The stabilization of (105) facets during the early stages of Ge deposition under compressive strain was deeply investigated, see e.g. [92,93]. High resolution STM images of the surface demonstrated a new atomistic mechanism of (105) formation [119]. This mechanism was particularly well evidenced on misoriented substrates where the (105) develop in the

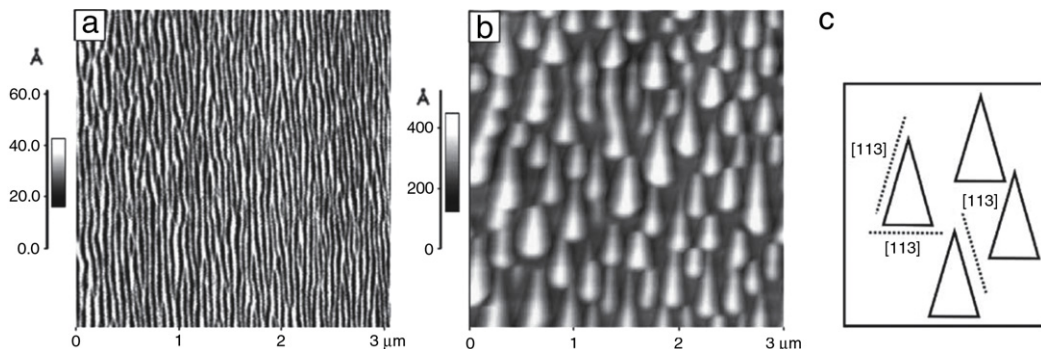


Fig. 37. AFM image ($3 \times 3 \mu\text{m}^2$) of $\text{Si}_{0.7}\text{Ge}_{0.3}$ islands obtained for a deposited thickness of 10 nm: (a) as-grown; (b) 18 h anneal; (c) is a schematic representation of (113) facets in the annealed sample.

Source: from [105].

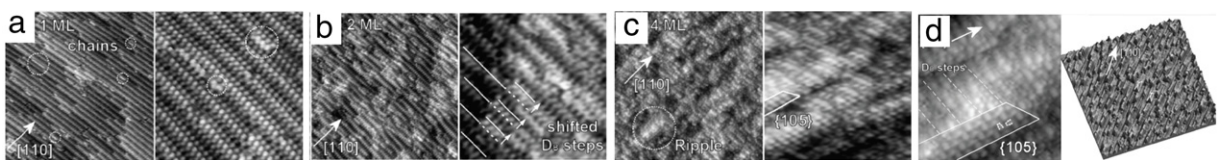


Fig. 38. STM images of the $\text{Si}(001)$ 8° off misoriented surface during the early stages of Ge deposition, after the deposition of (a) 1 ML; (b) 3 ML; (c) 4 ML; (d) 6 ML.

Source: from [119].

shape of unidirectional ripples perpendicular to the step edges. A series of STM snapshots were recorded after successive deposition sets, in order to follow the morphological changes from the (2×1) initial surface to the (105) faceted surface [119]. It was observed that after deposition of 0.5 ML of Ge, the train of D_B steps becomes regular implying a strong reduction in the defect density. Instead of the usual (2×1) one, the $p(2 \times 2)$ reconstruction is observed on terraces. At 1 ML coverage, this reconstruction covers the whole surface and single atoms protrude at the step edge and short zigzag chains appear on the terraces (Fig. 38(a)). At 3 ML coverage new domains consisting of D_B steps equally shifted in the [110] direction appear (Fig. 38(b)). These domains are elongated towards the miscut direction and have irregular borders in the other directions. They represent the precursor state of the (105) facets. At 4 ML coverage (Fig. 38(c)), an abrupt morphological transition takes place with the onset of (105) domains oriented perpendicularly to the D_B step edge. These facets extend along the miscut direction, forming elongated ripples periodically distributed perpendicular to the step edges for larger deposited thickness (Fig. 38(d)). Finally, note that it was shown recently that on high-indexed substrates such as $\text{Si}(1110)$, the usual Stranski-Krastanov growth mode described above is replaced by a kinetics driven solely by surface energy and edge energy, which leads to the abrupt formation of a faceted wetting layer [120].

Contrarily to the low ordering effect of steps on vicinal $\text{Si}(001)$ [121,122], steps on $\text{Si}(111)$ prove to have a sensible influence on the QDs organization. Islands on 1° off (111) substrate are self-aligned along the upper edges of the steps [123], at least for moderate growth temperatures. On 0.3° off $\text{Si}(111)$ substrate, islands first decorate step edges but latter nucleate in the middle of terraces [124]. Another configuration concerns QDs grown on step bunches on vicinal $\text{Si}(001)$ which are located in the valley between steps bunches [7]. Recall that vicinal surfaces of $\text{Si}(001)$ is characterized either by a step bunching instability or a meandering instability [125,126] which originate from the alternation of terraces with different diffusion coefficients and stiffnesses [127,128].

2.1.8. Dome islands

Hut pyramids alone are only observed for a given range of the film thickness. When the deposited height is large enough, hut islands transform into dome shape islands, see Figs. 39 and 40 [14,129,130,32,131–133,57]. Cross-section TEM observations (Fig. 40) of domes evidence large {113} and {111} facets (at 25.2° and 54.7° of (001) surface respectively) that are low energy orientations already observed in the equilibrium shape of Si. Even if some smaller facets can also be distinguished, their angles could not be accurately determined (an angle about 13° was measured for the “meniscus” at the base of the island which could correspond to (116) facets). The rounded shape observed on the top of the island seems to deny the presence of (001) facets (for a detailed description of the dome shape, see [134]). The hut pyramids and dome islands characteristics (aspect ratio, facet orientations and elastic relaxation) are summarized in Fig. 41.

The island shape transformation is progressive and hut pyramids and domes may coexist in some conditions, see Fig. 42. This transformation is reported to occur from top to bottom, see Fig. 43 [135,136]. From a critical size on, atoms accumulate only on the partially relaxed topmost region of the island, which is an energetically favorable position [137]. Incomplete

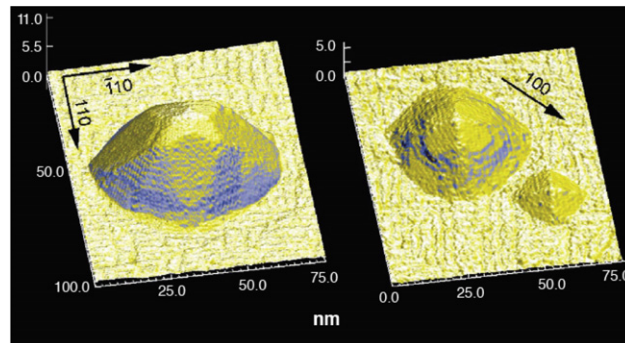


Fig. 39. (Color online) STM topograph [surface height $h(x, y)$ as a function of position] of strained Ge nanocrystals on Si(001), showing both pyramids and domes.

Source: from [32].

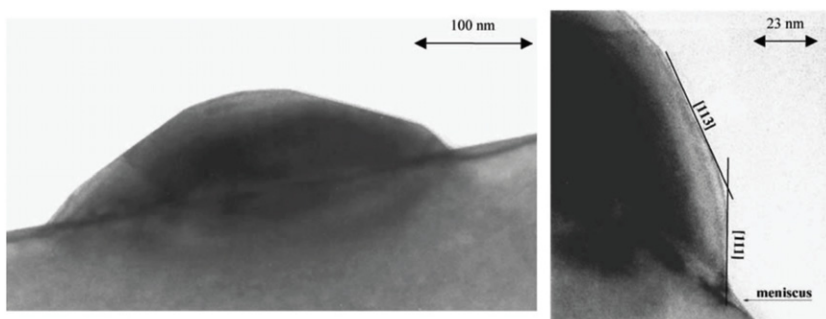


Fig. 40. TEM cross-section images of $\text{Si}_{0.5}\text{Ge}_{0.5}$ ($m = 2.1\%$) "domes" obtained for a deposited thickness of 5 nm. Only the angles of facets oriented along (110) can be accurately measured.

Island morphology	Huts	Domes
Aspect ratio (H/L)	0.04	0.15
Facets	(105)	Mainly (113), (111) Small (105) + others
Maximum	0.25%	0.85%

Fig. 41. Comparison of structural and morphological characteristics of huts and domes.

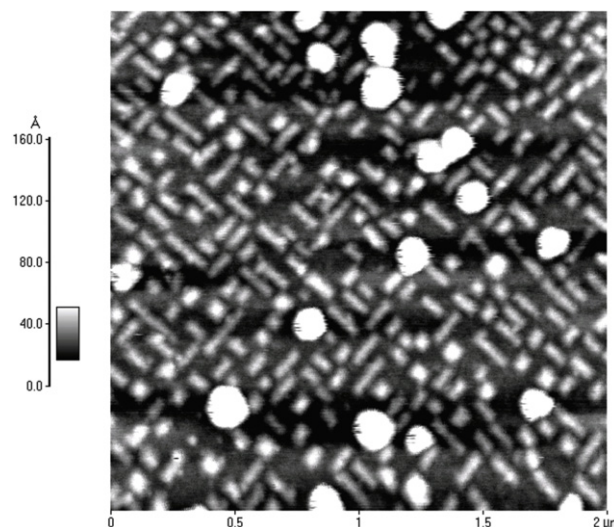


Fig. 42. AFM image of a 1.8 nm deposit of Ge at 550 °C. The coexistence of huts and domes can be well appreciated.

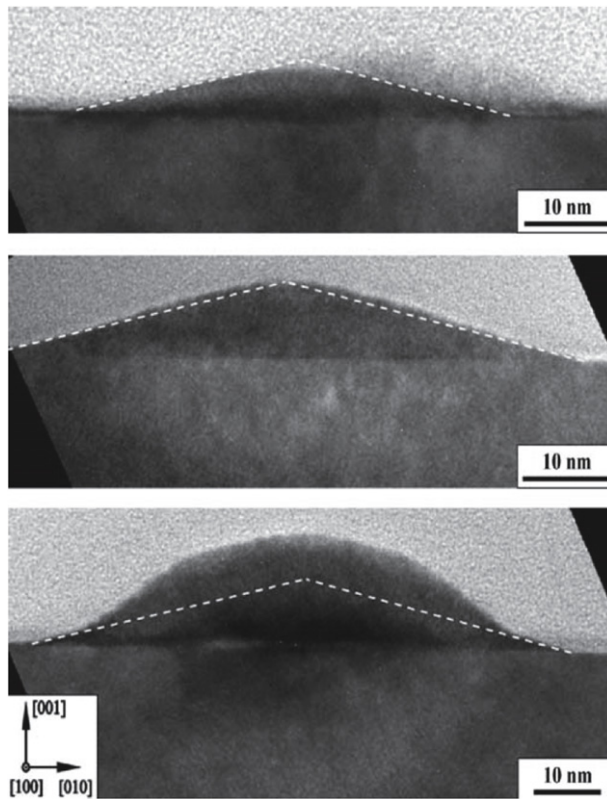


Fig. 43. [100] cross-sectional TEM images of Ge dots on Si(001). The dotted lines indicate the position of the {105} facets. The transformation from the pyramidal to dome shape due to a nucleation onto the {105} facets close to the top of the pyramids is visible.
Source: from [135].

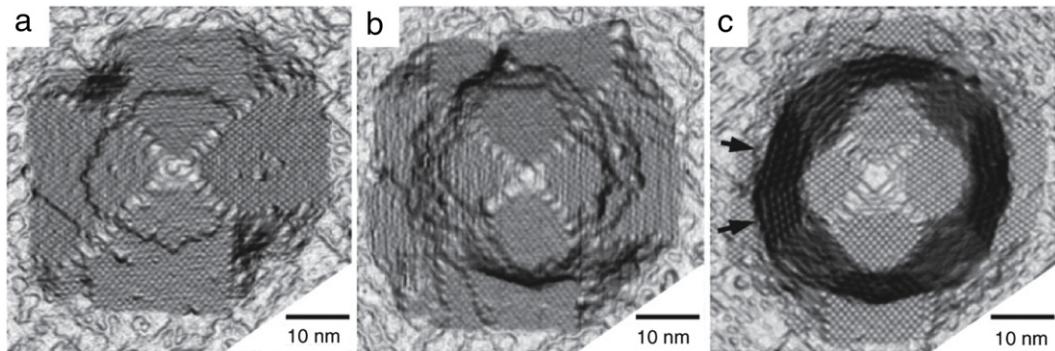


Fig. 44. STM topographs illustrating the pathway of the pyramid-to-dome evolution.
Source: from [136].

facets thus nucleate at the island apex and evolve into steeper facets after step bunching occurred, which eventually leads to the transition to domes, see Fig. 44.

In fact, the formation of hut islands with the onset of (105) facets and the subsequent development of multifaceted larger islands was matter of controversy. In particular, it was debated whether (105) islands are thermodynamically stable [138,139] or kinetic pathways to equilibrium states [140,141], see Section 3.7 for a discussion of the coarsening at work in these systems. We display here some results concerning the long time annealing of a 50 Å thick film with $x = 0.4$. The as-grown morphology presented in Fig. 45(a)) shows (105)-faceted islands which display a small relaxation of 0.18%, which represents a relative relaxation of 11% from the initial strain (Fig. 45(a)). After 18 h anneal at 550 °C the deposit has evolved towards a bimodal distribution of huts and domes, see Fig. 45(b) and (c). This transition is characterized by a larger level of relaxation of the order of 0.85%, which represents 53% of the initial strain (Fig. 45(b)). For larger misfit in regime III, as-grown islands already display a bimodal size distribution which corresponds to hut and dome islands

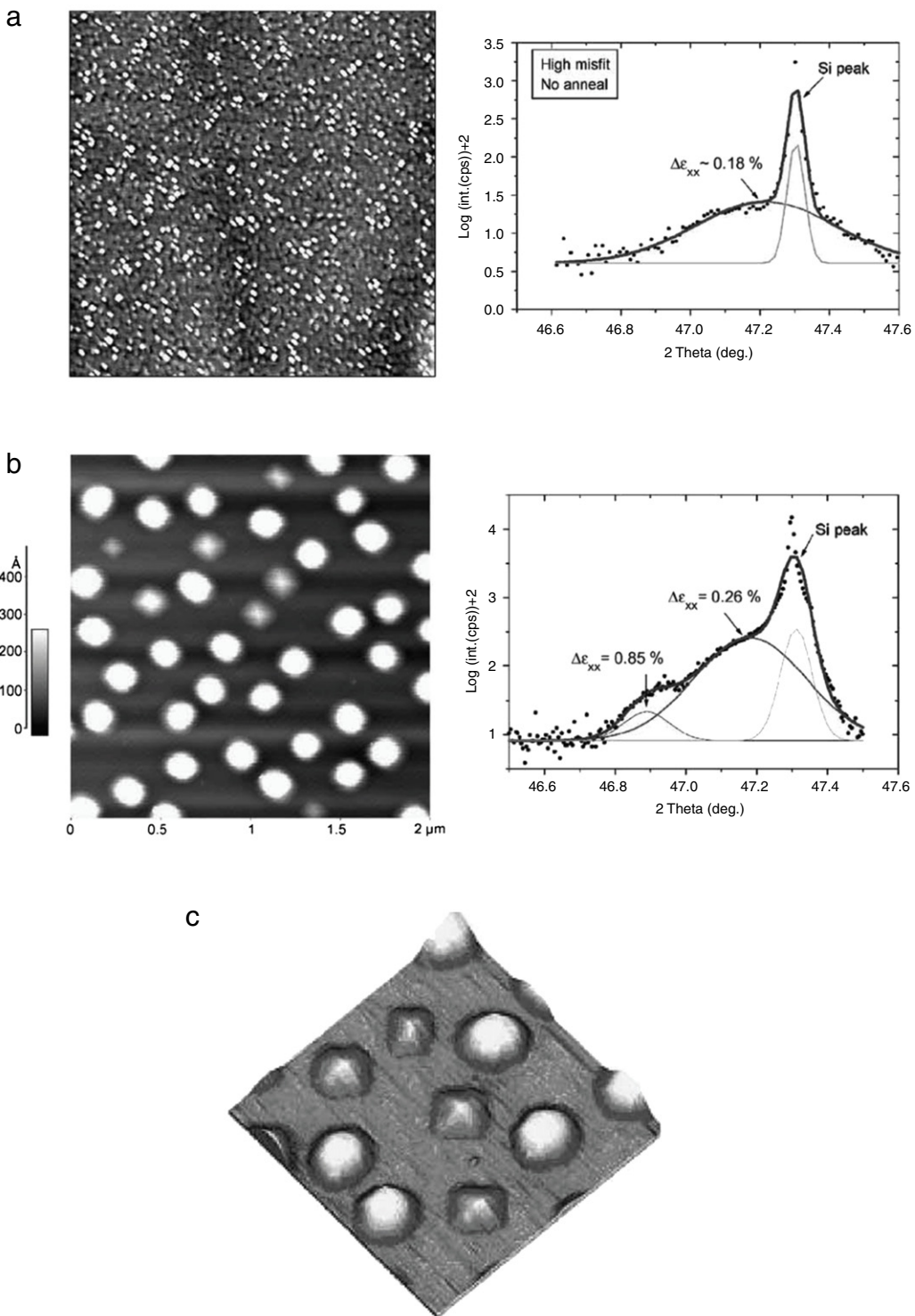


Fig. 45. Evolution of the morphology (AFM images on the left) and of the stress relaxation (GIXRD spectra on the right) of a 50 Å thick $\text{Si}_{0.6}\text{Ge}_{0.4}$ layer ($m \sim 1.7\%$) during annealing at 550 °C: (a) as-grown $5 \times 5 \mu\text{m}^2$; (b) 18 h anneal $2 \times 2 \mu\text{m}^2$; (c) is a $1 \times 1 \mu\text{m}^2$ zoom of (b) presented with a 3D view.

[142,32]. An example of this regime is displayed in Fig. 46 for a 50 Å thick film with $x = 0.45$. The associated elastic relaxation is also found to be bimodal with $\epsilon_{xx} = 0.26\%$ for huts and 0.78% for domes. Such a two-level relaxation is similar to the observation of the bimodal islands resulting from annealing in regime II, Fig. 29. Hence, the bimodal distributions resulting

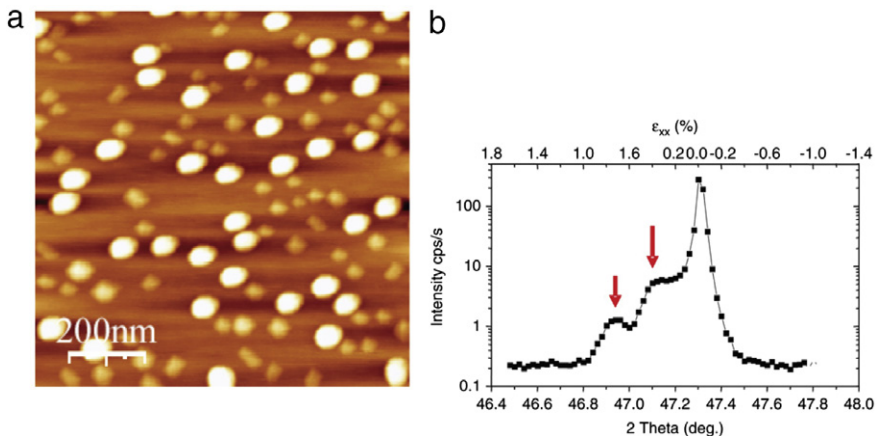


Fig. 46. (a) AFM image of $\text{Si}_{1-x}\text{Ge}_x$ as-grown hut and domes islands with $x = 0.4$ and $h = 5$ nm; (b) GIXRD spectrum of the sample.
Source: from [7].

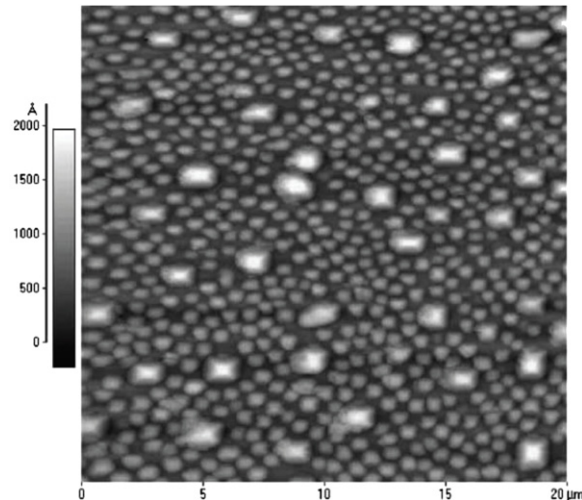


Fig. 47. AFM image ($20 \times 20 \mu\text{m}^2$) of a 50 nm thick $\text{Si}_{0.5}\text{Ge}_{0.5}$ film ($m = 2.1\%$) displaying a bimodal size distribution of dome islands. Denuded areas around the larger islands are clearly visible.

from growth or annealing display similar level of relaxation showing that relaxation is related to the morphology and not to the kinetics that leads to it. Moreover, when they coexist, huts and domes have densities which vary with the experimental conditions: domes are favored at large misfit while huts are more numerous at lower misfit [143]. This property can be linked to equilibrium and/or kinetic effects. Domes which are better relaxed (either by lateral elastic relaxation at the island step edges or by nucleation of misfit dislocations) are characterized by a lower elastic chemical potential. In parallel, a large misfit induces larger fluctuations of the elastic energy which favors overpassing kinetic barriers. The formation of domes islands is in both cases attributed to a higher strain relaxation. Eventually, in these conditions ($h = 50 \text{ \AA}$, $x = 0.4$, $T = 550^\circ\text{C}$), all the as-grown samples transform into large round shape domes during long-term annealing. Such islands with large elastic relaxation ($\Delta\epsilon_{xx} = 0.85\%$) represent the steady state morphology in these conditions.

For higher misfit and film thickness in regime IV, one gets a bimodal size distribution of domes and other shapes which correspond to dislocated and coherent islands, see Fig. 47. Domes are similar in shape and strain to those previously described. The new shapes correspond to barnes with new higher index facets such as (20423) or to plastically relaxed superdomes [144]. The introduction of new barn shapes in dilute $\text{Si}_{1-x}\text{Ge}_x$ is displayed in Fig. 48 [145]. During growth or annealing, these islands continuously merge into large dislocated domes while hut islands are not observed in this regime. The steady state morphology of this regime consists of large dislocated islands [2] which remain perfectly stable during days long annealing (up to 72 h). Such dislocated islands are not discussed in this paper, see e.g. [146]. Note also that some revert sequences or shape oscillations can also be found under some particular conditions when wetting and intermixing play a crucial role [147,148].

As already mentioned, the shape evolution from pyramids to domes is associated with strain relaxation. If hut pyramids relax at most 20% of their misfit stress, dome islands appear to be more efficient and to relax up to 50%–70% of the coherency

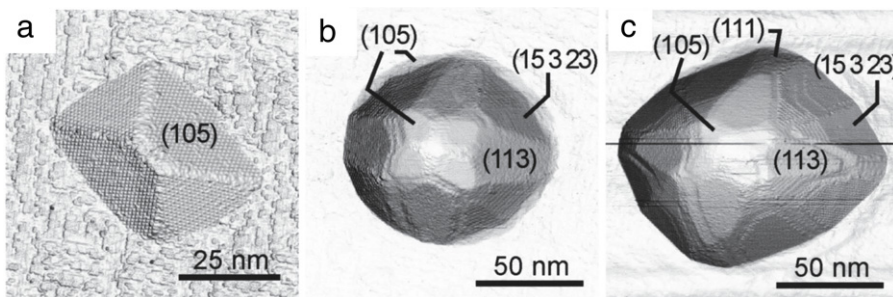


Fig. 48. Top-view STM images of coherent $\text{Si}_{1-x}\text{Ge}_x$ islands on $\text{Si}(001)$. Gray scale in the images encodes local slope on the surface. (a) "Hut". (b)"Dome". (c)"Barn". Families of facets bounding these island shapes are labeled.
Source: from [145].

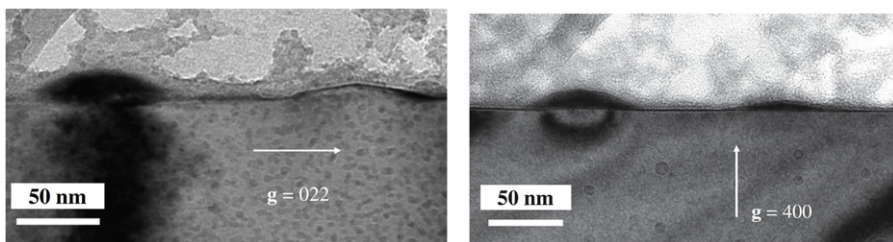


Fig. 49. Bright field cross-section TEM micrographs showing a dome (left) and pyramid (right) dot and recorded in (022) and (400) two-beam conditions.
Source: from [5].

stress depending on the growth conditions [107,149,106,150]. As regards domes resulting from the deposition of pure Ge on Si, GIXRD and ordinary X-ray analysis [149] reveal that the lattice parameters expand of 1.2% and 3.1% in the directions parallel and perpendicular to the surface respectively. Combined with the Poisson expansion following Vegard's law, this result characterizes domes made of a 50% strain relaxed $\text{Si}_{0.45}\text{Ge}_{0.55}$ alloy [149] and proves an important intermixing (see Section 2.2 for more details). For deposition of an alloy film, GIXRD analysis reveals that domes may relax up to 65% of the strain [106,7]. The larger relaxation in domes compared to pyramids is also operating in dots embedded in multilayers which can be analyzed through Raman scattering [151].

Strain in individual islands may also be extracted from TEM images contrast of pyramid and dome islands. This technique reveals that domes are heavily strained (about 2%) with respect to the substrate, while pyramids are almost commensurate with the substrate (i.e. tetragonally distorted with a strain lower than 0.5%) [150]. The difference in strain between domes and pyramids can be well appreciated on dark TEM cross-section images recorded in two different two-beam conditions, see the contrast in the substrate in Fig. 49. The (400) two-beam condition is sensitive to lattice distortion in the growth direction and shows that considerable strain is induced at the periphery of and underneath the dome island over a region corresponding roughly to the size of the dot. In contrast, little strain is evidenced in the substrate in the case of the pyramid islands. The same conclusions can be deduced from the (220) two-beam condition images. Similar strain gradients in $\text{Si}_{1-x}\text{Ge}_x$ dome dots have also recently been measured by quantitative high resolution TEM [152].

Strain relaxation can also be continuously monitored using a transmission electron microscopy technique based on two-beams dark-field strain imaging. The evolution of relaxation with the island size which increases either with the deposited height or during annealing is displayed in Fig. 50 [150]. Strain relaxation appears to change discontinuously between as-grown pyramids and domes as a function of the deposited height. However, it displays a smoother evolution with the annealing time when islands undergo Ostwald coarsening as pyramids transform into more stable domes. A similar continuous evolution was observed using high-resolution XRD of annealing pyramids, transitional domes and domes [154]. This relaxation is correlated with a decrease in the Ge composition, see Fig. 51, and the coarsening is found to be a combination of Si interdiffusion, Ostwald ripening, and consumption of the metastably thick Ge wetting layer.

The information concerning the local relaxation in domes can be addressed using anomalous X-ray scattering [155]. By combining X-ray results with atomic force microscopy, it is possible to disentangle strain and composition and get strain maps, see Figs. 52 and 53 [156]. These measures show that the local lattice parameter in pyramids decreases monotonically with the radii in the island. On the contrary, the non-monotonic behavior in domes indicates that the island impacts the local strain over a large area under its base [155]. The island in-plane parameter decreases from island top to bottom following the general trend describing stress relaxation inside the island. Quantitative high-resolution transmission electron microscopy was also performed in dome islands and lead to two-dimensional (2D) projected maps, with a high spatial resolution at

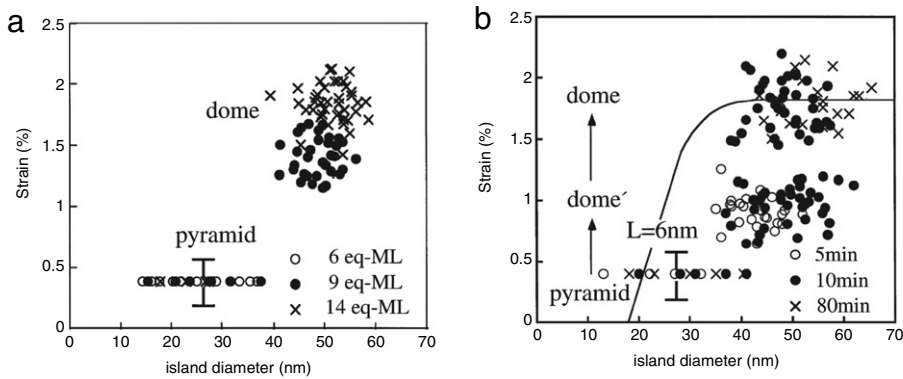


Fig. 50. Strain in Ge islands vs island diameter. (a) For as-deposited samples 6, 9, and 14 ML thick grown at 600 °C and (b) for 8 ML thick samples deposited at 550 °C and annealed at 550 °C for 5, 10, and 80 min. The error ranges both in diameter and strain are 10%. The solid curve in (b) represents the dependence of the island diameter on the strain of equilibrium islands with isotropic surface energies, derived from the work of Kukta and Freund [153] using $L = 6$ nm. The island populations in a sample annealed for 40 min are similar to that for 80 min (data not shown).

Source: from [150].

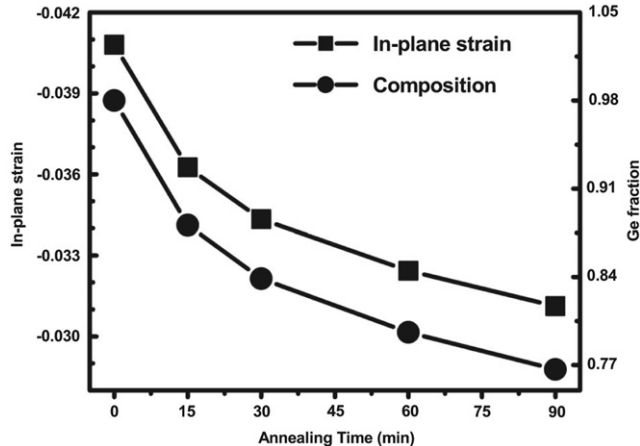


Fig. 51. Evolution of the in-plane strain ϵ_{xx} and Ge mole fraction x in SiGe alloy are plotted for different annealing durations at 650 °C.
Source: from [154].

different crystallographic orientations [157]. The strain map is shown in Fig. 54 for the [110] direction. It corroborates the expected conclusion that the island is relaxing the epitaxial strain, i.e. $\epsilon_{\parallel} < 0$ and $\epsilon_{\perp} > 0$. Relaxation is more important at the island apex where Ge has nearly its bulk parameter, while it is more constrained at the film/substrate interface. But the dome base itself is not uniformly strained: strain displays a maximum in the middle of the island while it is partially relaxed at the island periphery.

Dome islands grown by liquid phase epitaxy of SiGe on Si were analyzed by the combined use of conventional transmission electron microscopy, high-resolution TEM imaging (HRTEM) and digital analysis. The classical diffraction contrast method was applied to visualize the strain field in the surrounding of the islands. Dark-field imaging allowed a qualitative imaging of chemical composition using chemically sensitive reflections while quantitative HRTEM (QHRTEM) was used to determine the local strain and structural peculiarities at the atomic scale [152]. The islands under scrutiny displayed a morphology typical of dome islands with a square-like base with {111} and {115} side facets, edges parallel to [110] and an aspect ratio close to 0.5. Such dome islands have an equilibrium shape characterized by a level of strain relaxation which may be attributed to dislocations. The strain analysis of the (002) and of the (2-20) lattice planes at the basal region of the island was performed by QHRTEM. Considering the displacement of the $u_{[001]}$ vector, it was shown that the (002) lattice planes are bended towards [001] with a maximum of bending located directly underneath the island center. Moreover, from the analysis in the (220) direction, it was found that the lattice planes are compressed close to the island edge while an expansion is found closer to the island center. Strain distribution of the (200) lattice planes at the bottom region indicated again that the line of maximum strain runs close to the edge of the basal plane but is rounded when the corner is approached, see Fig. 55 [152].

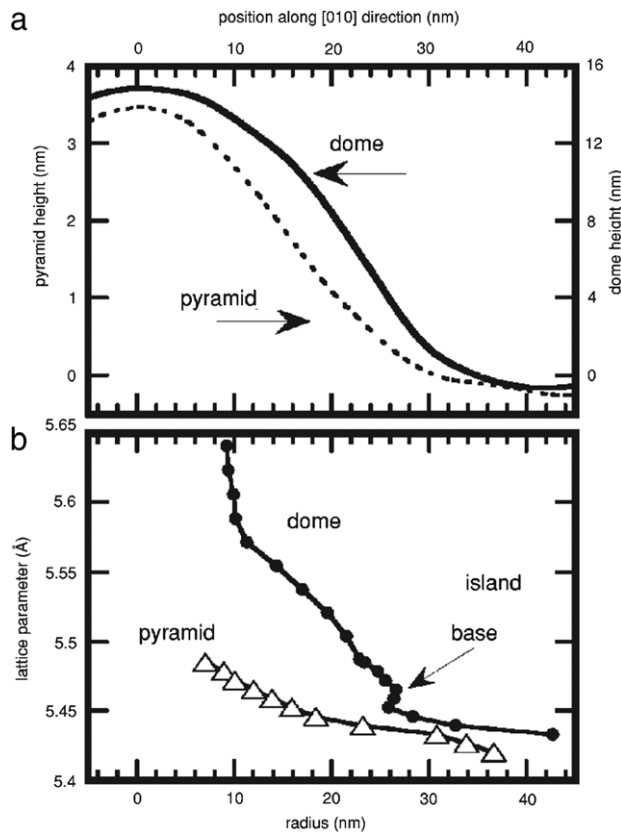


Fig. 52. (a) AFM line scans on a most statistically significant pyramid (left axis, dashed line) and dome (right axis, solid line). (b) Radius versus lattice parameter; filled circles correspond to domes and open triangles to pyramids.
Source: from [155].

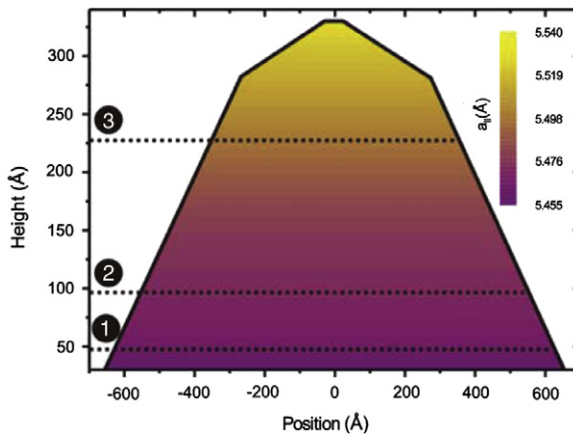


Fig. 53. Local lattice parameter map for MBE grown dome islands.
Source: from [156].

2.2. Composition

The systems under scrutiny are made of at least two species and alloying is an efficient mechanism for relaxing the epitaxial strain. We review below the degree of alloying depending on the growth stage and conditions.

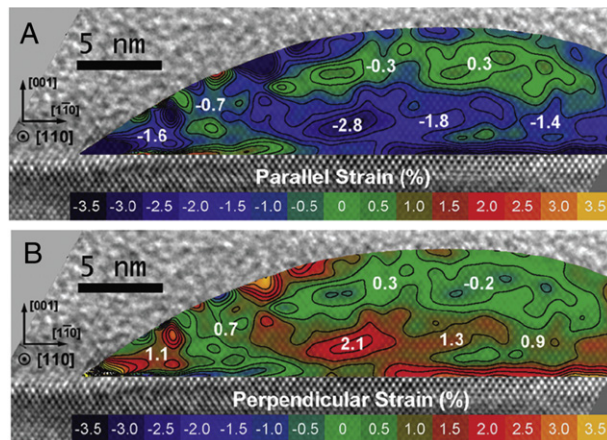


Fig. 54. (Color online) Two-dimensional strain maps of representative Ge-Si/Si(001) dome-shaped islands. (a) and (b) Strain maps obtained from the [110] projection, showing the parallel and perpendicular components (ϵ_{\parallel} and ϵ_{\perp}), respectively. The color scale indicates the strain level, where the positive values correspond to an expansion of lattice and the negative values to contraction [157].

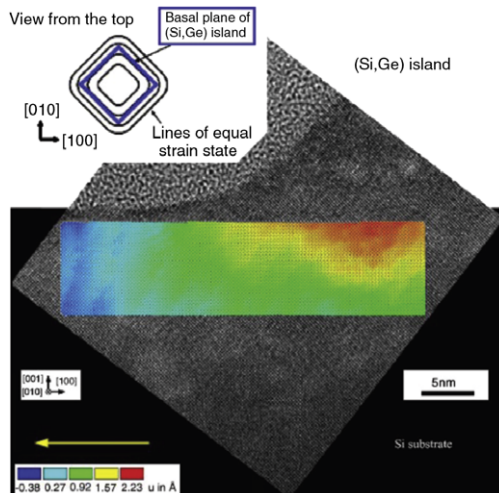


Fig. 55. Strain distribution of the (200) lattice planes at the bottom region of a (Si, Ge) island viewed along [010] which is inclined by 45° to the edge of the basal plane of the island [152].

2.2.1. Bidimensional layer

In the first stage of growth, intermixing may lead to Ge present throughout the top four layers after deposition by MBE of only 0.8 ML of pure Ge on Si(001) at temperature as low as 500 °C [158]. This intermixing was already visible by TEM in quantum wells with Si/Si_{0.75}Ge_{0.25}/Si slabs, see Fig. 56 [40]. X-ray diffraction was used to probe the Ge concentration profiles in asymmetrically strained, low concentration Si/SiGe heterostructures. The results evidenced an initial fast interdiffusion regime (almost an order of magnitude faster than the long time diffusion rate). This regime was shown to primarily result from the concentration dependence of the activation enthalpy for SiGe interdiffusion. Time dependent strain relaxation was shown to play a discernible, but secondary role in this regime and in the transition from fast to slow interdiffusion [159]. This relatively small effect of strain on interdiffusion is in contradiction with models which state the major role of strain [160]. Other experiments based on SIMS and Raman spectroscopy measurements showed that the diffusion coefficients of Ge in tensilely strained Si are higher than those in Si, see Fig. 57, and that the activation energy of the diffusion coefficient is 3.3 eV in tensilely strained Si, to be compared to 4.7–5.3 eV in unstrained Si [161]. These results also showed that Ge can diffuse into strained Si with nearly the same activation energy as in Si_{1-x}Ge_x alloy with $x = 0.3$. The change in the activation barrier of the diffusion coefficient D in strained Si may be attributed to a change in the number of interstitial sites while the diffusion path of Ge is sensitive to the formation energy of the interstitials. In parallel, a high value (4.1–4.8 eV) of the activation energy in compressively strained SiGe with $x = 0.3$ was found, to be compared with the one in unstrained SiGe (3.1 eV). Thus, the formation energy of interstitial atoms may rise with compressive strain if Ge diffuses in strained SiGe via interstitial sites [161].

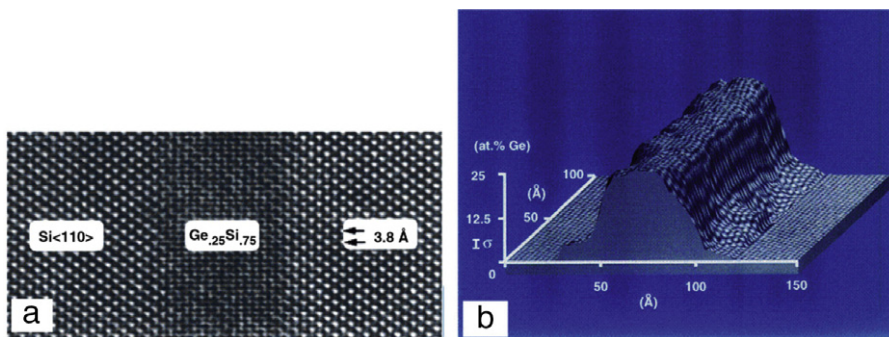


Fig. 56. (a) HREM cross-section lattice image of Si/Si_{0.25}Ge_{0.25}/Si quantum well structure observed along the [110] direction and (b) the corresponding quantitative composition map of the interfaces. In (b) height represents Ge concentrations and the bar is the accuracy.
Source: from [40].

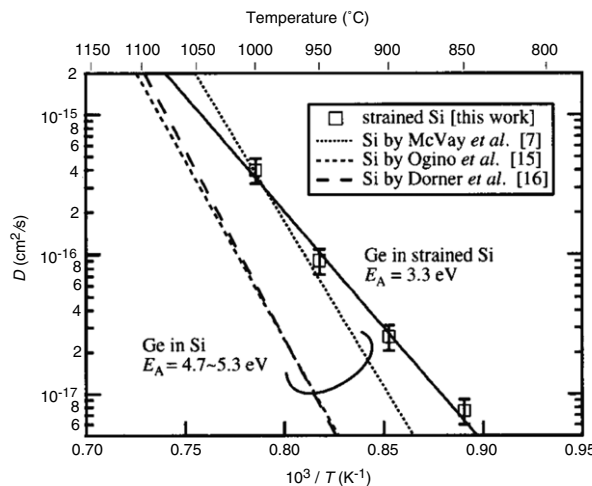


Fig. 57. Arrhenius plot of the Ge diffusion coefficients in strained Si. The diffusion coefficients in unstrained Si are shown for comparison.
Source: from [161].

More recently Atomic Probe Tomography (APT) was used to better quantify the 3D composition of SiGe layers. When a multilayer of Si and SiGe films are sequentially grown by CVD, transient compositions occur when the film type changes, see Fig. 58. At the interface between Si and SiGe, an elevated Ge concentration 14% higher than the rest of the layer was quantified with this technique using concentration profiles, see Fig. 58(a). The transition width measured as the position at which the concentration is halfway between the peak-to-valley difference on each side is 2.2 nm (Fig. 58(b)). The accurate quantification of the Ge content in Si evidences a decay length of 0.2–0.6 nm per decade of the Ge content [162] while the interface roughness computed from the measurement of the 2D isoconcentration profile of 6% Ge was found to be 0.52 nm in this situation.

The peak positions in photoluminescence (PL) spectra of Ge wetting layers was also used to derive the quantitative Ge composition profiles by fitting the slopes of the activation energy of photoluminescence versus the wetting layer thickness with the results of band structure calculations. The PL spectra is measured versus the Ge coverage with an extremely high relative resolution of 0.025 monolayers. A nearly linear redshift of the peaks with increasing Ge coverage was observed. At $T_c = 300 \text{ }^\circ\text{C}$ an almost boxlike Ge profile of the WL is obtained with a maximum Ge concentration as large as 86%, which is preserved for Ge coverages larger than 4.2 ML. The Ge composition profile in the WL was shown in this study to be dominated by surface segregation of Ge on Si [163].

2.2.2. Pyramid and dome islands

Different models have been proposed to explain composition gradients in quantum dots, considering either a bulk driven alloying which tends to minimize the total energy of the system, a surface mediated diffusion process, which occurs as a consequence of the higher mobility of one species of adatoms, intermixing which is favored near the surface etc. In the first case, the total energy can be minimized either by relaxation of the epitaxial strain resulting from the Si/Ge lattice mismatch or by a decrease of the enthalpy of formation of point defects responsible of Ge atoms motion. If the first phenomenon is predominant, a Si-rich island core should result as a consequence of atomic exchange processes at the island base

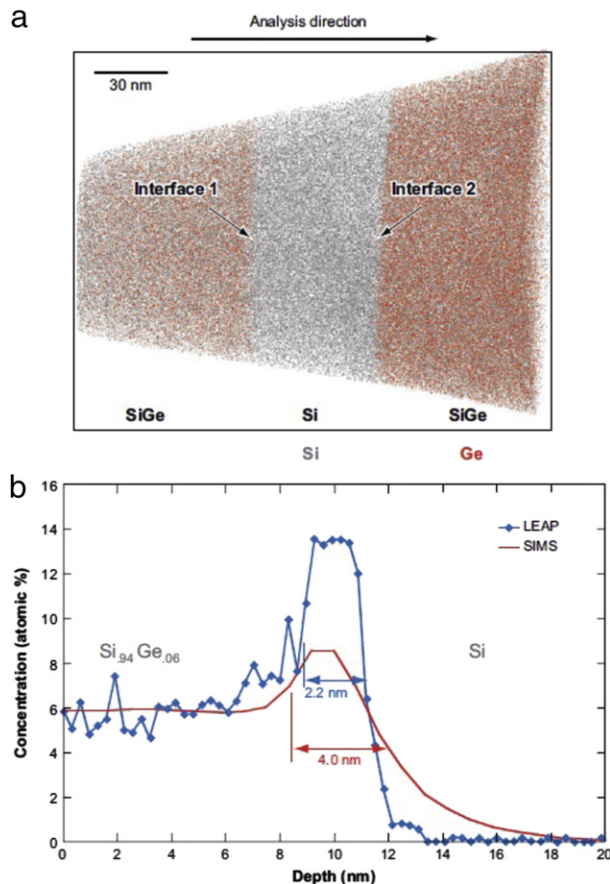


Fig. 58. APT analysis of a SiGe–Si multilayer stack. (a) Side view of an APT image of CVD Si/SiGe multilayer films. (b) Concentration profile at interface 1, obtained by APT and SIMS. The APT concentration profile is taken from the 10 nm on either side of interface 1. Source: from [162].

during growth. Conversely, if surface diffusion processes are dominant, one should expect Si rich island edges. Different experiments on systems with different growth conditions were performed to determine the driving force of intermixing and alternatively revealed Si or Ge rich cores.

The compositional maps of Ge islands grown by MBE on Si(001) at 620 °C were studied by selective chemical etching in [165] and revealed a higher Ge concentration close to the island apex. The main dependence of the composition on the temperature, growth rate and annealing time was satisfactorily accounted for within a simple model essentially based on surface diffusion, indicating that the bulk inter diffusion might not be a relevant effect. Composition maps of Ge dots deposited on Si(111) in the temperature range 460–560 °C were also obtained by X-ray photoemission electron microscopy (XPEEM) [164,166]. It was reported that the specific geometrical features of the islands observed by XPEEM images are unambiguously related to a definite chemical contrast and thus to a specific Si/Ge composition at the island surface [164]. The relation between surface composition and topography is determined by comparison with the contour plot drawn from LEEM images [167] and XPEEM yields quantitative information and surface concentration–morphology graphs for sets of individual islands. The images show triangular Ge(Si) 3D structures which is known to correspond to a strained coherent nanocrystal. The composition analysis shows first that the Si content is higher in the wetting layer than in the islands, see Fig. 59. However, since the algorithm uses the wetting layer as a normalization for the island signal, it cannot lead to the absolute composition in the wetting layer. Secondly, the composition maps clearly exhibit a highly inhomogeneous Si concentration at the nanoscale, ranging from about zero in the central region of the island to as much as 10% at the edges, especially at the corners. The Si contour plots are displayed in Fig. 60 and reveal a Si-poor central zone. The presence of two island configurations was also evidenced: strained triangular islands characterized by a Si surface concentration of 5%–20%, and ripened atolls which contain up to 30%–40% Si. Higher growth temperatures induce faster ripening of the 3D islands and an increase in the surface Si content of strained islands revealing a thermally activated interdiffusion process which partially relaxes the strain energy in the islands [164]. By comparison with Monte-Carlo simulations, dots were shown to display a substantial tendency towards island self-ordering [168]. It was concluded that energetic factors govern the competition among coexisting nanostructures to capture the deposited mass. A finite element analysis was used to generate the strain field of unburied SiGe QDs on Si(001) and was combined with multi-beam dynamical electron diffraction theory

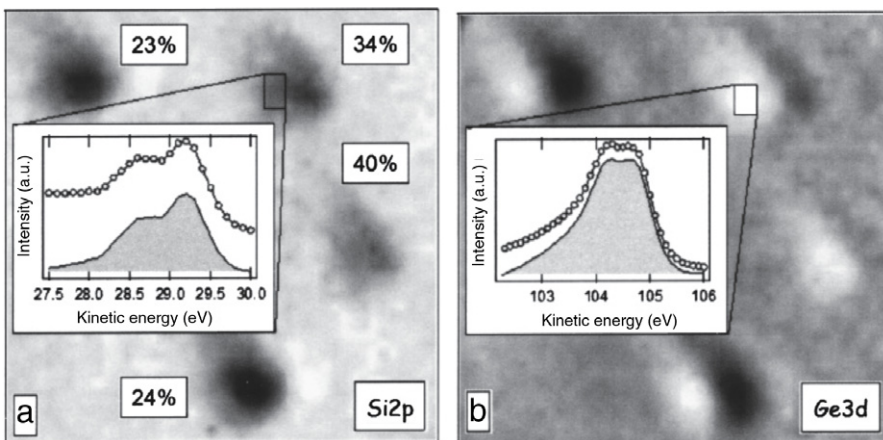


Fig. 59. $4 \times 4 \mu\text{m}^2$ integrated XPEEM images taken in correspondence of (a) the Si 2p core level peak and (b) the Ge 3d core level. Examples of spectra are shown in the insets. Circles: raw data; shaded curves: background subtracted data, averaged over the labeled regions. The measured Si concentrations for the 3D islands are labeled in panel (a).

Source: from [164].

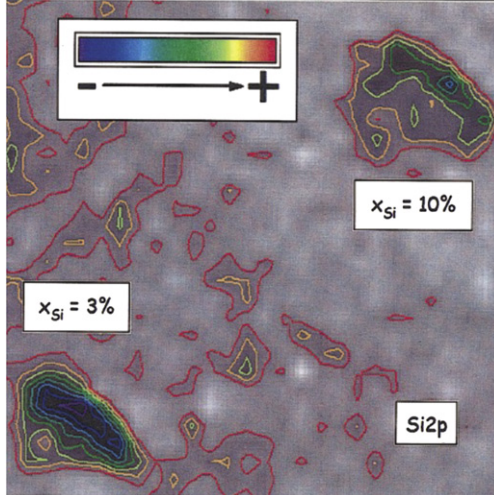


Fig. 60. (Color online) $2 \times 2 \mu\text{m}^2$ integrated XPEEM image taken at the Si 2p core level, together with the contour plots from a more (top) and a less (bottom) ripened island. Photo-electron yields are increasing from blue (lowest) to red (highest). The darkest regions in the panels are produced by the shadows of the 3D islands, due to the grazing incidence angle of the X-ray beam. The estimated surface Si concentrations for the selected islands are indicated. The wetting layer appears to be inhomogeneous.

Source: from [164].

with the column approximation in order to simulate the [001] zone-axis bright-field images [169]. Comparison between experimental and simulated images from these QDs pointed out the composition gradient within the QD with a higher concentration of Ge at the top of the QD [169].

Analytical TEM techniques were implemented to investigate the structure and composition of Ge nanostructures. An example is shown in Fig. 61 [5], showing the composition profile of Ge dots (pyramids and domes) grown by MBE derived by scanning transmission electron microscopy–energy dispersive spectroscopy (STEM–EDS). The mean Ge content in the pyramid is about 30%–35%, whereas in the dome, it is higher than 40%. For a pyramid dot, the Ge concentration increases almost linearly from close to zero at the base of the dot to about 0.5 at its apex due to a strong intermixing, see Fig. 61(a). EDS scans in the direction parallel to the interface show that the Ge concentration at a given height is uniform across the pyramid, with a small decrease at the dot edges. On the other hand, the domes show a different concentration profile, see Fig. 61(b). The Ge concentration displays a more pronounced gradient at the dot base and already reaches about 0.4 at a height of 5 nm. Beyond that point, the Ge concentration builds up slowly to reach approximately 0.6 at the top of the dome [171]. The Ge concentration at a given height was found to be uniform laterally in contradiction with the model of a Si-rich core and a Ge shell deduced from X-ray scattering studies [172]. Similar results were found on Ge domes grown by MBE at 650 °C on Si(001) using in situ electron energy loss spectroscopy (EELS) line profiles [170]. These dots were analyzed thanks to grazing

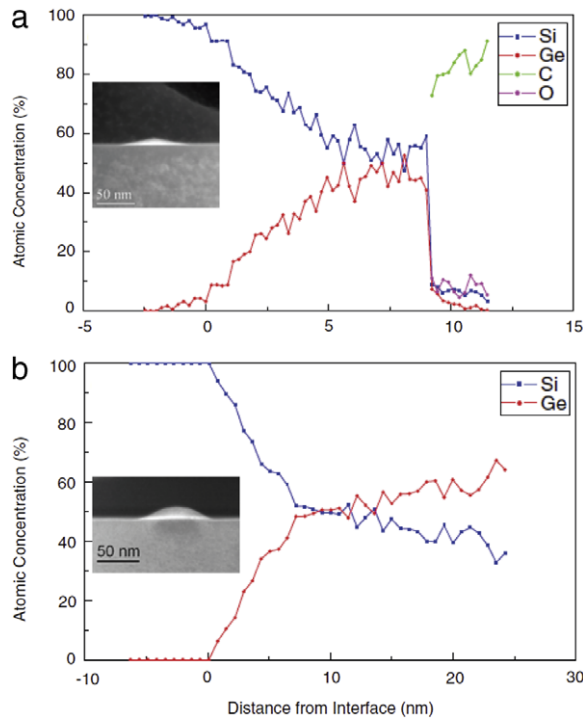


Fig. 61. EDS chemical profile in the growth direction for (a) a pyramid-like SiGe dot and (b) a dome dot. The spectra are from the same sample, obtained by MBE by depositing 5 ML of Ge on (001) Si at 650 °C.
Source: from [5].

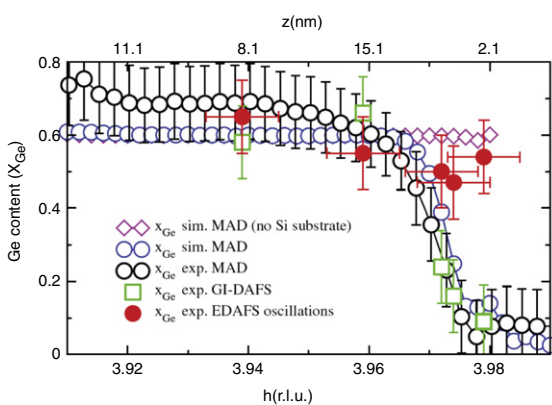


Fig. 62. (Color online) Experimental Ge composition x determined by grazing-incidence multi-wavelength anomalous diffraction (GI-MAD) (black open circles), by fitting grazing-incidence diffraction anomalous fine-structure spectroscopy (GIDAFS) lineshape (green open square) and extended diffraction anomalous fine-structure spectroscopy (EDAFS) analysis (red filled circle). The experimental curves are compared with simulated MAD data (pink diamonds and blue circles) obtained taking into account the scattering of the dome, and the {dome+substrate}. The curves are plotted as a function of reciprocal unit h around Si (400) and height z above the sample surface (from [170]).

incidence diffractions, with both a multi wavelength anomalous diffraction and an anomalous fine-structure spectroscopy, which lead to unambiguous composition maps when coupled to numerical diffraction calculations [170]. They evidenced a rather abrupt chemical change at the island/substrate interface and a slight increase in the Ge composition from the island base to its top with a strong intermixing, with an island composition of about 70%, see Fig. 62 [170]. Finally, the composition of Si/Ge QDs grown on a Si substrate by ultra-high vacuum (UHV) CVD was investigated in [173] by using enhanced Raman scattering by the tip of an atomic force microscope. This work concluded that the dots consist of a Si-rich core and a Ge-rich shell. The larger intermixing found in the pyramids may be attributed to a different level of strain, as the latter remain heavily tetragonally distorted as explained above, while domes relax strain more efficiently at their top where the lattice constant is close to that of bulk Ge. However, the lamellar structure with laterally uniform composition profile found in both

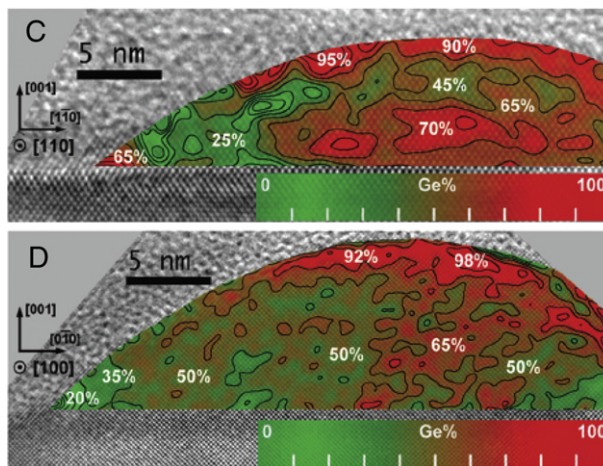


Fig. 63. Two-dimensional chemical maps of representative Ge–Si/Si(001) dome-shaped islands. Chemical maps are obtained along the [110] and [100] crystallographic directions, respectively. These maps show the average Ge content (%_{atom}) at the projected directions, obtained from the quantitative high-resolution transmission electron microscopy technique. The color code indicates the Ge content. All maps are superposed to the original HRTEM images, showing the coherently strained Ge–Si islands on the Si(001) substrate.

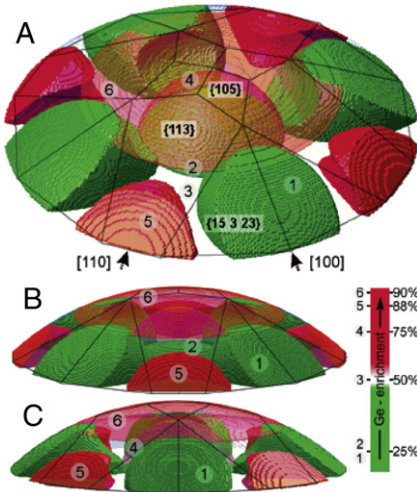


Fig. 64. (Color online) The 3D chemical model of the Ge–Si/Si(001) dome-shaped islands. (a) Perspective top view of the modeled chemical distribution within the island. The line boundaries show the faceted dome, where the facets families (braces) and the directions (brackets) are indicated. (b and c) Side views of the 3D model along the [110] and [100] directions, respectively. This model was constructed assuming a fourfold chemical symmetry. The colors differentiate Ge-rich (reddish) and Si-rich (green) regions. The numbers attributed to each region group refer to specific Ge content (%_{atom}), as indicated by the scale bar [157].

dots in some studies is in contradiction with the results from X-ray scattering studies which exhibit a shell-like composition with a Si-rich core and a Ge-rich shell [172,174,175].

The composition gradients found by microscopy were also investigated by X-ray diffraction. In [172], Ge islands grown at 600 °C on Si(001) by CVD were probed by grazing incidence anomalous X-ray scattering. The resulting composition maps revealed a continuous mound-like variation of the Ge composition [172,174], see Fig. 65. By comparing X-ray scattering results and AFM profiles, it was possible to determine the strain created by pyramids and domes and thus to have access to their composition. At a growth temperature of 500 °C, domes and pyramids grown by MBE displayed a mean Ge composition of 60%–70% and 30%–40% respectively [176] in agreement with other results which showed that pyramids are more Si intermixed than domes. To go further, a quantitative high-resolution transmission electron microscopy was performed in similar dome islands. It lead to two-dimensional projected maps with a high spatial resolution at different crystallographic orientations, see Figs. 63 and 64. Combining different projections, it was possible to get the reconstruction of the full three-dimensional chemical arrangement of the strained islands [157]. It clearly evidences that Ge-rich or Si-rich regions are embedded in the island core and depend on the projection plane under investigation. The [110] projected chemical map shows a Ge enrichment at the bottom of the {113} facets and at the {105} top facets, see Fig. 64, whereas the [100] chemical

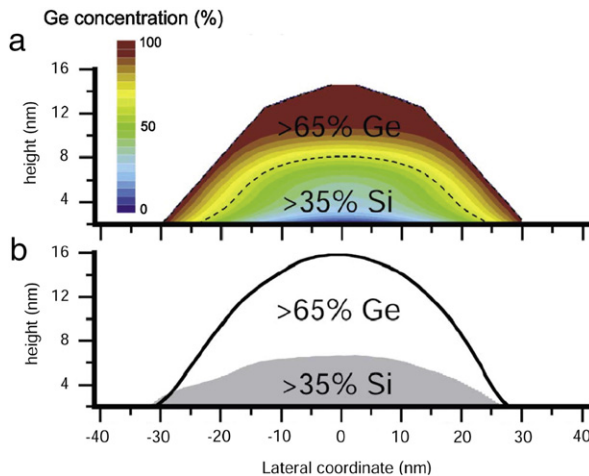


Fig. 65. (Color online) (a) Real space chemical composition map for Ge domes; (b) AFM line scans taken on two statistically averaged Ge domes, before and after 31% H_2O_2 selective etch, evidencing the Si-rich core.

Source: from [172].

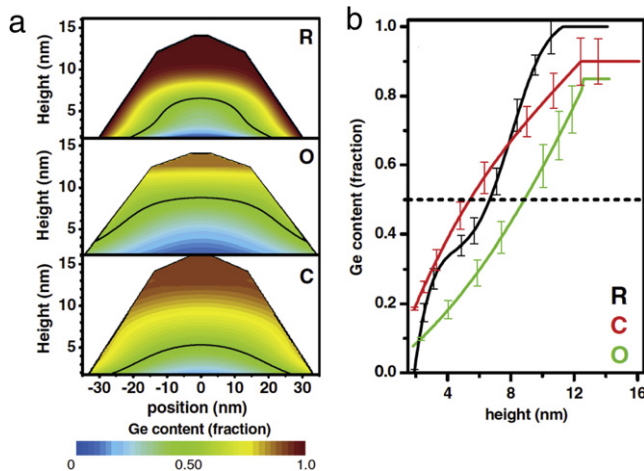


Fig. 66. (Color online) (a) Ge concentration (fraction) for samples R (reference), O (open), and C (closed). The black solid lines correspond to 0.50 Ge content. (b) Line scans taken along the growth direction at the island center for all samples for the Ge content as a function of the island height.

Source: from [177].

map indicates a Si rich region at the bottom of the common edge between the {15 3 23} facets and a Ge enrichment at the {105} top facets, see Fig. 64.

In order to distinguish between the main process which are predominantly at the origin of the composition gradients (thermodynamic intermixing, surface kinetic effects, ...), different islands were grown under different conditions. By affecting selectively the diffusivity of Si adatoms, one can inhibit or allow surface diffusion during CVD growth of Ge on Si(001) at 600 °C [177]. It was then possible to show that in the latter case, intermixing occurs via a Si inflow from the wetting layer, lowering the elastic energy and increasing the mixing entropy, see Fig. 66. However, the main pathway for intermixing appears as quite sensitively on the growth conditions [156]. Considering different growth conditions, CVD, MBE, liquid phase epitaxy (LPE), the same group found that surface diffusion strongly enhances the overall interdiffusion during MBE while CVD islands are closer to equilibrium [156]. In addition, correlated to the surface diffusion kinetics, an atomic ordering was found in dome islands which is possibly introduced in the system at the steeper faces, see Figs. 67 and 68 [156].

The monotonic increase in the Ge content from island bottom to the top free surface found in [5] significantly differs from composition profiles obtained at lower growth temperatures measured with other techniques. Both EELS and EDS line scans through the island axis show first an increase in the Ge concentration as one scans higher heights in the island, but this concentration reaches a maximum before decreasing in the middle of the island height, see Fig. 69. Such a different behavior was ascribed to the different growth temperature which is expected to modify the segregation of Ge. Note that, as a whole, the mean Ge concentration in the island decreases with T [165,178,179], see e.g. Fig. 70, while the interface width increases since Si/Ge intermixing results from a thermally activated process [180]. Ge QDs grown by CVD on Si(001) also showed a

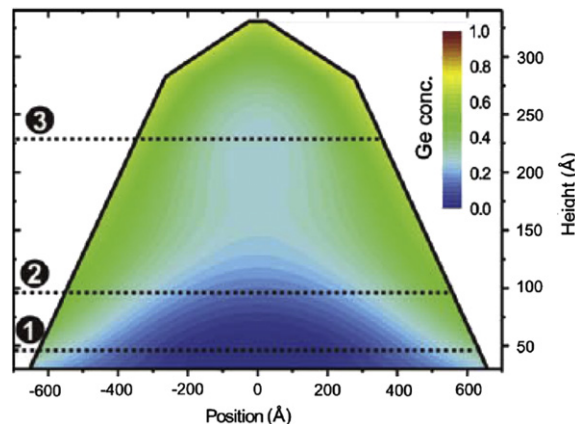


Fig. 67. (Color online) Lateral concentration profile map for MBE dome islands resulting from a 11 ML Ge film grown on Si(001) at 700 °C. Source: from [156].

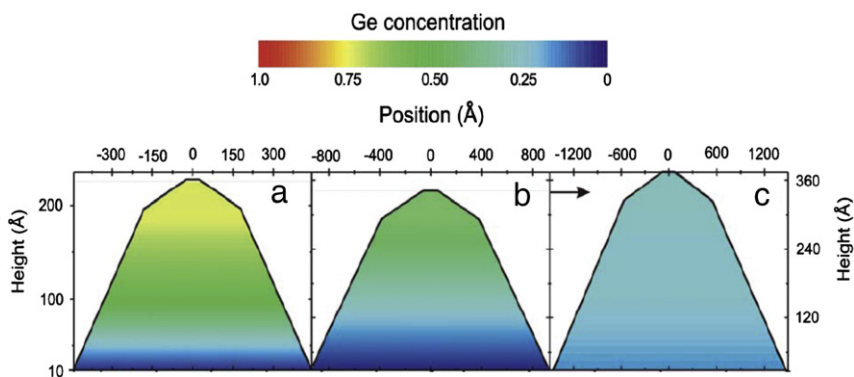


Fig. 68. (Color online) Representation of Ge vertical concentration profiles for islands of samples at (a) 620 °C 6.7 ML, (c) 750 °C 11 ML, and (d) 840 °C 6 ML. Source: from [156].

vanishing Si concentration at 550 °C while they display a 72% concentration at 850 °C [178]. This intermixing reduces the effective mismatch in the dots, which increases by a factor 10 the critical base for island nucleation [178].

This trend is corroborated by annealing experiments at 650 °C on dome-shaped Ge/Si islands grown by CVD [181]. EELS and Z-contrast imaging exhibited a significant diffusion with the presence of up to 40% Si in as-grown islands, and up to 70% after 60 min annealing at 650 °C. In this study specimen containing 11 ML of germanium deposited at 650 °C were investigated both by HREM, annular dark field imaging (ADF) and EELS. The deposited Ge created dome shaped islands that changed upon annealing at 650 °C to larger pyramid-shaped islands. In these conditions annealing resulted in the diffusion of silicon into the germanium islands. This reverse trend in the shape evolution was attributed to the decrease in the elastic strain due to interdiffusion, which shifts the critical volume for the hut to dome transition to a value which exceeds the current volume of the dome-shaped island, thereby driving the transition back to pyramidal shape. By combining ADF and EELS data, the amounts of silicon in both the as-grown and annealed islands were evaluated to 40% and 70% respectively. In addition to measuring the silicon content of the islands, the strain field under the as-deposited island was observed by ADF which mirrors approximately the size and shape of the island. For the annealed island, the interface was broadened over several unit cells and little or no extended strain field was detected in the substrate.

As explained before, stress calculations based on linear elastic theory show that besides the reduction in the strain energy, islanding also enforces a strain concentration at the island edge [88] which can favor a strain induced alloying [182]. This mechanism was confirmed by Fourier transform mapping of high resolution TEM images of Ge dome islands [183]. Molecular dynamics simulations of strain and stress distribution in Ge pyramids and domes [184] have reproduced these observations and shown that the Si lattice is significantly distorted below the edge of the Ge islands. In addition, a selective etching procedure was used to probe the lateral composition profile of SiGe pyramids on Si(001). The study confirmed that the pyramids consist of highly Si intermixed corners, whereas the edges, the apex, and the center of the pyramids remain Ge rich [185]. The strain gradient at the edge and underneath the island may enhance Si-Ge interdiffusion and thus alloying constitutes an alternative pathway for strain relaxation in large islands, especially when they are grown at high temperature or after annealing [186].

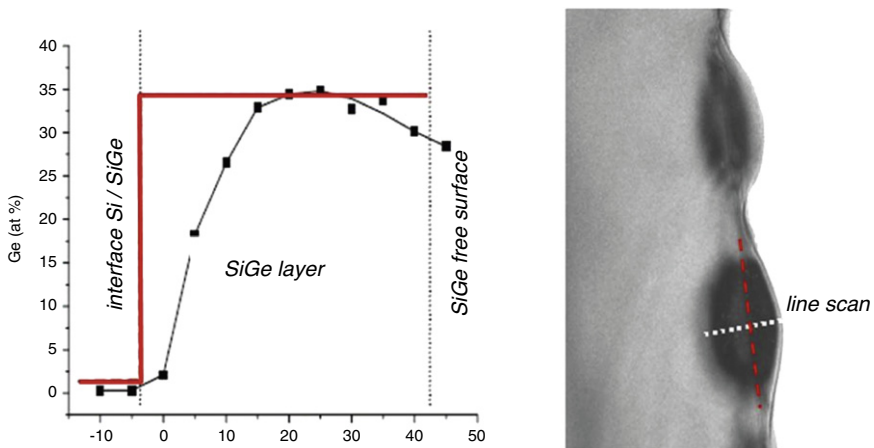


Fig. 69. (left) EDS composition profile through the hut island from the Si substrate to the top free surface; (right) TEM cross-section image of SiGe layer with SiGe islands. The line scan position is indicated by an arrow.

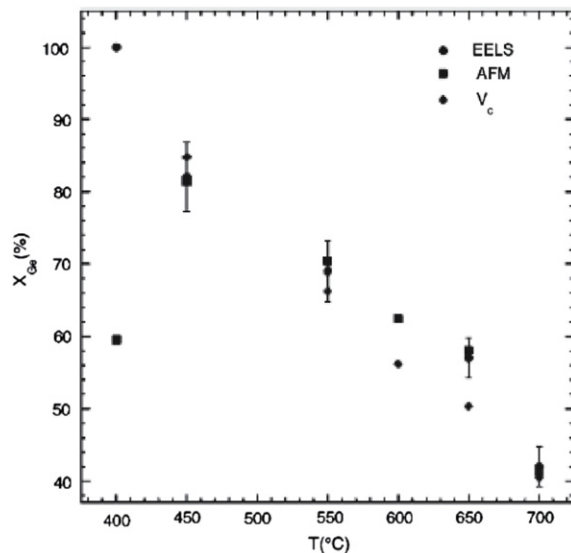


Fig. 70. Average Ge concentration in dome clusters vs substrate temperature T . Points labeled “EELS” were measured using that technique. Those labeled “AFM” were measured by scaling the integrated island volume by the Ge coverage. Those labeled “ V_c ” were calculated by determining the misfit dependence of the minimum dome cluster size for each T .

Source: from [180].

Different other techniques were dedicated to the composition analysis of SiGe quantum dots. In [78], finite element calculations and kinematic scattering theory allowed to compute reciprocal space maps of Ge islands grown by LPE on Si(001). They evidenced the concentration gradient inside the islands with typically an abrupt change in the Ge content at about one third of the island height [78]. Finally, in [187], a scanning probe microscopy combined with selective etching was used to determine 3D composition profiles of Ge dots grown by MBE on Si(001). It evidenced a Si-rich island base arising possibly from initial Si-rich prepyramids collecting material from the wetting layer. The kinetics of the alloying phenomena was recently analyzed through isotope tracing (Fig. 71) [188]. It evidenced the strong incorporation of Ge atoms into islands coming from the initial planar layer, while direct beam atoms deposited at and after the onset of the 3D islands have only a partial contribution to the island composition, Fig. 71.

As we have seen in this section, some results concerning the compositional mapping of the SiGe nanostructures are still contradictory and depend both on the experimental growth conditions and on the analysis technique used to measure it. A better understanding of the differences and consistencies would need to compare the different methods, with their advantages and drawbacks, in general as well as in the specific SiGe/Si system. This comparison is out of the scope of this paper, but a critical and comprehensive review of techniques of compositional mapping may be found in Ref. [189].

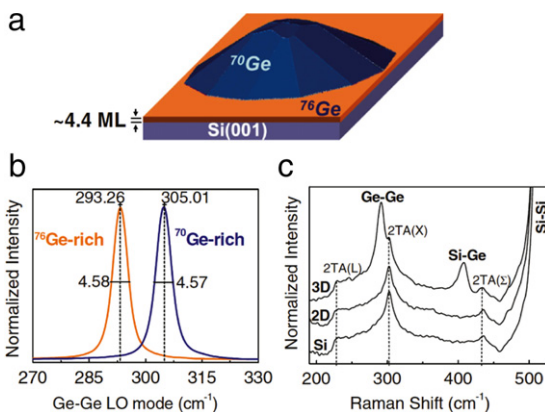


Fig. 71. (Color online). (a) Schematic illustration in the abrupt configuration of the two-isotope growth of a Ge/Si(001) island. (b) Ge–Ge modes of ⁷⁰Ge and ⁷⁶Ge sources used in this study. (c) Raman spectra of Si(001) bare substrate (Si), 4.4 ML of ⁷⁶Ge deposited on Si(001) (2D), and a ⁷⁶Ge 3D island grown by depositing 1 ML of ⁷⁶Ge on the 2D layer (3D).

Source: from [188].

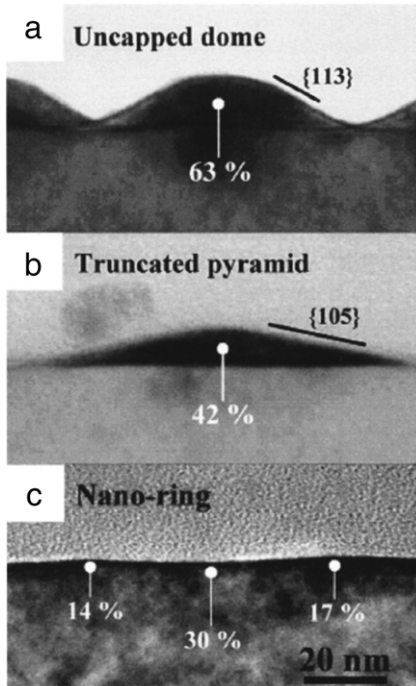


Fig. 72. TEM cross-section images of Ge/Si QDs: (a) uncapped, (b) capped with 14 ML Si and (c) with 28 ML Si. Ge concentrations determined by EDX are indicated.

Source: from [190].

2.2.3. Multilayers and superlattices

The segregation of Ge which occurs at the growth front during the growth process is traditionally studied mostly for Si capped SiGe layers and superlattices by surface-sensitive in situ techniques such as Raman and medium-energy ion scattering [191,192], X-ray photo-electron spectroscopy [193], reflection high-energy electron diffraction [192] and Auger electron spectroscopy [194,195]. The evolution during capping of Ge/Si(001) quantum dots was monitored as a function of the deposition of Si on the islands by UHV-CVD at 600 °C [190] and by UHV magnetron sputter epitaxy at 550 °C [196], while the evolution of their shape, composition and microstructures was investigated by atomic force microscopy combined with selective wet etching procedures in [197]. It was shown that the initial prevalently dome-shaped islands transform first into pyramids upon capping after deposition of ~3 nm Si [190]. As a consequence, the island height decreases upon capping with Si, as a tendency to develop a stable (001) surface replacing the higher angle and higher energy facets, see Fig. 72(a) and (b). At the same time, a strong material intermixing is observed by EDS, with a Ge content decreasing from 0.63 in the initial dome to about 0.4 in the hut islands. When the Si coverage increases, the Ge islands are found to change from domes to truncated pyramids, nanorings and eventually to fully buried islands. These structures are shown in TEM images in Fig. 72

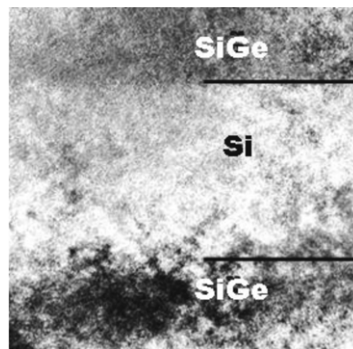


Fig. 73. Bright field TEM image of a multiquantum well structure. The SiGe–Si interface (lower interface) is much broader than the Si–SiGe interface which appears almost flat at this scale.

and are associated to an increasing intermixing: the Ge content decreases from 0.63 in the initial dome to about 0.3 in the ring core and 0.15 on the rims. The nanorings display a Ge-rich core with a Si-rich periphery. These morphological changes are associated to the lateral redistribution of Si from the highly strained apex to the less strained island sides, which critically depend on the composition and volume. The crucial atomic redistribution in islands during capping with Si is ascribed firstly to the intermixing between the Si capping layer and Ge islands, but also to a strain-driven process [197]. A preserved Ge-rich core was also observed after capping, even after a strong change in the island shape and after the production of a flat Si surface. The initial stages of the capping process were followed by *in situ* STM and GIXRD in [198]. As already reported by the same group [199], capping was shown to produce a shape transformation from dome to hut clusters with a decrease in the island height. The Ge composition x starts with a value of 0.4 at the island base in both huts and dopes and increases monotonically to the top to about 0.7 without capping. After capping, due to the incorporation of in the island, x decreases near the island top, down to about 0.4 for 5 ML capping, while the Ge content in the island core remains unchanged. A reduction of the strain after capping was observed, which was argued to be the reason for the shape transformation from dome to hut. STM observation of the island shape upon capping at a much lower temperatures (340°C) evidenced no such shape transformation as a low growth temperature prevents intermixing, as was confirmed by the composition analysis of islands [200].

Another scenario occurs during the growth of 2D Si–SiGe superlattices. The persistence of a large Ge concentration in the Si capping layer coming from the SiGe layer is commonly observed [201] and is interpreted in terms of Ge atoms segregating towards the surface by swapping with Si atoms in the monolayer beneath (see the so-called two-state-exchange model detailed in Section 3.5). In conventional bright-field TEM, this effect traditionally leads to apparently diffuse interfaces between Si and SiGe, see Fig. 73, but cannot be quantified as the image contrast is sensitive only to changes in the Ge content at low concentration. The compositional profiles of the three last layers of a multilayer structure grown by gas source MBE of Ge on Si(001) were extracted from high-angle annular dark field (HAADF) images, see Fig. 74. They exhibit a slightly lower Ge concentration in the lower two layers compared to the top layer, together with Ge tails extending along the growth direction into Si in all layers. These effects are characteristic of Ge segregation. However, even when bulk diffusion is taken into account, the two-state-exchange cannot fully explain the large interface widths measured by HAADF, which might indicate that the segregation process involves more than just the top two layers [202]. Composition profiles of buried Ge QDs on Si(001) grown by gas source MBE were obtained using EDS in STEM, see Fig. 75 and showed that the material of the cap layer is pure Si, while it is $\text{Si}_{0.75}\text{Ge}_{0.25}$ in the QD center and $\text{Si}_{0.83}\text{Ge}_{0.17}$ in the wetting layer. Linescans of the Ge composition across the WL show that the upper SiGe/Si interface is smeared out into the surrounding Si, due to Ge segregation, see Fig. 75(d). In the vicinity of a dot, the line-scan reveals a thinner WL which contains less Ge, see Fig. 75(c), while a line-scan through the QD axis reveals that the Ge concentration is highest at the apex of the dot. It was suggested that these composition variations result from the migration of Ge atoms from the region immediately around each dot towards a nucleation center where Ge piled up to form a dot.

A detailed description of the Ge composition of SiGe superlattices grown by MBE was also performed by using STEM-EDS, see [5]. Fig. 76 compares the Ge profiles in the growth direction measured along a crest and a valley of an island superlattice with $x = 0.48$. Considerable Si–Ge intermixing occurs in this system. The Ge peak concentration in the crests is only about 0.2 or half the nominal Ge concentration expected from the deposition rate. The integrated Ge signal per superlattice period is however close to that of the nominal structure. In the troughs, the Ge concentration is significantly reduced and the integrated Ge signal corresponds to approximately 50% of that of a nominal superlattice period, indicating significant surface lateral diffusion during growth. Moreover, the Ge profiles clearly evidence a Ge surface segregation, as revealed by the exponential decay of the Ge concentration at the trailing edge of the SiGe layers, see Fig. 76. In these conditions, the decay length is found to be about 3.3 nm, in good agreement with values of the decay length in planar $\text{Si}/\text{Si}_{1-x}\text{Ge}_x$ heterostructures [5]. As growth proceeds, an enhanced chemical contrast is obtained between the islands and the WL, with better defined Ge-rich islands but no increased intermixing in the upper islands, in contrast to what is observed by selective etching [204]. A similar STEM-EDS analysis performed on an island superlattice grown by UHV-CVD revealed

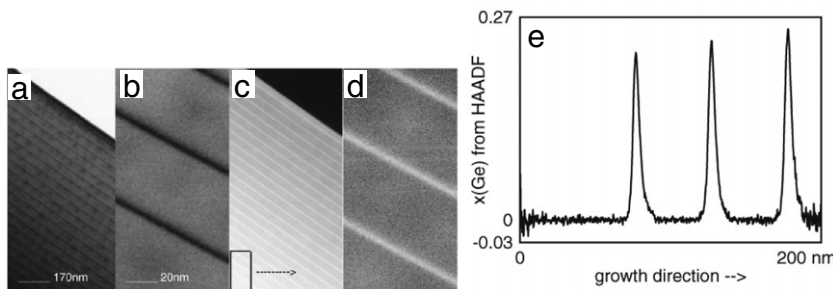


Fig. 74. HAADF profile concentration of the three top layers of a multiquantum well structure. The profiles exhibit long tails of low Ge composition extending into the Si barrier layers for a multi-quantum well structure under bright-field conditions.
Source: from [202].

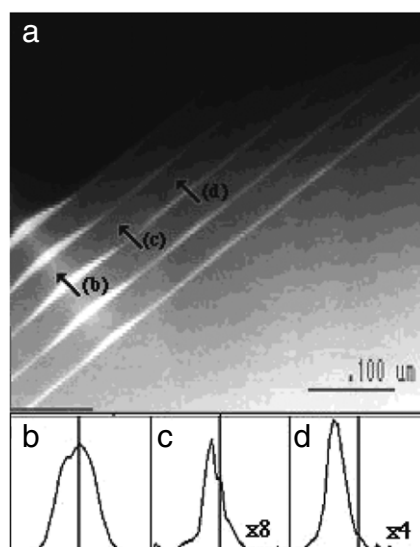


Fig. 75. (a) High-angle dark field STEM image of the QD sample. Linescans through (b) the middle dot, (c) the thin 2D SiGe layer, and (d) the normal 2D SiGe layer.
Source: from [203].

interesting differences as illustrated in Fig. 77. In these growth conditions, the Ge profile in each superlattice period exhibits a symmetrical triangular shape, suggesting that inter-diffusion occurs both at the leading and trailing interfaces of the $\text{Si}_{1-x}\text{Ge}_x$ alloy layers. The decay length of the Ge concentration is smaller than in MBE superlattices (about 2.5 nm) and no appreciable Ge segregation is measured, possibly because of the surfactant effect of hydrogen created by dissociation of silane and germane (see Section 2.2.4 for a detailed description of the surfactant effect).

Raman spectroscopy was also widely used to characterize the alloy composition and strain state of $\text{Si}_{1-x}\text{Ge}_x$ dot superlattices grown on Si by a variety of methods, MBE, CVD, ... [205–209]. Raman scattering is particularly well suited for studying the electronic and vibrational properties of SiGe island superlattices and for determining lattice strain and interface sharpness and composition [5]. This is due to the lattice vibrational energies, which are governed by short range forces between atoms which are very sensitive to atomic bond lengths, angles and atomic masses. The identical diamond crystal structures of Si and Ge yields a triply degenerate optical mode of vibration at zero wavevector, which appear around 505, 415, and 295 cm^{-1} in the Raman spectrum of $\text{Si}_{1-x}\text{Ge}_x$. By measuring the peak frequencies of these modes as a function of the Ge concentration, it appears that the Si-Si (and Ge-Ge) mode frequency decrease (increase) linearly with x , while the Si-Ge mode behavior is best represented by a fourth order polynomial [5]. All these optical modes are also sensitive to the presence of strain, which causes a shift in their mode frequencies [210]. Biaxial strain found in epitaxial layer growth on Si induces a phonon frequency shift compared to the zero strain frequency ω_0 given by [211]

$$\omega - \omega_0 = b\epsilon_{||}, \quad (2)$$

where b is the strain-shift coefficient relating the displacement of the phonon frequency with the lattice distortion $\epsilon_{||}$. For the Si-Si mode, results for the strain-shift coefficient b measured as a function of x may well be fitted by a linear function as [211]

$$b(\text{cm}^{-1}) = -715 - 825x, \quad (3)$$

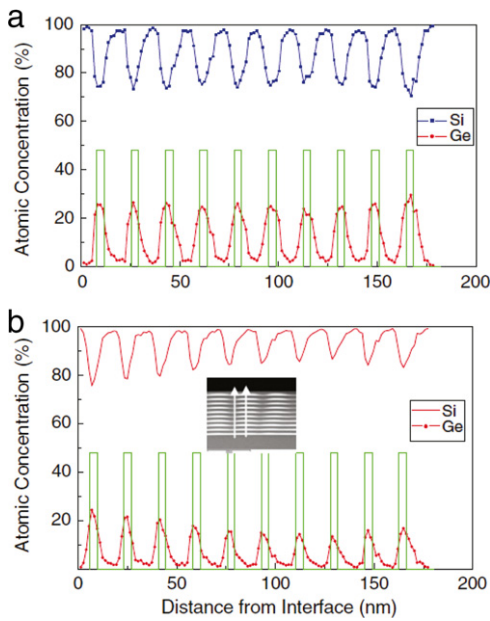


Fig. 76. EDS chemical profile in the growth direction for a ten-period $\text{Si}_{0.52}\text{Ge}_{0.48}$ (3.7 nm)/Si (13.7 nm) island superlattice grown by MBE at 625 °C and measured (a) along an interface crest and (b) along an interface valley, as shown in the micrograph in the inset. Also indicated on the graph (by vertical bars) is the nominal Ge concentration profile based on the growth parameters.

Source: from [5].

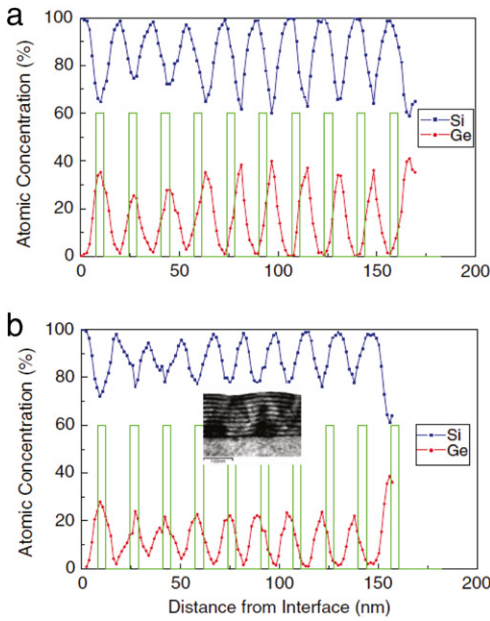


Fig. 77. EDS chemical profile in the growth direction for a UHV-CVD grown ten-period $\text{Si}_{0.60}\text{Ge}_{0.40}$ (4.0 nm)/Si (12.5 nm) island superlattice measured (a) along an interface crest and (b) along an interface valley, as shown in the micrograph in the inset. Also indicated on the graph (by vertical bars) is the nominal Ge concentration profile based on the growth parameters.

Source: from [5].

while the film lattice constant is well approximated by the quadratic form [212]

$$a_{\text{epi}}(\text{nm}) = 0.5431 + 0.02x + 0.0027x^2. \quad (4)$$

The Ge-Ge and Si-Ge mode frequencies in island superlattices appeared to be noticeably lower than those of the planar superlattice, indicating a significant relaxation of the lattice constant towards the unstrained bulk alloy values in island superlattices, see Fig. 78. Moreover, an inhomogeneity of the Ge content and the existence of a slightly tensile strain in the

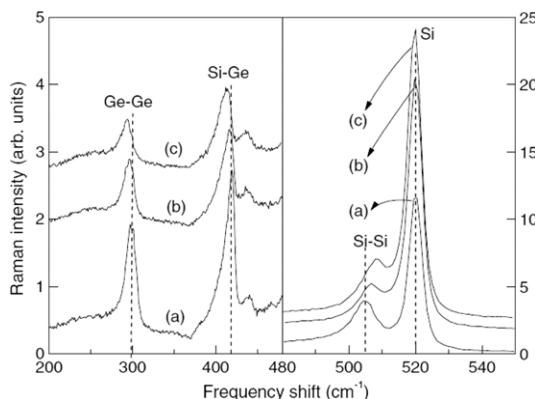


Fig. 78. Room temperature Raman spectrum showing the optics modes of (a) a $\text{Si}/\text{Si}_{1-x}\text{Ge}_x$ planar superlattice for $x = 0.52$, (b) an island superlattice for $x = 0.56$, and (c) an island superlattice for $x = 0.45$. Dotted lines emphasize the shift of the main Raman lines.
Source: from [5].

alloy layers were also revealed by the analysis of the Si optical mode. This inhomogeneity is caused by the sideways diffusion of Ge during growth and the Si layer is thus under weak tensile strain above the dome islands and compressively strained between the domes [151]. This analysis evidenced also that the Ge atoms form nanometer clusters with a nearly pure Ge core surrounded by a $\text{Si}_{1-x}\text{Ge}_x$ shell in domes with a high Ge concentration [213,214].

When the superlattice involves morphological undulations, the x dependence of the three optical modes revealed an accumulation of Ge at the crest of an undulation, which causes a decrease in the Ge fraction in the continuous alloy layer between islands, producing a shift down in the frequency of the vibration modes. In fact, the vibrational frequencies in the undulated case are close to those measured in planar superlattices with a 10% less nominal Ge concentration, which is consistent with analytical TEM results. In undulated superlattices, there is also a clear evidence of Ge diffusion into Si in the limiting case of a pure Ge layer. In addition, the out-diffusion of Ge results in Si-rich regions in the valleys between the $\text{Si}_{1-x}\text{Ge}_x$ crests which are under compression. Finally, note that annealing of these dome island superlattices at temperatures ranging between 700 and 850 °C did not lead to an observable effect on the Raman spectrum, due to the absence of interface interdiffusion and strain relaxation in these conditions [5]. On the contrary, pyramidal-shaped Ge dot superlattices [215,216] undergo a significant Si/Ge intermixing during annealing, and the difference in thermal stability of the dome and pyramid superlattices may be attributed to the difference already discussed of the strain distributions.

The capping of SiGe islands with Si was also investigated by more indirect techniques such as atomic force microscopy combined with a selective etching procedure and by XRD in [217]. The samples were grown by solid source MBE at 640 °C and the analysis gives Ge isocomposition profiles during growth. Without capping, the islands are enriched with Si at their base corner while after capping, intermixing with Si is higher along the pyramid base diagonals. The enrichment with Si inside the islands during capping may be attributed to the exchange of Si atoms coming from the capping layer, which incorporate into the island by exchange with Ge atoms both by atomic surface segregation and interdiffusion. Nevertheless, it was also argued that elastic anisotropy in the (001) plane and especially the larger Young's modulus in the (110) direction, produces a higher strain energy and then a higher Si-Ge intermixing. Note that in parallel to the composition evolution, the islands transform in these conditions from a dome shape to a (103) faceted pyramid at a Si capping thickness of 0.32 nm, followed by a decrease in the pyramid facet inclination during further capping [217].

2.2.4. Surfactant

Surfactant mediated growth was extensively studied in order either to suppress the formation of islands or to modify their size and shape. In the case of C-mediated growth, it may be expected that carbon atoms could suppress the formation of islands by reducing the elastic energy and modifying the surface and interface energetics. In fact, it was reported that in presence of C, the growth of Ge islands on Si proceeds without the formation of a wetting layer in the Volmer-Weber mode as opposed to the growth on a bare Si(001) substrate. The resulting islands draw attention because of their remarkably small size, with a typical diameter which can be as small as 10–15 nm in diameter and with a height of about 1–2 nm. Two different scenarios were put forward to explain these observations. It was first suggested that the dots are characterized by a gradual composition profile from homogeneous SiGeC below and at the bottom of an island to pure Ge near its apex [218]. On the other hand, it was suggested that the dots are free of C but are located between C-rich patches, with a gradual composition profile from SiGe at the dot bottom base to Ge at its apex [219]. These systems were analyzed by Monte-Carlo simulations which quantify the stress fields and associated composition profiles both in small pyramidal islands and their neighborhood for various carbon contents [220]. At equilibrium and after relaxation by intermixing at 800 K, the dots are found to be free of C and located between C-rich regions. The size reduction may thus be attributed to the enhancement of the island Ge content compared to the C-free case, which results from the presence of C atoms in deeper layers. These C atoms act as traps for Si atoms, decelerating the diffusion of Si in the dot and the out diffusion of Ge.

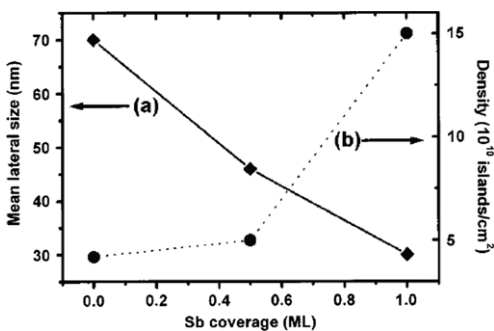


Fig. 79. Evolution of the mean lateral size of islands (a) and of their surface density (b) with Sb coverage.
Source: from [221].

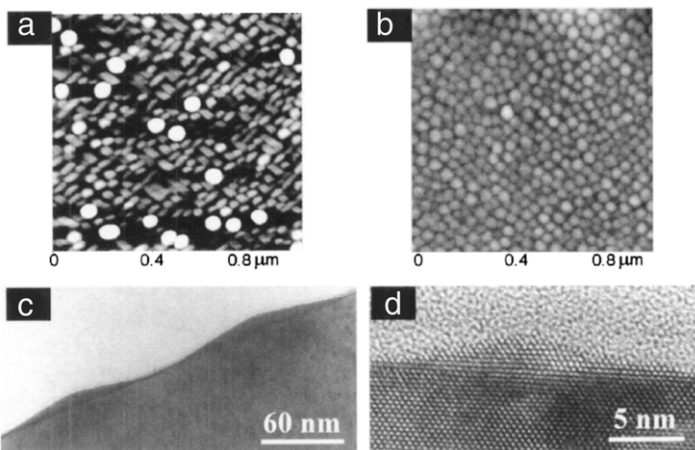


Fig. 80. AFM (a), (b) and TEM (c), (d) images of 13 MLGe/θ MLSb-Si(001) obtained at 550 °C with $\theta \sim 0$ (a) and (c), $\theta \sim 1/2$ (b), and (d).
Source: from [221].

The effect of a phosphine environment on the growth of SiGe islands was investigated by selectively etching in [204]. The etchant used was known to remove efficiently $\text{Si}_{1-x}\text{Ge}_x$ when $x \geq 0.65$, while the etching rate is negligible when $x \leq 0.65$, thus allowing to characterize isocomposition surfaces [204]. The samples were scanned by AFM before and after etching and demonstrated that the PH_3 atmosphere produces not only a reduction of the island size but also a noticeable enrichment by Ge as compared to islands produced in a H_2 ambient. It was also concluded in CVD experiments in [222] that surface diffusion of Si prevails during annealing in a H_2 atmosphere, whereas Ge surface and intra-island diffusion dominates during annealing in a PH_3 environment. This observation was attributed to the suppression of Ge/Si intermixing during growth resulting from the modification of the surface energy by PH_3 [223]. Similar results were found for Sb surfactant mediated growth [221].

3. Formation mechanisms

The production of quantum dots in strained SiGe systems results from a morphological evolution which is one route for strain relaxation in competition with other mechanisms such as surface reconstruction, strain induced step bunching, alloying, dislocation introduction, etc., see [1,19] and references therein. We mainly focus here on the mechanisms responsible for the morphological evolution leading to QD assembly in coherent epitaxy.

3.1. Low strain regime

3.1.1. Basics of the Asaro–Tiller–Grinfeld instability

The morphological instability experienced by a strained film originates basically from the stress relaxation allowed by a surface corrugation. It was first described in the framework of liquid epitaxy by Asaro and Tiller [59] and re-derived by Grinfeld [60] and then by Srolovitz [224], and is referred to as the Asaro–Tiller–Grinfeld (ATG) instability even if more complex mechanisms may also come into play as additional effects. In the field of semiconductor epitaxy, the elastic stress is due to the film and substrate lattice mismatch characterized by the relative difference of lattice parameters $m = \delta a/a$. When m is not too large, as is the case in SiGe systems where Ge and Si lattice parameters differ by 4%, the film can remain coherent

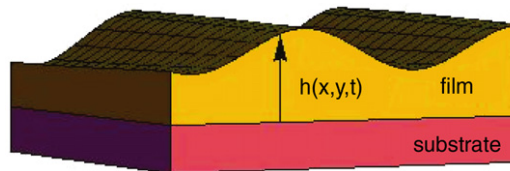


Fig. 81. A film coherently deposited on a substrate with a misfit δ experiences a bi-axial strain which can be relaxed during a morphological evolution.

with the substrate which generates an elastic stress throughout the system. When Ge is deposited on Si(001) in molecular beam epitaxy, the film surface develops some roughness resulting from thermal and kinetic fluctuations [34]. Morphological inhomogeneity enforces inhomogeneity in the local elastic energy density on the surface which initiates surface diffusion. The latter diffusion is mainly activated at the usual temperature of MBE. Interdiffusion on the first surface layers also occurs and impacts composition gradients (see below) but volume diffusion may be neglected in the usual conditions where T lies in between 400 and 900 °C.

The description of surface diffusion may be done using a continuum modelization of the system which is backed by the roughness of the SiGe surface on a Si(001) substrate, see below. Diffusion is induced by the inhomogeneity of the local chemical potential on the surface, μ , and surface mass currents may be considered as simply proportional to gradients of μ [225]. We consider a geometry where the film is characterized by its height $z = h(\mathbf{r}, t)$ with respect to the substrate, see Fig. 81 where \mathbf{r} is the 2D vector on the biaxial strain plane. In this framework, mass conservation enforces

$$\partial h / \partial t = F + D \sqrt{1 + |\nabla h|^2} \Delta_S \mu, \quad (5)$$

where F is the deposition flux, D , a diffusion coefficient, Δ_S , the surface laplacian, see e.g. [226]. The chemical potential may be conveniently related to the functional derivative $\mu = \Omega \delta \mathfrak{F} / \delta h$ [227] of the system energy \mathfrak{F} as a function of the film height $h(\mathbf{r})$. This energy is given by the sum of a surface energy contribution $\mathfrak{F}^s = \int \gamma \sqrt{1 + |\nabla h|^2} d\mathbf{r}$ and an elastic one $\mathfrak{F}^{el} = \int_{z < h(\mathbf{r})} \mathcal{E}^{el}(\mathbf{r}, z) d\mathbf{r} dz$, where \mathcal{E}^{el} is the elastic energy density. In the original ATG instability, the surface energy γ is basically constant and depends neither on the film height nor on its orientation. The functional derivative leads to

$$\mu(\mathbf{r}) = \Omega \gamma \kappa(\mathbf{r}) + \Omega \mathcal{E}^{el}(\mathbf{r}) + \mu_0, \quad (6)$$

where Ω is the atomic volume, γ , the film surface energy, and μ_0 , the crystal reference formation energy. The first contribution is a stabilizing one which favors surface smoothing to reduce the surface energy of a corrugation and is proportional to the mean curvature $\kappa = -[\Delta h + h_y^2 h_{xx} + 2h_x h_y h_{xy} + h_x^2 h_{yy}] / (1 + |\nabla h|^2)^{3/2}$. On the contrary, the second contribution is a destabilizing one related to the elastic energy density computed at the surface $\mathcal{E}^{el}[\mathbf{r}, z = h(\mathbf{r})]$ [in short-hand notation $\mathcal{E}^{el}(\mathbf{r})$]. The elastic properties may be computed at mechanical equilibrium which is reached over the relevant time scale of the instability. As explained below, mechanical equilibrium equations can be solved when one studies the initial stage of the evolution when the surface is weakly departing from its initial flat configuration. A perturbation $e^{i\mathbf{k}\cdot\mathbf{r}+\sigma t}$ of the film height is then found to grow exponentially with a typical growth rate [59,60,224,228]

$$\sigma = |\mathbf{k}|^3 - \mathbf{k}^4, \quad (7)$$

in dimensionless units to be defined below. The non-analytical term $|\mathbf{k}|$ betrays the long range of the driving elastic interactions, and is in competition with the local and analytical term depicting the surface smoothing induced by the surface energy. The growth rate is positive for small k , see Fig. 82, and the morphological instability occurs for a perturbation with a wavelength beyond the critical wavelength

$$l_0 = \frac{\gamma(1-\nu)}{2(1+\nu)Ym^2}, \quad (8)$$

chosen to be the length scale, with Y and ν , the film and substrate Young modulus and Poisson ratio. The length scale and thus the characteristic wavelength of the ATG instability basically behaves as $1/m^2$, or, for a $\text{Si}_{1-x}\text{Ge}_x$ film, as $1/x^2$. If the trend is correct as compared to experiments, additional alloying effects are sometimes required to find a good comparison. Given this length scale, one can define also a typical time scale $t_0 = l_0^4/D\gamma$. For example, for a $\text{Si}_{0.75}\text{Ge}_{0.25}$ film on Si, one finds $l_0 = 27$ nm and $t_0 = 23$ s at 700 °C (see [229] for an estimate of surface diffusion coefficients). Note that in the case of different film and substrate elastic constants, the coefficients of Eq. (7) involve some functions which depend on the mean film height [228] and in the singular case of a rigid substrate, a critical height has to be overcome before the instability may occur.

Mechanical equilibrium is described by the Lamé equations

$$\partial_j \sigma_{ij}^\alpha = 0, \quad (9)$$

with summation over repeated indices. In the isotropic case, the stress tensor σ is related to the strain tensor ϵ by $\sigma = Y/(1+\nu)[\epsilon + \nu/(1-2\nu)\text{Tr}(\epsilon) \mathbb{1}]$ with the identity matrix $\mathbb{1}$ and the Young modulus Y . If one considers that the film

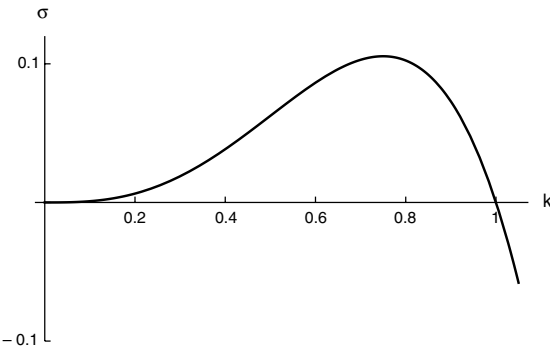


Fig. 82. Variation of the basic growth rate $\sigma(k) = |\mathbf{k}|^3 - \mathbf{k}^4$ of the ATG instability.

and substrate have identical elastic constants, the solution in the film is identical to the solution of a unique semi-infinite film under an external bi-axial strain [230] corresponding to the misfit m . Displacements are computed with respect to a reference state chosen to be the substrate free of deformation so that the full strain is $e_{ij} = \frac{1}{2}(\partial_j u_i + \partial_i u_j) - m \mathbb{1}_{ij}$. The solution for the displacement vector may be fully determined considering appropriate boundary conditions. In MBE where the film grows in an ultra-high vacuum chamber, the film surface may be considered as free of stress. Moreover, surface stress may also be neglected in SiGe systems [231] so that one must enforce $\sigma \cdot \mathbf{n} = \mathbf{0}$ at the film free surface $z = h(\mathbf{r})$ with the normal vector \mathbf{n} . The coherence of the film/substrate interface requires the continuity of both the displacement \mathbf{u} and the force $\mathbf{e} \cdot \hat{\mathbf{z}}$, where $\hat{\mathbf{z}}$ is the normal to the film/surface interface.

The simplest case is the flat film configuration $h(\mathbf{r}) = \bar{h}$, where the solution is $\mathbf{u}_0^s = \mathbf{0}$ in the substrate and $\mathbf{u}_0^f = (0, 0, \Sigma z)$ with $\Sigma = m(1 + \nu)/(1 - \nu)$ in the film. The non-zero solution in the film keeps track of the Poisson effect for a bi-axially strained film which relaxes its stress in the third direction. The elastic energy density $\mathcal{E}^{el} = \frac{1}{2}e_{ij}\sigma_{ij}$ is then merely $\mathcal{E}_0 = Ym^2/(1 - \nu)$. In the general case however, the nonlinear boundary conditions at the free film surface ($\sigma \cdot \mathbf{n}$ involves the product of two h -dependent terms) cannot be solved exactly for any arbitrary film shape. It is nonetheless possible to solve it when the surface satisfies the small slope approximation, i.e. when the film surface may be written as $h(\mathbf{r}) = \bar{h} + \epsilon h_1(\mathbf{r})$ where \bar{h} is arbitrary, ϵ is small, and the derivative of h_1 is of order unity. This approximation is justified in the early stage of the instability and, in SiGe films, as long as the system involves small slopes as is the case in a hut assembly where (105) facets with 11.3° side angles are the steepest orientations. The solution may be sought as a power series in ϵ which can be conveniently computed using 2D Fourier transforms $\mathcal{F}[h](\mathbf{k}) \equiv (2\pi)^{-2} \int d\mathbf{r} e^{i\mathbf{k} \cdot \mathbf{r}} h(\mathbf{r})$. The solution at first order is then given by [230]

$$\mathbf{u}_1(\mathbf{k}, z) = m \frac{1 + \nu}{1 - \nu} \frac{e^{|\mathbf{k}|(z - \bar{h})}}{|\mathbf{k}|} \begin{pmatrix} [2(1 - \nu) + |\mathbf{k}|(z - \bar{h})]ik_x \\ [2(1 - \nu) + |\mathbf{k}|(z - \bar{h})]ik_y \\ [1 - 2\nu - |\mathbf{k}|(z - \bar{h})]|\mathbf{k}| \end{pmatrix} \mathcal{F}[h](\mathbf{k}). \quad (10)$$

The solution is exponentially damped in the vertical direction but with a cut-off length $|\mathbf{k}|^{-1}$ given by the surface wavelength. Therefore, the influence of a corrugation is sensible in the vertical direction over a depth of the order of the horizontal scale of the surface modulation. This property also characterizes relaxation in islands. Given Eq. (10), one can compute the in-plane relaxation $\epsilon_{||} = \epsilon_{xx} + \epsilon_{yy}$ for a given geometry. This is done in Fig. 13 for the surface resulting from the growth of the ATG instability when the surface peak to peak amplitude is 2 nm for a $\text{Si}_{0.75}\text{Ge}_{0.25}$ film on Si. One realizes that this relaxation is small in this early geometry, as corroborated by experiments performed in films where the instability is developed. With the solution (10), one can compute the elastic energy at first order and find the elastic chemical potential $\mu^{el} = \Omega \mathcal{E}^{el}(\mathbf{r})$,

$$\mu^{el}(\mathbf{r}) = \Omega \mathcal{E}_0 \{1 - 2(1 + \nu)[\mathcal{H}_{xx}(h) + \mathcal{H}_{yy}(h)]\}, \quad (11)$$

in terms of the generalized Hilbert transform defined as

$$\mathcal{H}_{ij}(h) = \mathcal{F}^{-1} [(k_i k_j / |\mathbf{k}|) \mathcal{F}[h](\mathbf{k})]. \quad (12)$$

In Fourier space, \mathcal{H}_{ij} behaves as a multiplication by $|\mathbf{k}|$ which, combined with the \mathbf{k}^2 associated with the surface Laplacian in Eq. (5), gives the destabilizing $|\mathbf{k}|^3$ term in the growth rate (7).

3.1.2. ATG instability with wetting and anisotropy

The ATG instability has been experimentally evidenced either during a long enough growth or during annealing of a thin film. In the latter case wetting interactions between the film and the substrate come into play and yield a dependence of the surface energy on the film height h [232,87,233,15]. This dependence results from the change over a few atomic height of the local environment of a particle which rules the surface energy. This effect may be quantified in Ge on Si thanks to

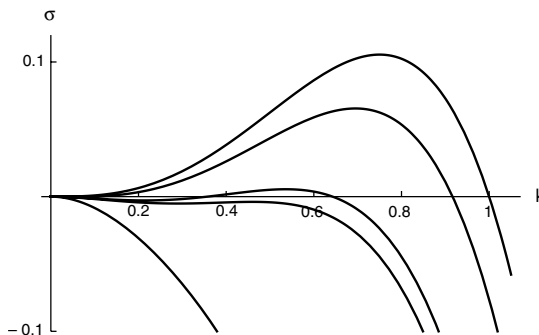


Fig. 83. Variation of the growth rate $\sigma(k)$ for, from top to bottom, $c_w = 0$ and then $c_w = 0.05$ and $h_0 = 10, 9.5, 8.4, 8.25, 7\delta_w$.

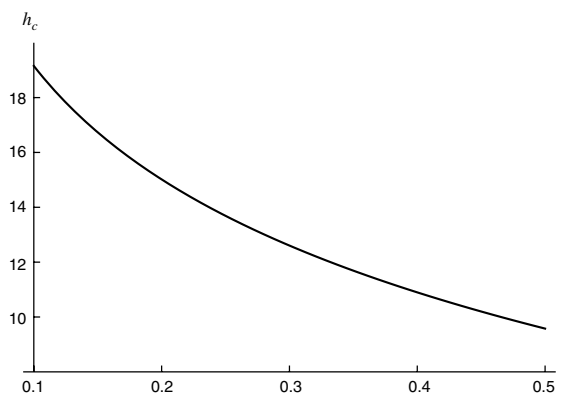


Fig. 84. Evolution of the critical height (in ML) above which the ATG instability occurs in the presence of stabilizing wetting interactions, as a function of the film composition x of a $\text{Si}_{1-x}\text{Ge}_x$ film on a Si substrate. The value of h_c is computed from (15) with $c_w = x/3$ and $\delta_w = 2a$.

atomistic calculations [234,235,49] where it is found that the film surface energy varies from 90 to 60 meV/ \AA^2 for thin to thick film heights with a monotonically decreasing trend [49]. When needed in the following, we use the fit of the latter variation [87,15]

$$\gamma(h) = \gamma_f [1 + c_w \exp(-h/\delta_w)], \quad (13)$$

where γ_f is the thick film surface energy, while the amplitude c_w is of the order of 10% while δ_w is a few atomic layer heights [49].

Taking into account the dependence of γ on h in \mathcal{F}^s , one finds an extra term in the surface chemical potential which now reads

$$\mu = \Omega \gamma(h) \kappa + \Omega \frac{d\gamma}{dh} n_z + \mu^{el} + \mu_0, \quad (14)$$

with n_z , the z-component of the surface normal vector. The second term in the r.h.s. (referred to as the wetting potential) enforces a modified spectrum with a general lowest-order \mathbf{k}^2 term

$$\sigma = -\frac{d^2\gamma}{dh^2}(\bar{h}) \mathbf{k}^2 + |\mathbf{k}|^3 - \mathbf{k}^4, \quad (15)$$

where $d^2\gamma/dh^2$ is a priori positive and vanishes for large \bar{h} . The first negative term in (15) qualitatively changes the behavior of the growth rate, see Fig. 83. For small enough \bar{h} , σ is always negative and the instability does not develop. On the contrary, for larger \bar{h} than some wetting dependent h_c , σ exhibits positive values over a finite wavelength interval and the instability can develop as in growing films (where wetting effects are quickly damped due to the increasing film thickness) [234,232,15, 236]. These conclusions agree with the experimental observation that the morphological evolution of SiGe films on Si do not occur below a critical thickness [5] which corresponds to 3 monolayers (ML) for pure Ge films [13,14] (where nevertheless the ATG instability is hidden by the 2D–3D transition, see below) and to larger thicknesses for $\text{Si}_{1-x}\text{Ge}_x$ films [107]. The decrease in h_c when the misfit strain increases results from this simple analysis, see Fig. 84, but may also arise from alloying effects [237].

Another extension of the ATG instability concerns the situation where the film and substrate have different elastic constants. The solution of the elastic equations in the small slope approximation for an arbitrary film thickness exhibits then

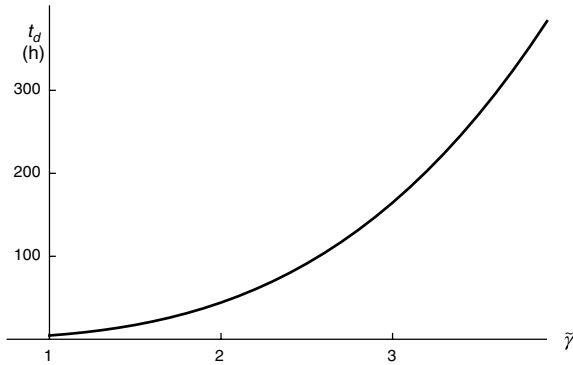


Fig. 85. Characteristic time in hours for the instability to be fully developed as a function of the normalized surface stiffness for a $\text{Si}_{0.85}\text{Ge}_{0.15}$ film on a Si substrate [52].

a non-trivial dependence on the mean film height \bar{h} [228]. As a consequence, the range of unstable wave-vectors depends both on \bar{h} and on the difference of elastic constants, and the instability onset depends on the growth rate [228]. In a simpler case with different elastic constants but in the thin film approximation (i.e. \bar{h} is also supposed small compared to the lateral length scale), the latter \bar{h} dependence disappears and one finds similar results as in the small-slope approximation but where $2(1 + \nu)$ in the r.h.s. of Eq. (11) and in l_0 is replaced by $2E_f(1 - \nu_s^2)/E_s(1 - \nu_f)$ [238,236].

When one considers the development of the instability on a wavy-substrate as a modelization of growth on a patterned system, one can also use a Fourier transform computation of the elastic field provided that the film/substrate interface satisfies the small-slope approximation [239]. One then finds [240] that the instability is enhanced compared to the flat interface case and that the film minimizes its energy in a configuration with the same wavelength but out-of-phase compared to the substrate. A generalization of this study in presence of wetting interactions may be found in [241] where kinetic phase diagrams enable to distinguish the different in and out of phase configurations depending on the growth time and film thickness.

Anisotropy is also known to be a crucial factor in crystal growth which dictates both equilibrium and growth shapes [242–244]. It certainly plays a role in the ATG instability since it was shown experimentally that it can develop on Si(001) substrates but not on Si(111) [56] where long enough growth eventually leads to dislocations [245] while long enough annealing does not allow any significant evolution [52], see Fig. 12. A crucial anisotropy which is missing in the basic ATG modelization is the surface energy anisotropy which dependence on the surface local orientation \mathbf{n} dictates equilibrium shapes [242,243]. When one accounts for both anisotropy and wetting effects, the surface chemical potential reads [246–248]

$$\mu = \gamma(\mathbf{n}, h)\kappa + h_{ij} \frac{\partial^2 \gamma}{\partial n_i \partial n_j} + \frac{\partial \gamma}{\partial h} n_z + \mu^{el} + \mu_0, \quad (16)$$

and the linear analysis leads to the growth rate

$$\sigma = -\frac{\partial^2 \gamma}{\partial h^2}(\bar{h}, \mathbf{n}_0) \mathbf{k}^2 + |\mathbf{k}|^3 - \tilde{\gamma}(\mathbf{n}_0) \mathbf{k}^4, \quad (17)$$

with the initial orientation \mathbf{n}_0 and the dimensionless surface stiffness $\tilde{\gamma} = (\gamma + \partial^2 \gamma / \partial h_i \partial h_i) / \gamma_f$, which generalizes the 2D formula $\gamma + \partial^2 \gamma / \partial \theta^2$. Consequently, the dependence on the surface stiffness weakens the instability growth rate and diminishes the interval of unstable wave-vectors. The subsequent increase in the critical height h_c with $\tilde{\gamma}$ is not significant [52] contrarily to the dependence of the kinetics. Indeed, if one defines the time t_d for the instability onset as the time needed for an initial roughness to be larger than some threshold, one finds [52] a marked increase in t_d as a function of $\tilde{\gamma}$, see Fig. 85. The onset time becomes rapidly beyond experimental reachable time scales for a relatively modest stiffness, revealing a notable stiffness induced retardation of the instability. The inhibition of the ATG instability on Si(111) may hence be attributed to this effect as the (111) orientation in SiGe is known to be stiffer than (001) [249,250,34,251]. The previous analysis applies to regularized anisotropy where the stiffness is always well-defined. In the framework of a singular surface anisotropy which describes true facets below the roughening transition, the singularity in the second derivative of the surface energy was shown in 2D to imply the existence of a critical amplitude for the instability to arise [252].

Anisotropy is all the more important as it was shown recently to be responsible for a new effective kinetic pathway in competition with the usual strain relief. Growing Ge on high-indexed Si(1110) lead [120] to the formation of {105} faceted one-dimensional nanoripples which differ from the usual quantum dot growth. This formation was supported by ab-initio calculations which computed the lowering in the surface energy responsible for the kinetic pathway.

Another source of anisotropy which may be relevant is the elastic anisotropy which is also disregarded in the basic ATG calculation and which can induce anisotropic film morphologies [253–258]. As shown by numerical computation of

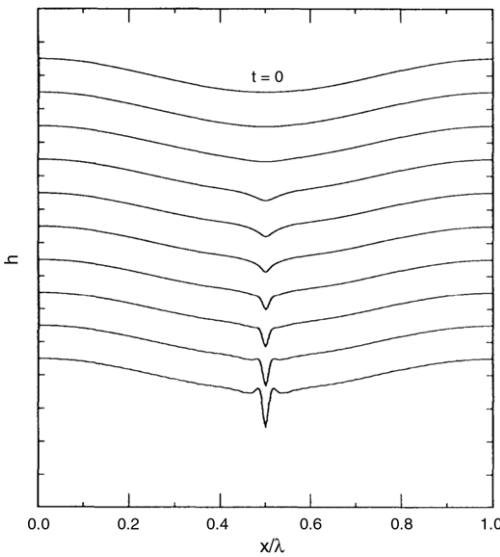


Fig. 86. The temporal evolution of the surface profile under the influence of a bulk stress [259].

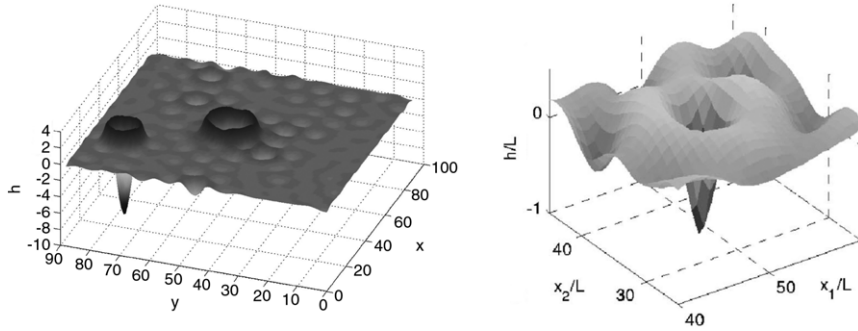


Fig. 87. Blow-up solutions of the morphological instability from (a) [263], and (b) [264].

anisotropic interactions [255], cubic elasticity may result in a pattern alignment driven by the instability. On the other hand, new diamond-like morphologies occur in a solid subject to an anisotropic bi-axial stress with different signs in two orthogonal directions and a large enough ratio [253]. Combined with isotropic elasticity, such an anisotropic external stress can also lead to pattern selection in the early-stage of the instability [257,258].

3.1.3. Isotropic islands

If the linear analysis is satisfactory for the description of the instability first stage, the study of the instability long time dynamics requires the analysis of non-linear effects. Non-linear terms are present both in the elastic energy and in the decay of the wetting interactions. The first non-linear analyses concerned the elastic non-linear terms [260,259,261–263] which can be handled either with a finite-element method, within the small-slope approximation or with a decomposition of the surface shape in terms of cycloids. The long time dynamics of the ATG instability is then characterized by finite-time singularities associated with blow-up solutions: after the instability initial corrugation, deep crack-like grooves grow on the surface before the blow-up occurs for a dimensionless time $t = 0.07$ (Fig. 86). In two dimensions, the elasticity problem may be reduced to a boundary integral equation which may be solved numerically showing the deepening of a groove [259,260]. In 3D, the cusp deepening was numerically evidenced base on a perturbation analysis both near the instability threshold and in the small-slope approximation [263], and more recently, using a numerical implementation of the full non-linear elastic analysis [264], see Fig. 87. This singular behavior recalls the cycloid solution of the elastic problem in 2D where stress is concentrated at the cusp and is relaxed elsewhere when the cycloid wavelength is larger than some critical value [265]. The singular stress concentration [266,265,260,267] is related to the occurrence in experiments of dislocations in the long time dynamics of strained thick films along singular points in the valleys of the surface corrugation [266,265,260,267]. To corroborate this result, the non-linear analysis reveals that deep, crack-like grooves grow by surface diffusion on a strained film and exhibits finite time singularities as the solution blows up (Fig. 87) [259–263].

For thin film however, wetting interactions completely change this scenario. It was shown using a numerical non-linear elastic computation that a wetting potential with large variations can lead on the long run to stable islands separated by a wetting layer [264]. A regularizing non-linear wetting potential diverging as $1/h^2$ coupled to a linear elastic chemical

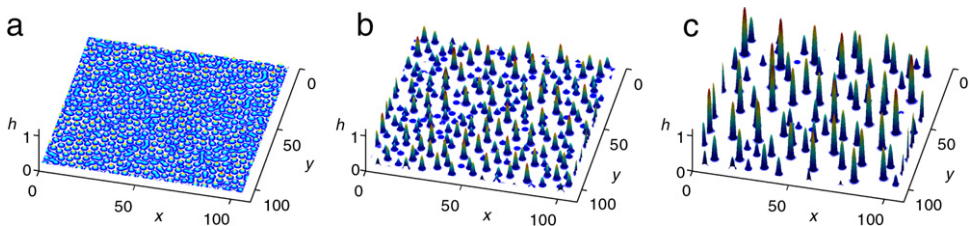


Fig. 88. (Color online) Non-interrupted coarsening resulting from the long time non-linear evolution of the ATG instability regularized with wetting interactions. The initial picture displays the initial exponentially growing stage of the instability, which is followed by the non-linear regime where islands, separated by a wetting layer, grow thanks to surface diffusion on the wetting layer which allows Ostwald ripening.

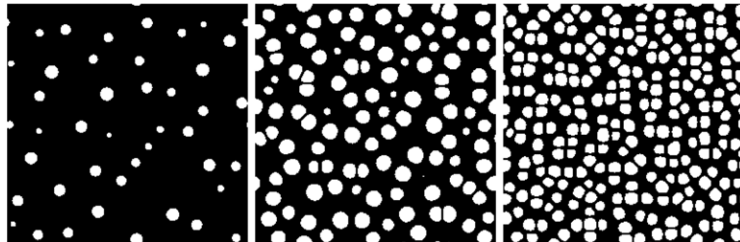


Fig. 89. Different non-linear regimes of the wetting ATG instability for increasing (from left to right) deposition flux.
Source: from [269].

potential also evidenced the formation of such islands [231]. However, ab-initio calculations, see e.g. [49], indicate that the variation of the surface energy with h is rather a continuous and small one. Based on the non-linear analysis of the elastic energy, it was shown that a wetting potential with small variations leads to a regularized dynamics and avoids the formation cusp-like singularities [236]. The film evolution driven by non-linear elasticity and wetting interactions may be written as [236]

$$\frac{\partial h}{\partial t} = \Delta \left\{ - (1 + c_w e^{-h/\delta}) \Delta h - \frac{c_w}{\delta} \frac{e^{-h/\delta}}{\sqrt{1 + |\nabla h|^2}} - \mathcal{H}_{ii}(h) + 2h\Delta h + |\nabla h|^2 + 2\mathcal{H}_{ij} [h \theta_{ijkl} \mathcal{H}_{kl}(h)] + \mathcal{H}_{ij}(h) \theta_{ijkl} \mathcal{H}_{kl}(h) \right\}, \quad (18)$$

with summation over repeated indices being either x or y and with the coefficients $\theta_{ijij} = 1$, $\theta_{iiji} = -\theta_{ijji} = \nu$ when $i \neq j$ and 0 otherwise. Non-linear local terms are present in the second line which are related by functional derivation to each other, similarly to the non-local non-linear terms of the last line. The term $h\Delta h$ which is non invariant by a shift in the height reference should be forbidden by usual symmetry account but is allowed here thanks to its combination with $\mathcal{H}_{ij} [h \theta_{ijkl} \mathcal{H}_{kl}(h)]$. Finally, the first line includes exponentially decreasing wetting interactions. The numerical resolution of this dynamical equation leads at its beginning to growing mounds which go deeper in the film. Once their bases touch the region where wetting is relevant, this growth slows down and a flat wetting potential spreads in between mounds, see Fig. 88. The result of this computation is that the combination of both non-linear non-local and small wetting interactions allows the regularization of the instability long-time dynamics. During annealing, these islands undergo a non-interrupted coarsening, see Fig. 88, similar to the Ostwald ripening where large islands with lower chemical potential grow at the expense of small ones. The dynamics enforces power-laws for the different morphological properties (roughness, coverage, island density ...) [236] but with exponents not related to the usual predictions of the Lifshitz-Slyozov theory [268], see Section 3.7.

The wetting potential present in the dynamical equation (18) breaks the system invariance in the growth direction. As a consequence, the long-time dynamics of the instability is noticeably impacted by a deposition flux since the symmetry breaking enforces an explicit dependence on the film thickness h which grows as $F t$. As a result, different non-linear regimes ruled by the deposition flux F are found which are characterized by different coarsening dynamics and spatial order, see Fig. 89 [269]. For a large enough flux (above 0.1 ML/s for $x = 0.25$), coarsening is frozen and islands mainly grow by collecting new deposited material. The resulting surface morphology exhibits a striking ordering where islands gather in clusters with a small nearest-neighbor distance as a result of the inhibition of coarsening. It is noteworthy to compare this result in the low strain regime with the spatial ordering as a function of the flux obtained in the nucleation regime during gas source MBE at 600 °C [270]. The latter display a similar behavior, see Fig. 90, where spatial correlation appear for large flux. This result was explained by the exclusion of islands, as the statistical properties (correlation function, nearest-neighbor distance, ...) may be reproduced using a model of random non-overlapping islands, see Fig. 91.

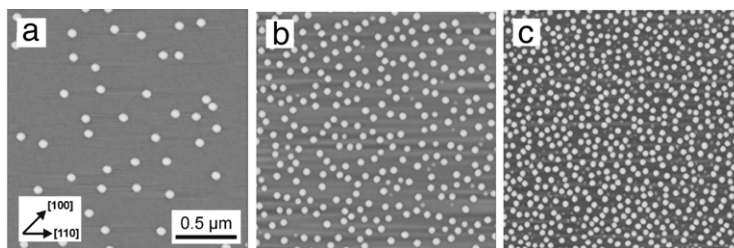


Fig. 90. $2 \times 2 \mu\text{m}^2$ AFM images of Ge/Si(001) layers grown at varying deposition rates R : (a) 1.2 ML min^{-1} with layer thickness $\bar{h} = 5.9 \text{ ML}$ and island area density $\rho = 10.9 \mu\text{m}^{-2}$; (b) 6.6 ML min^{-1} , $\bar{h} = 8.0 \text{ ML}$, $\rho = 68.2 \mu\text{m}^{-2}$; (c) 47.1 ML min^{-1} , $\bar{h} = 8.9 \text{ ML}$, $\rho = 154.4 \mu\text{m}^{-2}$. Dome-shaped islands appear as light disks. Small pyramidal-shaped islands are visible in the background of (b) and (c).

Source: from [270].

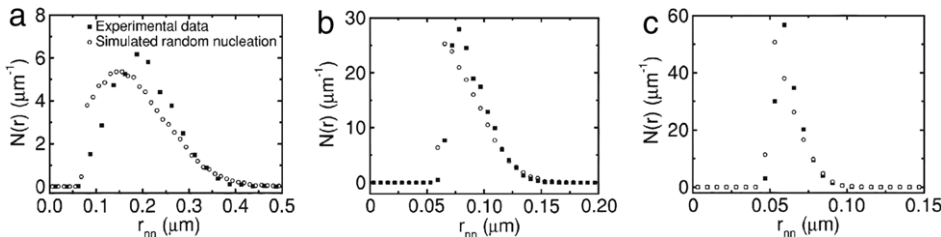


Fig. 91. (a)–(c) Filled symbols are the nearest-neighbor distribution function $N(r)$ plotted as a function of the nearest-neighbor island separation r_{nn} for the Ge/Si(001) layers shown in Fig. 90(a)–(c), respectively. (Note that the scale of the x axis is different in each figure.) Open circles are $N(r)$ for computer simulations of the random placement of circular islands with an exclusion zone given by the measured average diameter of the islands and with an areal density matching the experimental value.

Source: from [270].

3.2. High strain regime

If the ATG instability is a fruitful description for the barrierless evolution in low strained SiGe films, it is hidden in the high strain regime ($x \gtrsim 0.5$) where the films undergo an abrupt 2D–3D transition after a few deposited layers [86–88]. Different atomistic mechanisms should then be accounted for and nucleation can no longer be ignored. As for the ATG instability, the elastic relaxation is the driving force for this evolution [271,81,272,19]. While the first monolayers grow as a 2D wetting layer with an optimal surface reconstruction, the elastic relaxation induced by the morphological evolution is in competition with relaxation by misfit dislocations. The 2D–3D transition may occur as soon as 3 monolayers of Ge on Si are deposited [13,14] once wetting interactions are no longer strong enough to enforce a layer by layer growth. This scenario is typical of the Stranski-Krastanov growth mode [30].

3.2.1. Submonolayer aggregation

The very first stages of deposition may be described using the usual modelization of submonolayer aggregation. It should involve the description of atomic processes such as deposition, diffusion and aggregation and generalizes to surface growth the common understanding of aggregation phenomena [16,273]. The comparison between experiment and theory in this regime can be useful e.g. for measuring atomic diffusion coefficient otherwise hard to measure [274,275]. The basic quantity of interest is the island size distribution, usually characterized by the absence of any characteristic length beside the mean island size. In the irreversible case [244,276] where adatoms stick to clusters, the size distribution [277,278,273] depends only on the mean size (which depends on the coverage) and follows the scaling form

$$N_s = \Theta / \langle s \rangle^2 f(s / \langle s \rangle), \quad (19)$$

where N_s is the density of cluster with s atoms and $\Theta = Ft$ is the areal coverage. The scaling function f can be obtained via kinetic equations as a function of the ratio D/F of the diffusion coefficient over the deposition flux [279–282]. However, common semiconductor surfaces, and especially SiGe ones, are characterized by low binding energies of adatoms to clusters, so that adatoms may detach from clusters with a non-vanishing probability at the working temperature. The scaling function and statistical properties may then depend on a new parameter which is either the binding energy [283] or the critical cluster size beyond which adatoms can no longer detach from clusters [281,284].

In the case of heteroepitaxy, extra long range elastic interactions come into play and introduce a non-trivial dependence on the cluster size. These interactions decrease as $1/r^3$ with the distance r between ad-adatoms [244] and are repulsive in isotropic systems while they can be attractive in some directions in sufficiently anisotropic ones [285]. In the case of repulsive interactions, elasticity both repel adatoms from existing clusters and favor detachment from clusters [286–288,86], which enforces smaller aggregates at equilibrium. The influence of elasticity on the adatom diffusion was considered in [286]

by a multigrid scheme for computing U^{el}/r^3 repulsive elastic interactions with the elastic strength U^{el} . The resulting scaling theory was generalized to these systems by considering an elastic time $\tau^{el} \propto e^{U^{el}/k_B T}$ in addition to the usual diffusion time $\tau^d \propto e^{E_S/k_B T}$. Scaling was suggested to hold when the governing ratio D/F is replaced by

$$\frac{4D}{F} \rightarrow \frac{4D}{F} \frac{1}{1 + e^{(U^{el}-E_S)/k_B T}}. \quad (20)$$

Considering this rule, monomer and island densities for different flux and strain do indeed merge into one graph, see Fig. 92. The irreversible growth in presence of elasticity was investigated by considering the shift due to elasticity in the energy barrier from site i to site j [288]

$$\Delta E_{ij}^{el} = \frac{1}{2}[E_j^{el} - E_i^{el}], \quad (21)$$

where E_i^{el} is the interaction due to strain between an atom at site i and the others, $E_i^{el} = U^{el} \sum_{ij} 1/r_{ij}^3$. Elastic interactions, which repel atoms from clusters, enforce an increase in the island density while the scaled island-size distribution is found to be only weakly affected by strain [288].

The kinetic Monte-Carlo (KMC) method enables to investigate the time evolution of surface growth. This method may be basically based on a solid-on-solid model of a simple cubic lattice structure with neither vacancies nor overhangs. The atomistic processes included in this description are adatom deposition, surface diffusion (desorption is neglected under usual growth conditions) and adatom binding. The diffusion rate of a single adatom is defined as the probability of a diffusion jump per unit time, and is given by the Arrhenius-type expression

$$k(E, T) = k_0 \exp(-E/k_B T) \quad (22)$$

where E is the activation energy of an attempted atomic move. The prefactor k_0 corresponds to the frequency of atomic vibrations which may be estimated as $k_0 = 2k_B T/h$ with the Planck constant h . In the basic model, the activation energy E for the diffusion of a trial atom includes a substrate bonding energy E_S and a nearest-neighbor bonding energy E_N ,

$$E = E_S + nE_N, \quad (23)$$

where n is the number of in-plane nearest neighbors at the initial site. When elastic interactions are present, this barrier reads

$$E = E_S + nE_N + E^{el}, \quad (24)$$

where the elastic energy E^{el} is the contribution from elastic interactions to the diffusion energy barrier. The latter may be estimated as the elastic energy difference between the configuration without the trial atom and the configuration with this atom [289]. In this basic model of diffusion, if a diffusion event is not rejected, the trial atom land with equal probability to any of its four neighboring columns. The elastic energy may be estimated using a Green function calculation

$$\mu^{el}(\mathbf{r}) = \sum_{\mathbf{r}'} h(\mathbf{r}') G(\mathbf{r} - \mathbf{r}'), \quad (25)$$

where G is the elastic Green function conveniently given in Fourier space by [290]

$$G(\mathbf{r}) = \frac{2\pi}{N^3} \sum_{\mathbf{k}_1, \mathbf{k}_2=-N/2+1}^{N/2} |\mathbf{k}| \cos(2\pi \mathbf{k} \cdot \mathbf{r}/N), \quad (26)$$

for a lattice of size N . The $|\mathbf{k}|$ non-analytic factor keeps track of the long range of elastic interactions. In the case of reversible aggregation with a typical binding energy $E_N = 0.3$ eV, kinetic Monte-Carlo simulations of a SOS model with such a Green calculation showed that the growth kinetics leads to larger clusters in presence of repulsive elastic interactions [290]. This effect results from the paradoxical enhancement by elasticity of adatom detachment from clusters which allows atoms to explore a larger phase-space. Indeed, elasticity is significant in the barrier (24) mainly near the island edge where it favors atom detachment from clusters; it is nevertheless still smaller than the binding energies so that sites with minimum energy correspond to a high coordination number. As a consequence, elasticity which allow atom detachment from clusters, favors atom to minimize the system binding energy forming large and compact clusters. This kinetic effect may also be rationalized in a mean-field description [290] and was also found in a spring model [291]. Moreover, as shown in Fig. 93, the resulting scaling function describing the cluster size distribution is not affected by elasticity [290]. This conclusion was also found in a model with only $1/r^3$ interactions between island atoms [287] and in a KMC study with effective elastic interactions [283]. On the contrary, it was shown in Ref. [292] that strain may lead to a narrowing of the island size distribution in the submonolayer regime. In this study, a level set technique is used with a numerical time step larger than microscopic time scales, which allow to avoid computing the full elastic problem at every microscopic event. The narrowing of the island size distribution was shown to arise from the increase in the detachment rate of atoms from islands when the strain increases, making small islands less stable. The difference with the previous study arises from the amplitude of the elastic energy used.

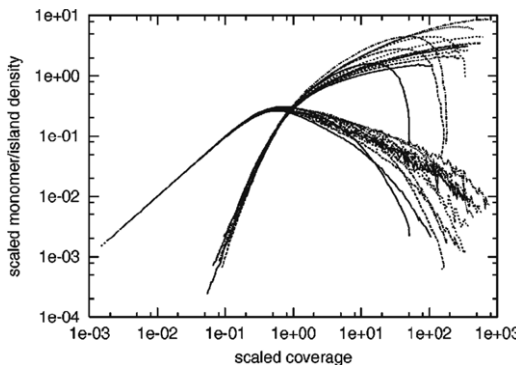


Fig. 92. Scaled monomer $\tilde{\rho}_1$ and island densities $\tilde{\rho}$ vs scaled coverage $\tilde{\theta}$. All scaled curves are on one graph.
Source: from [286].

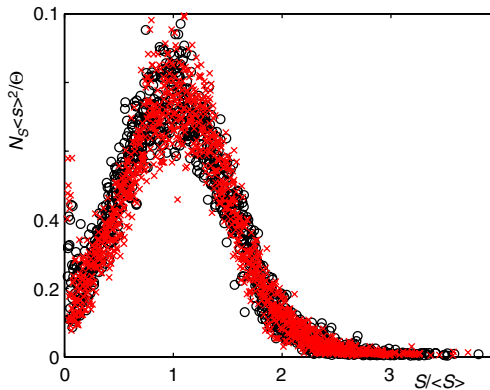


Fig. 93. Cluster size distribution of submonolayer growth with ($x = 1$, red/gray crosses) and without (black circles) elastic interactions.
Source: from [290].

3.2.2. 2D–3D transition

The 2D–3D transition observed for large strain requires account of microscopic processes. A first description was done considering a calculation of a Frenkel–Kontorova chain [293] but it was also suggested that 3D islands could result from energetically favored 2D platelet precursors [85]. Simple energetic considerations may give some insights into its origin. Considering directly 3D islands, the formation energy which is the difference between the island energy and the energy of the same amount of matter in a flat geometry, includes at least elastic and surface contributions,

$$\Delta E = \Delta E^s + \Delta E^{el} \propto \gamma V^{2/3} - \alpha^{el} V, \quad (27)$$

with a constant α^{el} . As a first approximation, elastic relaxation should give a contribution proportional to the volume $\Delta E^{el} \sim -Ym^2V$, with the Young modulus Y . On the other hand, the cost in surface energy is proportional to the surface $\Delta E^s \sim \gamma V^{2/3}$ with a coefficient of order unity depending on the cluster shape. As a whole ΔE displays a typical nucleation barrier, see Fig. 94 which has to be overcome before the island can grow and which explains the first order, rapid transition that is observed experimentally. Only once fluctuations have led to clusters larger than the critical size, do the 3D structures grow. A more realistic description, appropriate to describe Stranski–Krastanov growth mode was provided in [87] by accounting also for wetting interactions

$$\Delta E = \Delta E^s + \Delta E^{el} + \Delta E^w(z), \quad (28)$$

where the wetting energy depends on the number of deposited layers. The energy barrier for the 2D–3D transition may be overcome only after some deposited thickness. Additional effects may also be incorporated in this simple description: step interaction [81], surface stress, elastic anisotropy, elastic corrections, edge energy etc. [81,138]. One may also consider the dependence of the surface energy with strain as done in [294] by writing

$$\Delta E^s = \int_{(001)} [\gamma_{001}(\epsilon_{ij}) - \gamma_{001}(\epsilon_0)] d^2S + \int_{(105)} [\gamma_{105}(\epsilon_{ij}) - \gamma_{105}(\epsilon_0) \cos \alpha] d^2S, \quad (29)$$

where the surface energy explicitly depends on the local strain ϵ_{ij} while ϵ_0 is the mean strain. For an island size in the range of 10 nm, the magnitude of this surface-energy correction is found to give rise to a significant reduction in the surface energy

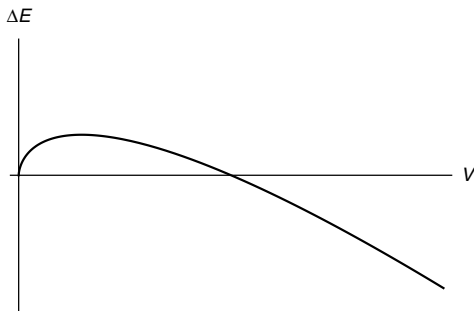


Fig. 94. Typical variation of the energy difference between a cluster of volume V and a flat configuration.

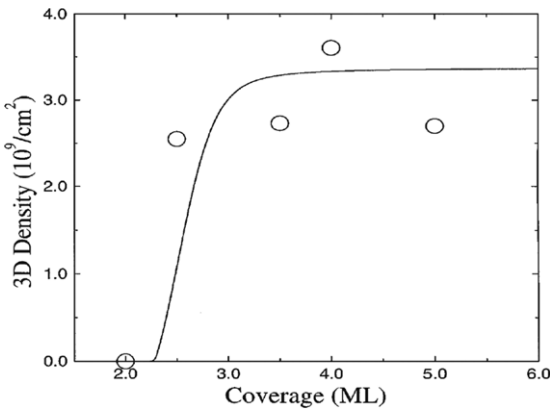


Fig. 95. Measured (symbols) and calculated (solid line) 3D island density versus coverage at a growth temperature of 853 K and a growth rate of 0.5 ML/s. Source: from [296].

and to be comparable to the elastic relaxation energy. It is then necessary to determine the total energetics of Ge under compressive strain to improve the understanding of the stability of hut clusters. More recently, a density functional theory of 2D and 3D clusters with up to 20 000 atoms showed that a 2D–3D cross-over between fully relaxed structures may occur after completion of 3 monolayers as a result of the system energetics alone [295].

To go beyond energetic considerations, the dynamics of this sudden transition has to be assessed for example on the basis of rate equations which already account well for the submonolayer regime [244]. This was done with self-consistent rate equations with three species: adatoms, 2D clusters and 3D ones [296]. Rate equations provide a mean-field description of the growth kinetics. Considering three species, adatoms, 2D islands and 3D islands with density respectively n_1 , n_2 and n_3 , these equations reads [296]

$$\dot{n}_1 = F + \frac{n}{\tau} - D[(i^* + 1)\sigma_{i^*} n_{i^*} + \sigma_2 n_2 + \sigma_3 n_3], \quad (30a)$$

$$\dot{n}_2 = D\sigma_{i^*} n_{i^*} n_1 - \delta n_2, \quad (30b)$$

$$\dot{n}_3 = \delta n_2. \quad (30c)$$

The critical nuclei below which a 2D island is unstable and breaks up into adatoms, contains i^* atoms and have a density n_{i^*} . The capture number of species α , $D\sigma_\alpha$, may be computed using a self-consistent scheme. Finally, the escape rate from 2D islands $1/\tau$ together with the rate δ at which 2D islands transform into 3D islands depend crucially on strain. The resulting evolution of the density of 3D islands during growth is plotted in Fig. 95 [296]. It clearly exhibits the rapid and sudden onset of the 2D–3D transition. In this model, elasticity enhances adatom detachment from clusters and enforces the presence and creation rate of 3D clusters. As a result, the 3D island density as a function of the coverage displays a steep increase after a critical deposited height which is indeed in agreement with the 2D–3D transition. After this increase, the 3D density saturates, once 3D islands have formed and serve as sinks for adatoms prohibiting further 2D nucleation. The island size (or more precisely volume) distribution of these QDs is supposed to follow a scaling similar to the one found in 2D islands as checked first in InGaAs systems, see Fig. 96 [297]. A similar self-consistent mean-field rate theory augmented by elastic interactions between islands was derived to explain the experimental decrease in the island size after the 2D–3D transition [298]. The scaled form of the island size distribution as a function of the island volume was also checked in [299] for Ge islands on Si (100). It was correlated to the island Voronoi surface distribution, which, compared to the generalized Wigner distribution of the capture zone size distribution, lead to a critical nucleus (above which islands are

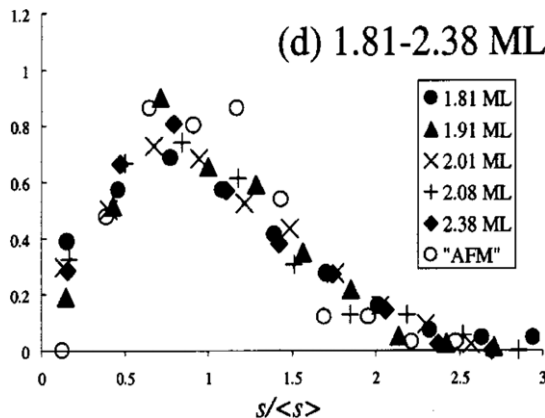


Fig. 96. Scaled quantum dot volume distribution for different InAs coverages.
Source: from [297].

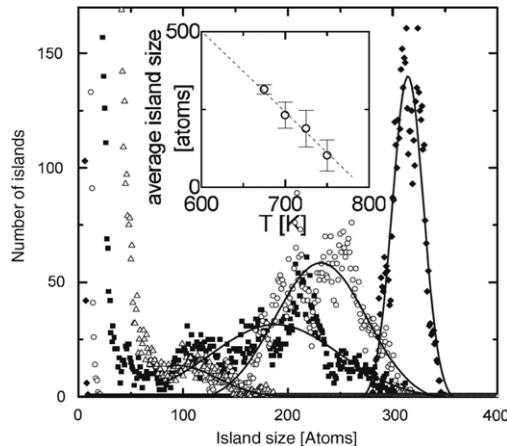


Fig. 97. Equilibrium size distributions for temperatures $T = 675$ K (diamonds), $T = 700$ K (open circles), $T = 725$ K (squares), and $T = 750$ K (open triangles). The solid lines are numerical fits to the kinetic MC data. The inset shows the dependence of average island size on temperature. The prediction from thermodynamic equilibrium theory (dotted line) and the results from kinetic MC (open circles) are plotted.
Source: from [304].

stable) $i \sim 4$ [299]; This value, quite small compared to the experimental observations of critical nuclei of order of a few hundreds of atoms, is in fact only associated to the statistical properties within the capture zone model.

The 2D–3D transition was widely investigated using KMC simulations which allow to account for atomic processes and growth kinetics. It was first examined considering the basic energy barrier (24) and elastic energy barriers derived from a Frenkel-Kontorova model [300,301] or on barriers modified by elasticity at the island edge [86,302]. The former study showed that the transition occurs when the misfit is larger than some critical value, which was also found in [303]. Kinetic MC simulations were also derived using a Green function calculation of the elastic energy between island edges, in order to study the competition between kinetics and equilibrium [304]. It reveals that the size distribution after deposition is ruled by kinetics, with smaller islands at low temperature, while for long time, a cross-over to the equilibrium size-distribution is found, see Fig. 97, see also [305,306]. Different evolutions were also found depending on the growth temperature [307]. While closely packed islands occur at high temperature, pits which subsequently grow into grooves, form at low temperature via a multi-step layer-by-layer nucleation. Island formation from KMC simulations was also investigated in [308] using a spring model and an accelerated algorithm. Growth at low deposition rates was found to follow a layer-by-layer nucleation pathway characterized by a continuous lateral expansion interrupted by a sequence of independent two-dimensional 2D upper-layer nucleation events, see Fig. 98 [308]. Finally, note that if the high and low strain regime are well evidenced experimentally, few studies have tackle the cross-over between the two. This was done in [289] considering KMC simulations based on a coarse-grained version of a Green function calculation in 1 + 1D. At low misfit and high T , ripples form on the surface, which subsequently evolve into islands and which are reminiscent of the ATG instability. Conversely, at high misfit and low temperature, pits or islands nucleate in the system, see Figs. 99 and 100 [289].

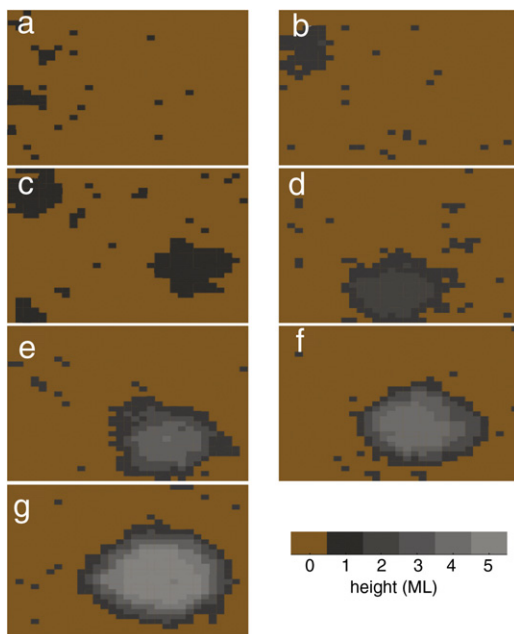


Fig. 98. (Color online) Snapshots from simulation of deposition at rate 1 ML/s, temperature 600 K, and coverage $\theta = 0.04$ (a), 0.07 (b), 0.12 (c), 0.25 (d), 0.36 (e), 0.50 (f), and 0.94 (g).

Source: from [308].

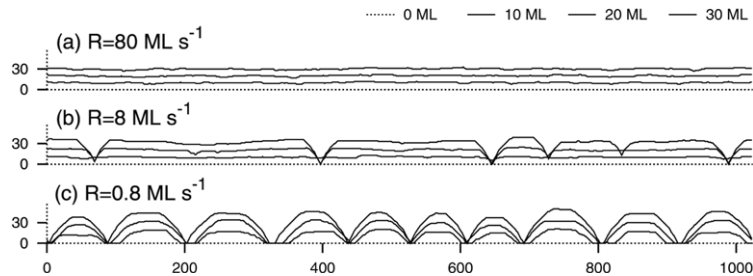


Fig. 99. Simulations of deposition of Ge films at $T = 600$ K.
Source: from [289].

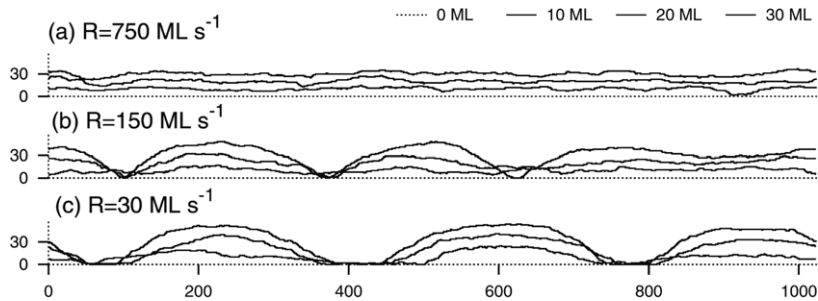


Fig. 100. Simulations of deposition of $\text{Si}_{0.5}\text{Ge}_{0.5}$ films at $T = 1000$ K.
Source: from [289].

3.3. Hut pyramids

3.3.1. Stabilization of the (105) facet

In order to give some insights into the microscopic origin of the strain-induced (105) facets, we first turn to first principles calculations. STM studies and first-principle calculations pointed out that the electronic effect strongly affects STM imaging on this surface [93]. Basic entities on the (105) surface are dimer structures arranged on narrow terraces with a width of a

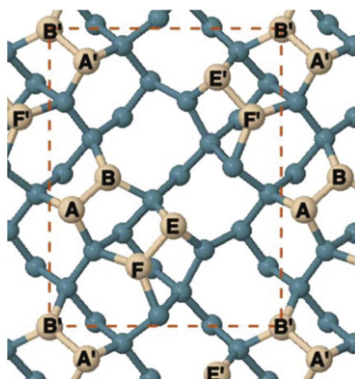


Fig. 101. Structure of the PD model of Ge(105) surface. Indices of the atoms of the dimers are shown on the figure.
Source: from [309].

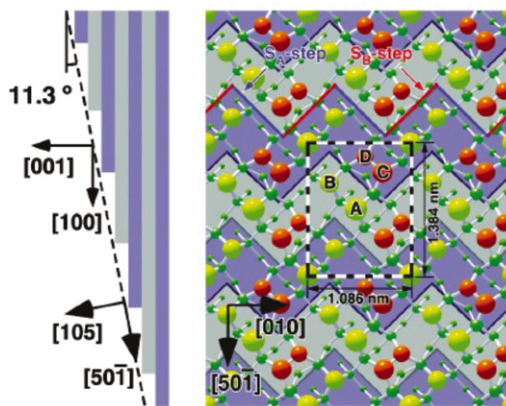


Fig. 102. Rebonded step (RS) model of the Ge(105) (1×2) surface from first-principles calculation including an effect of the lattice mismatch with the substrate. The unit cell is indicated by a rectangle. The size of a ball reflects the vertical height of the atom.
Source: from [94].

few nanometers corresponding to the tilt of 11.3° from a (001) plane. Initially, the pair dimer (PD) model of the structure was proposed, as shown in Fig. 101 [309]. In this model, the paired dimers are separated by S_A and S_B steps. In S_A steps, dimer rows are parallel to the step, whereas in S_B , they are perpendicular and unbonded. The dangling bonds present in this model are energetically unfavorable.

For this reason a model called rebonded step (RS) model was proposed based on STM studies, as shown in Fig. 102 [92]. In this model, the normal dimer is located in the upper terrace of the S_B step (colored orange with C and D atoms in Fig. 102). Atoms in the lower terrace are rebonded with the step-edge atoms in order to reduce the number of dangling bonds per unit cell. Four types of dangling bonds were identified on the surface structure in [310]. Such RS model was also supported by AFM investigations by taking highly resolved AFM images and atomically resolved electrostatic potential images with a Kelvin Force Microscope method [94], see Fig. 102. New refinements of the RS model were reported recently using a combination of tight-binding and pseudo-potential and plane-wave DFT calculations, see Fig. 101 [309]. In particular, the effect of buckling of surface dimers on the stability and structure of the reconstructed Ge (105) surface was investigated. Two structures called zigzag and flat structures with a small energy difference (about 51 meV/dimer) were found to be the most stable ones. Under compressive strain, the zigzag structure is expected to favor the formation of irregular sites such as surface edges owing to the locality of its buckling [309].

The stability of (105) facets may also be described by considering the surface energy of a stepped surface misoriented with a small angle θ with respect to the (001) surface which may be decomposed as the sum of the step formation and the dipolar interaction energies [95].

$$\gamma(\theta, \epsilon) = \gamma_0(\theta) \cos \theta + (\beta_1 + \tilde{\beta}_1 \epsilon_{\parallel}) |\sin \theta| + \beta_3 |\sin \theta| / \cos^2 \theta \quad (31)$$

where ϵ_{\parallel} is the biaxial strain, γ_0 , the surface energy of (001), β_1 , the step formation energy, $\tilde{\beta}_1$, the sensitivity of the step formation to strain and β_3 is the strength of the step-step dipolar interaction. In this framework, it was shown by atomistic simulations using the Tersoff potential [311] that monopole interactions between steps can stabilize the (105) orientation.

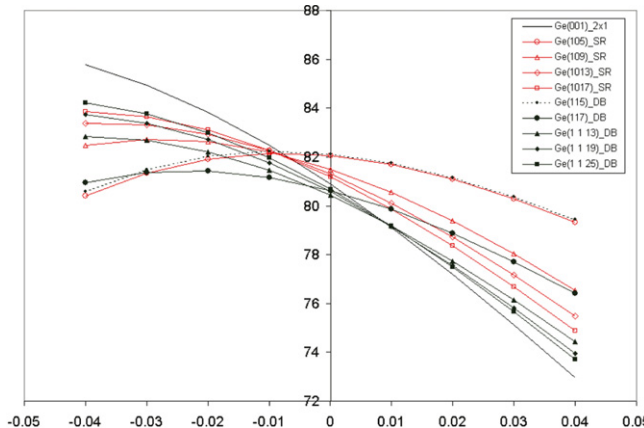


Fig. 103. (Color online) Surface energy of stepped surfaces in meV/Å² consisting of [100] SR (red) and [110] D_B (black) steps as a function of the biaxial strain for Ge.

Source: from [312].

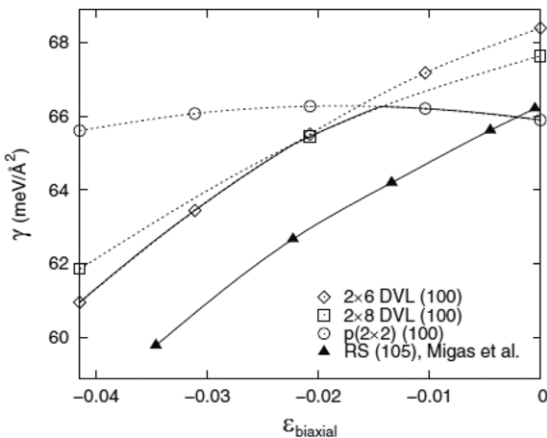


Fig. 104. Ge (001) and (105) surface energies (per unit area of deformed surface) versus biaxial strain. Triangles denote (105) results from [95]. Circles, squares, and diamonds are (001) results obtained for p(2 × 2) and 2 × 6 and 2 × 8 DVL reconstructions, respectively. Solid lines highlight the surface energy for the stable reconstruction of a given orientation.

Source: from [294].

The strain dependent step formation energies for various step structures are shown in Fig. 103, for Si and Ge [312] and were supported by a calculation based on the Stillinger–Weber potential [311].

More precise values of the Ge (001) and (105) surface energies were plotted as a function of biaxial strain using first-principles calculations, see Fig. 104 [294,313]. One can note that while the stress-free values of (001) and (105) surface energies are nearly equal, the (105) reconstruction quickly becomes energetically favored when the compressive strain increases. While the (105) surface energy decreases monotonically with the in-plane strain, the (001) orientation displays a more complex dependence on strain. In both cases, strain gives rise to a significant reduction in the surface energy and thus to the surface contribution to the island formation energy.

3.3.2. Hut growth dynamics

The initial mainly isotropic prepyramids appear as unfaceted mounds which grow by increasing their aspect ratio in order to favor an efficient elastic relaxation until their slope reaches the (105) orientation when prepyramids start to transform into faceted pyramids. A mean-field phase diagram was computed in [34] considering a generic chemical potential accounting for surface, edge and elastic energy, together with a small anisotropy of the surface energy $\gamma(\theta)$

$$\mu = \mu^{el} + \tilde{\gamma}(\theta)\kappa + \beta C(\kappa), \quad (32)$$

with the stiffness $\tilde{\gamma}$ and a curvature-dependent corner energy $C(\kappa)$. This analysis leads to the conclusion that the prepyramid-to-pyramid transition corresponds to a first order transition occurring when the island size reaches a critical value, which is possible for large enough deposited heights, see Fig. 105 [34].

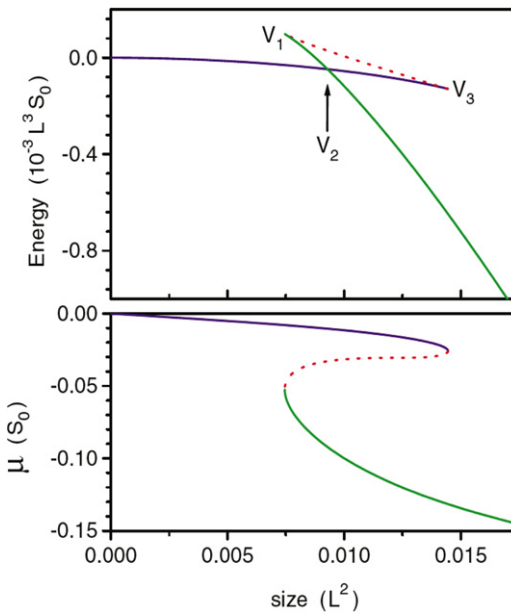


Fig. 105. (Color online) Island energy E and chemical potential (per volume) μ , relative to a planar film, vs volume V . The dotted line represents unstable solutions connecting smooth and faceted branches.

Source: from [34].

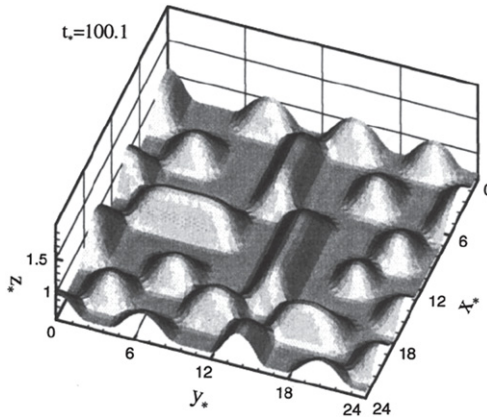


Fig. 106. Steady state of the evolution of a strained anisotropic film with two shallow minima corresponding to (001) and (105) orientations according to [246].

To describe the growth dynamics of hut pyramids in the low strain regime, one must include the crystalline anisotropy in the instability evolution [246,314,315] which may be done by considering an ad-hoc variation of $\gamma(\mathbf{n})$ based on experimental observations. First, the (001) orientation is expected to be a stable but not a facet orientation with a shallow minimum thanks to which the nucleationless development of the elastic instability [33] can be rationalized [246,34]. The (105) facet is particular to strained SiGe systems as it is not an equilibrium orientation but is stabilized by the surface reconstruction under stress [92–96], see Section 3.3.1. In addition, it is expected that the (105) orientation have a stiffer minimum as well-defined (105) facets develop as opposed to the roughness of the (001) orientation [34].

Considering an ad-hoc anisotropy for these two orientations, the dynamics of the morphological instability was analyzed by different means. Despite intrinsic limitations, finite element methods were implemented on these systems [316,246,314, 256,315,248]. Considering a model with a large mismatch and dominant wetting interactions, it was shown that when the (105) surface energy $\gamma_{(105)}$ is 0.9% lower than $\gamma_{(001)}$, square base pyramids indeed arise after some time. Different surface configurations were found depending on the maximum surface coverage. When the latter increases, the film morphology increases gradually from a sparse array of huts to a faceted ripple structure [315,248]. On the other hand, a small anisotropy characterized by a tiny variation of the surface energy, with a barrier between (001) and (105) as small as 10^{-4} in relative amplitude, also leads to the appearance of hut pyramids [246]. Little variations in the anisotropy of $\gamma(\mathbf{n})$ can lead either to ripening or non-ripening islands which may be strongly or weakly self-organized, see Fig. 106 [246]. Using a cylindrical

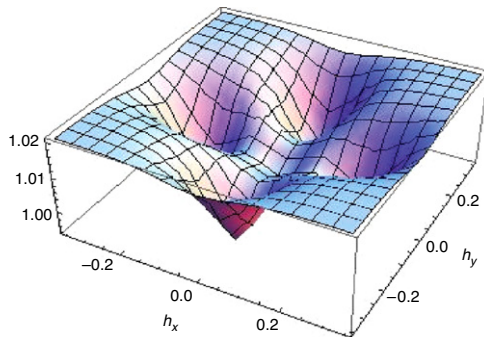


Fig. 107. Typical dependence of the surface energy of a strained SiGe film as a function of the local slopes h_x and h_y .
Source: from [230].

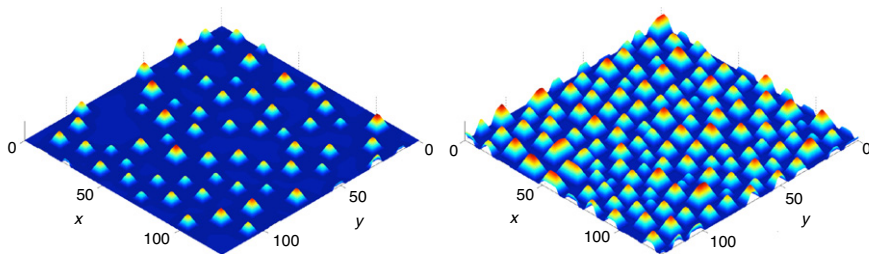


Fig. 108. Simulation of the ATG instability with a SiGe dedicated anisotropy. If only square base pyramids are visible for low film thickness (left), a coexistence of both square base and rectangular base pyramids occurs for larger deposited height (right). The movie of the time evolution is available on-line [317].
Source: from [230].

anisotropy, a Green function elastic calculation at linear order and the hypothesis of an unstable (001) surface with a negative step formation energy due to stress, it was found in [247] that arrays of well-separated islands, or alternatively, intersecting ridges may arise depending on the growth kinetics. It is also possible to include crystalline anisotropy in the non-linear analysis of Eq. (18) by accounting for a n -dependent surface energy [230]. A typical gamma-plot in accordance with experimental observations is displayed in Fig. 107. With such an anisotropy, one finds that the film evolution describes the different steps of the morphological evolution in the low strain regime. After the initial instability and the subsequent prepyramid regime, square-base pyramids arise when the island side angle reach the (105) orientation. These huts grow at the expense of smaller rather isotropic ones (a movie of this evolution may be found in [317]). They may arise from the initial mounds and not from elongated ridges as initially thought with such an anisotropy [247]. Depending on the deposited height, a coexistence of both square and rectangular base pyramids is found (Fig. 109), the latter being favored for a large film thickness, see Fig. 108. Beside its natural impact on the growth shapes, the striking effect of crystalline anisotropy is its influence on the long time dynamics: contrarily to isotropic systems, coarsening may be interrupted in thin films, see Section 3.7.

3.4. Coexistence of pyramids and domes

For thick enough films, the evolution from prepyramids to pyramids is followed by the appearance of new island shapes such as domes. This shape transition was suggested to occur when, at a critical pyramid size, new steeper facets are able to nucleate close to the pyramid apex where relaxation is maximum [97,135,136] following the modelization of [137]. An energetic analysis describing the energetic barrier for nucleation on the islands investigated the microscopic origin of this shape transition [136]. The difference of energy between a configuration with a full {105} layer and another one with the same amount of material in N partially filled layers at the top of the pyramid, see Fig. 110 is merely

$$E_{flat} - E_N = \alpha L^2 (1 - 1/\sqrt{N}) - L \gamma_{(105)} \sqrt{N}, \quad (33)$$

where L is the island width, $\gamma_{(105)}$, the {105} step energy and α , a constant. The first term related to the surface energy favors a flat configuration contrarily to the second one. The resulting energetic diagram is plotted in Fig. 110(b). For small enough pyramids, growth is energetically favored with addition of full {105} facets. However, beyond some island size, the configuration which is preferred consists in N partially filled layers at the top of the pyramid where elastic relaxation is maximum [137], see Fig. 110(a). This configuration opens the path to step bunching which ultimately induces the pyramid to dome transition. A shape transition leading to bimodal distribution can be derived by considering an anisotropy

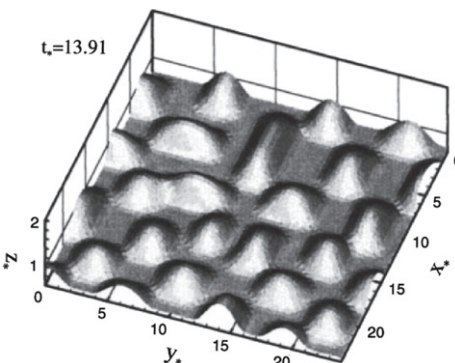


Fig. 109. Evolution of islands for an anisotropy describing (105) and (103) minima beside the (001) orientation. The islands with squared bases are formed first, thereafter develop into a bimodal distribution of islands.

Source: from [246].

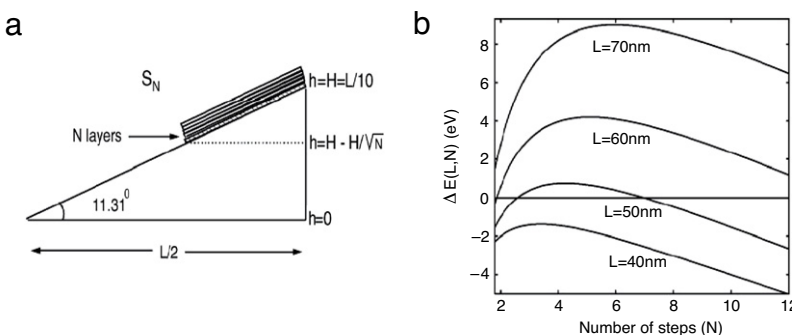


Fig. 110. (a) Geometry of a configuration characterized by N steps bunched together. (b) Energy difference between the flat-facet state and the stepped state plotted as a function of the pyramid base L and of the number of steps N .

Source: from [136].

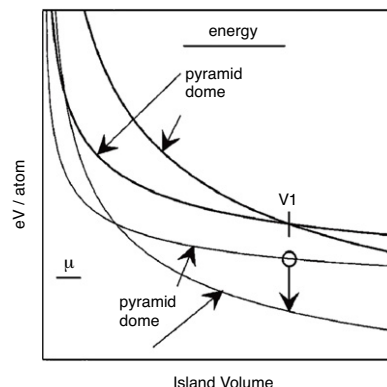


Fig. 111. Energy per atom and chemical potential μ of islands with two types of facets with values of α in the ratio 1:2. The shape transition occurs at volume V_1 , where the energy curves cross, at which point there is a discontinuity in μ .

Source: from [140].

with two minima in the long-time evolution of the morphological instability (Fig. 109) [246] or with a multi-phase field modeling [318].

It was argued that the shape transition corresponds to a first order transition with the island size where steep facets are introduced discontinuously at the island edge [32,141,150,74]. In [141], based on an energetic description of fully faceted islands with an elastic energy computed in the small-slope approximation, a shape transition was predicted to be first-order with a discontinuous change in chemical potential. The experimental island size distributions reveals two peaks associated with pyramids and domes which may result either from a first order transition between two equilibrium states [32,139,319] or from an anomalous coarsening [320]. In Refs. [32,139], the pyramid and dome size distributions in the high strain regime

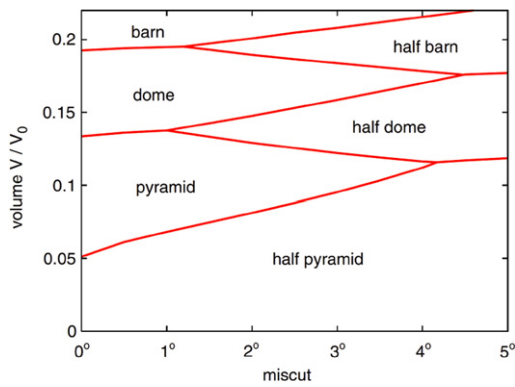


Fig. 112. (Color online) “Phase diagram” showing which shape is stable as a function of island volume in units of V_0 and miscut.
Source: from [322].

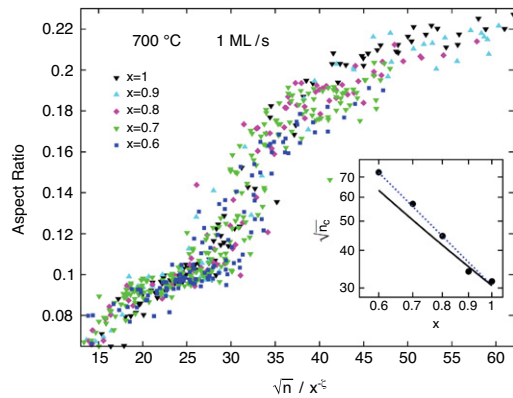


Fig. 113. (Color online) (a) Plot of island aspect ratio r vs root of island size n for various T and R from 2D simulations of deposition. (b) Plot of r vs n_c and x .
with $\zeta = 1.69$ for various x from similar simulations. Inset: log–log plot of n_c vs x where n_c is the transition island size. The dotted line shows a linear fit to the data giving $\zeta = 1.69$. The solid line represents a theoretical result.
Source: from [323].

($x = 1$) were found to be stable after the first stages of coarsening where small pyramids disappeared. A model describing the energetics of islands with strain, surface and edge energy allows to describe a nanostructure diagram indicating the relative numbers of pyramids and domes [319]. It was also shown in [133,321,320] that islands below the size of the pyramid-to-dome transition shrink in the same but reversed sequence of growth states (pyramids, truncated pyramids, prepyramids). In fact, different observations of coarsening in the low strain regime ($x = 0.25\text{--}0.3$) [132] exhibited a rather smooth increase in the island size. This behavior was explained by an anomalous coarsening model where the kinetics is altered by an abrupt drop in chemical potential, see Fig. 111 [140].

Note that a recent study investigated the equilibrium shape as a function of vicinality [322]. It was found using a fully faceted, two-dimensional model, that the equilibrium shapes which are favored for a given volume, depend on the miscut angle of the underlying vicinal substrate. The resulting phase diagram, see Fig. 112, which involves both the island volume and miscut angle gives predictions consistent with experiments. Finally, the pyramid-to-dome transition in $\text{Si}_{1-x}\text{Ge}_x$ on $\text{Si}(001)$ was also investigated atomistically using a multi-state lattice model in two-dimension with a mean-field analysis [323,324]. It shows that the shape transition occurs for an island size n_c independent of the temperature and deposition flux, which follows the scaling relation $\sqrt{n_c} = x^\zeta$, with $\zeta \sim 1.7$ in simulations while $\zeta = 2$ based on a mean-field energetic analysis, see Fig. 113 [323].

3.5. Composition evolution

In this section, we review the theoretical aspects of alloying in quantum dots under strain. The deposition of alloys in heteroepitaxy involves many complex mechanisms such as the compositional elastic stress, the difference of surface diffusion coefficient for different atomic species, surface segregation, mixing entropy, intermixing at the surface, bulk diffusion but also faceting, see e.g. [325]. The interplay between these different phenomena leads to a wide range of experimental and theoretical observations. Some of these observations were already rationalized by the seminal work of Cahn [326] in the context of metallurgy, who noted that elastic forces tend to act against phase separation in the bulk, see

e.g. [327]. However, different mechanisms also come into play at the nanometer length scale. This study can be tackled using different approaches such as continuum equations, finite-element analysis, atomistic simulations (KMC or MD) depending on the case of interest. We first review the linear analysis of the basic continuum description which may well describe quantum dots with low aspect ratio such as pre-pyramids. We then describe more recent results obtained using the finite-element method on various geometries (pyramids, domes, barns, ...).

3.5.1. Continuum model

In the continuum framework, the basic continuity equations for an alloy describe both mass conservation and mechanical equilibrium in presence of two species [67,328–334,239]. These equations describe the coupled evolution of the elastic displacement $\mathbf{u}(x, y, z, t)$ at mechanical equilibrium to the composition field $c(x, y, z)$ of say e.g. Ge, which is supposed to be frozen in the bulk once growth has proceeded. The latter hypothesis describe the negligible importance of bulk diffusion compared to interdiffusion near the surface. First, the Lamé equations in presence of composition inhomogeneities which produce a composition stress read [333]

$$(1 - 2\nu)\nabla^2\mathbf{u} + \nabla \cdot \nabla\mathbf{u} = 2(1 + \nu)\eta\nabla c, \quad (34)$$

with the Poisson ratio ν , the solute expansion coefficient $\eta = (a_{Ge} - a_{Si})/a_{Si}$, with a_{Si} and a_{Ge} , the Si and Ge lattice parameters. If the left hand side is the usual divergence of the stress tensor, the source term on the right hand side, called compositional stress, arises from the change in the local lattice parameter due to local inhomogeneities. Besides mechanical equilibrium, the continuum model must describe mass conservation upon surface diffusion. Then, mass conservation in presence of surface diffusion enforce the global continuity equation

$$v_n = \Omega(Fn_z - \nabla_s \cdot \mathbf{J}), \quad (35)$$

where v_n is the normal component of the surface velocity, n_z , the vertical component of the outward unit vector \mathbf{n} while ∇_s is the surface gradient operator. In (35), Ω is the atomic volume, F , the total deposition flux and $\mathbf{J} = \mathbf{J}_{Si} + \mathbf{J}_{Ge}$ is the total surface diffusion current of adatoms. As a minimal model, one may assume that the surface currents are proportional for each species to the gradient of their chemical potential,

$$\mathbf{J}_{Si} = -(1 - c)M_{Si}\nabla\mu_{Si} \quad \text{and} \quad \mathbf{J}_{Ge} = -cM_{Ge}\nabla\mu_{Ge}, \quad (36)$$

where M_{Si} and M_{Ge} are the Si and Ge surface mobilities. Moreover, in order to describe the alloy dynamics, one needs another mass conservation equation, e.g. describing conservation of Ge alone during surface diffusion. It reads

$$\delta \frac{\partial c}{\partial t} + cv_n = \Omega(F_{Ge} - \nabla_s \cdot \mathbf{J}_{Ge}) \quad \text{at the surface } z = h(x, y, t), \quad (37)$$

where F_{Ge} is the deposition flux of Ge. Here δ is the thickness of the surface layer where intermixing occurs, which is supposed to be a mesoscopic length. Eq. (37) concerns precisely the surface layer and the concentration field c to be considered there is, in a Lagrangian description, the surface concentration. Finally these equations must be supplemented by a mass conservation equation in the bulk, which reads merely $\frac{\partial c}{\partial t} = 0$ in the bulk in absence of volume diffusion.

This set of dynamical equations must be completed by the values of the chemical potentials for each species. One must carefully account for the compositional stress in the thermodynamic definition of this potential, see e.g. [333], and one finds for the Si and Ge chemical potentials μ ,

$$\mu_{Si} = \mu_{Si}^0 + \Omega \left[\frac{1}{2}\sigma_{ij}\epsilon_{ij} + \gamma\kappa + \eta c\sigma_{kk} \right], \quad (38)$$

$$\mu_{Ge} = \mu_{Ge}^0 + \Omega \left[\frac{1}{2}\sigma_{ij}\epsilon_{ij} + \gamma\kappa - \eta(1 - c)\sigma_{kk} \right], \quad (39)$$

where $\frac{1}{2}\sigma_{ij}\epsilon_{ij}$ stands for the elastic energy in an atomic volume, $\gamma\kappa\Omega$ is the usual surface energy cost of a modulation, and the last terms account for the compositional stress. Here, μ_{Si}^0 and μ_{Ge}^0 are the chemical potentials under zero stress and zero external pressure, which may be reasonably approximated by their ideal gas expressions

$$\mu_{Si}^0 = k_B T \log(1 - c) \quad \text{and} \quad \mu_{Ge}^0 = k_B T \log(c), \quad (40)$$

since SiGe is a solid solution for the temperatures relevant for growth experiments.

3.5.2. Instability and pre-pyramids

Even though the continuum model is rather complex, one can check first that an homogeneous film with a flat interface growing at a constant velocity is a trivial solution of the above equations in the presence of a biaxial strain. One can then perform a perturbation analysis with a linear expansion in $h - \langle h \rangle$ and $c - \langle c \rangle$ [333]. As a result, one finds an instability which most unstable wavelength is proportional to $1/x$ and not $1/x^2$ when the difference of mobility between Si and Ge

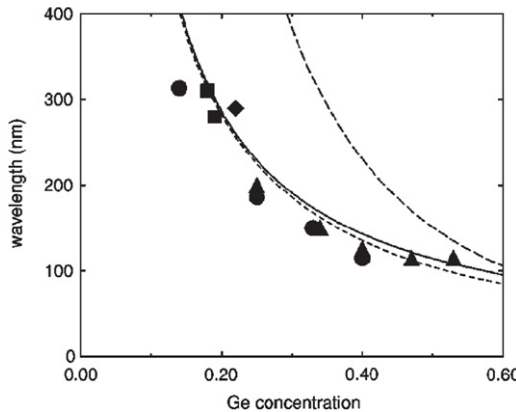


Fig. 114. Wavelength of the instability for SiGe films on Si as a function of the germanium composition. The solid curve corresponds to the most unstable wavelength for immobile Si atoms at small deposition rates. The dotted curve (close to the solid curve) corresponds to the corresponding predictions with $v = 0.3$ and $\beta = 0$ which are defined in [333]. The dashed curve corresponds to $v = 0.3$ and $\beta = 1$. Data point are from Refs. [33] (circles), [58] (triangles), [53] (squares) and [337] (diamonds).

Source: from [333].

is accounted for in the limit of nearly immobile Si atoms [333]. A cross-over from a x^2 to a x dependence of the maximum wave vector of the instability was also rationalized in a non-linear phase field crystal model [335].

This behavior was supported by some experiments [33,58], see Fig. 114, even though the range of x which can be experimentally investigated is rather limited as experiments are difficult and time consuming near the instability threshold at low x . The linear analysis of the strain/composition coupling in asymmetric alloys was performed in [336] which generalizes the work for symmetric films where $x = \frac{1}{2}$ [239]. It tackled the coupling between the alloy-segregation instability and the elastic morphological instability and was applied to the stability of both III-V and group IV films.

Furthermore, this model allows to investigate analytically the composition map of small pre-pyramids (in the small slope approximation) [338]. The predicted composition profile are characterized by a noticeable segregation of the larger misfit component to the island peak, see Fig. 117 which is enhanced by the misfit strain. As shown in Fig. 117, germanium is concentrated at the island apex and exhibits large scale variations especially at the island foot where strain is larger. This model may also be used to study the origin of the apparent critical thickness for island growth without having to refer to a wetting potential [237] where it was suggested that a kinetic crossover occurs rather than a sharp transition. This threshold depends sensitively on the misfit strain and on intermixing at the surface which retards the instability, see Fig. 116, but depends only weakly on the growth rate. An extension of this model which accounts for mobility differences was given in [339]. During the first deposition step, Fig. 115(a), some intermixing is visible as well as the formation of a thin Ge-rich surface layer due to surface segregation. When time increases, ripples grow and trenches start to form, digging into the substrate, see Fig. 115(c), and create a Si mesa underneath the island. The authors argue that after penetration of the trench into the substrate, the ejected Si mixes with the Ge of the growing dot in the outer layer of the islands, see Fig. 115(e)–(h) but only after a long enough post-growth annealing [339].

While the linear analysis leads to qualitative interesting results, it cannot account for most of the experimental observations which are in the pyramid and dome regime. A weakly non-linear bifurcation analysis of the continuum model was performed in [343] and exhibited a transition from hexagons to roles close to the instability threshold. However, this study is limited to the vicinity of the instability threshold and cannot account for fully developed islands and coarsening phenomena. Further work is still needed in these directions.

If the continuum model is relevant for the analysis of low strained films, it does not describe nucleation processes which occur at higher strain*. The analysis of the energetic barrier for island nucleation in presence of a mixing energy $E^{mix} = Vg(c)$ was performed in [344] taking into account the dependence of the misfit strain on the mean composition c of the film. The energy of an island of composition c compared to a flat layer of composition \bar{c} may be decomposed as [344]

$$E = \gamma V^{2/3} + V [g(c) - g(\bar{c}) + (\bar{c} - c)g'(\bar{c})] + YV \left(1 - \frac{a_{Ge}}{a_{Si}}\right)^2 [(c - \bar{c})^2 - \alpha c^2], \quad (41)$$

where α is the fraction of elastic relaxation of the island relative to a planar geometry. The first term describes surface energy while the second is linked to the mixing energy and chemical potential. Finally, the last term describes the elastic relaxation of the island in the case of a SiGe island with the concentration c of Ge on a Si substrate. The mixing energy may be described by its ideal value

$$g(c) = \frac{k_B T}{\Omega} \{c \log c + (1 - c) \log(1 - c)\}. \quad (42)$$

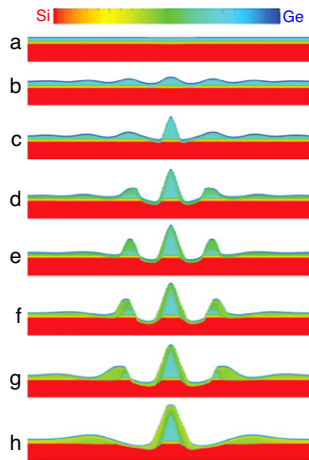


Fig. 115. (Color online) Selected snapshots from the simulation. Taking the beginning of deposition as $t = 0$, images (a)–(h) correspond to times 3 (end of deposition), 12, 14, 19, 23, 29, 35, and 161, respectively, in arbitrary units. The width of the images is 410 nm, one unit cell of our periodic system. The vertical scale is exaggerated by a factor of 5. The wetting layer thickness in trough provides a visual marker of w_s (i.e. ~ 0.4 nm) vertically, with the top third enriched by surface segregation. The color bar shows the composition scale.

Source: from [339].

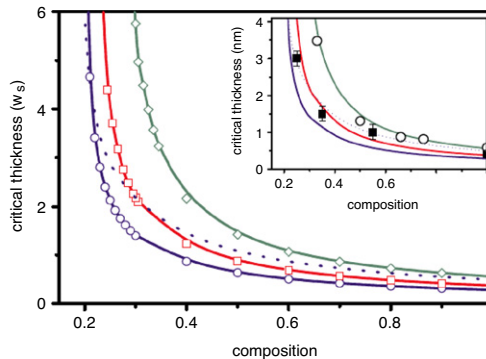


Fig. 116. Apparent critical thickness vs composition of the deposited material for growth rates 1, 10^2 and 10^4 (in arbitrary units). The bottom curve corresponds to the slowest growth rate critical height as a function of the concentration [340]. The inset are from Ref. [340] (open circle) and Refs. [341,342] (solid square). The lines in the inset are theoretical curves copied from the main panel, with arbitrary vertical scaling chosen to emphasize similarity with experiment.

Source: from [237].

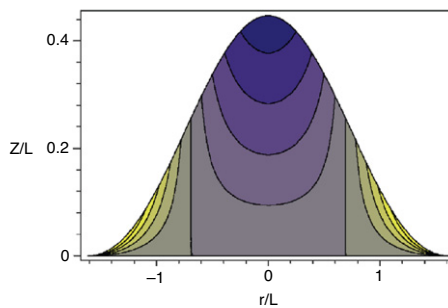


Fig. 117. (Color online) Island shape and composition map. The step between contours is 0.25, vertical lines are the zero contours and dark correspond to negative values. Results are for $\nu = 0.276$.

Source: from Ref. [338].

Looking at the dependence of the nucleation energy barrier described by Eq. (41), it was shown that alloying can enhance the island nucleation rate by decreasing the nucleation barrier, and that islands may more favorably nucleate at a different composition compared to the flat layer case [344].

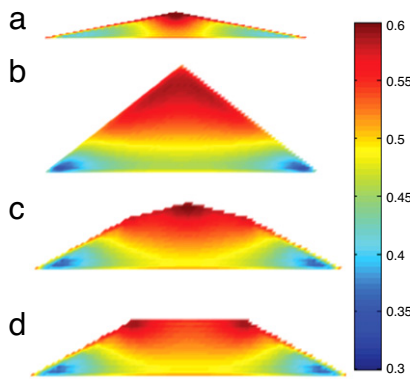


Fig. 118. (Color online) The calculated various composition pattern in the typical shaped SiGe dots: (a) prepyramidal dot, (b) pyramid dot, (c) dome dot, (d) truncated pyramid dot.
Source: from [345].

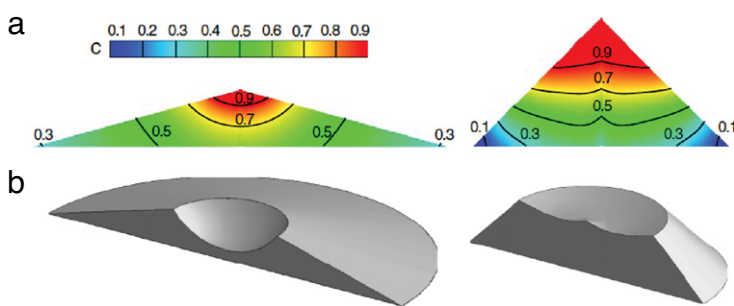


Fig. 119. (Color online) (a) Composition profiles in axially symmetric quantum dots of identical size, but with shallow ($\theta = 15$) and steep sidewalls ($\theta = 30$). The composition are obtained with $F_0 = -0.2$ and $\bar{c} = 0.2$ [346]. (b) The 3D rendering of the shapes of the quantum dots in (a) upon etching with a selective chemical agent that dissolves regions of dot whose composition c exceeds 65%.
Source: from [346].

3.5.3. Simulations and numerical results

An epitaxial alloy quantum dot was studied by means of a phase-field model in [345]. The system is described by an order parameter ϕ being 0 in the vacuum and 1 in the crystal. The total free energy of the system with a local concentration c may be decomposed as

$$\mathfrak{F} = \int d^3\mathbf{r} \left[f(c, \phi) + \beta_c (\nabla c)^2 + \beta_\phi (\nabla \phi)^2 + \frac{1}{2} \sigma_{ij} \epsilon_{ij} \right], \quad (43)$$

where the second and third terms describe interfacial energies while the last one is the usual elastic energy density. The first term is the chemical potential of the alloy which may be written as

$$f = \frac{k_B T}{\Omega} \left[\frac{1}{2} w c (1 - c) + c \log c + (1 - c) \log(1 - c) \right] \phi^2 + A \phi^2 (1 - \phi^2), \quad (44)$$

where w describes the atom exchange interaction energy and A is associated to the usual double-well in phase field. Mass conservation is enforced by the usual Cahn–Hilliard evolution equations

$$\frac{\partial c}{\partial t} = \nabla \left[\frac{\Omega}{k_B T} D_c \nabla \frac{\partial \mathfrak{F}}{\partial c} \right], \quad (45)$$

$$\frac{\partial \phi}{\partial t} = \nabla \left[\frac{\Omega}{k_B T} D_\phi \nabla \frac{\partial \mathfrak{F}}{\partial \phi} \right]. \quad (46)$$

The resulting composition maps are plotted in Fig. 118. They are found to depend strongly on the dot shape and size and the composition heterogeneity appears to be enhanced when the height to width ratio increases [345].

Extensive numerical studies have also been used in order to compute the equilibrium composition field inside a dot with a given shape. This problem was tackled by several groups using finite-element simulations [346,347]. Even though this technique is limited to one or two quantum dots, it leads to insightful results. In [346], the composition and elastic fields

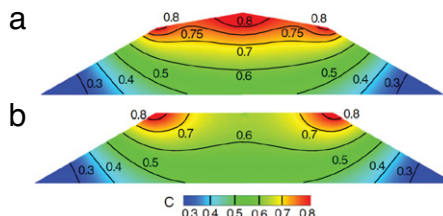


Fig. 120. (Color online) Equilibrium composition profiles in axisymmetric quantum dots with (a) “dome” shape, the angles of the sidewalls being 30° and 15° , and (b) a truncated-cone shape with a sidewall angle of 30° . While the composition profiles are similar near the base, larger strain relaxation in the regions near the corners results in a greater segregation in the apex of the dome-shaped quantum dot. The composition profiles are obtained for $F = -0.2$ (thermodynamic favorable mixing) and $\bar{c} = 0.5$.

Source: from [346].

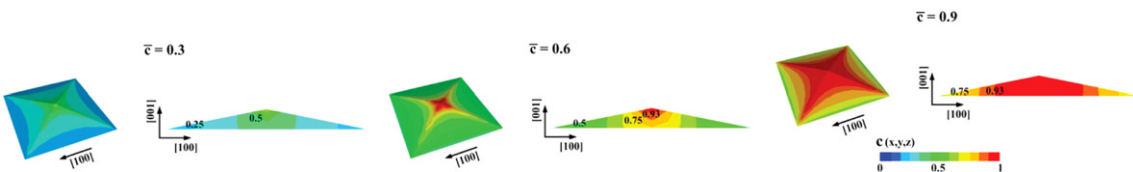


Fig. 121. (Color online) Distribution of Ge minimizing the elastic energy within $\{105\}$ pyramid with average Ge content $\bar{c} = 0.3$, $\bar{c} = 0.6$ and $\bar{c} = 0.9$.
Source: from [347].

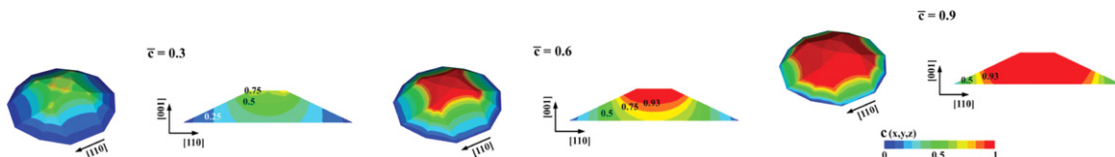


Fig. 122. Distribution of Ge minimizing the elastic energy within a dome-shaped island pyramid with average Ge content $\bar{c} = 0.3$, $\bar{c} = 0.6$ and $\bar{c} = 0.9$.
Source: from [347].

at equilibrium were investigated using finite-element methods combined with optimization techniques. The composition profiles of dots with a thermodynamic favorable mixing were found to depend strongly on the island slopes and curvature, and on the presence of corners and edges, see Figs. 119 and 120. In [347], a Monte-Carlo approach implemented with finite-element methods was dedicated to the study of islands with realistic shapes. It showed that the islands which provide the largest relaxation at equilibrium also lower the elastic strain through a significant non uniform alloying. Different shapes were investigated with different aspect ratio, pyramids, domes and barns. As shown in Figs. 121 and 122, the composition maps are strongly dependent on the island morphology and the general trend is that the composition inhomogeneity increases when the aspect ratio increases. The composition profiles in faceted quantum dots with steep sidewalls are found to be characteristically different from the corresponding case of shallow dots (Fig. 119). In the case of unfaceted quantum dots, both the slopes and curvatures of the surface are found to influence compositional patterning [348]. In the case of domes and truncated pyramid shaped quantum dots with multiple facets, the results evidence the formation of a rich array of compositional patterns with enrichment in the larger alloy component at the corners and edges formed by the intersection of different facets.

More recently, the dynamical evolution of alloyed and strained islands was investigated on the basis of simulations of a fully faceted model [349]. It resulted in composition maps which depend significantly on the growth-history of the island formation. As expected, the increase in the growth rate leads to a decrease in the composition inhomogeneity, see Fig. 123. In addition, the island aspect ratio is also affected by the composition distribution as a result of the morphology–composition coupling, and the composition inhomogeneity also increases when the aspect ratio increases.

Besides the use of finite-element methods, semi-empirical potentials and Monte-Carlo simulations were also devoted to the study of SiGe strained islands at equilibrium [350,351]. Even if homogeneous islands were found in [350], the simulations in [351] did find strong inhomogeneities with Si-rich cores and outer Ge-rich shells. The latter equilibrium islands result in addition to surface intermixing, from stress driven intermixing and volume diffusion [351]. In this work, diffusion processes were simulated by a quasi-equilibrium MC approach which considers high temperature processes and a large diffusion (in the island, WL, and top substrate layers) due to strain. Individual processes account for the surface and elastic energies, the alloy mixing energy, and the configurational entropy. The composition profiles derived in this framework evidence the formation of a Si-rich core which is formed under the condition of a strain-enhanced diffusion, including Si–Ge exchange at the central basal region of the island. In these equilibrium simulations, mainly volume events occur, near both the island center and edges (in a Si enriched corral region in the WL and in the compressed regions near the island edges). Moreover,

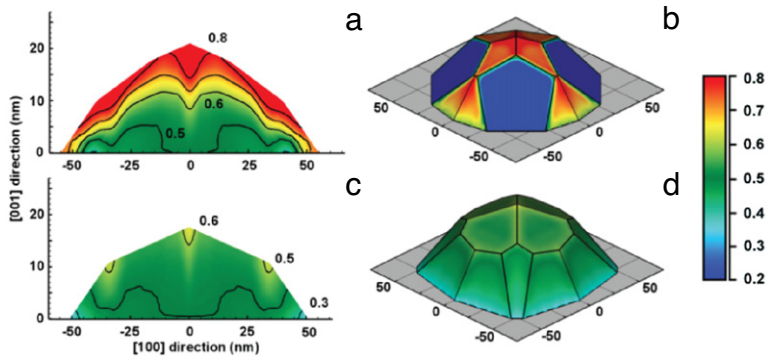


Fig. 123. (Color online) Vertical cross-sectional composition distribution as a result of different growth rates (a) low growth rate (c) high growth rate. For each profile, the corresponding shape and surface composition are shown in panels (b) and (d), respectively. By comparing the panels, the effect of growth rate is evident: Composition distribution become more uniform at higher growth rates. Due to the coupling among shape, strain and composition, the final shape is also affected by the growth rate: Panel (b) and (d) show that the size of the {15 3 23} facets is smaller at a lower growth rate, while it is larger at a higher growth rate (d).
Source: from [349].

these equilibrium simulations showed that much of the compression in the island is relieved by alloying at equilibrium especially in the core, while elastic energy is still stored in the compressive ring near the edges and in the corral below [351]. However, bulk diffusion may be considered as negligible in molecular-beam epitaxy, and the composition evolution mainly occurs by surface diffusion in experimental conditions. The effect of strain enhanced diffusion on alloying was also inferred by MC simulations of heterostructures which are fully relaxed by dislocations [352]. This study showed that intermixing is totally suppressed even at high temperatures because it would otherwise increase the strain, see Fig. 124 [352].

To go further and study the growth shapes and compositional maps resulting from the growth kinetics and not from equilibrium, kinetic Monte-Carlo simulations were implemented more recently [353,354]. In [353], the growth mode (with either planar growth of the island or a tilted one) was found to lead to different inhomogeneities, see Fig. 125, depending on the dominant growth kinetics. In [354], a KMC simulation was performed using an evaluation of the elastic displacements with a rejection-reduced algorithm. It showed the retardation due to intermixing of the onset of the instability, see Fig. 126. It also showed that the elastic stress is concentrated at the bottom of valleys between islands in the intermixing case, as opposed to the no-intermixing case where stress is concentrated at the island foot [354].

3.6. Microscopic processes

We review in the coming Section the basic mechanisms responsible for the mass transfer which lead to alloying in the system under scrutiny.

3.6.1. Defect diffusion

In order to study defect diffusion, self-diffusion and interdiffusion in SiGe alloys, non-lattice kinetic Monte-Carlo simulations of atomistic processes were implemented in [160]. In unstrained systems, atom diffusion in Si, Ge and SiGe crystalline alloys is assisted by native point-defects (vacancies, V , and self-interstitials, I , named A in the general case), both for lattice atoms (self-diffusion) and for dopants. In a homogeneous $\text{Si}_{1-x}\text{Ge}_x$ alloy at equilibrium, the concentration $C_{A^0}^{eq}$ of neutral point-defects (V or I) is given by an Arrhenius law $c_{A^0}^{eq} = \bar{c}_A \exp(-E_A^f/k_B T)$ where E_A^f is the formation energy of the neutral species A , which is composition dependent. Similarly, if one considers charged points defects, the concentrations of these species depend on the Fermi level e_F at equilibrium. The diffusivity of a species may then be given by an Arrhenius law $D_A = \bar{D}_A \exp(-E_A^m/k_B T)$ with the migration energy E_A^m . The resulting diffusion coefficient of a defect A is thus given by the sum over all charged state of the species diffusion coefficient which is the product of the concentration of the species by its diffusivity.

In semi-conductors, self-diffusion results from point-defect diffusion as direct exchange is negligible. The self-diffusion coefficient D_τ of a species τ (Ge or Si) may then be written as the sum of the species self-diffusion coefficients due to the point-defects. If one defines the ratio $\alpha_A(x) = D_{\text{Ge}}^A(x)/D_{\text{Si}}^A(x)$, a point defect A has the probability to move a Si atom

$$P_{\text{Si}}^A = f_A \frac{1-x}{1-x+\alpha_A x} \quad (47)$$

and a probability $1 - P_{\text{Si}}^A$ to move a Ge atom, where f_A is a correlation factor of defects which is 0.5 for V and 0.7 for I [160]. For interstitials, atom movements are in the same direction as the point defect jumps, whereas for vacancies they go in the opposite direction. The resulting self-diffusivities are displayed as functions of the Ge fraction x in Figs. 128 and 129.

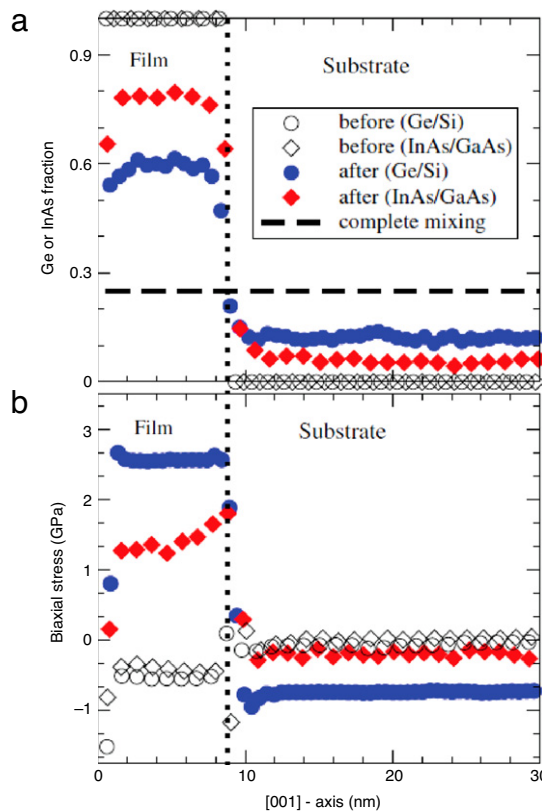


Fig. 124. (Color online) Equilibrium composition and stress in the system at 300 K. (a) Composition variations along the [001] growth axis of Ge and InAs dislocation-relaxed films on thin Si and GaAs substrates, respectively, before and after intermixing, as indicated in the legend. Points denote local atomic compositions averaged over slices having thicknesses of ~ 0.63 nm (Ge/Si) and 1.03 nm (InAs/GaAs). Dashed horizontal line shows the limit of perfect mixing in the non-dislocated case. Dotted vertical line denotes the interface position. (b) Biaxial stress at 300 K in the above structures, before and after intermixing. Points denote local atomic stresses averaged as in (a).

Source: from [352].

In addition to the previous mechanisms, one must also consider in strained films, the strain dependent diffusion of point-defects and atoms, and, in some cases, the anisotropy introduced by the biaxial geometry. The strain dependence of the transport capacities of neutral defects, is due to the modification of both formation and migration energies. In addition, the biaxial strain alters the band structure of the alloy and thence, the electronic level energies, Fermi level and transport capacities of charged point defects. The diffusion of a neutral species in the presence of a strain ϵ may be described by its effective diffusion coefficient DC_{A0}^i (accounting for the species concentration)

$$DC_A(\epsilon) = DC_A(0) \exp(\epsilon V_A^i / k_B T), \quad (48)$$

where V_A is an effective volume. In inhomogeneous systems, the ratio α_A between Ge and Si diffusivities depends not only on the local alloy composition, but also on its gradient and includes an extra Arrhenius weight $\alpha'_A = \alpha_A \exp(-\Delta E_{total}^i / k_B T)$, where ΔE_{total}^i is the difference of the total energy between the configurations resulting from the displacement of a Si or Ge atom corresponding to the jump of a defect, which includes both the elastic energy and the mixing enthalpy. As the elastic energy depends quadratically on ϵ , the system tends to minimize its elastic energy through composition homogenization, so that strain relaxation enhance interdiffusion. On the other hand, if the lattice formation enthalpy per atom (E_{total}^i) is not linear with the alloy composition, the total energy will change with the alloy mixing. When $d^2E_{total}^i/dx^2 < 0$, an homogenization results in an enthalpy increase which tends to hinder interdiffusion [160]. The compositional maps resulting from KMC simulations which include these microscopic processes is plotted in Fig. 127 concerning Si/Si_{1-x}Ge_x/Si quantum wells grown onto Si_{1-y}Ge_y pseudo-substrates of different compositions. In all cases, the simulated profiles are in good agreements with the experimental ones, thus validating the approach.

3.6.2. Incorporation in surface steps

An enhanced segregation and superlattice formation was observed in [355] during the step-flow growth of an alloy on a vicinal surface. When a strained alloy grows by step flow, the surface steps form periodic bunches which strain field biases the incorporation of the alloy components in the steps. This effect was clearly evidenced by experimental observations of

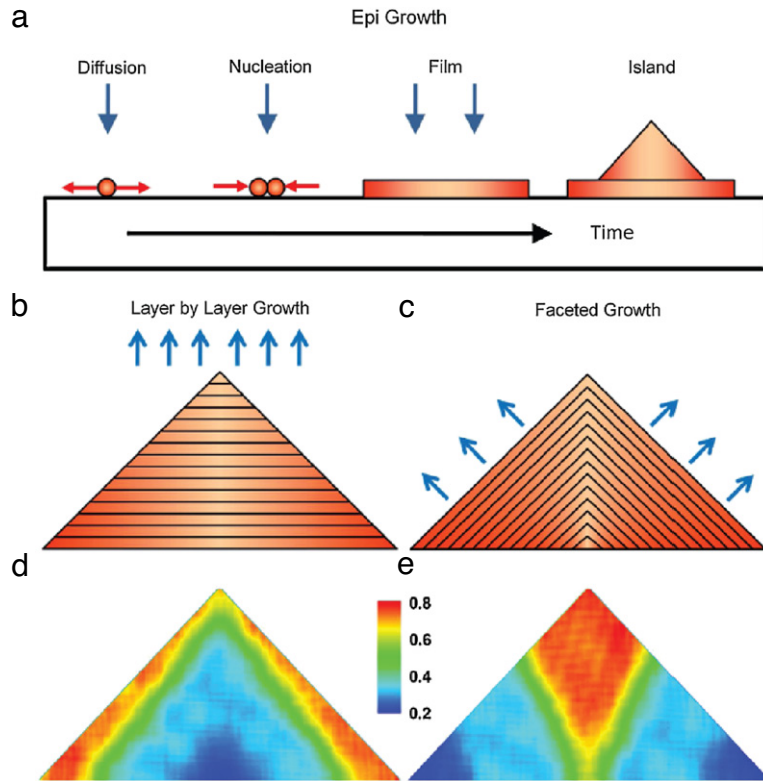


Fig. 125. (Color online) (a) Schematic of the typical SK epitaxial growth process of a strained QD. (b) Schematic illustration of the layer-by-layer growth of a QD. (c) the faceted growth of a QD. (d) Contour plot of the compositional profile of a QD with a triangle-shaped Si-rich core, resulting from the layer-by-layer growth. (e) Contour plot of the compositional profile of a QD with a V-shaped Ge-rich core, resulting from the faceted growth. The color bar marks the Ge concentration.

Source: from [353].

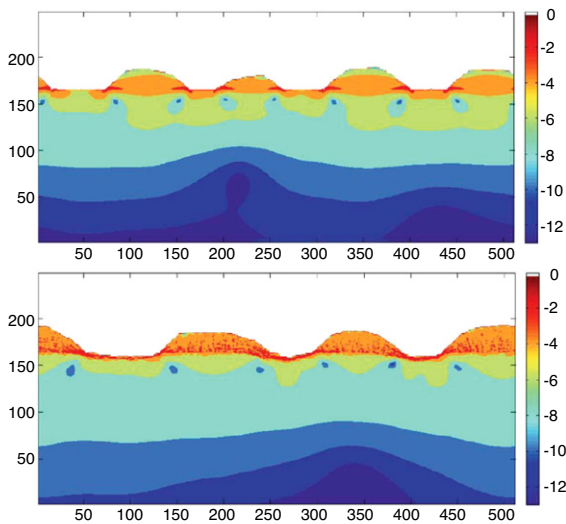


Fig. 126. (Color online) Elastic energy density plots: the figures show the plots of the elastic energy density (logarithmic scale). The figure on the top corresponds to the crystal configuration at 10 monolayers without intermixing and the bottom one corresponds to the crystal configuration at 10 monolayers with intermixing.

Source: from [354].

SiGe alloy grown on Si by X-ray diffraction and electron microscopy, see Fig. 130. The basic mechanisms related to strain and alloying may be described by the composition and strain-dependent chemical potential at the steps. The step bunches alter

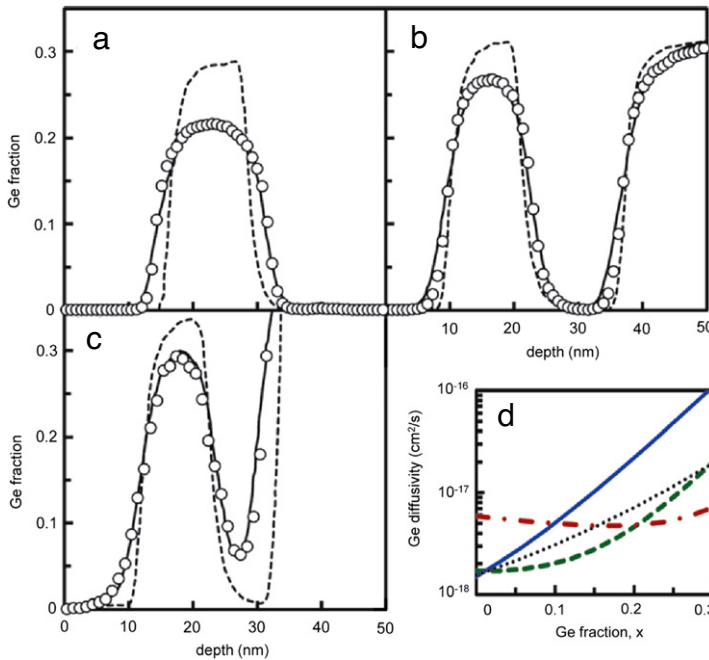


Fig. 127. (Color online) Experimental (solid lines) and simulated (circles) 880 °C, 90 min annealed profiles of Si/Si_{1-x}Ge_x/Si structures grown on three different relaxed Si_{1-y}Ge_y pseudo-substrates with: (a) $y = 0$, (b) $y = 0.3$, and (c) $y = 0.56$. As-grown profiles are also included in (a)–(c) (dashed lines). Panel (d) displays the calculated Ge diffusivities $D_{Ge}(x)$ for the strain situations of panels (a) (blue solid line), (b) (green dashed line), and (c) (red dashed-dotted line), as well as for the unstrained case (black dotted line).

Source: from [160].

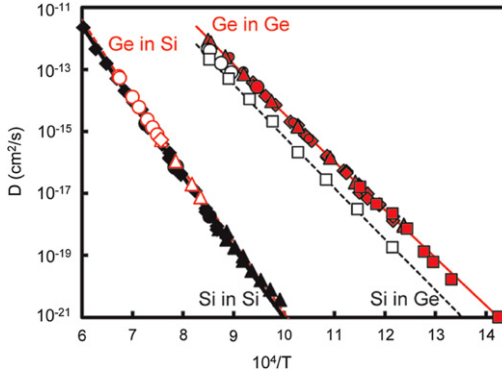


Fig. 128. Experimental and calculated Si and Ge diffusivities in silicon and germanium crystals in intrinsic material under equilibrium conditions vs the inverse of temperature. Calculated self-diffusivities (Si in silicon or Ge in germanium) are represented by solid lines, whereas, calculated impurity diffusivities (Ge in silicon or Si in germanium) are represented by dashed lines.

Source: from [160].

the surface elastic field, producing different strain level at different steps. The smaller (larger) adatoms are incorporated preferentially at steps having a relatively compressive (tensile) strain. In addition, steps having the lowest absolute strain are overall favored so that atoms of the more mobile species can more readily reach these preferred steps.

The usual conservation equations on vicinal surface [356] can be generalized to describe the growth of an alloy [357]. First, the evolution of the surface morphology may be written as

$$\frac{\partial u_m}{\partial t} = \frac{1}{2}(u_{m+1} - u_{m-1}) + \bar{M}^3 \phi_m, \quad (49)$$

where u_m is the displacement of the step m , \bar{M} , an average mobility and ϕ_m , an interaction energy between steps. The local composition at a step of a species τ may be related to the step velocity in an equation which depends on two competing terms [355]. The deviation from the average composition is first proportional to a factor α related to the decomposition

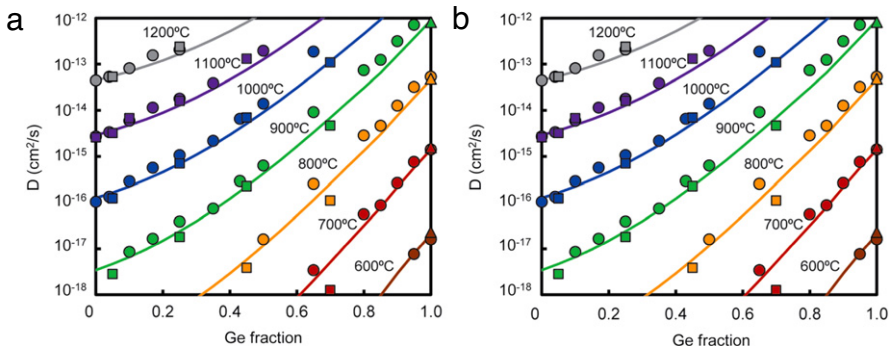


Fig. 129. (Color online) (a) Ge and (b) Si self-diffusivities in $\text{Si}_{1-x}\text{Ge}_x$ alloys as a function of Ge fraction ($D_{\text{Ge}}(x)$ and $D_{\text{Si}}(x)$, respectively) at different temperatures in intrinsic conditions. Symbols correspond to experimental values (extracted from various references), obtained by Arrhenius interpolation from the available measurements. Lines correspond to the calculated values.

Source: from [160].

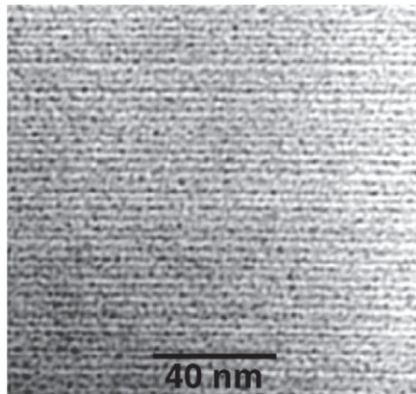


Fig. 130. TEM cross-section image of a $\text{Si}_{0.84}\text{Ge}_{0.16}$ alloy grown on $\text{Si}(001)$, obtained with (002) two beam diffraction conditions. The top edge is towards the growth surface. Despite 'noise', horizontal layers with spacings around 3 nm are clearly visible.

Source: from [355].

mechanisms. The differences in size and mobility of the two species, which favor decomposition, enter in this parameter as

$$\alpha = 4 \frac{\eta}{\epsilon} + 3 \frac{\Delta M}{\bar{M}}, \quad (50)$$

where η is the lattice expansion parameter and ΔM is the mobility difference. The other important parameter γ acts in the opposite way in order to suppress decomposition, and is proportional to the second derivative g'' with respect to the composition of the free energy of mixing of the alloy. As long as the alloy is stable against spinodal decomposition, $g'' > 0$ and $\gamma > 0$. As a result, an ordered pattern of composition modulation is found in these vicinal systems, showing spontaneous superlattice formation, see Fig. 131. This effect is also supported by experimental observations [355] and a good comparison may be found when the absolute composition modulation is of the order of 10% [355]. Even though the quantitative predictions of this theory could be affected by effects such as diffusion barriers, step permeability, and step-repulsions, the self-organization found there are expected to be robust. Note that a recent study found that the mean number of permeability events per atom shows a scaling law with the mean distance between the kinks, but that in any case, the step permeability does not change the rate of step propagation as the atoms inevitably join kink sites although not in the first encountered step [358].

3.6.3. Mobility differences

Another well established process which rules the composition of SiGe nanostructures is the surface segregation of Ge during growth. It may be explained by a two site exchange mechanism, see Fig. 132 [360] and leads to non-abrupt interfaces and lower Ge content. Segregation occurs by the exchange of segregating atoms between surface and subsurface sites. It can be described by rate equations [360,359]

$$\frac{d\theta_s}{dt} = f_1 \theta_b (1 - \theta_s) - f_2 \theta_s (1 - \theta_b), \quad (51)$$

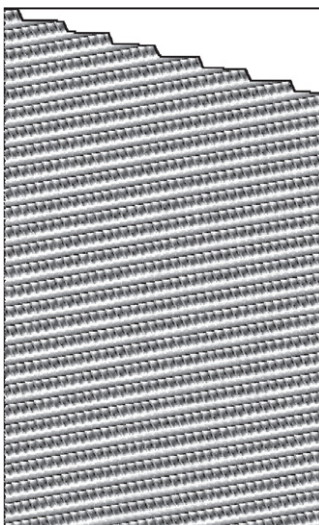


Fig. 131. Cross-sectional view of simulated superlattice formation. The parameters used in this calculation are $\bar{M} = 0.446$, $\eta_0 = 0$ and a minimum-energy distance between two isolated steps $l_0 = 0.192$. The vertical axis has been exaggerated for clarity. The black and white regions are enriched in one or the other component, while the gray regions have composition close to the average composition.

Source: from [355].

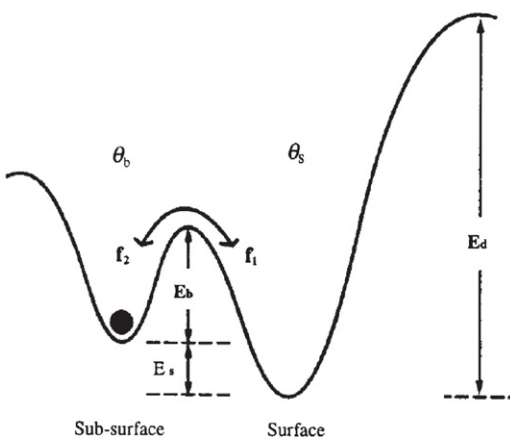


Fig. 132. Energy-level diagram representing the two-site exchange model of surface segregation. E_d is the energy barrier of desorption, which is assumed to be so large that desorption not occur for the growth conditions used.

Source: from [359].

$$\frac{d\theta_b}{dt} = f_2 \theta_s (1 - \theta_b) - f_1 \theta_b (1 - \theta_s), \quad (52)$$

where θ_s and θ_b are the coverage of the segregating atoms (Ge) in the surface and subsurface layer respectively. The rate constants for the exchange are $f_1 = v_0 \exp(-E_b/k_B T)$ and $f_2 = v_0 \exp[-(E_b + E_s)/k_B T]$, where E_b and E_s are the kinetic barrier and Gibbs energy of segregation respectively and v_0 is the attempt frequency $\sim 10^{13} \text{ s}^{-1}$. For a layer-by-layer growth at ML completion, it is only possible to exchange atoms between the completed outermost layer (θ_s) and the subsurface layer (θ_b) and when segregation is fast compared to growth, a steady-state concentration of the segregant in these layers is found, which satisfies [359]

$$\exp(-E_s/k_B T) = \frac{\theta_b (1 - \theta_s)}{\theta_s (1 - \theta_b)}. \quad (53)$$

A lower mobility of Si atoms was invoked in order to explain nonuniform distribution of Si in SiGe systems, including enrichment with Si in the wetting layer compared to islands [164] in the island base relative to the island top [108], or in the ripple valleys relative to the ripple top [361]. It could decrease the number of Si adatoms compared to the faster Ge adatoms which can diffuse upward the steeper island or ripple surfaces. Quantitative first-principles calculations of the surface mobility difference between Si and Ge were performed in [362]. It showed that Ge surface diffusion is generally faster than Si. The ratio of the Ge surface mobility to the Si one exhibits a strong exponential dependence on surface strain ϵ ,

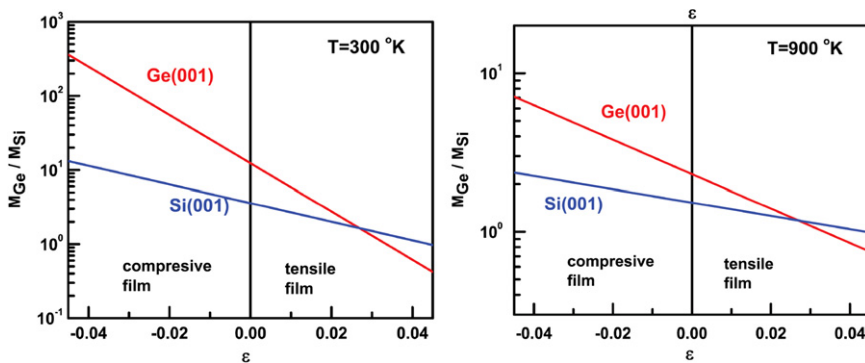


Fig. 133. Semilog plot of the Ge/Si surface mobility ratio as a function of in-plane strain on Si(001) or Ge (001) at 300 (left) and 900 K (right). The left side of top and bottom panels shows the results for a compressive SiGe alloy film grown on a Si substrate; the right side of top and bottom panels shows the results for a tensile SiGe alloy film grown on a Ge substrate.

Source: from [362].

$\beta = M_{Ge}/M_{Si} \approx e^{\alpha\epsilon}$ with a constant α . This makes the growth of a compressive SiGe film on a Si substrate drastically different from that of a tensile SiGe film on a Ge substrate. However, the mobility ratio depends drastically on the growth conditions. During the growth on the Ge wetting layer on Si(001), Ge diffuses only slightly faster than Si whereas on the Ge (105) island surface, Ge may diffuse 10³ times faster than Si. More generally the difference between Si and Ge surface diffusion and its dependence on strain must be considered on the unstrained Si(001) and Ge (001) surfaces. Diffusion on Si(001) and Ge (001) is highly anisotropic mostly along the dimer-row direction, with diffusion barriers around 0.65 and 0.62 eV on Si(001) and 0.59 and 0.53 eV on Ge (001), for Si and Ge adatoms respectively [363]. Moreover, the adatom diffusion barrier is found to depend linearly on the in-plane surface strain for strains up to a few percents, due to the fact that the adatom binding energies at both the minimum energy site and the transition state depend linearly on strain [364]. The quantitative strain dependence of the diffusion barrier for Si and Ge adatoms on Si(001) under a strain ϵ can be described by

$$E_{Si}^{Si}(\epsilon) = 0.65 - 5.29\epsilon, \quad (54)$$

$$E_{Si}^{Ge}(\epsilon) = 0.62 - 4.54\epsilon, \quad (55)$$

in eV, whereas they are given on a strained Ge (001) surface by

$$E_{Ge}^{Si}(\epsilon) = 0.59 - 8.09\epsilon, \quad (56)$$

$$E_{Ge}^{Ge}(\epsilon) = 0.53 - 6.15\epsilon. \quad (57)$$

The strain dependence of the surface mobility ratio β is then plotted in Fig. 133.

However, these general trends must also be supplemented by surface reconstruction in order to get a realistic description. Indeed, it is well-known that the top Ge (001) surface reconstructs into a (2 × N) reconstruction and that a SiGe hut island develop (105) facets. The issues of Si and Ge adatom diffusion on strained Ge (001)-(2 × N) and Ge (105) surfaces was also analyzed in [362]. It showed that the mobility difference between Si and Ge on a Ge (001)-(2 × N) surface is relatively small. This effect is due to the (2 × N) reconstruction which overcompensates the compressive strain leading to a tensile surface stress on (001)-(2 × N). On Ge (105) the situation is quite different since the (105) surface strain is high and the Ge (105) is much rougher than Ge (001). The Ge (105) surface can be viewed as a stepped (001) surface consisting of a sequence of small (001) terraces separated by single atomic height steps in the [010] direction (or zigzag segments of S_A and S_B steps). The evolution with temperature of the surface mobility ratio on these two surfaces is plotted in Fig. 134. The results show that the surface mobility ratio is much larger on Ge (105) than on Ge (001). At room temperature, this ratio can be as large as ∼10⁴ times on Ge (105) while it is of the order of 20 on Ge (105), but roughly of order unity on a flat reconstructed Ge surface. Moreover, one can note that as Si and Ge adatoms diffuse from the wetting layer surface to the hut island surface, their mobility difference will increase by 100 to 1000 times, depending on the growth temperature.

When the amount of Sb increases, one finds a strong reduction of the island size which is accompanied by a higher Ge content and higher island density, see Fig. 79. The presence of Sb also causes a change in the island morphology which display a rounded shape and do not exhibit any visible facet neither on their top nor on their side, see Fig. 80. The shape modification and size reduction were mainly attributed to a change in the Ge surface energy and diffusion induced by the adsorption of even a small amount of Sb. Indeed, neglecting the possible changes of the microscopic surface state (surface reconstruction, roughness, etc.), it is reasonable [221] to assume first that the surface energy follows a Vegard's law with the Sb coverage θ ,

$$\gamma(\theta) = \theta\gamma^{Sb} + (1 - \theta)\gamma^{Ge}, \quad (58)$$

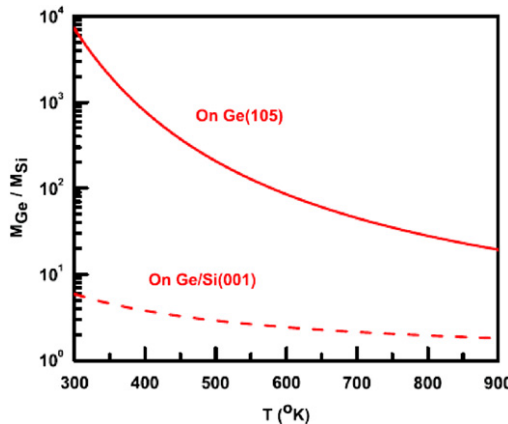


Fig. 134. The temperature dependence of the surface mobility ratio between Ge and Si adatoms on the strained Ge (001)-(2 × 8) and Ge (105)-(2 × 1) surface in the typical range of growth temperatures.
Source: from [362].

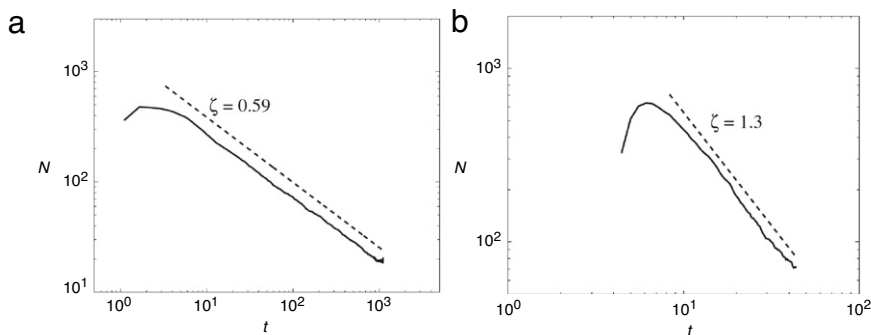


Fig. 135. Long time evolution of the island density in (left) 1 + 1 dimension and (right) 2 + 1 dimension.
Source: from [236].

with the Sb and Ge surface energies γ^{Sb} and γ^{Ge} . Similarly, the morphological and compositional changes may be attributed to a reduced surface diffusion of Ge in presence of Sb, with a surface diffusion coefficient D_S which may be given by

$$D_S = a^2 Z_s \nu_s [\theta \exp(-E^{Sb}/k_B T) + (1 - \theta) \exp(-E^{Ge}/k_B T)], \quad (59)$$

where E^{Sb} and E^{Ge} are the activation energies for the diffusion of Ge on a Sb and Ge surface respectively, while Z_s and ν_s are the surface coordination number and atomic frequency. In addition, because of the dynamic segregation of Sb during growth, the two sites exchange between adatoms and Sb atoms directly below the surface must also be considered. It can be described by an activation energy E^{ex} and the exchange rate Γ^{ex} is merely $\Gamma^{ex} = 2\theta \nu_s \exp(-E^{ex}/k_B T)$. Defining the diffusion time τ for Ge diffusion before exchange with Sb subsurface atoms, $\tau = 1/\Gamma^{ex}$, one may estimate the Ge diffusion length on the surface, $\lambda = \sqrt{D_S \tau}$, with the result

$$\lambda = a\sqrt{2Z_s} \left[\exp\left(\frac{E^{ex} - E^{Sb}}{k_B T}\right) + \frac{1 - \theta}{\theta} \exp\left(\frac{E^{ex} - E^{Ge}}{k_B T}\right) \right]^{1/2}. \quad (60)$$

It can reasonably be assumed that the energetic barriers of the Ge surface diffusion and of the Sb surface segregation are in the same range with $E^{ex} > E^{Sb}$ (the barrier of inter-planar atomic exchanges is expected to be larger than the barrier of atomic jump on the surface). In the limiting case of $E^{ex} = E^{Sb}$ at $\theta = 1$, one gets the minimal value of $\lambda = a\sqrt{2Z_s}$. The decrease in λ with the amount of Sb explains the reduction of the island size and the decrease of segregation and thus the increase in the Ge content. At $\theta = 1$, the diffusion length is directly related to $E^{ex} - E^{Sb}$, and one may also expect that the diffusion length λ decreases when the activation energy for atomic exchange decreases, resulting in a decrease in the island size and an increase in the Ge density.

Table 1

Scaling law of the roughness and island density, $w(t) \sim t^\beta$ and $N(t) \sim t^\zeta$, characterizing the long time dynamics of the ATG instability with wetting interactions, AFV 07 from [236], LGDV 07, [231] and PH 06, [264]. The roughness w is $\langle (h - \langle h \rangle)^2 \rangle^{1/2}$ while N is the island density.

	AFV 07	LGDV 07	PH 06
β	0.7	2.9	0
ζ	1.3	2.9	/

3.7. Coarsening

The kind of coarsening that islands undergo is crucial for the possibility of a self-organization with suitable size distribution and spatial order. A lot of attention was devoted to this study as the island evolution in SiGe revealed a peculiar dynamics specific of systems under strain. In particular, the film dynamics which does not follow a simple common behavior was at work as regards the possibility of an anomalous Ostwald ripening [140] or the possibility of an evolution towards stable islands [138]. In fact, island coarsening occurs for a specific range of parameters (temperature, film thickness, composition ...) while stationary states may also be found in some conditions as discussed in the following.

3.7.1. Initial mound coarsening

The early stages of island formation can be monitored in the low-strain regime where the evolution from the initial ripple corrugation is continuous. It involves the long-time dynamics of the ATG instability which can be investigated using a non-linear analysis in the small-slope approximation. We focus here on isotropic systems which is relevant for the description of the initial prepyramids. As explained before, wetting interactions between the film and substrate are also important to circumvent finite-time singularities in the theory and dislocations in experiments. Steady state solutions were first found considering a regularizing wetting potential which diverges as $1/h^2$ and linear elasticity [238]. Non-coarsening islands were found in [264] in a model which considers a dominant but non diverging wetting potential and a numerical scheme for computing the non-linear elastic energy. On the contrary, a weakly non-linear analysis near the instability threshold with a singular e^{-h}/h^{α_w} wetting potential shows that spatially regular arrays of QF are unstable as a result of a subcritical bifurcation [231]. Consequently, a non-interrupted coarsening is found where larger islands grow at the expense of smaller ones, as is characteristic of Ostwald coarsening.

Finally, the full elastic non-linear analysis with an exponentially decreasing wetting potential, see Eq. (18), exhibits a non-interrupted coarsening characterized by a power-law dynamics which depends substantially on the space dimension (Fig. 135) [236]. It is found that the island density N behaves for large time as $1/t^\zeta$ where $\zeta > 1$ in 3D, which describes a coarsening faster than the usual one. Indeed, the usual Lifshitz-Slyozov [365] mean-field theory of Ostwald ripening limited by attachment and detachment of atoms, predicts a $1/t$ decrease (see [133]), while the Chakraverty extension to the diffusion limited case [366,367] leads to a $1/t^{3/4}$ decrease. A fast dynamics was also found in [231] but with a large dynamical exponent, see Table 1. Results for the dynamical behavior and exponents are obviously under debate. In the non-interrupted coarsening analyses, growth proceeds by increasing the island aspect ratio (height to width) at a nearly constant base. This increase allows a better strain relaxation and thus a decrease in the island chemical potential. This potential was plotted as a function of the island volume in Fig. 136 for equilibrium states obtained at the very end of the coarsening when only one island is left [236]. The monotonic decrease in the island chemical potential with V corroborates the hypothesis of a non-interrupted coarsening. Note also that equilibrium between islands and the wetting layer which is realized for a given μ , may be achieved during coarsening with a small variation of the wetting layer thickness.

3.7.2. Pyramid coarsening

For thin enough films, the evolution drives the surface into square and/or rectangular base pyramids. These huts first coarsen but remain stable after some time both in the low [105] and high strain [368,369] regimes. This behavior is completely different from the non-interrupted coarsening of isotropic prepyramids and the continuous evolution from prepyramids to pyramids, and thus reveals the usual impact of anisotropy on the growth dynamics.

Initial coarsening. A mean field description of the island evolution governed by the difference in chemical potential between islands and adatoms showed that elastic repulsion by cone-shape islands may suppress coalescence and promote Ostwald ripening [370]. In fact, experiments revealed that the initial coarsening displays a super-linear behavior [371]. The usual understanding of Ostwald ripening describes a driving force (the energy difference between large and small islands) which decreases during the film evolution. However, the real-time light-scattering measurements of the initial coarsening revealed a super-linear coarsening where the mean-island volume increases super-linearly with time while the island areal density decreases faster than linearly, see Fig. 137. This behavior was rationalized by considering a size-dependent elastic chemical

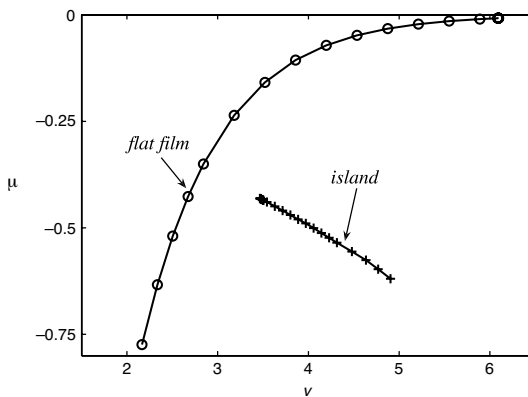


Fig. 136. Equilibrium surface chemical potential as a function of the island or wetting layer volume in dimensionless units.
Source: from [236].

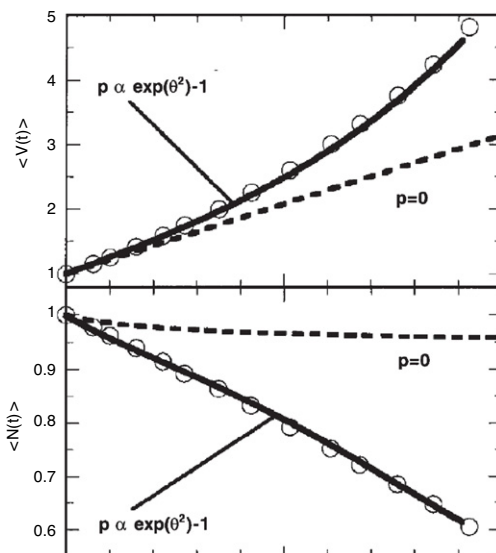


Fig. 137. Mean field model results incorporating elastic interactions at large deposition flux F (solid line). Also shown for reference is $\mu^{el} = 0$, i.e., no elastic interactions, but the same F (dashed line). The open circles are the data from experiments on a 100\AA^2 thick $\text{Si}_{0.8}\text{Ge}_{0.2}$ film on Si(001) scaled for comparison.

Source: from [371].

potential. In a mean-field description, the growth rate of islands of volume V may be written as [140,371]

$$\frac{dV}{dt} = cV^{1/3} \left[e^{\mu^*/k_B T} - e^{\mu(V)/k_B T} \right], \quad (61)$$

where c is a constant and μ^* , a reference potential which allow to fulfill mass conservation. Finite element calculations of the elastic energy may be fitted as $\mu^{el}(\theta) \sim e^{\theta^2} - 1$ for an island of area θ . The mean-field continuity equations in phase space then leads to a super-linear coarsening which reproduces the experimental behavior, see Fig. 137 [371].

Equilibrium description. For larger time however, the coarsening of huts can be found to be interrupted or at least dramatically slowed down. Both equilibrium and kinetic explanations were put forward to explain these steady states. Accounting for strain and edge energy, it was argued that the energy of an array of three-dimensional coherent strained islands may display a minimum for an optimal island size [138]. This conclusion would predict a stable configuration which does no longer undergo ripening and would enforce a narrow island size distribution [138]. The phase diagram describing the different morphologies of stable islands depending on the growth conditions was computed in [372]. A stable island size distribution was found on Si(001) in [139] which was first explained by the presence of an equilibrium state.

A dense system of interacting islands is a system of elastic domains and we consider following [373] a periodic domain of islands with volume V . The elastic energy per atom of interacting islands may be conveniently computed in the small-slope

approximation in Fourier space as

$$\Delta E^{el} = -C^{el} A \Omega / V \sum_{\mathbf{k}} |\hat{h}(\mathbf{k})|^2 k_{\alpha} k_{\beta} \hat{G}(\mathbf{k}; z, z') \Big|_{z=z'=0}, \quad (62)$$

where $\hat{h}(\mathbf{k})$ is the Fourier transform in the horizontal directions of the surface profile $h(\mathbf{r})$ and $\hat{G}(\mathbf{k}; z, z')$, the Fourier transform of the elastic Green function of a semi-infinite medium bounded by a planar stress-free surface at $z = 0$, see [373]. In Eq. (62), A is the unit cell area of the surface, Ω , the atomic volume and C^{el} is a constant depending on the elastic properties of the materials. The energy ΔE^{el} yields the sum of the energy of the volume elastic relaxation of the islands and of the interaction energy between islands. The formation energy ΔE of the island array is then given as the sum of three contributions

$$\Delta E = \Delta E^{el} + \Delta E^s + \Delta E^{ed}, \quad (63)$$

where ΔE^s is the cost in surface energy and ΔE^{ed} from the edges [138,373]. A minimum in the formation energy as a function of the island size L or array period D may exist depending on the ratio between the surface energy and edge relaxation. It was shown that the morphology of the 2D island array depends on the fraction q of the surface covered by islands. When $q < 0.06$, islands form a chainlike arrangement along the [100] (or [010]) direction with a weak coupling between chains. For $0.06 < q < 0.17$, the favorable arrangement is a base-centered rectangular lattice. For $0.17 < q < 0.33$, the preferred arrangement is rectangular, the aspect ratio of the rectangular unit cell decreasing from 1.7 for $q = 0.17$ to 1 for $q = 0.33$, where the rectangle transforms into a square. For $0.33 < q < 1$, a square lattice is preferred. A perfect hexagonal lattice with a 60° angle is never preferred but the square lattice may be favored by the cubic elastic anisotropy and by the square shape of the base of a single island. Finally, the energy minimum corresponds to a square lattice with a period D which depends on the size L of the islands. There also exists an optimum island size L_{opt} , corresponding to the absolute minimum of the energy.

Kinetics. Contrarily to the previous description, real time observations revealed an evolution characterized by a continuous and smooth increase in the island size which led in fact to the conclusion of an anomalous coarsening where islands are subject to a slowed-down Ostwald ripening [132]. Real-time STM reveal different stages where pyramids clusters appear more stable than hut clusters with larger volumes which become small pyramids before eventually dissolving. The analysis of the growth sequences suggest that a preferred island size does not exist in these conditions. Real-time STM also reveals that small enough islands shrink during the evolution with a reverse sequence of states compared to the growing ones in some conditions [133,321,196,320].

Kinetic arguments were put forward to explain steady-state configurations. A kinetically self-limited growth can be rationalized by the reduction of the growth rate when islands grow to larger sizes due to a change in the nucleation energy barrier on the island facet when the island size increases [368,1]. The growth rate of the small and large facets may be written respectively as

$$\dot{d} = \frac{4b}{l} v_0 s e^{-\Delta E_{small}/k_B T}, \quad (64)$$

$$\dot{s} = \frac{4b}{l} v_0 (s + d) e^{-\Delta E_{large}/k_B T}, \quad (65)$$

with the geometry of Fig. 138, the attempt frequency v_0 and where the nucleation barrier ΔE depend on the geometry $\Delta E_{large} = (1 + d/s)\Delta E_{small}$. The size-dependent nucleation barrier which accounts for elastic interactions, is plotted in Fig. 138. Its increase with the island size is the reason of the self-limiting growth given by the numerical integration of the evolution equations (64) which compares favorably with the experimental observations [368]. This self-limiting evolution is consistent with the model of [97] where the elastic energy barrier was computed at the island base where facet embryo were supposed to nucleate. The increase in this barrier when the island size increases leads to a reduction of the island growth and thus to a self-limited growth. The evolution of systems with a preferred island size was investigated using a mean-field Fokker-Planck analysis [374] and revealed that metastable states ruled by kinetic factors may arise before equilibrium is reached. Note that energetic calculations demonstrated the existence of such metastable states stabilized by elastic short-range interactions [375].

The suppression of Ostwald ripening was investigated more precisely by annealing experiments which lead to days-long stable QD assembly. Real-time microscopy confirmed a decreasing growth rate of islands, which was explained by the decrease in the Ge supersaturation during island growth which, in turn, reduce island growth [369,376]. The energy barrier for nucleation $\Delta G(i)$ as function of the number i of dimers in a critical nucleus was given as

$$\Delta G(i) = c\sqrt{i} + (A - \Delta\mu)j + Bj^{3/2}, \quad (66)$$

which results from step energy, edge energy and elastic energy computed with a FEM [369]. The supersaturation $\Delta\mu$ drives the growth of islands and the mean-field evolution accounting for nucleation leads to Fig. 139 which reveals a self-limited growth. Ripening suppression occurs as soon as no lower chemical potential islands are present, which could further reduce the Ge supersaturation, i.e., when the critical nucleus size is smaller than the smallest hut facet.

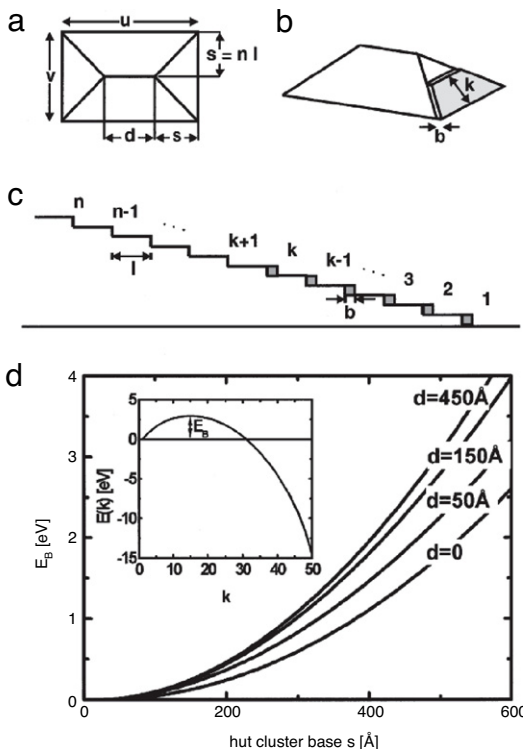


Fig. 138. Plan-view schematic (a) and perspective view (b) of a hut cluster. In (b) the nucleation of a new facet is indicated as a shaded area. (c) Cross section of a facet consisting of individual steps separated by terraces of the width l . A partly covered facet (shaded blocks) is completed up to the k th step. (d) The inset shows the island energy as a function of the facet completion k ($d = 0$). An energy barrier E_B has to be overcome to nucleate growth on a facet. Panel (d) shows the energy barrier to nucleate a new facet as a function of the cluster base s and the elongation d .

Source: from [368].

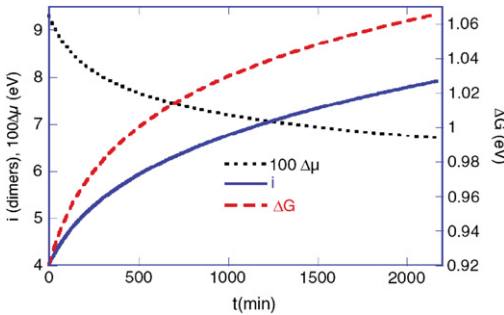


Fig. 139. (Color online). Supersaturation $\Delta\mu$, critical nucleus size i , and facet nucleation barrier $\Delta G(i)$ vs t . $\Delta\mu$ falls during the anneal, slowing the island growth rate, but i remains smaller than the smallest end facet size so that Ostwald ripening is suppressed.

Source: from [369].

The study of the dynamics of coarsening hut islands requires the account of anisotropy. This was done in [316] by considering both an anisotropic surface energy $\gamma(\mathbf{n})$ and wetting interactions, see Fig. 140. Numerical simulations in [316] indicated that the dynamic evolves towards an array of nearly uniform islands, stable against coarsening. This stability is due to strong surface energy anisotropy and strong wetting interactions which lead to the suppression of strain relaxation [314]. The resulting film morphology changes gradually from a sparse array to the localized wetting layers and finally to a faceted ripple structure depending on the film parameters [248].

The non-linear evolution equation in presence of small wetting interactions and an ad-hoc anisotropy dedicated to SiGe under strain, see Fig. 107, was numerically integrated in [230], see Fig. 108. The resulting dynamics reveals a stationary state, see Fig. 142 which does no longer undergo coarsening when the film thickness \bar{h} is not too large. The resulting stationary state depends on \bar{h} : for low thickness, mainly square-base pyramids are visible, see Fig. 108, and the island density increases with \bar{h} ; on the contrary, when \bar{h} increases, more and more rectangular base pyramid arise and the island density depends more weakly on \bar{h} . For large film thickness, after some coarsening of hut pyramids, steeper islands arise and accelerate

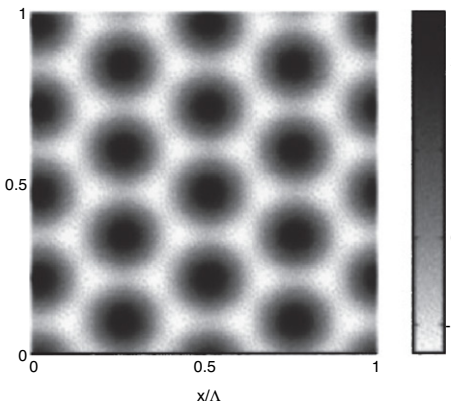


Fig. 140. Uniform island array stable against coarsening resulting from the evolution of an anisotropic strained film.
Source: from [316].

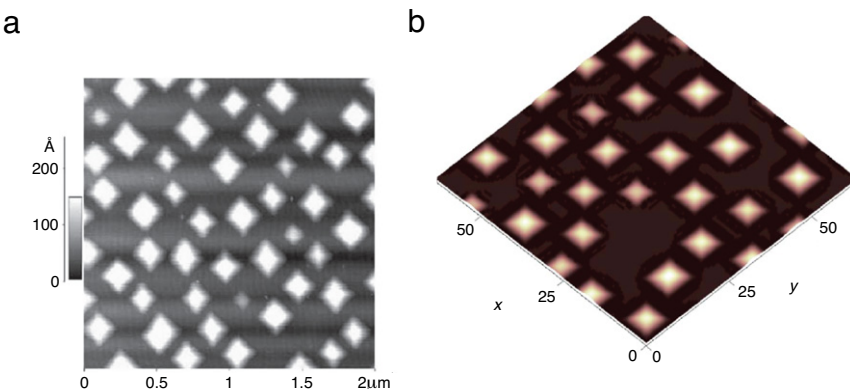


Fig. 141. (a) AFM image of a 50 Å thick $\text{Si}_{0.75}\text{Ge}_{0.25}$ film annealed at 550 °C, which does not evolve up to 72 h; (b) stationary regime resulting from the numerical resolution of the non-linear evolution equation of the elastic instability in presence of anisotropy and wetting. Note the size dispersion in both cases resulting from an interrupted coarsening.
Source: from [105] and [230].

the coarsening. The stationary state which results from this analysis for \bar{h} not too large displays a visible size dispersion in agreement with the stationary state found in experiments, see Fig. 141. Note that a power law coarsening was found in [377] in a continuum model accounting for an anisotropic surface energy, elastic and wetting interactions. However, the thin film approximation in this work leads to a $1/\bar{h}^2$ divergence of the wetting potential, and more importantly, the anisotropy under consideration treats a non stable (001) orientation which makes difficult the comparison with other results.

3.7.3. Energetic pathways

Another approach to investigate the island dynamics considers the energetic pathway for coarsening. To this end, one may first consider a uniform model with periodic islands characterized by a given pyramidal shape with an angle α and surface density n , see Fig. 143 [378]. The energy difference between the island configuration and the flat film with the same volume is given by (27). The generic energy difference ΔE is characterized by a nucleation barrier as depicted in Fig. 94 and leads once it is overcome to a continuous coarsening. The typical barrier does not include wetting effects which are known to be crucial in thin films to understand energetic landscapes [378,379,348], with the geometry of Fig. 143. Considering an exponentially decaying wetting potential [378], one gets

$$\Delta E = \gamma v^{2/3} + (v_0^{2/3} - v^{2/3})(e^v - 1) - \alpha^{el} v, \quad (67)$$

with the reduced volume $v = nv/\delta_w$ and the initial volume $V_0 = h_0/n$. The resulting energetic profile is typically depicted in Fig. 144. After the initial nucleation barrier, it displays a minimum ΔE_c for a volume V_c [32,378,379] which is associated with the increase in the energy cost of the wetting layer surface energy. Indeed, the wetting height h decreases when the island volume V increases due to mass conservation $h = h_0 - nV$, so that $\gamma(h)$ increases when the wetting layer is peeled. This result is valid for a given density n . However, when one looks at the energy of this minimum as a function of the density n , one finds [378] that ΔE_c decreases when n decreases, leading to the conclusion of a non-interrupted coarsening as n should continuously decrease in order to find the energy minimum.

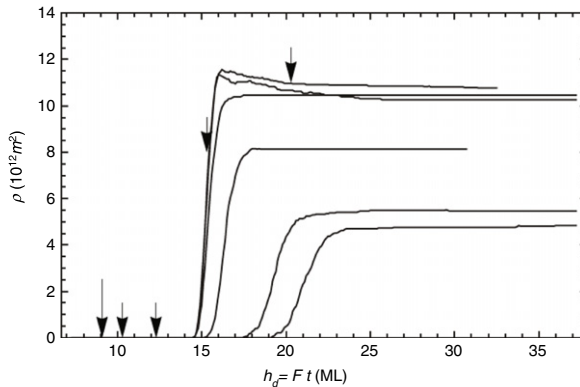


Fig. 142. Numerical integration of the island density evolution in the stationary state of an anisotropic thin $\text{Si}_{0.75}\text{Ge}_{0.25}$ strained film for (from bottom to top) increasing deposited height. Arrows indicate the time when annealing begins, while time is given in units of deposited monolayers via the deposition flux F .

Source: from [230].

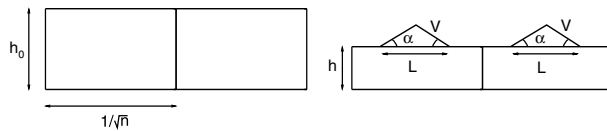


Fig. 143. Geometry of the uniform island model.

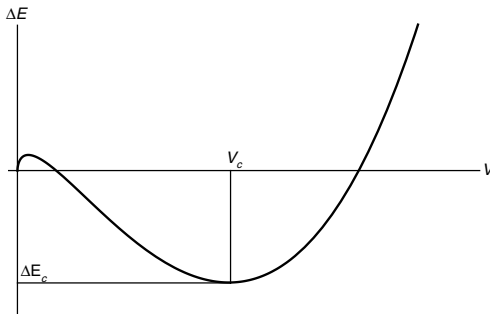


Fig. 144. Energy of a strained island as a function of its volume according to (67) with wetting interactions.

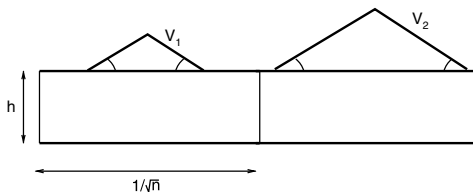


Fig. 145. Islands with a given aspect ratio undergoing Ostwald coarsening.

However, the previous model does not describe islands with different sizes which may grow at the expense of one another. In order to study the energy landscape during coarsening, a model with different sizes was introduced in [230] considering islands with a fixed aspect ratio, see Fig. 145. Neglecting elastic interactions between islands, the energy difference of the system is $\Delta E_{\text{tot}} = \Delta E(V_1) + \Delta E(V_2)$. The energetic landscape associated with this ripening pathway is depicted in Fig. 146, see [230]. After the initial nucleation barrier ruled by the competition between surface and elastic energy, the saddle point for $V_1 = V_2 = V_c$ is enforced by wetting which increases significantly the energy when the wetting layer is consumed. However, one finds a valley in the energy landscape with small energy gradients, while the strict energy minimum is still associated with complete coarsening (when either V_1 or V_2 vanish). Putting reasonable estimates of the parameters of the model, one finds energy gradients following this valley of states which can be as small as 10^{-5} eV/atom [230]. The energy difference between different configuration being the driving force for coarsening, this energy landscape agrees with a self-limiting process which slows down because of an insufficient driving force following the

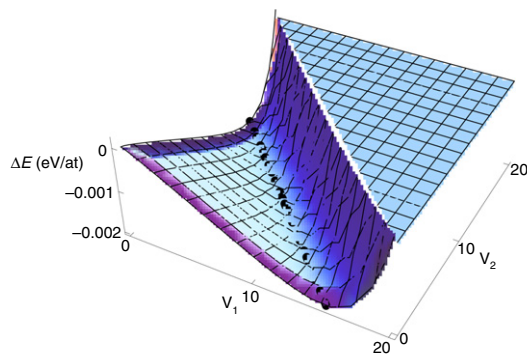


Fig. 146. Energy landscape for two islands which transfer matter to each other.

pathway under scrutiny. Note that this interruption is not associated with a local minimum of energy where the system could be trapped.

3.7.4. Pyramid to dome transition

The pyramid to dome transition was also a matter of controversy. The pyramid and dome coexistence was suggested to follow either a description with two equilibrium states [32] or an anomalous coarsening [140]. In the former description, pyramids and domes are supposed to have two minima at two different volumes with a thermal broadening of the width of each distribution, and with an energy barrier which has to be overcome for the transition to occur. However, real-time TEM revealed rather a smooth and continuous increase in the island size with time, which was explained by an anomalous coarsening, see Fig. 147 [140].

Following [140], one may note that pyramidal islands with given shapes and a facet angle α , have a typical elastic and surface energy given by

$$E \propto \alpha^{4/3} V^{2/3} - \alpha V. \quad (68)$$

Their chemical potential $\mu \sim \partial E / \partial V$ is therefore merely $\mu \sim \frac{2}{3} \alpha^{4/3} V^{-1/3} - \alpha$. When the growth dynamics is limited by attachment of adatoms to the island perimeter, the mean-field coarsening equations lead to [140]

$$\frac{dV}{d\tau} = V^{1/3} \alpha^{-1/3} (\bar{\mu} - \mu), \quad (69)$$

with $\bar{\mu}$ a reference chemical potential allowing to satisfy mass conservation. The discontinuity in μ when the shape transition occurs results in an anomalous coarsening dynamics [140]. This drop, which occurs once islands change their shape after some critical volume, accelerates the coarsening of the largest islands so that the bimodal island size distribution is only a transient [140,132].

Real-time observations [132] showed that many small islands shrink and dissolve instead of having all islands growing, and that islands evolve with a slow transformation via transition states. It was argued that intermixing which allows a significant strain release in the islands, favors a change in the favored island shape [321,133]. More recently [320], a detailed statistical analysis of island properties showed that the critical size dividing shrinking from growing islands corresponds to the pyramid to dome transition, as predicted by the anomalous coarsening hypothesis, see Fig. 149. Moreover, the reverse sequence of states of growing and shrinking islands, see Fig. 148, indicate the island shapes are thermodynamically determined. Note that the coarsening analysis is complicated by its sensitivity on the growth conditions [133]: the coarsening at work in these systems is not described by the usual Ostwald ripening theory and can be best observed for a given temperature and annealing time before steady states occur. One can define a critical volume for the pyramid to dome transition which corresponds to the volume above which pyramid transform into dome and the critical size which distinguish shrinking and growing islands [320]. This volume was shown to depend on coverage [131], and it was shown numerically to depend on anisotropy [380]. It also depends on the average strain [131,379] and the simple scaling resulting from the competition between surface and elastic energy leads to $V_c^{1/3} \sim \gamma/m^2$, which describes well the experimental results [131].

4. Substrate design and self-organization

The previously described quantum dots grown on nominal substrates naturally display large size distribution and low spatial order which may destroy the desired quantum dot properties [299]. A way to produce better ordering consists in growing films on a pre-patterned substrate. Indeed, the spontaneous formation of periodic domain structures with microscopic periodicity offers the possibility to control the self-organization of quantum dots growing on such patterns, and to achieve better morphological properties. The typical features of quantum dots rely on the electronic properties of

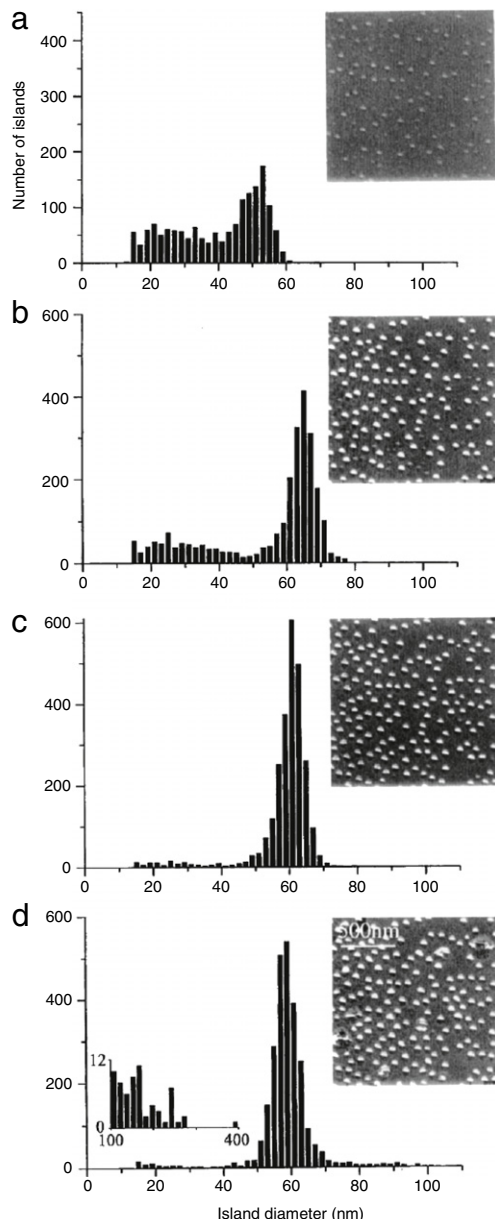


Fig. 147. Images (inset) and histograms obtained during Ge deposition from 2×10^{-7} Torr di-germane at a substrate temperature of 640 °C. Images were obtained (a) 21 s, (b) 51 s, (c) 98 s, (d) 180 s after “nucleation” (i.e., the time at which distinct strain contrast is first seen). Nucleation occurred after a dose of approximately 50 L of di-germane. The flux remains on during this sequence. The low contrast from the smallest islands is responsible for the cutoff at about 15 nm diameter. In (d) the inset histogram shows the very large islands making up the tail of the distribution.

Source: from [140].

zero-dimensional systems which enforce the nanostructures size to lie within a given range. A lower size is imposed by the constraint that the confinement potential should have at least one localized state. Second, the larger size limit arises from the energy-level spacing which should not be too small to avoid thermal smearing and evaporation of carriers from the dot. Well ordered structures with laterally controlled features have a good potential as templates to produce a controlled self-organization. Various ways were followed to achieve substrate patterning and may distinguish patterns created by full scale spontaneous growth processes and patterns fabricated by nanotechnological tools.

Five classes of spontaneously formed nanostructures which serve as templates for subsequent growth (which are called nanopattern or nanostructure) may be distinguished following [373], see Fig. 150. These nanostructures are periodically faceted surfaces, Fig. 150(a), periodic structures of planar domains (monolayer high islands), Fig. 150(b), ordered arrays of three-dimensional coherently strained islands in lattice-mismatched heteroepitaxial systems, Fig. 150(c), multi-sheet arrays of two-dimensional islands, Fig. 150(d), and multisheet arrays of three-dimensional islands, Fig. 150(e). A common feature

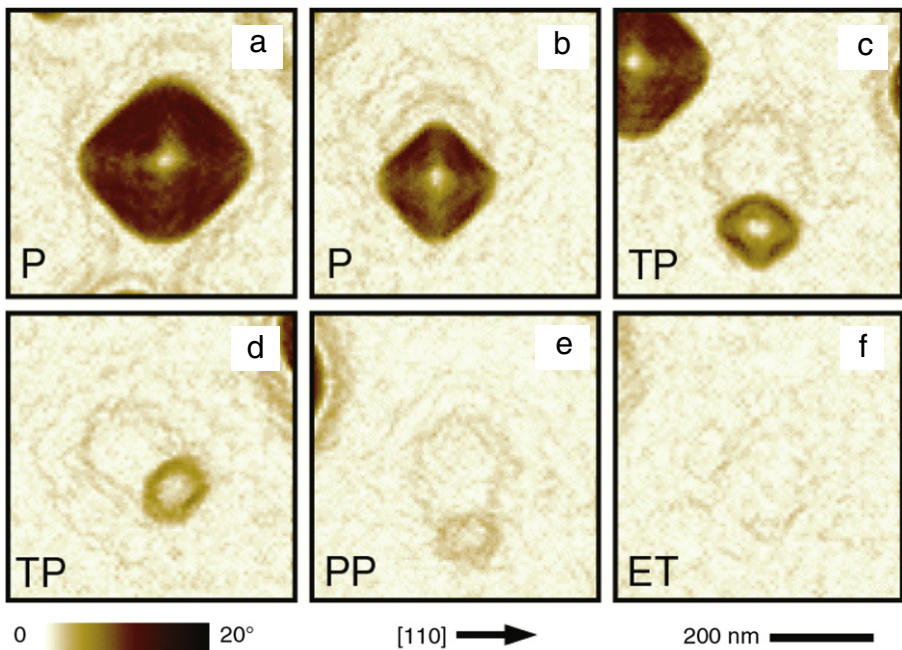


Fig. 148. (Color online) Sequence of AFM magnifications illustrating shrinking pyramids and the pyramid-to-prepyramid transition occurring with decreasing volume during the ripening process. Images have color scale according to local surface slope with respect to the (001) plane. Source: from [320].

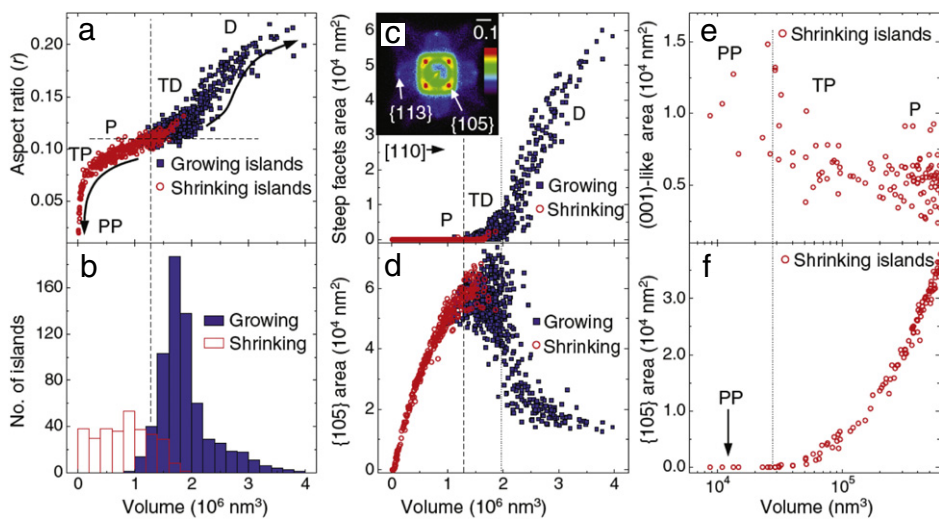


Fig. 149. (Color online) Statistical analysis of islands contained in the sample grown at 840 °C: (a) Shape (aspect ratio r) vs volume and (b) histogram of volumes. The area of (c) steep, (d), (f) {105}, and (e) shallow facets vs volume were computed from the “facet plot” [381] (with logarithmic intensity) shown in the inset of (c). They show that prepyramids (PP), truncated pyramids (TP), and pyramids P are shrinking, while truncated domes (TDs) and domes (D) are growing, and that the critical size distinguishing shrinking and growing islands corresponds to the P-TD shape transition. Source: from [320].

of these nanostructures is the long-range elastic interactions induced by the periodic ordering which further drives the QD growth. The elastic strain field is created by the discontinuity of the intrinsic surface stress tensor on the domain boundaries and/or by the lattice mismatch between two materials.

4.1. Lithographic patterning

In order to control the positioning of individual islands, several groups have developed templates using lithographic patterning, such as UV-interference lithography or focused ion beam patterning [382–387,119]. In all cases, the islands are

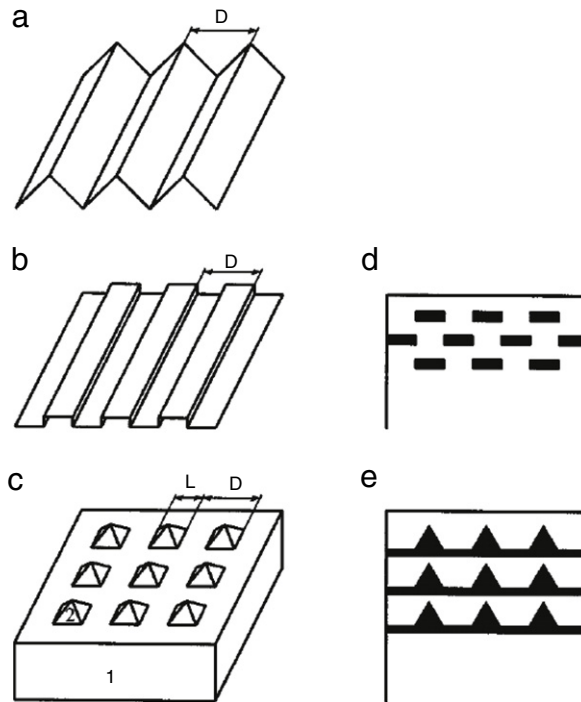


Fig. 150. Various classes of spontaneously ordered nanostructures: (a) periodically faceted surfaces; (b) surface structures of planar domains; (c) ordered array of three-dimensional coherently strained islands (2) lattice-mismatched to the substrate (1); (d) cross-sectional scheme of a multisheet array of two-dimensional islands; (e) cross-sectional scheme of a multisheet array of three-dimensional islands.
Source: from [373].

organized around or in the patterns. The smallest island size and separation which can be achieved with these techniques are $d \sim 40$ nm and $L \sim 80$ nm. New strategies based on a combination of ordering and size control were recently developed. In all cases, island nucleation is controlled by the interplay between kinetic and energetic parameters. Before describing the various patterning processes, we first give an overview of the theoretical issues concerning the preferential nucleation of Ge islands on a geometrically patterned substrate.

4.1.1. Simulations

The basic ingredients ruling island localization on a modulated pattern are the elastic relaxation and surface energy cost [388]. The resulting surface chemical potential ruling adatom diffusion is given in Eq. (6). The surface energy part, proportional to the curvature, favors diffusion towards convex parts of the surface, i.e., within trenches or holes. In faceted holes, the favorable positions are the intersections between facets. In view of the surface curvature alone, the hole bottom is favored. In this position, however, the possibility of lateral strain relaxation is rather limited [388]. On the contrary, the stress part in Eq. (6) favors mass diffusion towards concave areas, i.e., on top of ridges, mesas and patterns, due to a more efficient relaxation. It should also favor dot positioning on tensile-strained surface areas. From an energetic point of view, the dot positioning results from the competition between these two effects which should depend on the pattern geometry: while growth of dots at the four intersections of the facets within the holes is promoted by surface curvature, nucleation at the four edges of the hole is promoted by strain relaxation [388].

Equilibrium. The energetic features of a film deposited on the surface of an array of V-shaped grooves separating mesas of small size was considered in detail in Ref. [389]. The effect of different design parameters was investigated, such as the distance D separating two neighboring groove bottoms (which is not the mesa width), the groove depth d and the facets orientation: (111) facets were first considered and then smoother and sharper ones. The nanomesas considered in this study are typically separated by 7 to 25 nm which is about one order of magnitude smaller than the patterns obtained by classical lithography. This small mesa size, which is comparable to the size of the islands which nucleate on a flat Si substrate, leads to quite specific results. The model in [389] includes an atomistic description and uses a Keating's potential to describe elastic relaxation. Surface energy is included by attributing to each dangling bond an energetic cost and by minimizing the dangling bond number. The results of this analysis show that both wetting, surface energy anisotropy and relaxation are crucial parameters. Different configurations were investigated. Two typical behavior were found: one where Ge atom are more stable on tops of mesas and the other one, where they tend to fill the grooves. In fact, in the case of (111) groove facets, the key parameter is not the groove aspect ratio but its depth, indicating that anisotropy has also an important effect. In the case of smooth facets, Ge atoms either decorate the top of the groove facet before filling it or before being localized on top

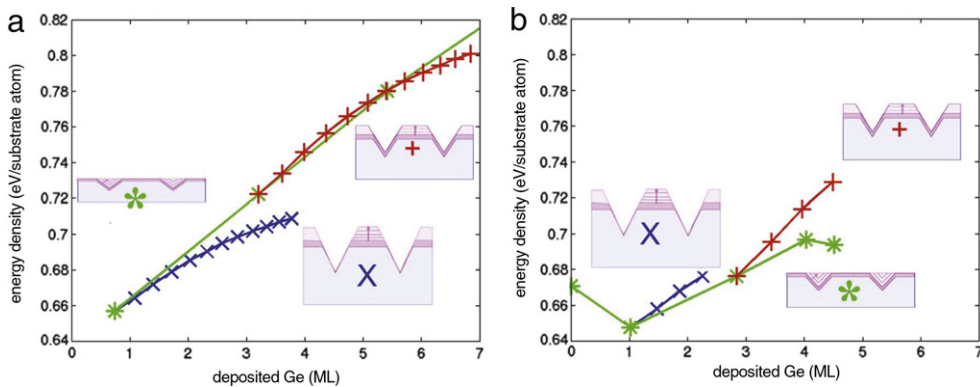


Fig. 151. Energy density variations for different growth processes: (*) groove filling, (x) growth on top of mesas, (+) deposition of an atomic bilayer followed by the growth on top of mesas. (left) $W = 15.36$ nm, in this case the growth is strictly located on top of mesas; (right) $W = 7.69$ nm, in this case Ge is first filling the grooves.

Source: from [389].

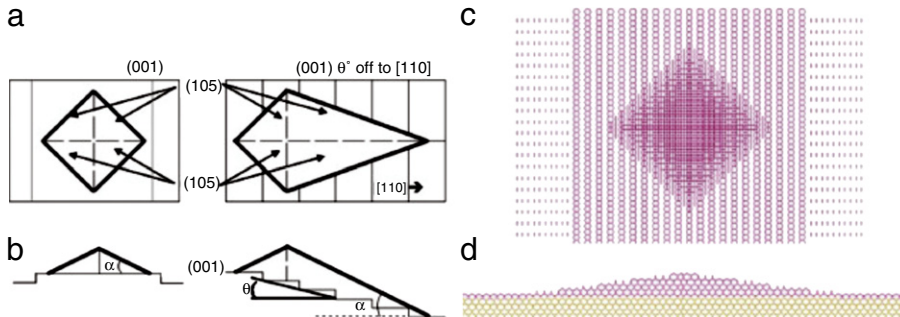


Fig. 152. (a) Top view and (b) side view of a pyramidal island with (105) facets located on the terrace between two holes (left) and on the side of the hole (right). (c) Top view and (d) side view of the simulated structure consisting of a Ge island on top of the $2 \times 1-1 \times 2$ reconstructed Ge WL (between pits) itself on top of the Si substrate.

Source: from [390].

of the mesa. In the case of sharp facets, Ge atoms accumulate first at the groove bottom before either growing on the top of mesas or filling grooves. Moreover, this study reveals a strong effect of the width between two patterns in the case of (111) faceted grooves (Fig. 151). When $W = 15$ nm, the growth on top of the mesas is energetically favored (Fig. 151(a)) while for smaller $W = 7$ nm, the filling of the patterns is energetically favored (Fig. 151(b)). Note that the groove aspect ratio has almost no effect on the dot location. As a consequence, in the case of well faceted V-shaped grooves separating mesas of small size, depending on the pattern geometrical parameters and the side wall facetting, either well-separated Ge dots or partial or full coverage of Ge can be obtained [389].

Equilibrium simulations. In order to better elucidate the energetic balance at the origin of a pattern-induced ordering, Monte-Carlo (MC) simulations of an island lying on a modulated substrate were performed in Ref. [390]. The continuous-space MC analysis simulates the equilibrium structure, stress state, and energetics of a Ge island on a patterned Si(001) surface. Atomic interactions are modeled using the Tersoff potential for multicomponent systems. Bonding and strain fields induced by the Si(001)- 2×1 surface reconstruction are accurately described when the top of the wetting layer and the island facets have a 2×1 reconstruction. In this empirical scheme, one computes the system cohesive energy E resulting from the Gibbs free energy minimization at finite T which can be decomposed into atomic contributions. This property allows to define energy-dependent atomic level quantities and the key quantity is the atomic level stress, related locally to the stress field and defined by $\sigma_i = -dE_i/d\ln V$ where E_i is the energy of atom i [391]. The σ_i 's may be summed up over a specific region to yield its average level stress. Since atomic energies encompass all possible contributions, including surface energies, the atomic level stress describes the driving factors governing island nucleation and growth. The simulated structures concern Ge islands on top of a Ge WL and a Si substrate in the (001) orientation, with a pit pattern representing the holes produced by lithography (Fig. 152). The pit walls are modeled by trains of monolayer high steps. It is assumed that islands nucleate along this sequence of steps in agreement with experiments evidencing nucleation at the step edges of the silicon surface [119]. For the sake of simplicity, only pyramidal-shape islands were considered. Islands located in the middle of terraces between pits display a square base with (105) facets, whereas islands located on the steps are elongated perpendicular to the step edges in order to preserve the (105) faceting enforced by the surface energy minimization [392]. The relevant geometries are portrayed in Fig. 152(a) and (b) which show the top view and side view of a simulated cell. The base of the island is oriented

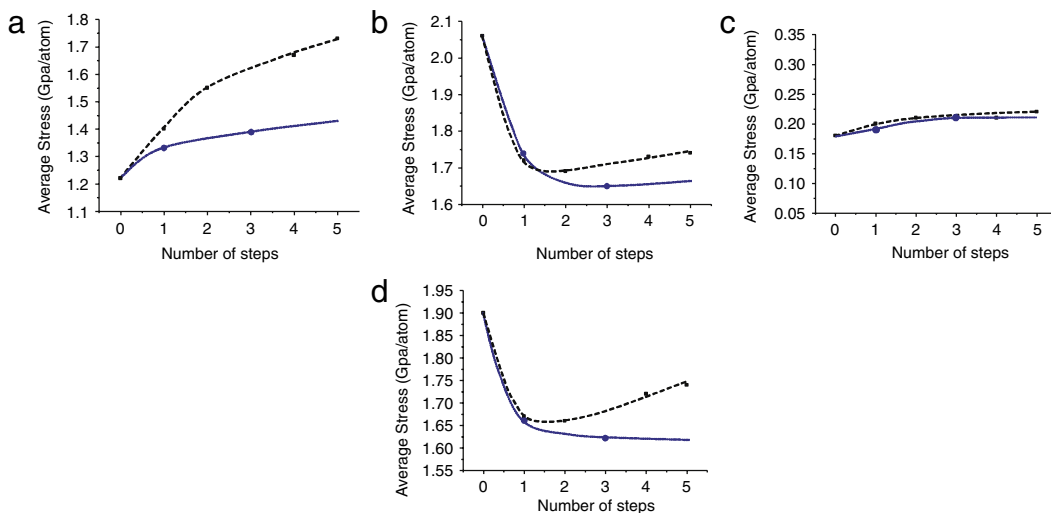


Fig. 153. Analysis of stress state in the various components of the QD structure: (a) island, (b) wetting layer, (c) substrate; (d) complete structure. Values for structures with islands located on the hole side (terrace) are denoted by black squares (blue circles).
Source: from [390].

with an angle of 45° with respect to the dimer rows of the WL. The top layer of the WL and (105) faceted pyramids are reconstructed in the usual 2 × 1 dimer configuration. The pit walls consist of alternating S_A and S_B steps (T_A and T_B terraces) with dimer rows running parallel and perpendicular to the step edges respectively. The width of the WL is 3 ML, while the Si substrate consists of 8 ML and the epitaxial strain is imposed by constraining laterally the cell to the Si lattice parameter with periodic boundary conditions. Atoms are free to relax in plane by moving to their lowest-energy positions while both lattice and atomic relaxations occur vertically. The evolution of the total stress with the depth of the holes (or equivalently the number of steps) in the structure (including the QD, the WL, and the substrate) are depicted in Fig. 153. The resulting trends with an increase in the hole depth are clear and can be expected to hold for deeper holes as well. The comparison of the average stress of a dot located on a terrace between holes, with a dot located in a hole along the sequence of steps exhibits two remarkable aspects (Fig. 153). First, the compressive stress in all structures involving a patterned surface is drastically reduced with respect to the nominal stress (QD on the flat surface without patterns). For example, when pits are only one step deep, stress is reduced by ∼13%, corresponding to a drop in energy of ∼0.04 eV/atom which is quite significant compared to thermal energies. Second, for patterns consisting of 2 or more ML-high steps, islands have a lower energy and prefer to locate on the terraces between the pits rather than on the stepped pit walls because of a considerable decrease in the average energy and stress in the grown overlayer. This suggests that islands grown in the pits are metastable structures which are not promoted by energy minimization of the structure [390].

Kinetics. In fact, the QDs produced during heteroepitaxy are not necessarily equilibrium configurations but may depend crucially on the kinetics of their growth. The spatial order of these dots thus depend on the ability to direct the a priori random nucleation process. This may be commonly achieved by generating surface strain gradients or by using steps, step bunches, or patterned topographic features. In general, the criticality of nucleation is determined by the competition between strain energy and surface energy. There can be also an edge energy term but it is usually negligible in Si/Ge systems. Two key issues are still under debate: what is the effect of patterns on the island nucleation barrier and what are the parameters which control island nucleation on patterns?

In order to estimate kinetic energy barriers of nucleation, a basic energetic calculation on a sawtooth pattern, which may or may not be a facet, was developed in [393]. As usual, the strain energy difference between the island and the uniformly strained film, may be computed using the half-plane Green function within the small-slope approximation,

$$E^{el} = -\frac{\sigma^2}{2} \int \int dx dx' G(x-x') \partial_i h(x) \partial_j h(x') \quad (70)$$

where σ is the bulk stress in the island, x , the position along the surface, and G , the Green function relating the displacement at $h(x')$ induced by a force at $h(x)$. When considering only the force monopoles induced by the film thickness variation, i.e. $\partial_i h(x)$ and neglecting the force dipoles induced by the surface waviness, $E^{el} = -\epsilon_0 S(\tan \theta - \tan \phi)$. Accounting for the surface energy created by the island, the total island formation energy is

$$E = -\epsilon_0 S(\tan \theta - \tan \phi) + 2\Gamma S^{1/2}(\tan \theta - \tan \phi)^{1/2}, \quad (71)$$

where $\epsilon_0 = 2 \ln 2 \sigma^2 (1 - \nu^2) / \pi Y$ is the scaled elastic energy density, $\Gamma = (\gamma_f \sec \theta - \gamma_w \sec \phi) / (\tan \theta - \tan \phi)$ with γ_f and γ_w , the surface energy of island facets and wetting layer respectively. The competition between the strain relaxation which

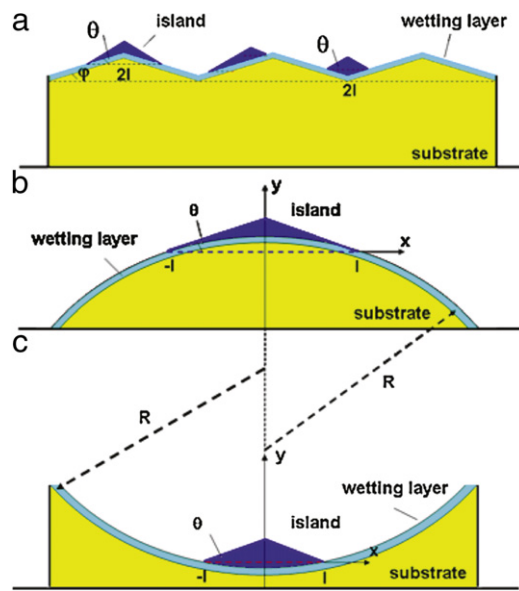


Fig. 154. Schematic illustration of island nucleation: (a) on a saw tooth patterned substrate; (b) on the apex of a concave surface; (c) in the valley of a convex surface.

Source: from [393].

is positive and the surface creation energy which is negative defines a critical island size $S_c = (\Gamma/\epsilon_0)^2/(\tan \theta - \tan \phi)$ and an energy barrier $E_c = \Gamma^2/\epsilon_0$. The wetting layer surface energy γ_w may be considered to be function of the surface slope ϕ following $\gamma_w = \gamma_0 [1 - \alpha \cos(n\phi)]$ where α quantifies the surface energy anisotropy and n defines the angle of low-energy facets. Naturally, both S_c and E_c decrease when the anisotropy α increases as the surface energy cost decreases.

In the case of an isotropic surface energy, for a given slope of the patterns and island facets, the analysis in [393] shows that both S_c and E_c are smaller in the valley than on the apex proving that in this situation, valleys are kinetically-favored nucleation sites. The result is explained by a more effective strain relaxation for islands in the valley than on the apex when surface energy has a minimal effect. This is due to the geometrical effect related to the smaller thickness variation on the apex compared to the thickness variation in the valley, see Fig. 154. Consequently, island strain is more relaxed in the valley than at the apex, by geometric factors $\tan \theta + \tan |\phi|$ and $\tan \theta - \tan |\phi|$ respectively.

This counterintuitive result originates from the minimization of the elastic kinetic barrier [393]. In the case of a highly anisotropic surface energy (large α), S_c and E_c become smaller both in the valley and on the apex than those on a flat substrate. For a given set of parameters, the larger the anisotropy strength α is, the smaller S_c and E_c are. This indicates that if surface patterns are steeper, the strained islands preferentially nucleate on the apex or in the valley rather than on a flat region. In these conditions, the driving force is different since island nucleation on the apex is favored by surface energy anisotropy, while nucleation in the valley is favored by both strain and surface energy effects [393]. The high sensitivity in the surface energy anisotropy provides a critical role to the local surface curvature (i.e. step density) on the position of nucleation sites. This argument was used to explain the nucleation of islands sometimes at pattern sidewalls [394] or at their edges [395,396]. However, these theoretical predictions are to be confronted to experimental results obtained on mesas where islands nucleate preferably on the edges of the mesas i.e. on the concave parts of the surface as explained in the following [397,394].

In order to further investigate the growth dynamics and especially island nucleation, kinetic Monte-Carlo simulations are valuable in order to describe atomic processes. The sole effect of diffusion barriers was investigated using KMC simulations of Ge island nucleation but without elastic relaxation [398]. In the case of a patterned substrate, an additional diffusion barrier E_D may be introduced in the basic energy barrier of the well known solid-on-solid model equation (23) which now reads $\Delta E = E_S + nE_N + E_D$. The extra barrier E_D depends both on the hop direction and on the lateral position of the adatom on the surface and its strength is given by the distance of the adatom from the boundary [398]. With this basic description in hand, it is found that a periodic inhomogeneity in the activation energy for adatom diffusion significantly alters the nucleation process and, in specific narrow conditions, the nanoscale patterning can lead to the formation of an ordered array of 2D islands with a narrow size distribution. The simulations also indicate that the confinement effect of the patterned substrate is strong in a narrow temperature range. The length scale of the substrate pattern determines the optimal growth temperature (and alternatively the particle flux) at which the fluctuations in island size reach a minimum value. The variation of island nucleation with the temperature is illustrated on Fig. 155. Increased island ordering and size homogeneity are clearly visible at intermediate temperature [398].

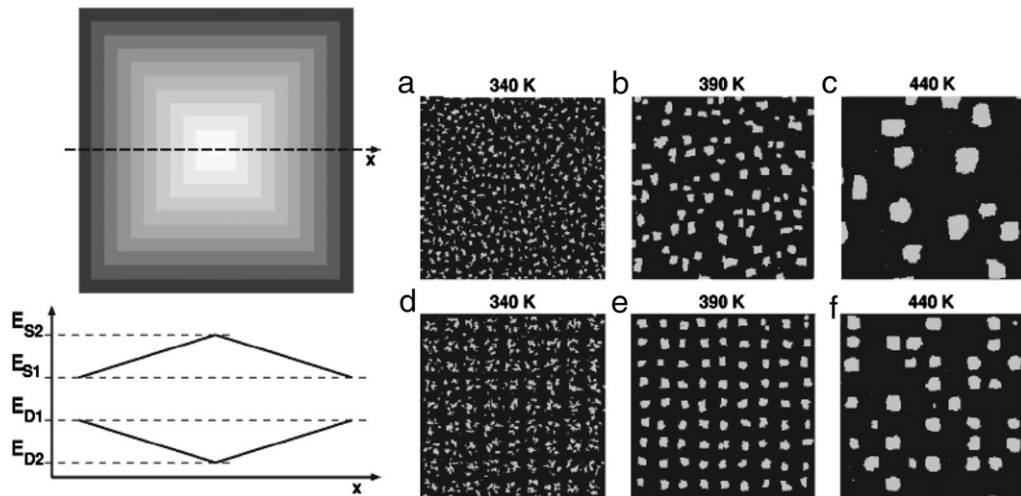


Fig. 155. (Left) Schematic representation of the diffusion activation energies inside a single domain on the patterned substrate (top) and the corresponding variations of the simulation model parameters E_S and E_D when traversing through the cross section of the domain (bottom); (Right) Island morphologies obtained at three different temperatures for the homogeneous substrate (a)–(c), and for the patterned substrate (d)–(f).
Source: from [398].

KMC simulations were also performed for a patterned substrate with denuded areas produced by the circular diffusion barriers in order to depict some experimental conditions [399]. In this situation, Ge adatoms deposited onto the barrier are incorporated into the barrier and discarded while Ge adatoms which migrate to the barrier edge are reflected. Moreover, Ge islands overlapping the barrier are partially incorporated into the barrier and the island size is subsequently decreased (as an island grows, its center of mass describes a random walk which may extend into the denuded zone). The results show that when the radii of the denuded zones are comparable with their separation, no island ordering occurs at the center sites. However, when the diffusion barriers are close, islands begin to order. Ordering is more pronounced when the diffusion barriers are separated by approximately 1/3 of their radii. As the barrier separation distance decreases, the nucleation-allowed areas are localized near the center sites. The physical origin and actual strength of the diffusion barriers are not fully described but chemical potential changes across the surface may be invoked to rationalize the formation of denuded zones [399] (Fig. 156).

More recently, an hybrid Kinetic Monte-Carlo simulation accounting for elastic relaxation was developed in order to expand the typical length and time scales treatable in standard KMC and to further explore the ordering and homogeneity of Ge islands grown on pit-patterned Si(001) [400]. The dependence of ordering and homogeneity on key parameters such as temperature, deposition flux and pit spacing was analyzed. In this model, the adatoms are described as in a standard KMC model which describes island nucleation, island coalescence and atomic detachment. The latter occurs only for atoms along the island perimeter through a thermally activated process. Its energetic barrier is assumed to be equal to the energy of an atom inside an island which includes chemical bonding and elastic relaxation. The latter is included in the model as a chemical potential term $\mu^{el}(V)$ which depends on the island volume V . The effective detachment rate R_{det} for an island of volume V is taken as $R_{det} = N_p(V)v_0 \exp\left\{-[E_S + nE_N - \mu^{el}(V)]/k_B T\right\}$ where N_p is the number of atoms along the island perimeter and v_0 is an attempt frequency. Three typologies are distinguished: small 2D aggregates, {105} pyramids and domes. Small atomic aggregates, which may not be considered as three-dimensional, are assigned a vanishing elastic chemical potential and are assimilated to 1 ML high cylinders with perimeters enforced by the conservation of atomic volume. Pyramids and domes are treated differently with a size-dependent chemical potential $\mu(V)$, set as $\mu_{dome} < \mu_{pyra}$ reflecting the increased elastic-energy relaxation in domes. The results exhibit the same trends with temperature and flux than those reported previously in [398]. Three different growth regimes arise: at low temperature (or high flux F), there is no positional order and islands are non-uniform in size. When the temperature increases (or when F decreases), selective nucleation is achieved: mobility is now sufficient to enable nucleation in the energetically most favorable sites (which are fixed by the model at the center of the pits), ensuring the desired positional order. If the temperature is further raised, Ostwald ripening between islands in different pits becomes dominant and reduces the size homogeneity and island ordering [400].

In conclusion, if the presence of a gradient of chemical potential (which encompasses elastic and surface energy) and of diffusion barrier favors the nucleation of islands correlated with the patterns, further discussion and investigation should be devoted to the interplay between different mechanisms, and to the origin of the spatial ordering, especially as regards the competition between kinetics and energetic effects. As discussed below, the presence of impurities should also be examined. In the case of lithography, the presence of carbon inside the pits was reported in various situations. While the effect of this contamination is commonly considered as negligible, it could be at the origin of Ge islands preferentially nucleating inside the pits [388,398]. We also report below the large impact of impurities on additional diffusion barriers [399].

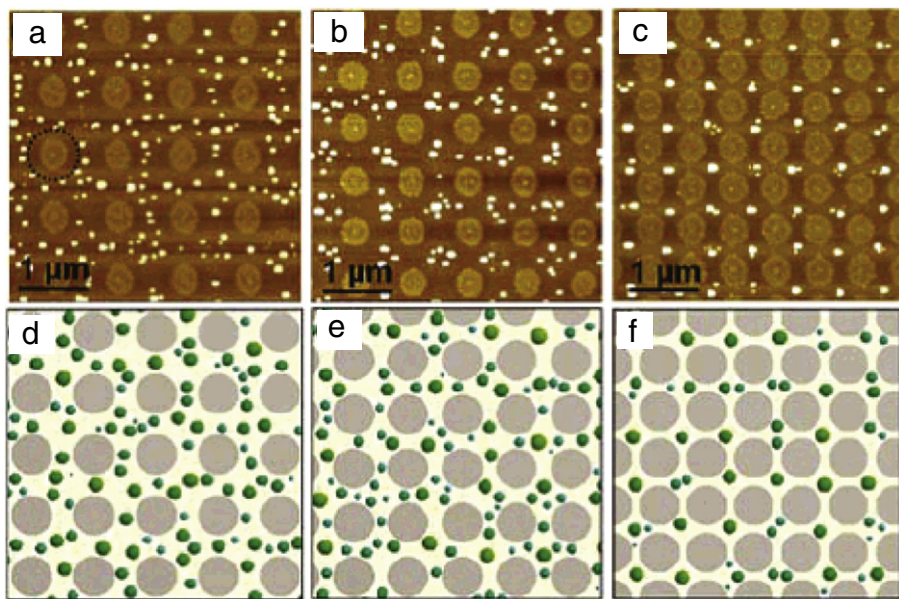


Fig. 156. Effect of Au-pattern spacing on Ge island ordering observed by AFM (a, b, and c): (a) the Au spacing is more than twice the denuded zone radius (R_d), and Ge islanding occurs around each Au-site; (b) the Au-spacing is slightly larger than R_d ; (c) the Au spacing is approximately R_d and almost one island-per-site ordering is obtained. Growth and nucleation of 3D islands determined by KMC simulations result in the corresponding island distributions shown in (d), (e), and (f).

Source: from [399].

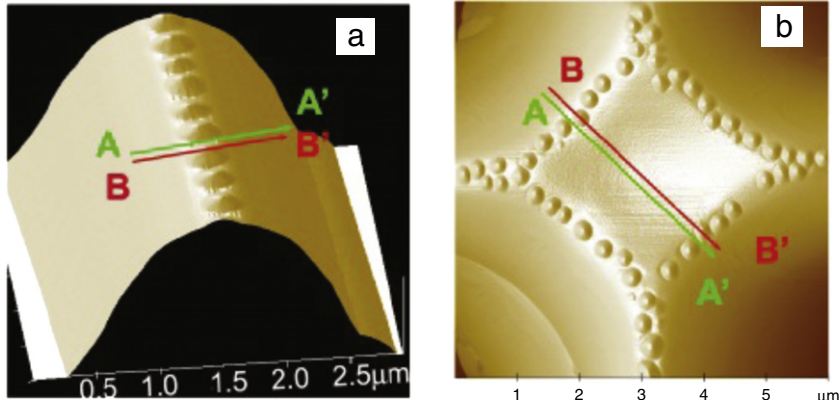


Fig. 157. AFM images of Ge 3D island ordering on patterned Si(001) structures: (a) a stripe ridge; (b) a diamond-shaped stripe cross.

Source: from [396].

4.1.2. Conventional lithography

Ordering of Ge islands on patterned Si wafers using optical lithography was first proposed by Kamins et al. [395]. The size and position of Ge dots on patterned wafers was found to depend on the window size [23]. It was observed that lateral ordering of Ge islands along the [100] directions can be obtained by depositing Ge islands on high index Si facets generated by selective epitaxial growth, and the islands order in one-dimensional rows. It was suggested that under appropriate conditions, {01h} crystallographic planes are energetically more favorable for island nucleation compared with nucleation on the (001) plane [401]. Crossed stripes with a 2 μm top width and etched to a depth of 2.5 μm were performed in the micrometer range on Si(001) via conventional lithography. Their orientation does not influence the Ge QD alignment. Ge is deposited on top of the patterned substrate. The results show a regular alignment of Ge dots on the stripes and mesas (Fig. 157) with nucleation in the most concave part of the surface [396].

Preferential nucleation may be described by the generic chemical potential equation (6). Convex regions with negative curvature have a smaller surface chemical potential compared to concave regions with positive curvature. Hence, based on the sole surface-energy contribution, the convex part is expected to be the most favorable region for island nucleation and growth. On the contrary, the Ge wetting layer is under compressive strain because of the lattice mismatch between Ge and Si. The concave regions are more favorable for strain relaxation and are therefore associated with a smaller elastic

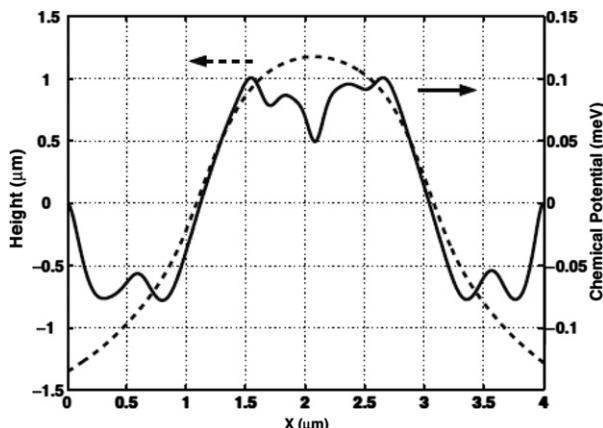


Fig. 158. Variation with position X , of the local surface chemical potential on a stripe structure. The dashed line is the surface profile measured by AFM. Source: from [396].

chemical potential which opposes the contribution from the surface curvature [396]. Microscopically, the effects of both surface curvature and strain may be explained in terms of atomic bonding; in a concave region, an atom has fewer neighbors and its chemical-bonding is smaller, increasing the surface chemical potential. On the other hand, its strain relaxation is larger, as the compressed Ge atoms can stretch out more easily, decreasing the elastic chemical potential. Thus, a curved strained film, partially relieves its strain in the concave regions, contrarily to the compression in the convex regions. It is assumed that the Ge wetting layer follows the shape of the underlying pattern. The local strain-relaxation energy relative to a flat film may thus be expressed as [396]

$$E^{el} = -\frac{C}{2} \left\{ \frac{\kappa}{|\kappa|} [\kappa(z_s - z_0)]^2 - \epsilon^2 \right\}, \quad (72)$$

where C is an elastic constant, $\kappa(z_s - z_0)$, the strain of the Ge film with z_s the position of the top surface, z_0 , the position of the neutral plane of the bent film and ϵ , the misfit strain between the bent film and the substrate. The calculation of the chemical potential shows multiple local minima due to the competition between the surface-energy and strain-energy terms (Fig. 158). The surface energy term produces minima in convex regions at the stripe foot, and maxima in concave regions on the top ridges of the stripes while the strain-relaxation term produces local minima in the most concave regions on the top ridges of the stripes. It is found that the positions of these local minima agree well with the localization of Ge islands observed in experiments on the top ridges of the stripes. One can notice that the local minima on the concave areas are narrow and relatively deep, suggesting a good alignment and size uniformity of islands at these positions.

Holographic lithography was also used to perform 2D pit-patterned Si templates, with periodicity in the sub-micrometer range on a centimeter-scale field. The deposition by solid-source MBE at 620 °C of Ge on these surfaces leads to the regular self-organization of islands at the bottom of the pits. It is shown that a unimodal distribution of islands with dominant (111) facets and moderate aspect ratio (~ 0.37) can be achieved using such a process, see Fig. 159(c) [402]. It was explained on the basis of finite element calculation and molecular dynamics simulations which showed that islands in pits can have a lower misfit strain with respect to islands with the same shape but on a flat substrate [402]. In a complementary geometry where Ge islands are grown by MBE at 620 °C on a hill-patterned template, islands appear to nucleate as pairs in the V-shaped troughs between neighboring hills as a result of energy minimization [403]. However, TEM cross-section image of dome islands nucleated in the pits, see Fig. 159, seem to indicate that they are partially relaxed by dislocations. The position of the islands was ascribed to a decrease in the elastic energy. Similarly, islands grown on the grooves resulting from the trenches that form spontaneously around large islands, are also centered near their equilibrium position when grown by MBE at 740 °C [404].

Ordered arrays of Ge islands on prepatterned Si(001) surface were also obtained using interference lithography for pre-patterning and subsequent growth by CVD. Si(001) substrates were spin-coated with photoresist and illuminated for UV optical interference lithography (UV-IL) using a laser beam at 325 nm wavelength [405]. Subsequently, the resist was developed and the pattern was transferred into the substrate by reactive ion etching (RIE). The patterns form arrays of holes 10–30 nm deep, with a periodicity of about 300 nm and an occupation probability for single Ge islands in patterned holes of almost 100% [405].

4.1.3. e-beam lithography

In order to locate dots intentionally at desired positions, e-beam pre patterning was widely investigated. The process consists often of e-beam lithography, etching and partial overgrowth on the substrate, forming trenches, holes, ridges or mesas that act as preferential nucleation sites for dot formation [406]. As seen in Section 4.4.2, an alternative method

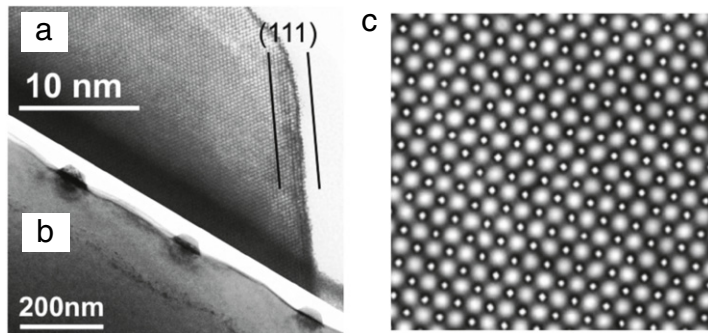


Fig. 159. TEM cross-section of the Ge dome shaped islands which exhibit the presence of (111) facets on their side (a) and their ordering on the bottom of the patterns (b); (c) Corresponding AFM image of the sample on $5 \times 5 \mu\text{m}^2$ large scale.
Source: from [402].

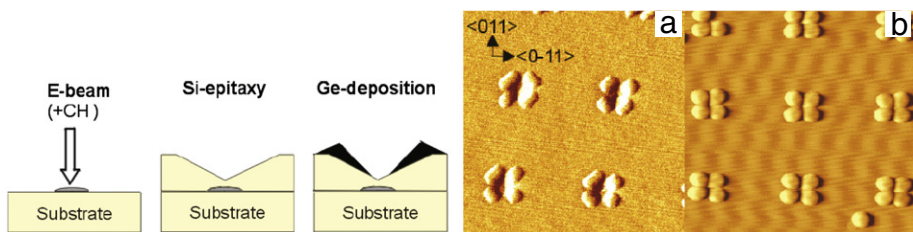


Fig. 160. Schematic representation of the combined e-beam lithography/Si pits patterning process and the corresponding AFM images of Ge islands (a) huts and (b) domes ordered inside the Si pits.
Source: from [388].

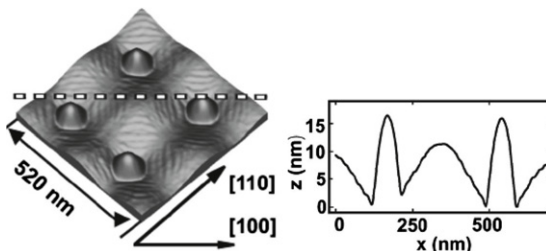


Fig. 161. AFM image (left) of the prepatterned Si substrate with 5 ML of Ge. (right) Line scan in [100] direction along the dashed line in (a).
Source: from [408].

is to use electron-beam-induced carbon deposits as growth masks which are deposited on H-passivated Si substrates by electron-beam lithography. In this case, SiC clusters are formed during annealing which can either directly control the self-organization of Ge dots by chemical effects (C-effect), or form Si pits during overgrowth on the C-mask (See Fig. 160.) [388, 407]. The pits serve as nucleation centers during the subsequent Ge deposition, and faceted pits of Si are formed during the MBE Si overgrowth on the C masks. Pits develop {11n} facets, with n increasing with increasing Si deposition. In this case, it is expected that only the geometrical shape of the pits controls the nucleation of Ge dots (and therefore the chemical effect of C becomes negligible) [388]. The results show a selective nucleation of Ge dots in and around the pits with first the onset of nucleation at the intersection between the {11n} facets in the pits and the formation of quadruples pyramid-shaped Ge dots. Transformation in dome-shaped Ge dots is observed after further supply of Ge (as is observed on a flat nominal Si(001) substrate).

In other studies, prepatternd Si(001) substrates were obtained by e-beam lithography and subsequent reactive ion etching (RIE). Patterns obtained by this process have commonly a large periodicity and a small aspect ratio ($h/L \sim 0.05$ with a side slope of about 8°). In these conditions, the pattern field is limited to sub-millimeter scales. After the RIE process, an ex-situ RCA cleaning and an in-situ thermal treatment at 900°C were performed before growth. It should be noted that the thermal annealing commonly produces the formation of C-clusters in the pits. A thick (> 100 nm) Si buffer layer is systematically grown prior to Ge deposition in order to reduce the impurities on the surface and the roughness induced by RIE, while preserving the pattern shape [408]. An example of the Ge domes islands ordered on the ultra-shallow e-beam patterns is given in Fig. 161.

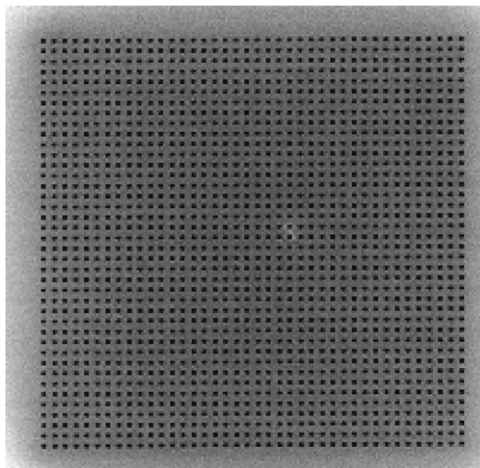


Fig. 162. AFM image of the patterns after Ga removal and perfect cleaning, just before the introduction into the growth chamber.

Initially, the e-beam patterning was used to create windows into a SiO₂ sacrificial layer. The aim is to impose the nucleation of Ge dots inside the windows. In this situation, the terminology “self-assembly” may not be applied since there is no Ge adsorption on SiO₂ during CVD growth. The patterning process involves a first step of thermal oxidation of the Si(001) substrates to form ~300 nm-thick SiO₂; in a second step, stripe and circular windows with size of about 500 nm are patterned by electron-beam lithography and processed by reactive ion etching. During the third deposition step, the Ge adatoms stick only to the Si substrate (inside the windows) and not to the oxide layer. In a last step, the SiO₂ layer is removed leaving the Ge dots ordered on the Si substrate [409].

4.1.4. Focused ion beam

In this section, we describe an original approach to form self-assembled Ge dots on Si(001) based on the combination of focused ion beam nano-patterning and spontaneous formation of QDs on the patterns. With this technique, one can adjust different parameters (hole pitch, size, ...) to control the spontaneous formation of islands. Depending on the growth temperature, different mechanisms may be evidenced. At low temperature, QDs form inside the pits, while they form in the concave areas close to the pits at high temperature. These behavior may be explained by kinetically limited nucleation at low temperature and stress induced nucleation at high temperature as explained in the following.

The main steps of the process consist of: (i) FIB nanopatterning on $10 \times 10 \mu\text{m}^2$ areas located by lithographic patterns; (ii) restoring process of the patterned sample; (iii) formation of Ge QDs. FIB patterning was carried out directly on the Si(001) substrate. Milling investigations were performed with a dual FIB system in order to minimize the possible gallium implantation during image grabs required for target area location. The FIB instrument is equipped with a gallium liquid metal primary ion gun. With such a field emission gun, the minimum spot size is ~10 nm and the brightness is very high. Both features combined with the ion mass and the energy used allow a sharp and fast milling of silicon. FIB at normal incidence angle with impact energy of 30 keV and 1 pA primary current was used for milling.

After FIB milling, presence of Ga can be detected, which is detrimental for many applications and must therefore be suppressed. To achieve a perfect cleanliness of the patterned areas, the FIB patterned substrates is chemically cleaned in an HCl : H₂O solution followed by an annealing and another HCl bath to remove Ga contamination [410]. The samples are then chemically cleaned and oxidized before being loaded into the growth chamber. Fig. 162 shows an example of such a clean pattern before introduction in the growth chamber.

The native oxide was desorbed into the MBE chamber at 900 °C (2 min) and a thin 4 nm Si buffer layer was then grown at 750 °C. At this point, AFM images of the patterned samples do not differ from the one obtained after the ex-situ cleaning treatment. After buffer growth, the substrate temperature was lowered to the Ge growth temperature. Growth temperature and Ge thickness were varied to map out the effects of growth kinetics on the dot ordering. The deposition of Ge on the patterned substrates resulted in three different configurations. At high temperature ($T \sim 700$ °C), domes with a mean diameter of 120 nm and a density of $\sim 10^9 \text{ cm}^{-2}$ are produced on the surface. These domes are organized in-between the FIB holes when the distance between the pits is comparable with the island size (Fig. 163(a)). For a larger distance between the pits (350 nm), domes remain outside but nearby the holes (inset of Fig. 163(a)). The island density and mean size are almost independent of the distance between the patterns even if their position may be influenced by the presence of holes. Indeed, one can note that islands nucleate preferentially near the hole edges at this temperature. Moreover, as commonly observed on a Si bare substrate, a higher density of organized domes ($\sim 5 \cdot 10^9 \text{ cm}^{-2}$) can be achieved by increasing the thickness of the deposited Ge layer. For a thinner Ge film, huts coexist with domes and are also organized close to the FIB drilled holes. At intermediate growth temperature ($T \sim 650$ °C), islands arise randomly inside and outside the patterned areas with an equal

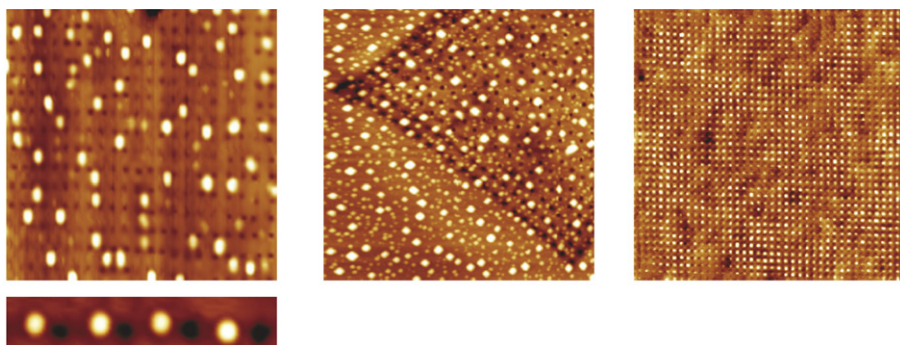


Fig. 163. AFM images of the patterns after deposition of 7 ML Ge at: (left) $T = 700\text{ }^{\circ}\text{C}$; (middle) $T = 650\text{ }^{\circ}\text{C}$; (right) $T = 550\text{ }^{\circ}\text{C}$. The images evidence the three different nucleation and growth regimes.

probability (Fig. 163(b)). They display similar morphologies without any visible effect of the FIB patterns on their geometrical features. In this growth regime, the island morphology depends on the deposited thickness (similar to the configuration on unpatterned substrates).

Finally, at low growth temperature ($T \sim 550\text{ }^{\circ}\text{C}$), Ge islands fill the FIB holes with a correspondence of one island per hole whatever the pattern pitch is, from 350 nm, to 200 nm and 75 nm, see Fig. 163(c). Consequently, the island density and mean size are directly related to the hole pitch L , and the island density clearly follows a $1/L^2$ evolution as expected for a filling of one dot per hole. The high level of organization reached on FIB patterns is displayed in Fig. 163(c) where a nicely ordered island array with density as large as $2\ 10^{10}/\text{cm}^2$ and mean diameter $\sim 45\text{ nm}$ can be obtained.

These results evidence three different nucleation and growth regimes: inside the FIB holes at low temperature ($550\text{ }^{\circ}\text{C}$); random position at intermediate temperature ($650\text{ }^{\circ}\text{C}$) and on the edges of the holes at higher temperature ($700\text{ }^{\circ}\text{C}$). We first discuss the influence of the holes on the local chemical potential at the surface. The surface chemical potential equation (6) is lower on convex areas [388] while the elastic term is lower on concave areas. In the experiments described above, the nucleation of dots at $700\text{ }^{\circ}\text{C}$ takes place preferentially on the edges of the holes i.e. on concave areas so that the effect of stress is dominant compared to the surface energy part, similarly to what was found for the nucleation of Ge dots on mesas [396]. As regards lower temperatures, no change in $\Delta\mu$ is expected so that the change in the preferential nucleation sites at lower temperature cannot be explained by energetic arguments. However, decreasing the temperature dramatically decreases the mobility of surface adatoms. Moreover, the energy barrier for diffusion is expected to be larger inside the FIB holes than on a planar (001) terrace, because of the presence of steps. The closer the adatoms are to the hole bottom, the lower is their surface diffusion. Kinetic Monte-Carlo simulations were performed in [388] to investigate the effect of a patterned substrate on the surface diffusion and on the nucleation of 2D islands. The diffusion rate of an adatom is given by the usual rate given by Eqs. (22) and (23) for a basic solid-on-solid model but with a diffusion barrier E_S which depends on the position on the surface. The inhomogeneity of $E_S(\mathbf{r})$ is described by a constant value E_{S_1} inside the hole larger than the barrier E_{S_2} on the planar surface ($E_{S_1} > E_{S_2}$), thus producing a net flow of adatoms towards the hole centers. Consequently, these centers act as preferential nucleation sites and strongly influence both the island size and positioning. At higher temperature, this effect becomes negligible as the difference of diffusion barriers $E_{S_2} - E_{S_1}$ becomes negligible with respect to the thermal energy $k_B T$ leading to similar diffusion rates in the holes and on terraces. In addition, if we consider that domes are formed by merging of small Ge dots at high temperature, even if 2D islands kinetically nucleate at the hole bottom, it may be expected that Ge dots will grow on the energetically most favorable positions given by the minimization of μ [411].

When Ga is not removed from the surface, the interplay between chemistry and topographic effect controls the nucleation of Ge dots [412]. In this case, the Ga ion implants significantly modify the surface in several ways. The sputtered material creates local topographic modulations as the surface is damaged by the incident energetic ions thereby changing local crystallinity. The implanted Ga also change the local surface chemistry, and for the CVD growth, may change the local surface reactivity and hence Ge deposition rate. Local damage and implantation also create local strain fields. In principle, each of these modifications should favor Ge QD nucleation at the impacted template sites. It was shown that the dominant localization mechanism is related to the surface topography which arises during implantation and subsequent annealing. This topography evolves with the experimental conditions (sputtering and annealing) following a complex dependence. It was observed that the presence of a surface corrugation beside ionic implantation is a necessary condition to obtain QDs templated to the initial template features. However, depending on the patterns morphology either one QD is templated at each implant feature (in the case of transient morphology) or more than one QD per feature is observed (in the case of annulus morphology [412]). Moreover, it was found that the resulting QDs have morphologies different from those grown on unmodified substrate: in particular, the aspect ratio of non-dislocated QDs is lower than that of conventional {510} hut clusters grown on pure Si(001) surfaces while the aspect ratio of dislocated clusters is greater than that of the conventional {311} dome clusters. The transition between coherent and dislocated structures occurs at a lower size than for the pure Si(001) surface. Another critical feature of the templated QD array is the dose of Ga ions implanted, since the wetting layer

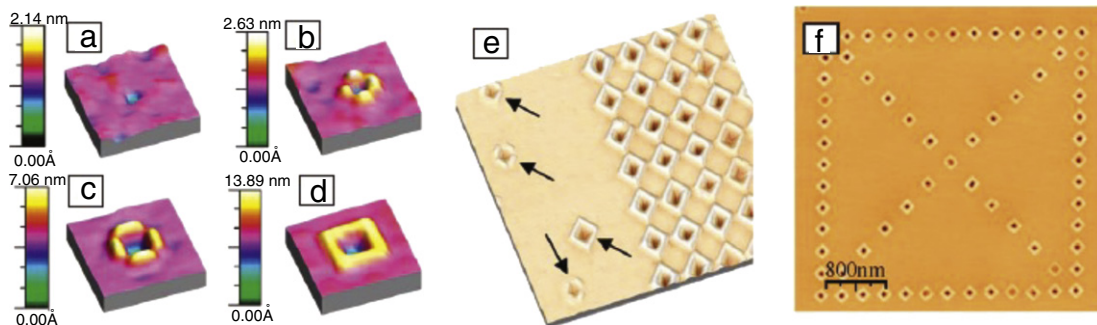


Fig. 164. (a-d) Evolution of the QDM nanostructure for growth of h (nm) of Ge_{0.3}Si_{0.7}/Si(001) at 550 °C and 0.09 nm/s: (a) $h = 5$ nm, (b) $h = 15$ nm, (c) $h = 20$ nm, (d) $h = 30$ nm. (e) and (f) show ex-situ Ga⁺ FIB-templated QDM arrays, with off-site QDMs arrowed in (e).

Source: from [412].

thickness decreases as the net Ga⁺ dose is increased. Finally, it was also found that if the patterns are too closely spaced then an accurate filling of the pits with one QD at each site cannot be reached due to overlapping adatom capture fields between adjacent features [413]. In particular, when the site separation drops below 100 nm, the site occupancy becomes increasingly unreliable, depending on the growth conditions. Using particular conditions it was possible to organize “quantum dot molecules” (four Ge islands) surrounding the patterns (Fig. 164).

4.2. Substrate designed by instabilities

Growth instabilities that develop during homoepitaxy on vicinal substrates or during heteroepitaxy produce large scale self-organized surface modulations which may be used as templates for QD growth [414,7]. Self-organization and geometric features of the nanopattern clearly depend on the driving force of the instability. We briefly review in the two first subsections below both the morphological evolution of the substrates and the physical mechanisms explaining the development of each type of instability. The step bunching and step meandering instabilities created by electromigration are not considered here. They were mainly studied for fundamental aspects and did not lead yet to application in semiconductor nanostructure self-organization since they cannot be produced in conventional growth chambers (for a review on these instabilities see [415]).

4.2.1. Instability driven patterning on Si(001)

Under specific growth conditions, vicinal surfaces undergo a kinetic step bunching instability [416,125,56,417–420] which self-organizes and creates 2D periodic array of nanopatterns. Many theoretical studies have investigated the dynamics of step trains [421–425] and the origin of the kinetic instability: surface kinetics [20,426,427], elasticity [59,60,428], faceting [429], impurities [430], electromigration [431,432], etc. In the case of a vicinal Si(001), step bunching of the substrate is explained by various microscopic processes such as the asymmetry of adatom attachment at step edges [432], anisotropy of surface diffusion [73,433] and of kink diffusion [434], inverse Ehrlich Schwoebel (ES) barrier [426,427], multi-species diffusing particles [435], etc.

The morphological evolution during growth of Si(001) vicinal surfaces misoriented from 1.5 to 10° off was experimentally investigated and successfully compared with KMC simulations dedicated to such surfaces [433]. The main ingredient introduced in the model is the anisotropy of the surface diffusion barrier which allows to reproduce first the (1 × 2)–(2 × 1) reconstruction and second the transformation of a regular train of monoatomic steps into double steps during growth [436]. Three main growth regimes were identified. The first growth regime (at low T) corresponds to the nucleation of 3D islands and results in a rough surface with a root mean square (RMS) roughness $w = \langle [h - \bar{h}]^2 \rangle^{1/2}$ (where \bar{h} is the average surface height) of order 1.5 nm. Further deposition induces a gradual amplification of the roughness, as explained in [437]. The second growth regime (at intermediate T) is characterized by the onset of a step bunching instability which produces self-organized periodic ripples parallel to the step edges with a well-defined in-plane length scale [438]. At higher T the instability gradually vanishes and the correlation length and the ripples wavelength increase. This third regime corresponds to the normal step flow growth mode characterized by a very flat surface consisting of a regular train of equidistant steps. AFM images of these three growth regimes are given in Fig. 165 together with the KMC simulations which perfectly reproduce these three growth regimes (the onset of the three growth regimes is shifted by ~100 °C towards lower temperature with respect to the experimental result because of the larger misorientation angle used in the simulations).

The second growth regime produces an instability which increases with the deposited thickness and which may be described by the usual description of kinetic instabilities [439]. At short times, the roughness behaves as $w \sim t^\beta$ while it saturates for large time $w \sim L^\alpha$, where L is the system size and α and β , the roughness and growth exponents. The fluctuation correlation length also behaves initially as a power law $\xi \sim t^\gamma$ where scaling enforces the general relation $\alpha = \beta/z$. The experimental evolution on Si(001) [433] may be described by $\alpha \sim 0.3$ and $\beta \sim 0.53$. These results are in good agreement

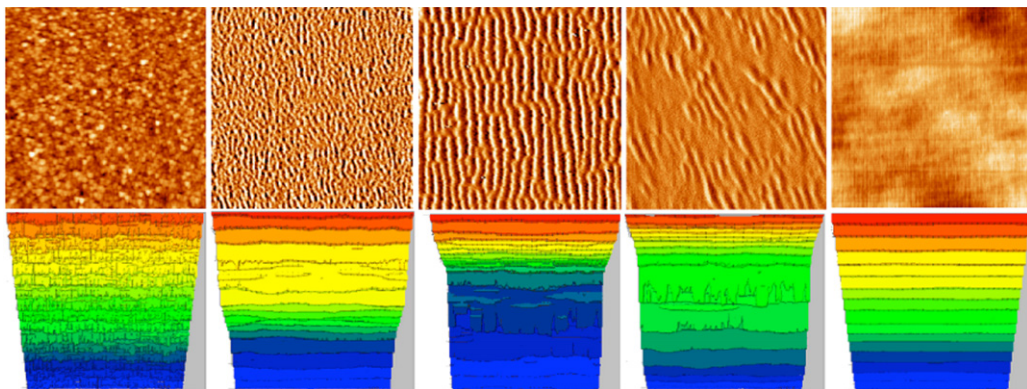


Fig. 165. Morphology of silicon layers obtained: experimentally (upper images) and by KMC simulation (lower images) after the deposition of 800 ML at (a) 300, (b) 350, (c) 400, (d) 450 and (e) 550 °C. Simulation cell consists of 320 × 320 sites with 32 terraces of 10 sites wide, separated by monoatomic steps. Experimental AFM images of the morphologies obtained for each regime are presented in 5 × 5 μm^2 scan areas. The images evidence the 2D nucleation regime at 300 °C; the transition between 2D nucleation and step flow at 350 °C accompanied by the onset of the step bunching instability; the self-organization of nice step bunches at 400 °C. At 450 °C the step bunch start to vanish by enlargement of their periodicity; at 550 °C they have totally disappeared and one only sees the step flow regime which produces a fully flat surface. The same regimes are observed on the images obtained by KMC simulations in the lower part, in correspondence with the experimental images.

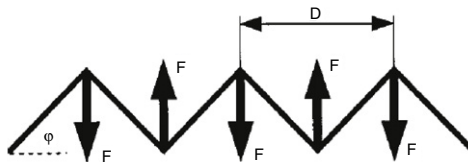


Fig. 166. Saw-tooth profile of a faceted surface. Effective forces of alternating sign are applied to neighboring edges.
Source: from [373].

with kinetic Monte-Carlo [433]. Similar results were found using a continuum growth model [127] where a step bunching instability appears as a consequence of asymmetry and elastic coupling. The asymmetry of kinetic coefficients on Si(001), related to the alternation of smooth and rough steps, introduces an extra elastic coupling between non-neighboring terraces. The combined action of these non-neighboring terraces was shown to break the symmetry between the ascending and descending adatoms currents. As a result, and in contrast with the usual inverse Ehrlich–Schwoebel effect, the unbalanced currents concern the interaction between two double terraces.

4.2.2. Periodic patterns on Si(111) and Si(113)

In order to compare the effect of (111) and (001) nanostructured surfaces, similar experiments were performed on vicinal Si(111). If a planar crystal surface is unstable and breaks up into a system of tilt facets, the conservation of the average orientation of the normal to the surface

$$\frac{1}{A} \int \hat{\mathbf{m}} dA = \hat{\mathbf{n}}, \quad (73)$$

implies the coexistence of alternating facets. Here, $\hat{\mathbf{m}}$ is the unit vector locally normal to the surface at each point, $\hat{\mathbf{n}}$, the unit vector normal to the initially planar surface, and A , the total area of the nominally planar surface. The intersection of neighboring facets consists either in sharp edges or narrow rounded parts that are both linear defects. These two types of intersection give a short-range contribution to the surface free energy and a long-range contribution due to elastic interactions. It was shown that if linear striction effects exist, they favor the formation of a periodic faceted surface with a macroscopic period [440].

The equilibrium theory of a periodically faceted surface was developed by Marchenko [441]. The free energy per unit projected area of a faceted surface with a one-dimensional periodic saw-tooth profile, see Fig. 166, is given by

$$F = F^s + E^{ed} + \Delta E^{el}, \quad (74)$$

where F^s is the free energy of the tilted facets, E^{ed} , the short-range energy of the edges, and ΔE^{el} , the elastic energy due to the discontinuity of the surface stress tensor τ_{ij} at the crystal edges. The free energy of tilted facets per unit projected area depends only on the orientation of the facets, $F^s = \gamma(\varphi) \sec(\varphi)$ and does not depend on the period of the structure D . The elastic contribution E^{el} is zero in the absence of strain and contains both linear and quadratic terms as a function of strain. Therefore the elastic strain energy at equilibrium is negative and corresponds to the relaxation of the surface stress at crystal edges.

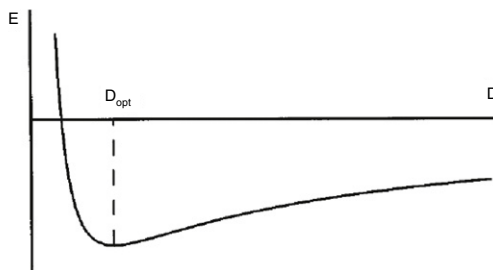


Fig. 167. The energy of a periodically faceted surface per unit surface area vs the period D . There always exists an optimum period of faceting D_{opt} due to the logarithmic dependence of the elastic relaxation energy on the period D .

Source: from [373].

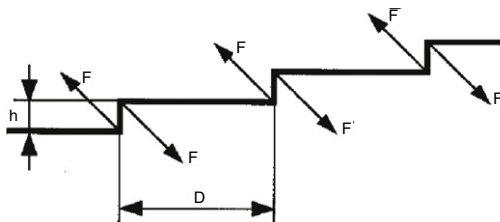


Fig. 168. A periodic array of macroscopic step bunches resulting from the faceting of a vicinal surface. Force monopoles are acting at the edges of the structure. The elastic interaction between the two edges of the same step bunch is the monopole–monopole interaction, whereas the interaction between different step bunches is the dipole–dipole one.

Source: from [373].

At equilibrium, elastic force monopoles are acting at the edges but forces applied to neighboring edges are balanced so that the total force applied to the system vanishes. Elastic strain generated by linear crystal edges propagates into the crystal over a distance of the order of D and decay at larger distances from the surface. Since the strain field is generated by the linear crystal edges, the elastic relaxation energy depends logarithmically on the period D of the structure such as:

$$\Delta E^{el} = -\frac{C(\phi)\tau^2}{YD} \ln\left(\frac{D}{a}\right) \quad (75)$$

where τ is the characteristic value of the intrinsic surface stress tensor, Y is the Young modulus, a , the lattice parameter, and $C(\phi)$, a geometric factor which accounts for the particular symmetry of the tensor τ_{ij} . The free energy of the faceted surface per unit projected area is then

$$F = \frac{\gamma(\varphi)}{\cos \varphi} + \frac{\eta(\varphi)}{D} - \frac{C(\phi)\tau^2}{YD} \ln(D/a) \quad (76)$$

and its dependence on the period of the faceted surface D is drawn in Fig. 167 [373]. Due to the logarithmic dependence of the elastic relaxation energy on D , there always exists an optimum period for faceting D_{opt} ,

$$D_{opt} = a \exp\left[\frac{\eta(\varphi)Y}{C(\phi)\tau^2} + 1\right]. \quad (77)$$

The optimal period can exceed the lattice parameter a by a orders of magnitude and periodic faceting with large periods has indeed been observed on vicinal Si(111) surfaces [442,443] and Si(211) [444]. For Si(111) the homogeneous vicinal surface consists of planar terraces with low Miller indices and the neighboring terraces are separated by equidistant monoatomic steps. The faceting of a vicinal Si(111) surface produces its breaking into two vicinal surfaces with different concentration of steps. In this situation, the discontinuity of the intrinsic surface stress tensor τ_{ij} at the edges results in effective force monopoles acting there, see Fig. 168.

On the other hand, the elastic interactions between step bunches is a dipole–dipole interaction which decreases with the separation L as $1/L^2$. Since the average orientation of the faceted surface in Fig. 168 coincides with the orientation of the initially homogeneous vicinal surface, there exists a relation between the height h of macroscopic step bunches and the period D of the structure, $h \simeq D\theta$, where θ is the misorientation angle of the vicinal surface. Due to the logarithmic dependence of the elastic relaxation energy on the height of the step bunch, there is always an optimum equilibrium height for the step bunches. Step bunching was obtained by the faceting instability on Si(111) substrates misoriented around [1–10] in the [11–2] direction. The geometry of vicinal (111) surfaces is displayed in Fig. 169 [445]. The faceting instability produces typical morphological features imposed by the underlying driving force. The starting surface consists of regular train of flat terraces separated by 3.135 high monolayer steps [445]. During Si growth (or during a high temperature

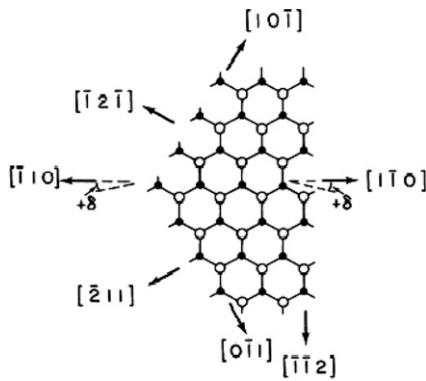


Fig. 169. Schematic representation of the different geometries of vicinal surfaces with misorientation directions around.
Source: from [445].

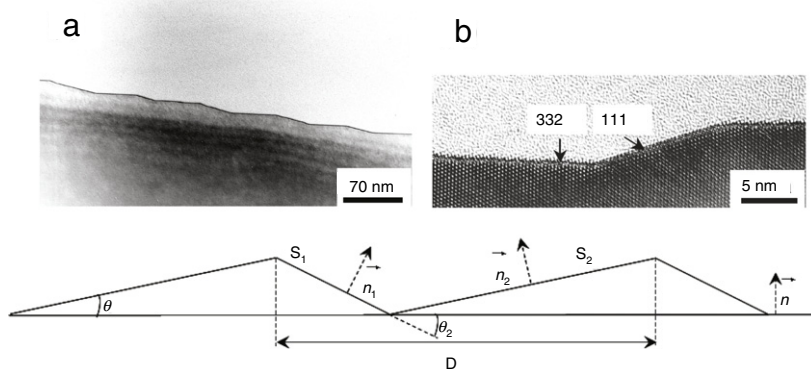


Fig. 170. (a) and (b) TEM cross-section images of Si(111) misoriented of 10° off towards [11-2] after Si deposition at 700 °C. (b) is a high resolution image of a period: (111) terrace and (332) facet. The last figure gives a one-dimensional schematic view of a faceted surface.

flash), the surface breaks down into a sawtooth morphology (Fig. 170a) consisting of (111) 7×7 terraces and (332) facets (Fig. 170b) [446–448]. This morphological transformation is explained by the minimization of the total surface energy of a vicinal surface S (free energy γ) when it breaks into two facets S_1 and S_2 that intersect with an angle θ_2 between their normal, with surface energies γ_1 and γ_2 , see Fig. 170. The vicinal surface S breaks into the two facets if

$$\gamma_1 S_1 + \gamma_2 S_2 < \gamma S, \quad (78)$$

while keeping the mean orientation of the surface, $S = S_1 \cos \theta + S_2 \cos(\theta_2 - \theta)$, and $S_1 \sin \theta = S_2 \sin(\theta_2 - \theta)$. The faceting instability may then develop if

$$\frac{\gamma}{\cos \theta} > \left(1 - \frac{\tan \theta}{\tan \theta_2} \gamma_1 + \frac{\tan \theta}{\tan \theta_2} \frac{\gamma_2}{\cos \theta_2} \right). \quad (79)$$

It was shown that the faceting instability on Si(111) leads to a periodic surface with a periodicity independent of the miscut angle while the facet width increases linearly with the miscut angle (Fig. 171(a)–(d)). Such a length scale relationship implies that the facet must have the same angle, i.e. facet structure, in all the samples [429]. The authors proposed a two-stage faceting model with a first stage dominated by minimization of the elastic energy which defines the universal periodicity and a second stage dominated by minimization of the facet energy which creates a common facet structure and controls the facet width.

4.2.3. Self-organization on spontaneously formed periodic surfaces

The patterned surfaces formed by self-organization of periodic arrays of macro-steps and flat terraces offer prototypal templates for the direct fabrication of ordered arrays of quantum dots or quantum wires. The deposition of new material on the corrugated surface allows in principle the fabrication of ordered nanostructures provided the growth proceeds in relation with the grooves of the substrate. The theory of quasi-equilibrium growth on periodically corrugated substrates offers several possibilities for the morphology of the heteroepitaxial system depicted in Fig. 172. The total energy of the heteroepitaxial system may be decomposed as [449]

$$E = E^s + E^{inter} + E^{ed} + \Delta E^{el}. \quad (80)$$

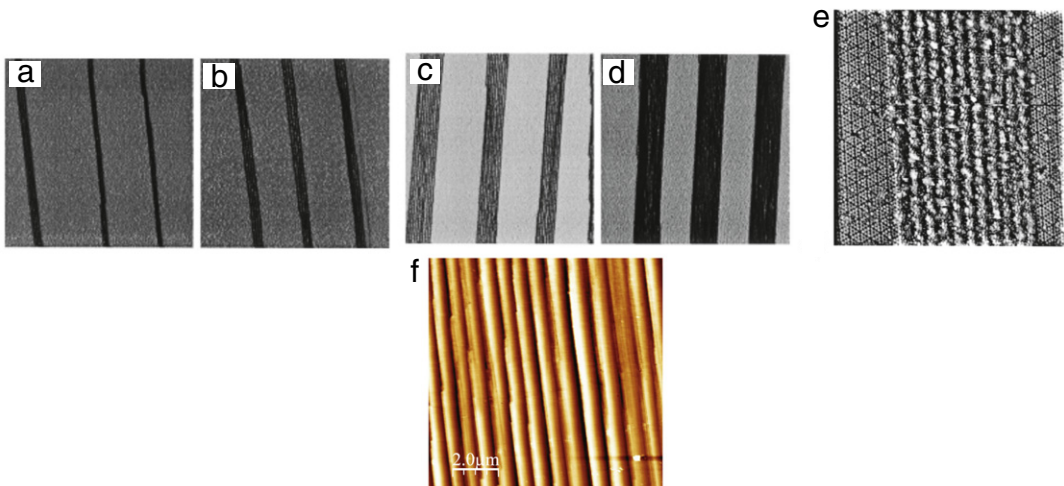


Fig. 171. (a) to (e) are STM images of Si(111) surfaces morphology at miscut angles of: (a) 1°, (b) 2°; (c) 4° and (d) 6° towards $[-211]$. (e) is a high resolution image of the stable facet. (f) AFM image of the nanopatterned substrate used for the deposition of Ge.
Source: from [429].

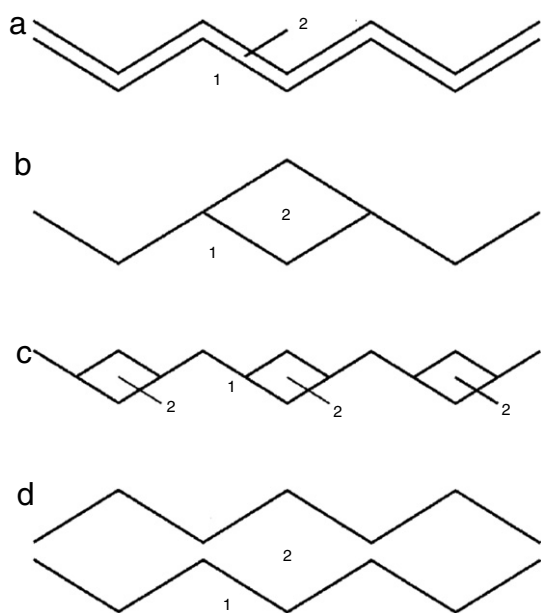


Fig. 172. Possible structures of an heteroepitaxial system in which material 2 is deposited on a periodically faceted surface of material 1: (a) homogeneous coverage; (b) separated "thick" clusters; (c) "thin" clusters; (d) high coverage, in which the periodic surface corrugation is restored, and the hills of the top surface appear over the valleys of the substrate, and vice versa.
Source: from [373].

Here, in addition to the usual three contributions to the energy of a faceted surface, an extra interface energy E_{inter} is accounted for. The selection between different growth modes is determined by whether the deposited material wets or not the substrate. If the deposited material wets the substrate, an homogeneous coverage of the periodically corrugated substrate occurs (Fig. 172(a)). If the deposited material does not wet the substrate, isolated clusters of the deposited material appear on the periodically corrugated substrate (Fig. 172(b)). In the case of an inhomogeneous cluster coverage, the periodic surface corrugation is restored after deposition of the first several monolayers (Fig. 172(c)). After further deposition, a continuous layer of the deposited material with periodically modulated thickness is formed where the hills of the top surface appear over the valleys of the substrate, and vice versa (Fig. 172(d)). Thus, the formation of clusters allows direct fabrication of nanodots or nanowires with a controlled spatial order. Since a periodically faceted surface is a structure of elastic domains, its geometrical parameters (and especially its period) can be tuned in a controlled way by applying an external stress.

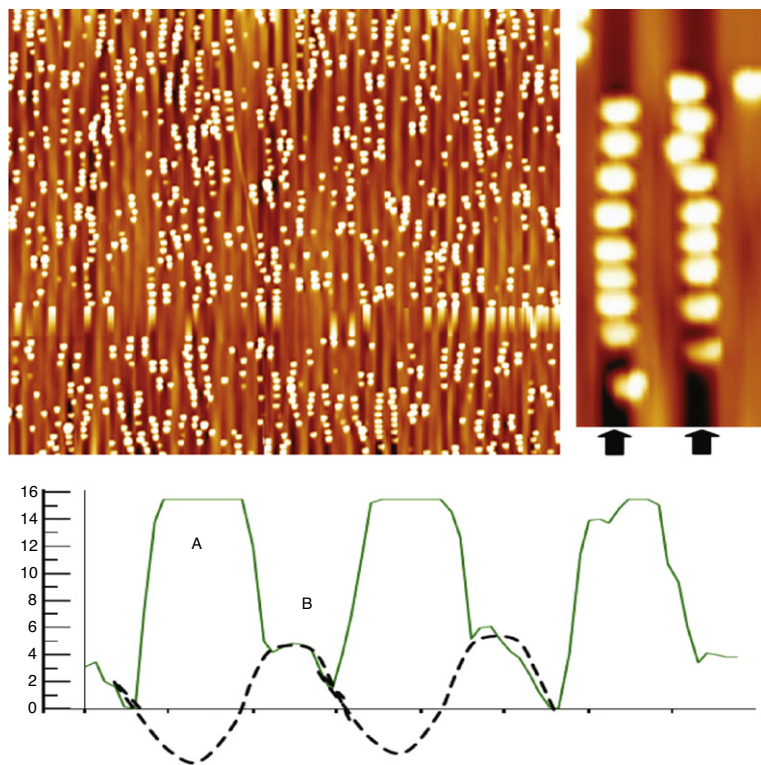


Fig. 173. (a) AFM image of Ge dots deposited on self-organized kinetic step bunching instability (the morphology of the initial surface is displayed in Fig. 165(c)); (b) gives a zoom of (a) where the QDs alignment is enlightened; (c) roughness line profile perpendicular to the ripples periodicity where one can see the QDs (A) and the ripple (B).

Experimentally, it was shown that the deposition of Ge on nanopatterned substrate results in Ge islands ordering which differs from one situation to another. On Si(001), the ordering of Ge islands on top of ripples resulting from kinetic growth instability was investigated in Ref. [119]. It was reported that Ge islands slightly order on these surfaces, see Fig. 173. While a large number of islands align along the step bunches, some of them nucleate on terraces between the bunches. The best ordering is obtained on 3 ML high step bunches with a spatial period of 250 nm. The localization of Ge islands along the step bunches is exhibited in Fig. 173. This behavior is also well visualized by the roughness line profile perpendicular to the ripples, see Fig. 173, which evidences the islands (noted A) aligned along the step bunches (noted B). From this experiment, it can be concluded that the (111) step bunches oriented along [110] represent preferential nucleation centers for Ge islands even if random nucleation occurs also in some conditions. In the case of a periodic Si(111) surface, it was shown in [414] that the Ge islands nucleate along the (332) nanofacets (Fig. 174(a)) only when the islands size matches the pattern periodicity. A high magnification image (Fig. 174(b)) emphasizes the lateral alignment of triangular shaped Ge islands along the step edges without nucleation of Ge QD on the flat terraces. This result is explained by the presence of kinks on (332) facets which represent favorable nucleation sites.

Similar positioning of Ge islands decorating the step bunches on Si(001) was obtained during the first stage of Ge deposition with a complete decoration of the step bunches when increasing the Ge coverage, see Fig. 175 [124]. In a second stage, Ge islands nucleate in the middle of the terraces, at a constant distance from each other and from the step edges, creating an ordered distribution of islands, see Fig. 175 [124]. Such a configuration is not observed on a vicinal substrate with a regular train of monoatomic steps. The comparison of Ge dots alignment on step-bunched Si(111) and regular surfaces is given in Fig. 175 [124].

Similar experiments performed on Si (113) surface resulted in slightly different results. Indeed, Ge islands are found to align along microfacets in straight rows with regular island separation [450] but they do not display any correlation in neighboring rows. Such a behavior may be attributed either to the large distance between the rows (some hundreds of nm with lengths of about 10 μm) or to short-ranged repulsive interaction of strain-relaxed islands mediated by their local strain fields within the Si substrate [451]. The first stage of the structural transformation during deposition of Ge on (113) nanofacets was determined at the atomic scale by STM, following step by step the detailed evolution of Ge adsorption on (5 5 12) vicinal surface, see Fig. 176 [452]. Among the high-index surfaces between (111) and (001), only (113) is a stable surface for both Si and Ge, while (5 5 12) belongs to a relatively stable surface only for Si. As a consequence, the unit cell of the (5 5 12) surface tends to be faceted into (113) and (112) nanofacets during the deposition of adsorbates, generating surface

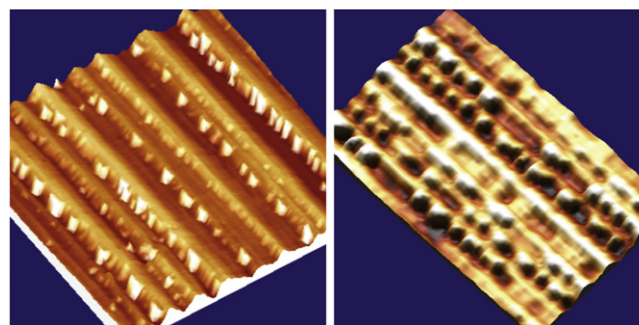


Fig. 174. (Color online) AFM images of QDs grown on a vicinal Si(111) substrate. Left, large scale area of the surface covered by Ge islands. The alignment of Ge islands along the (332) facets is well emphasized on the 3D shadowed zoom image of figure (right image).
Source: from [414].

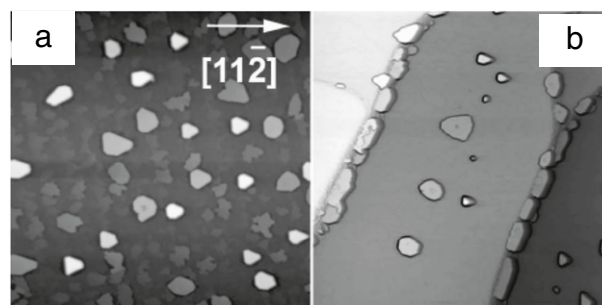


Fig. 175. STM topography of Ge dots deposited at $T = 50^\circ\text{C}$: (a) on a regular surface and (b) on a step bunched surface. While QDs are distributed randomly on the regular surface, a lateral alignment along step bunches is clearly visible in the latter situation.
Source: from [124].

stress. During Ge deposition, a Ge p-bonded chain is formed on the preferential adsorption site, creating subunit-switching between (337) and (225). By repeated subunit-switchings, the seed of the (113) sawtooth-like facet becomes visible and then expands until the (112) [or (335)] facet on the other side of the sawtooth facet develops also. When stress relaxation saturates with additional Ge, the (113) facet starts to develop 2×2 structures and loses its 1D symmetry. From these results it is concluded that the existence of (113) facets, a common major facet of Ge and Si, is a determining factor, from the seed generation of sawtooth-like facet to its deformation into Ge hut clusters [452].

A more comprehensive review of the effect of steps of different heights and orientations on 3D Ge island ordering was given in [453], see Fig. 177. The authors investigated this nucleation on the sidewall of a hole on a Si(111) surface. It is found that the formation of 3D Ge islands is greatly influenced by the step orientations and step-bunching conditions. Indeed, during Ge deposition, the heavily bunched [110]-type steps deviate from their initial [110] direction and form a lot of big kinks at the bunch edges which are precursors of 3D islands. Regarding the steps oriented to the [112] direction, they initially debunch with mixtures of single and triple-bilayer high steps which advance in the [112] direction and create a small bunching which does not initiate 3D islands nucleation. As a consequence, the lower number of Ge islands observed in the region of steps oriented to [112] may be attributed to an initially lighter bunching.

One may conclude from these experiments that (111) step bunches have a pronounced effect on 3D island position contrarily to the (001) bunches which have a low impact. This difference can be attributed to the different step height and step edge energy of these two surfaces. In addition, one may note that the height of the step bunch favors a better self-organization. However, many experimental results on the effect of the step orientation and step kinks on Ge nanostructures positioning are still lacking.

4.2.4. Periodic patterns on planar surfaces

Another class of spontaneously ordered nano patterns is associated with periodically ordered structures of planar surface domains, see Fig. 150(b). Surface domain structures occur if different phases coexist on the surface, e.g., phases of (231) and (132) surface reconstruction of Si(001). Then neighboring domains have different values of the intrinsic surface stress tensor τ_{ij} , and effective force monopoles are applied to the domain boundaries, see Fig. 178,

$$F_\alpha = (\tau_{\alpha\beta}^{(2)} - \tau_{\alpha\beta}^{(1)})m_\beta, \quad (81)$$

where m_β is the two-dimensional vector normal to the domain boundaries. This effective force gives rise to elastic relaxation and the existence of linear striction effects favors formation of periodic structures with a macroscopic period. Although the

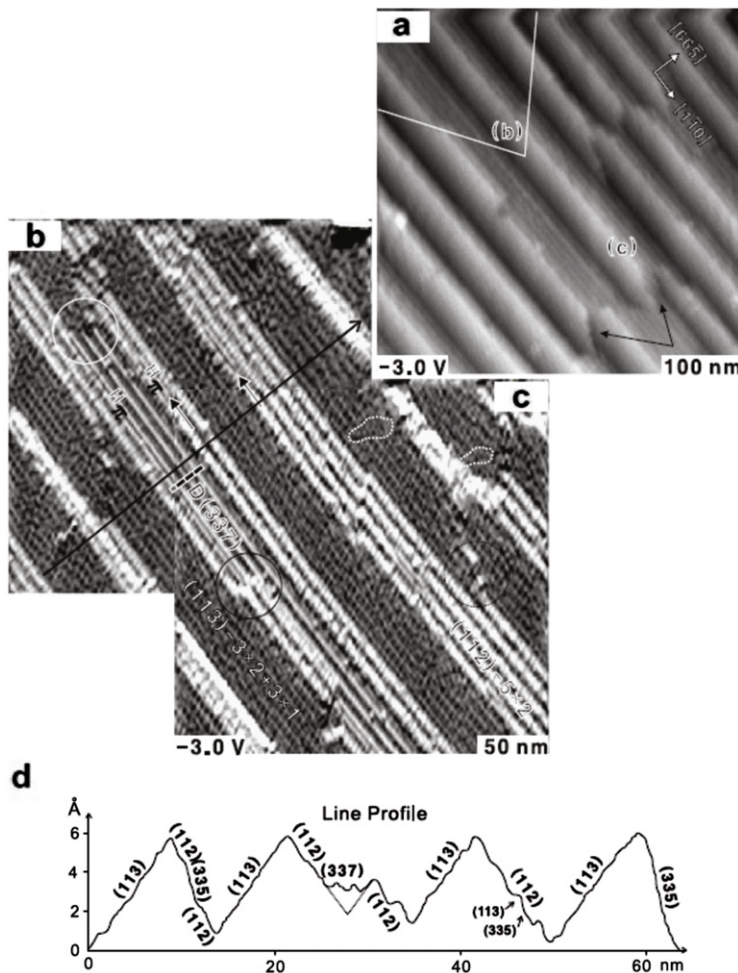


Fig. 176. STM images obtained from 1.5-ML Ge/Si(55 12)-2 × 1: (a) is a filled state topography image (scan size: 100 nm × 100 nm); (b) and (c) are error-signal images (scan size: 50 nm × 50 nm); (d) line profile following the black arrow in (b) and (c).
Source: from [452].

geometry of these structures is very different from the one of periodically faceted surfaces, the energetics is basically the same. The total energy of the domain structure per unit surface area includes three different terms:

$$E = E^s + E^{bound} + \Delta E^{el}. \quad (82)$$

The first term quantifies the change in the surface energy $E^s = p\gamma_1 + (1-p)\gamma_2$, where γ_1 and γ_2 corresponds to the surface energies of the first and second domain and p is the surface coverage of the first domain, $p = l/D$, where l is the step-step distance. The second term is the energy cost to form the domain boundaries $E^{bound} = C_1\eta D^{-1}$, where η is a short-range energy of domain boundaries. Finally, the elastic energy gained by the stress relaxation ΔE^{el} equals $\Delta E^{el} = -C_2(\Delta\tau)^2/(YD) \ln(D/a)$. Due to the logarithmic dependence of the elastic relaxation energy on the period of the structure D , the total energy displays a minimum for a given optimal period,

$$D_{opt} = a \exp \left[\frac{C_1\eta Y}{C_2(\Delta\tau)^2} + 1 \right]. \quad (83)$$

The best-known system exhibiting surface stress domain structures is the Si(001) surface and corresponding vicinal surfaces. In this system domains of (231) and (132) surface reconstruction coexist on the surface and are separated by single-height atomic steps. Force monopoles applied to single-height atomic steps lead to a variety of structures on vicinal surfaces as a function of the miscut angle.

Another typical example is the Si(111) vicinal surface with flat domains separated by monoatomic steps. While 3D large Ge islands grow randomly on such vicinal substrates with regular monoatomic steps, it seems that smaller islands (nanoclusters) first nucleate along the step edges as indicated in [123]. The high resolution STM study of Ge islands deposited on vicinal 1° off Si(111)-7 × 7 surface with atomically well-defined step edges reveals that the nanoclusters are self-aligned

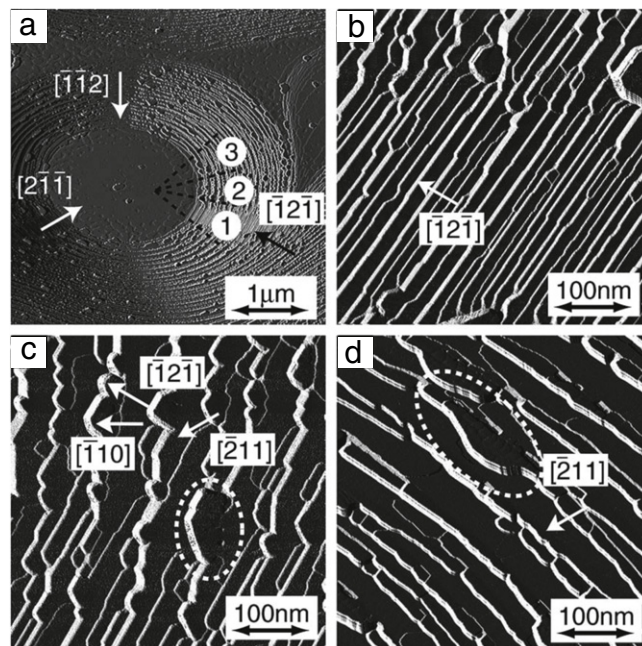


Fig. 177. STM differential images of 3D island formation after 3-BL Ge deposition. (a) Overview of the hole morphology. (b), (c), and (d) close-up images of regions 1, 2, and 3 indicated in (a), respectively.

Source: from [453].

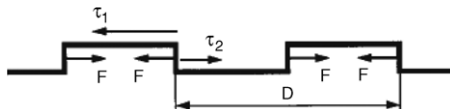


Fig. 178. Effective forces applied to domain boundaries in a system of planar surface domains.
Source: from [373].

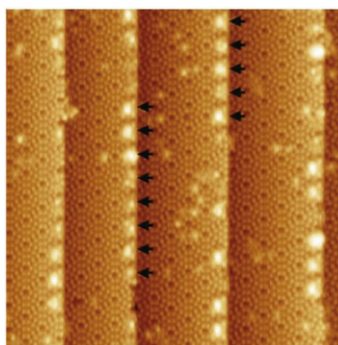


Fig. 179. STM image of the vicinal Si(111) template covered with 0.13 BL of Ge deposited at 250 °C followed by annealing at the same temperature for 24 min. Ge nanoclusters are aligned along the upper edges of the steps. On the terraces fewer smaller protrusions are seen. The whole area is $46.1 \times 38.1 \text{ nm}^2$.
Source: from [123].

along the upper edges of the steps. They are located preferentially within the unfaulted halves of the 7×7 structure right at the upper step edges so that their lateral size is less than 2.0 nm and their periodicity is 2.7 nm along the steps, see Fig. 179. In fact, STM images show that the alignment of nanoclusters forms a kind of nanowire 0.67 nm wide along the original Si(111) step edge beneath the nanoclusters, creating a decoration of the original Si(111) step edge. The nucleation of the Ge nanoclusters at the edges occurs predominantly on the unfaulted halves of the 7×7 structure, while it occurs preferentially on the faulted halves on the terraces [123]. The optimal ordering of clusters along the step edges was obtained at $T = 250$ °C when the thermal energy is high enough to allow Ge atoms to reach the steps leading to the nanocluster formation. At higher temperature, the same growth mode is observed but the number of nanoclusters along the upper step edges decreases due

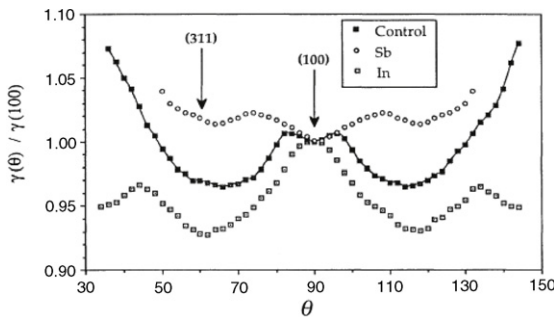


Fig. 180. $\gamma(\theta)$ plots of Ge on Si as a function of orientation near (001) 90°, extracted using the Wulff construction for clean Ge/Si, Ge:In and Ge:Sb. All the curves are normalized to $\gamma(001) = 1$ so absolute energies are irrelevant [454].

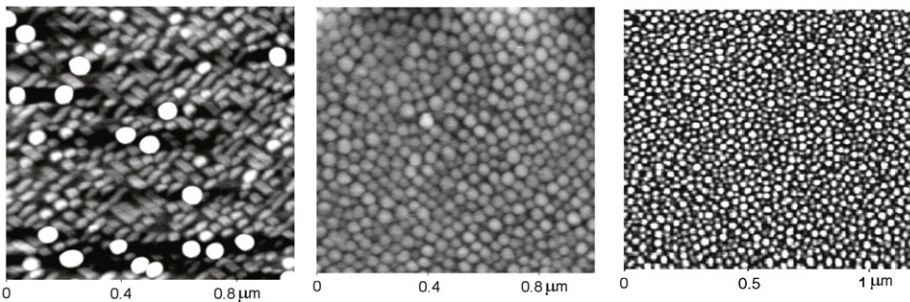


Fig. 181. AFM images of 13 ML Ge deposited at 550 °C on h (submonolayer coverage) of Sb itself deposited on Si(001): (left) $h = 0$ ML; (middle) $h = 1/2$ ML and (right) $h = 1$ ML.

Source: from [455].

to the accumulation of Ge atoms in the kink-bunching regions resulting from electromigration along the steps induced by the kink-up dc heating used in these experiments.

4.2.5. Surfactant effect

Another way to change the QD self-organization results from the modification of the surface energy anisotropy which may be achieved by partial coverage with surfactant impurities. This effect was investigated during the growth of Ge on Si. In particular it was reported that the presence of impurities such as H, In or Sb produces radical changes in the shape of Ge islands on Si. A Ge:Sb surface enhances (001) facets compared to clean Ge, as Sb impurities promote bi-dimensional growth and favor large flat islands. On the contrary, Ge:In favors {311} facets and promotes the nucleation and growth of faceted islands [454]. Such changes may be attributed to the modification of the surface energy anisotropy. The surface energy $\gamma(\theta)$, deduced by the Wulff construction from the equilibrium shapes of Ge islands, is plotted in Fig. 180 in presence of Sb and In and compared to the clean Ge/Si system. The Ge:In surface displays a pronounced minimum for the (311) orientation, deeper than the (001) one, as opposed to the Ge:Sb case.

In different experimental conditions, the addition of a submonolayer coverage of an impurity (Sb, Ga, Au ...) either during a predeposition step or during growth also produced a considerable morphological change of the Ge islands. An example of such a change was reported in Ref. [455], see Figs. 181 and 193. It was shown that the predeposition of a Sb submonolayer before Ge MBE growth enforces first an increase in the critical thickness for the 2D–3D transition and second, the reduction of the island size, a change in their shape and an increase in their density (by a factor 4). These trends may be rationalized by two effects. First, the increase due to Sb in the surface energy anisotropy and thence in the surface energy barrier for creating islands (an increase in the step edge to surface energy ratio) has a stabilizing effect against island growth. Second, the lowering of Ge diffusion on Sb resulting from the competition between surface diffusion and exchange with subsurface Sb atoms reduces the motion of Ge atoms and reduces the formation of islands [221]. In these experiments, surface diffusion is mainly controlled by the surfactant species which dictates the surface free energy of both Ge and Si [191,456]. For instance, As and Sb surfactants which float on the surface during growth decrease the surface diffusion of Ge atoms and provide a large driving force for the Ge atoms to incorporate into the surface, thus preventing island formation [457,458].

In similar experimental conditions, the same surfactant effect was observed when a small amount of boron is predeposited on the surface [459]. It also produces both a delay in the Ge islands formation and the nucleation of small islands with lateral size of about 40 nm. Considering the small size of B atoms, the authors concluded that the surfactant effect observed is due to the strain relaxation during Ge growth [459]. However, such strain relaxation cannot be invoked in

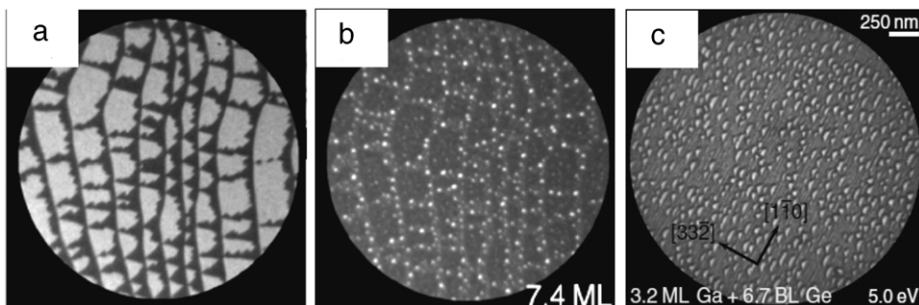


Fig. 182. Bright-field LEEM images of Si(111): (a) during Ga deposition at 650 °C where the nucleation of $\text{Ga}\sqrt{3}$ domains at step edges appear in dark at the 7×7 domain boundaries; (b) during Ge deposition at 450 °C ($h_{\text{Ge}} = 7.4$ ML) onto the surface shown in (a) with the preferential nucleation of Ge islands on the domain boundaries. Image scale is $5 \times 5 \mu\text{m}^2$.

Source: from [460].

(c) Bright-field LEEM images of Si(113) after the preadsorption of Ga on the surface and the subsequent deposition of Ge on the patterned surface.

Source: from [461].

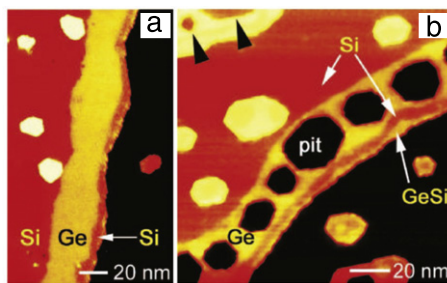


Fig. 183. (a) STM image of a one atomic layer high Ge stripe grown at a Si step edge. After Ge deposition a thin outer Si rim was grown. The apparent height contrast between Si and Ge is induced by the Bi termination of the whole surface. (b) After annealing at 733 K, unanticipated formation of pits and motion of the Ge originating from the pits to the outer Si rim is observed.

Source: from [462].

presence of Sb since Sb atoms are larger than Si ones. We will see later that a similar surfactant effect is observed in presence of Ga, which also cannot be attributed to strain reduction.

The surfactant effect of impurities can also be used to change the localization of Ge dots on Si when a controlled periodic geometry is produced by impurities. For instance, domain boundaries between ordered areas with different surface reconstructions may be used to self-organize Ge dots. The experiments evidence that when a Si surface is partially covered with Ga, $(\text{Ga/Si}(111)-\sqrt{3} \times \sqrt{3} - R30^\circ)$ domains nucleate at step edges and results in a two-dimensional phase separation between $(\text{Ga/Si}(111)-\sqrt{3} \times \sqrt{3} - R30^\circ)$ and 7×7 domains. This leads to the formation of large scale nanopatterning (Fig. 182a) with domains boundaries. The deposition of Ge on such patterned substrates induces the preferential nucleation of Ge islands at the former boundaries (Fig. 182b) where Ge islands preferentially nucleate on the step edges decorated by Ga between the domains. This leads to a site exchange of Ge and Ga, and thus to the formation of a $\text{Ga/Ge/Si}(111)-6.3 \times 6.3$ structure [460] which is attributed to a modulation of surface properties (such as diffusion length and chemical potential). Similar self-organization of Ge islands aligned along the $\{110\}$ step edges was observed on Si(113) when the step edges are decorated by Ga impurities, see Fig. 182 [461].

Another way to pattern the Si(111) substrate with a surfactant at the monoatomic level was recently demonstrated with the formation of pits aligned along the step edges [462]. In these experiments, a submonolayer amount of Ge is deposited on a Bi terminated Si(111) surface. The latter is prepared by deposition of one atomic layer of Bi on a clean Si(111) 7×7 substrate. During Ge deposition, Bi atoms float up on the surface as usual in surfactant mediated growth and the surface is fully covered by one atomic layer of Bi. After submonolayer deposition, Ge atoms attach to the step edges and form one atomic layer high stripes without any pit formation. Some Ge islands also grow at some distance from the step edges. It was found that after growth on such a surface, pits may grow inside the Ge stripe in some growth conditions, in particular after the deposition of a sufficiently wide, ~ 5 nm, Ge stripe followed by the deposition of a Si stripe and subsequent annealing, see Fig. 183. Note that the pit formation also occurs with the same mechanism at isolated Ge/Si islands (Ge core surrounded by a Si rim) located on terraces far from the step edges. During a first stage of the pit formation an initial amount of Ge is moving from the Ge stripe (pits) to the outer Si rim. The Ge atoms leaving the stripe during the pit formation attach at the Si covered Ge stripe and intermixes with the subjacent Si, see Fig. 183. The driving force for this first stage is the bond-energy gain: Ge–Ge bonds present in the Ge area are replaced by stronger Si–Ge bonds when Ge atoms attach to the Si terminated step edges. In a second stage, the entropy driven GeSi intermixing acts at the outer step edge and fresh Si atoms move to the

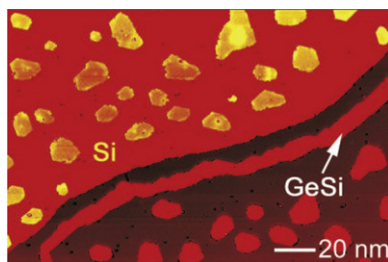


Fig. 184. Fabrication of a freestanding 8 nm GeSi wire on the Si(111) substrate obtained by pit coalescence.
Source: from [462].

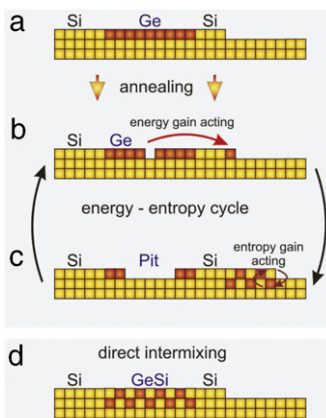


Fig. 185. (Color online). In (a) and (c) the initial and final states before and after pit formation are shown. In the first part of the energy–entropy cycle (b) the energy is reduced by replacing Ge–Ge bonds (at the Ge stripe) through stronger Ge–Si bonds at the Si terminated step edge. The subsequent GeSi intermixing is driven by a gain in mixing entropy (c). Because of the intermixing, Ge is trapped and the Si at the step edge is (partly) restored activating the energy driven part of the cycle again. An alternative simpler intermixing process without pit formation is direct intermixing with the Si from the lower layer (d).

Source: from [462].

outer step edge. These outer Si atoms are again amenable to bound to Ge atoms and therefore favor Ge diffusion driven by bond-energy minimization from inside the pit to the outer Si rim. These atomic processes may be considered as the energy driven and entropy driven parts of an energy–entropy cycle, see Fig. 185. Since the pit formation occurs after annealing, it was assumed that the formation of pits is a state close to local equilibrium. In special growth conditions, a large density of Si islands is produced. They provide a high density of sinks which drag Ge out of the pits and finally lead to pit coalescence. Fig. 184 shows the resulting continuous 8 nm wide freestanding GeSi wire obtained by pit coalescence. Such nanostructured surface could serve as template for the self-assembly of Ge islands.

4.2.6. ATG instability

In this part we describe the self-assembly of QDs grown on a substrate patterned by the morphological instability of $\text{Si}_{1-x}\text{Ge}_x$ films with low x on nominal and misoriented Si(001) substrates [2]. We first describe the morphological evolution as a function of the experimental parameters in order to give practical details to control and optimize the self-organized pattern created by the instability which may be used for subsequent ordering of Ge dots. This instability is not a step bunching one as periodic linear undulations formed during the growth of $\text{Si}_{1-x}\text{Ge}_x$ lie on the train of single-layer steps on vicinal Si(001) substrates perpendicularly to the step edges [105] with their sides consisting of (105) facets [121]. The morphological evolution of patterns with the misorientation angle is presented in Fig. 186. At low miscut angles ($<2^\circ$), undulations have rectangular bases aligned along the two {010} directions (Fig. 186(a)) while at higher miscut angles undulations transform into long wires perpendicular to the step edges (Fig. 186(b)). This change arises from the stabilization of (105) facets along the undulation sides as discussed above. In the situation of Fig. 186(b) (with a miscut angle of 10°), the (105) facets are almost parallel to the misorientation direction (see the stereographic projection in Fig. 186(c) for better understanding) which explains the linear shape of the instability. Regarding now the evolution of the instability topographic parameters (correlation length λ and roughness w), one should note that they do not change with the miscut angle but evolve with deposition time (deposited thickness) and with the Ge concentration as discussed above [121]. As an example, the morphological evolution with time and concentration is shown in Fig. 187. By choosing appropriate experimental conditions such as the Ge concentration x , deposited thickness and misorientation angle θ , it is possible to develop an instability with

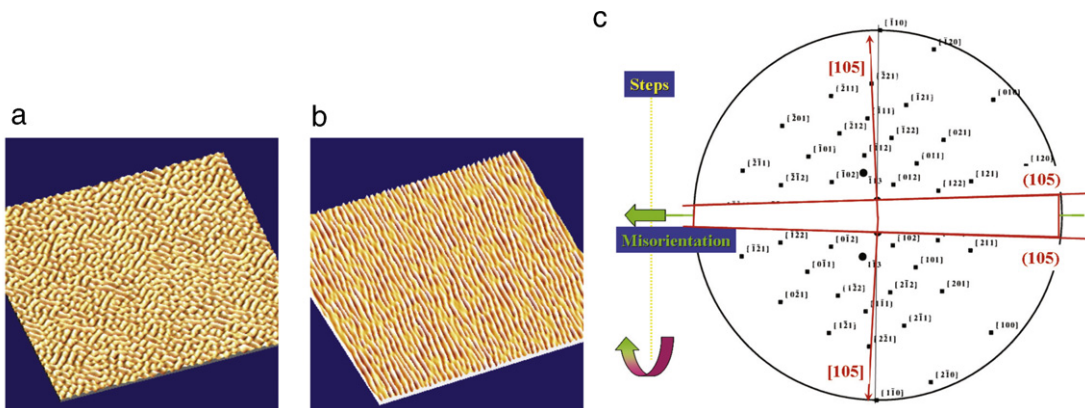


Fig. 186. Examples of patterns developed after the growth of 10 nm $\text{Si}_{1-x}\text{Ge}_x$ ($x = 0.35$) on vicinal (a) 1.5° off and (b) 10° off $\text{Si}(001)$. Stereographic projection of the 8° off Si substrate with indication of the (105) planes, the step edge direction and the misorientation.
Source: from [414].

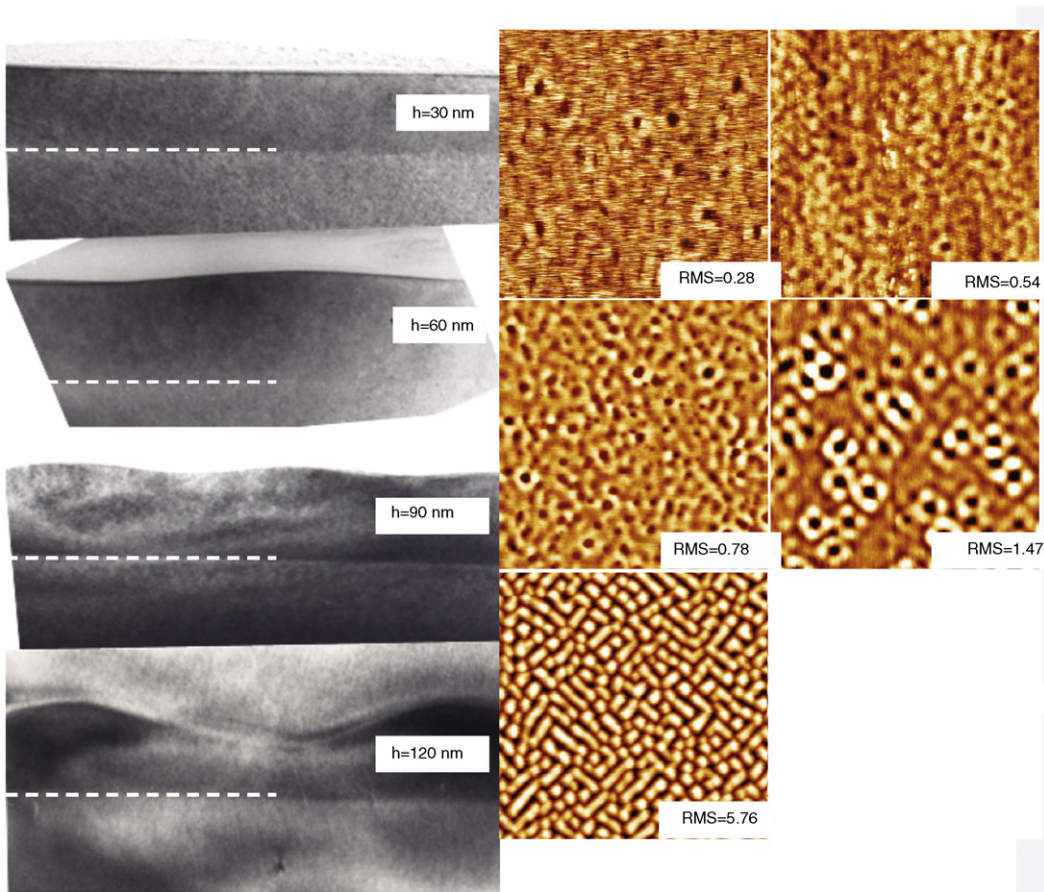


Fig. 187. (left column) TEM cross-section images of the $\text{Si}_{0.7}\text{Ge}_{0.3}$ instability: morphological evolution of with deposition time (t) (equivalent to a deposited thickness); (right column) AFM images of the instability of $\text{Si}_{1-x}\text{Ge}_x$ layers for $x = 0.22, 0.24, 0.26, 0.28, 0.30$ and $h = 50\text{ nm}$.

specific morphological features which may be used as a template layer for a controlled self-organization of quantum dots during subsequent Ge deposition.

Spectacular regular spatial organization can be achieved when QDs grow on a strain modulated template layer resulting from the ATG instability [7], where islands decorate the top of periodic mounds or align on top on the 1D structuration produced by the instability grown on a 10° off $\text{Si}(001)$ substrate, see Fig. 188. It was reported in Ref. [463] for a 40 nm thick, $x = 0.28$, $\text{Si}_{1-x}\text{Ge}_x$ template layer deposited on a 1.5° off $\text{Si}(001)$ substrate. The patterns form a 2D square lattice of

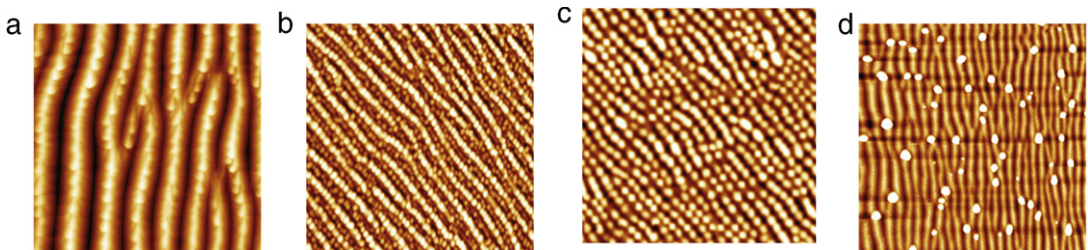


Fig. 188. AFM images of Ge dots self-organized on the top of SiGe undulated layer. Different situations are presented with different islands sizes: (a) Ge hut islands $1.5 \times 1.5 \mu\text{m}^2$; (b) Ultra-small Sb-mediated Ge islands $1.5 \times 1.5 \mu\text{m}^2$; (c) Ge domes islands $4 \times 4 \mu\text{m}^2$; (d) super-dome fully relaxed islands $4 \times 4 \mu\text{m}^2$.

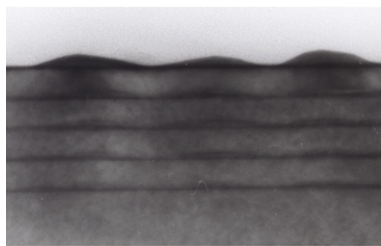


Fig. 189. TEM cross-section image of a multilayers SiGe/Si stack which evidences the self-alignment of SiGe islands on the top of underneath SiGe islands.

rectangular undulations. The deposition of Ge on such patterns results in a 2D array of homogeneous dome-like islands with Ge islands perfectly decorating the top of the underneath patterns [121]. Since stress relaxation is assumed to be larger at the top of the undulation than in its bottom, one may deduce that ordering of Ge islands is mainly induced there by stress relaxation. Other experiments on patterns with different shapes such as unidirectional periodic undulations developed on Si(001) substrate misoriented by 10° off confirmed this result [121]. AFM images of the deposited layers, see Fig. 188, show that Ge islands (dome and hut islands) perfectly align on the top of the undulations. In this case, since the monoatomic steps of the substrate are perpendicular to the undulations, they do not influence the nucleation of Ge dots. Stress relaxation induced by the presence of an underlying undulated SiGe layer may therefore be seen as being at the origin of the dots ordering. Finally, note that fully relaxed Ge islands such as superdomes are no more ordered with the underlying template layer and their spatial order vanishes, see Fig. 188(d).

4.3. Strain inhomogeneities

Ordering the QD self-organization may also be achieved by creating a modulation of elastic strain in order to create preferential centers for island nucleation [373]. Various nanofabrication techniques were developed to obtain large scale periodic arrays of elastic strain gradients at the cap layer surface. For instance, it was reported that uniform buried SiGe islands in SiGe/Si multilayers, could efficiently modulate the surface strain [464]. An example of vertical alignment of SiGe islands in multilayers stacks is presented in Fig. 189. Following [465], one may compute in $1 + 1$ dimensions the stress produced by a buried island at a depth x below a surface which leads to the total strain on the surface ϵ which is merely [465]

$$\epsilon(x) = C / (x^2 + L^2)^{3/2} [1 - 3L^2/(x^2 + L^2)], \quad (84)$$

where C is a constant, and x , the orthogonal distance on the surface plane from the point above the point inclusion at a depth L . Based on this energetic estimate, it was shown that for a single buried island, the favored nucleation position is directly above it while nucleation is disfavored at lateral offsets of $L\sqrt{2}$, with the strain dropping smoothly to zero at large distance [465]. The preferential nucleation centers were determined by minimizing ϵ in Eq. (84) [465]. Using this model, the evolution of the island distribution in successive layers on top of randomly distributed buried islands may be computed, see Fig. 190 [465]. It evidences vertical correlation between islands in successive layers together with an improvement of the spatial order and size uniformity during growth, in agreement with experiments. A more recent analysis based on a numerical resolution of elasticity used a phase-field model to describe the multilayer growth resulting from alternation of strained layers of e.g. Ge and strain-free spacer layers of e.g. Si. The buried islands produce a strain field which influences the surface chemical potential and thus the dot growth. The simulation reveal that islands (i) align with buried islands underneath the spacer layer and (ii) develop a narrow size distribution. The analysis of the chemical potential of the strained species indeed displays a minimum near the top of the buried islands which favors a columnar structure and improves

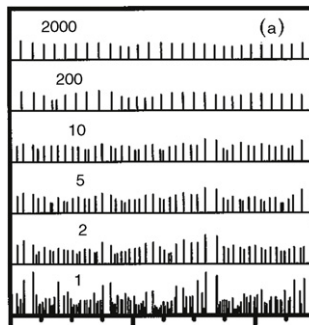


Fig. 190. Calculated island positions and sizes in selected successive layers (numbers indicated). Heights of vertical lines represent island volumes, relative to average for that layer. Sequences begin with closely spaced randomly distributed islands in layer 1.

Source: from [465].

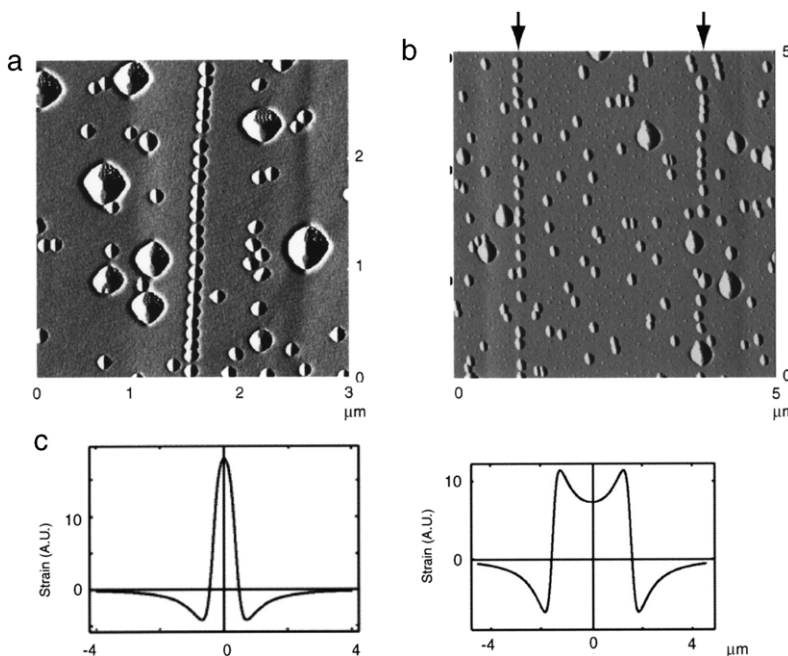


Fig. 191. Gradient-mode AFM images of the surface after growth of Ge on (left) 700 nm and (middle) 4 μm implantation width line patterns. Plots of the total strain function evaluated at the surface for a square lattice of inclusions in which the inclusions are 100 nm apart and 300 nm below the surface. The arrays are 10 μm long by 600 nm (c) and 4 μm (d) wide respectively. The cross section perpendicular to the center of the line pattern along a line is shown. The horizontal axes correspond to surface distances in micrometers; the vertical scales are in dimensionless units CL^{-3} .

Source: from [466].

strain-induced ordering upon subsequent growth. This effect saturates after some deposited layers in connection with the saturation in the island size.

In other experiments [466], oxide inclusions were put at selected places within the Si bulk by implanting O ions through a poly-Si and SiO_2 mask. Openings for implantation are created by optical lithography leaving behind only the thermal oxide layer. In a second step, the substrate and its pattern are annealed in an Ar atmosphere and finally the pattern is removed by a lift-off etch in a HF:H₂O 1:3 solution. As a result, inclusions at distances $L = 700$ nm and 4 μm were formed. The alignment of Ge islands on the higher strained areas of the substrate is evidenced on Fig. 191. The stress produced by the inclusions may be calculated using Eq. (84). The strain distribution depends on the width of the pattern as can be seen on the cross section perpendicular to the line pattern, see Fig. 191(c) and (d). It is shown that the Ge islands align on the higher strained areas of the substrate as evidenced in Fig. 191(a–b). In these areas, inclusions patterns widths of $L = 700$ nm, Fig. 191(a), and 4 μm , Fig. 191(b), were formed. The effect of L on the self-organization is both the strain distribution and the Ge dots alignment is clearly proven [466].

While energetic models can qualitatively reproduce the influence of strain produced by buried layers on the nucleation of islands in subsequently deposited layers, they cannot reproduce the exact positioning observed during experiments [467,468,185]. To better understand the nucleation of 3D islands using strain gradients at the surface, it is necessary to

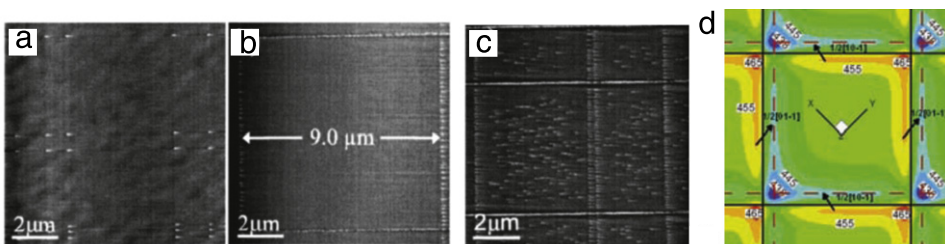


Fig. 192. (a–c) AFM images of Ge dots on a partially relaxed $\text{Si}_{0.9}\text{Ge}_{0.1}$ buffer layer with Ge coverages of: (a) 4.0 Å; (b) 4.5 Å; (c) 5.0 Å. Source: from [470].

(d) represents a square network of dislocations with mixed Burgers vectors. Solid lines represent the dislocation lines and dotted lines represent the intersections between the slip-planes and the free surface. The contours of $\mu(x, y)$ are in J/m^3 . Source: from [471].

develop models considering the interplay of strain relaxation and kinetics (deposition flux, diffusion barriers, ...). The thickness of the spacer is a crucial factor which rules the influence of the pattern on the subsequent QD self-organization: while for thin spacers the probability of nucleation on top of buried islands is near unity, a transition is observed from a correlated to an anti-correlated growth for a given thickness while the vertical correlation disappears for thick spacers [469]. Such experimental results have still not been fully elucidated.

The strain gradients induced by misfit dislocations were widely investigated for their ability to direct preferential nucleation of Ge islands [470,373]. Examples of preferential nucleation of Ge islands on dislocation lines are presented in Fig. 192 for increasing Ge coverages (from 4 to 6 Å). In this case, the localization of the QDs displays an offset to one side of the dislocation which may be explained by the calculation of the formation energy of Ge dots. The distribution of the surface chemical potential μ was computed in various configurations by solving the strain field induced by a misfit dislocation near a free surface. For an array of misfit dislocations, one can show that the QDs nucleate preferentially at sites with low formation energy: the minima of μ are located at dislocation intersections, or more specifically at positions where two intersection lines meet. The positions of low μ values are along the intersection lines. The study also reveals that the intersections of the slip-planes with the free surface corresponds to maxima of the tensile strain, so that, because of their positive misfit, Ge dots should preferentially nucleate at these site in agreement with experimental results [471]. The formation energy of a square network of dislocations was found to be of the order of 500 J/m^3 ($\sim 10^{-4}$ meV/atom) which is relatively low but enough to provide preferential sites as a difference $\mu_{\max} - \mu_{\min}$ as low as $10 \text{ J}/\text{m}^3 \sim 2 \cdot 10^{-6}$ meV/atom is enough to control the QDs spatial order. This difference gradually decreases as the thickness of the capping layer increases, while QDs randomly nucleate above a thickness of 300 nm [471].

In other experiments large scale nanopatterning was created by etching a silicon cap layer deposited on a periodic array of buried dislocations obtained by twist bonding [472]. The process produces regular square patterns whose pitch depends on the twist angle. Deposition of Ge on such a patterned substrate evidences the ordering of dots on the silicon bumps. This behavior was attributed to the elastic energy density associated with the dislocation strain field at the surface even if very low values (in the range of $2.5 \cdot 10^{-4}$ meV/atom) are measured for pure screw dislocations [472]. The elastic energy density immediately below the surface is merely

$$E(x, y) = \frac{1}{2} \sum_{i,j} \sigma_{ij}^d \epsilon_{ij}^d,$$

where σ_{ij}^d and ϵ_{ij}^d are the stress and strain on the free surface of the buffer layer due to the misfit dislocations at a depth h . The elastic energy of a square network of pure screw dislocations is maximum right above and along the dislocation line. Consequently, the well-defined square network of trenches with the same periodicity as the dislocation network obtained in [472] can be rationalized by a strain-selective etching [471], and the self-ordering of Ge dots may be explained by the elastic energy variations on the free surface.

4.4. Impurities

The use of impurities to control epitaxial growth has been widely investigated under the name of “surfactant mediated growth”. The major goal is to avoid the formation of islands and/or the nucleation of dislocations. In particular the retardation of Ge island formation in presence of As or Sb was reported in Refs. [454,221]. This effect was explained by the surfactant effect of the impurity which can imply either a lowering of the surface energy or a decrease in the surface diffusion. When lowering the surface energy, impurities force Ge to wet the substrate and maintains the 2D growth mode, while when decreasing the surface diffusion, it kinetically controls islanding. These two situations were reported in the literature [458].

In some experimental conditions, a focused ion beam is used to impact the surface in specific areas providing a local implantation of ionic species. The deposition of Ge on such patterned substrate was investigated at different temperatures [473]. It was reported that the presence of Au at the surface considerably modifies the islands ordering, size

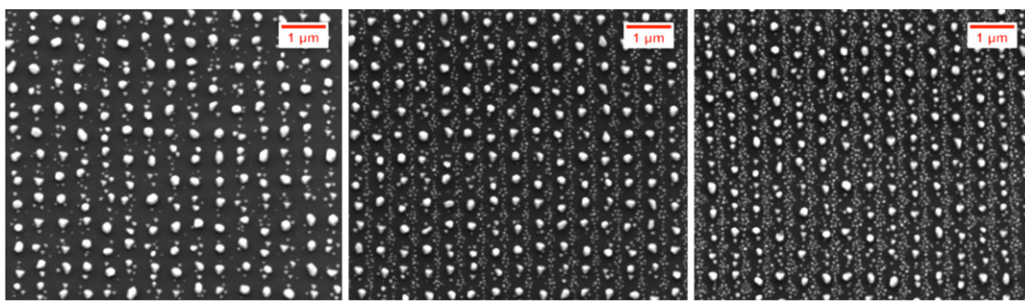


Fig. 193. Morphological evolution of the Ge islands grown on a prepatterned Si(111) surface as a function of Au coverage. Lines of Au were locally implanted in the subsurface using different doses of Au^{2+} ions: (left) low dose; (middle) medium dose; (right) high dose (from [473]). Arrows indicate the impacted lines. The scale is $5 \times 4.5 \mu\text{m}^2$.

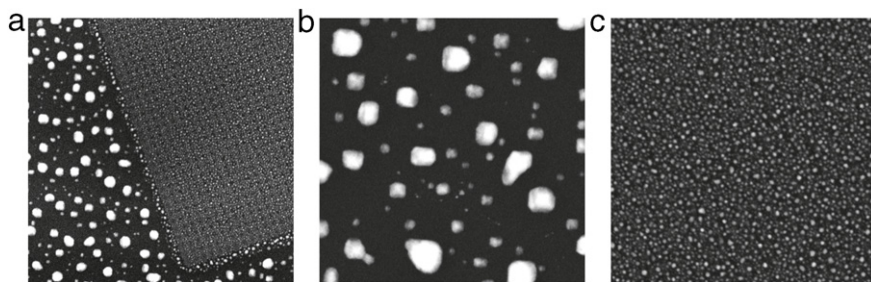


Fig. 194. SEM images of Ge islands on (a) both a patterned and an unpatterned area; zoom images on the same scale of the Ge islands on (b) the unpatterned and (c) the patterned areas. In (a) the scale is $10 \times 10 \mu\text{m}^2$. In (b) and (c) the scale is $1.7 \times 1.7 \mu\text{m}^2$.
Source: from [473].

and density. An illustration of this influence is displayed in Fig. 193. One can see that the density of Ge islands increases with the Au^{2+} ion beam dose while the islands size displays a constant reduction up to a factor 8. The situation is even more dramatic with a predeposition of Ga (using Ga^+ focused ion beam) which induces an increase in the island density by a factor 20 on the prepatterned area (Fig. 194) while the island size is about 10 times smaller. In parallel Ga predeposition also produces a modification of the island shape and aspect ratio [473]. Indeed, one can observe the onset of new facets and a large increase in the aspect ratio which can be as large as 0.8 with Ga predeposition, while 0.1 is commonly observed for Ge hut islands.

4.4.1. Surfactant effect

The surfactant effect of Ga was deeply investigated by following *in situ* the growth of Ge in a UHV chamber [474]. It was observed that the predeposition of 1 ML of Ga on a Si(001) substrate before exposition to di-germane delays the formation of islands and produces islands with different shape and aspect ratio with a higher surface density and a thinner wetting layer. Both kinetic (decrease in the adatom mobility) and energetic (change in the surface energy) arguments plead in favor of these trends [474]. It was mentioned that a decrease in the adatom mobility leads to a decrease in intermixing at the Si/Ge interface which is at the origin of a larger strain in the islands. The decrease in the island size was inferred to this strain increase, in contradiction with the interpretation of experiments on B-predeposition [459].

Moreover, using various predeposition conditions, it was noticed that a surfactant can modify the island geometry. For instance a 45° rotation of the island edges in presence of As was observed in Ref. [475] which results from a change in the surface energy anisotropy. Again with As, it was reported that long-range ordering of Ge islands doped As can be obtained in strain-relaxed epitaxial $\text{Si}_{0.5}\text{Ge}_{0.5}$ alloy layers after arsenic implantation and rapid thermal annealing (RTA). It was found that high temperature RTA causes the formation of Ge:As islands preferentially distributed along [110] directions in correlation with the cross-hatch dislocation pattern of the relaxed buffer layer, see Fig. 195 [476]. Ge islands on top of a $\text{Si}_{0.5}\text{Ge}_{0.5}$ alloy results from outdiffusion and segregation of As during a high temperature RTA and preferential nucleation of Ge islands on As occupied sites. The origin of the long-range ordering effect may be discussed in terms of strain-induced nucleation on the cross-hatch pattern and diffusion-limited growth of Ge due to As impurity [476].

As explained in Section 4.2.6, the deposition of a layer of Ge–Si alloy on a highly misoriented Si(001) substrate induces the formation of periodic undulations perpendicular to the step edges. The presence of an extra 0.5 ML of Sb causes Ge islands to have a strongly reduced size, but this dramatic reduction causes a scattering in their positioning. In order to obtain ordered and smaller islands, one has to shrink proportionally their lateral size [477] and the ripple wavelength [478]. For this purpose, one may use a Si(001) substrate 10° misoriented in the [110] direction, and a suitable composition of the $\text{Si}_{1-x}\text{Ge}_x$ alloy to obtain ripples of the desired wavelength [478]. A surfactant Sb sub-monolayer is deposited before the final

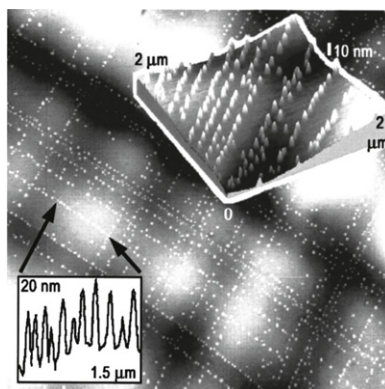


Fig. 195. AFM image of Ge:As islands on the surface of the $\text{Si}_{0.5}\text{Ge}_{0.5}$ alloy. The arrows indicate the chain of self-ordered Ge:As dots from which the height scan was taken (inset, bottom left). The inset at the top right corner is an enlarged three-dimensional image of self-ordered Ge:As chains.
Source: from [476].

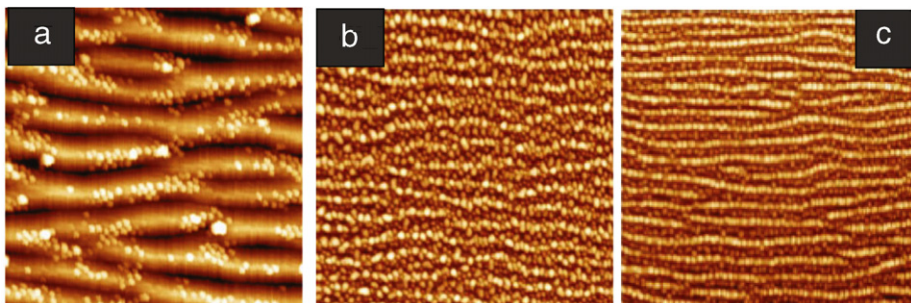


Fig. 196. [478] AFM images of 8 ML Ge deposited on (a) 1/2 ML Sb/15 nm $\text{Si}_{0.7}\text{Ge}_{0.3}/\text{Si}(118)$ at 600 °C; (b) and (c) 1/2 ML Sb/3 nm $\text{Si}_{0.5}\text{Ge}_{0.5}$. The half ML Sb is obtained in (b) by direct deposition and in (c) by a two step process with first the deposition of 1 ML and second the thermal desorption of 1/2 ML.

Ge layer. Fractional Sb coverage of 1/2 ML is obtained either by direct deposition of 1/2 ML Sb or by deposition of 1 ML Sb at $T = 400$ °C, followed by partial desorption in order to keep 1/2 of the initial layer. In the latter conditions the repartition of Sb provides a nice network of patterned and unpatterned areas. Ge islands grown on this template layer at 600 °C are shown in Fig. 196. The effect of partial coverage with Sb on the morphology and ordering of Ge islands is clearly visible. One can see that the islands align along the ripples and form close packed chains. The average island size is 35 nm. These islands are almost fully strained and display no visible facet, in contrast to the hut islands obtained during basic Ge/Si(001) heteroepitaxy with (105) facets. When the wavelength is much larger than the island size, there is almost no preferential nucleation of islands and they are randomly distributed on the surface, see Fig. 196(a). When the surfactant coverage is produced by direct co-deposition of Sb and Ge, Ge islands appear less ordered, see Fig. 196(b). We interpret this result as the consequence of the nucleation of Ge islands on Sb free areas which are randomly distributed below 1 ML coverage. When 1/2 ML Sb coverage is obtained by thermal desorption, the Sb repartition depends on the Ge concentration and stress distribution; this explains the better Ge islands ordering observed in this case, see Fig. 196(c). The Ge nucleation sites are better organized by preferential desorption of Sb from the step edges. In these experimental conditions, islands align much better along the ripples and their shape is more homogeneous. This conclusion demonstrates that it is possible to control the nucleation site and organize ultra-small Ge islands on a Si vicinal substrate by a combination of Sb surfactant-mediated growth of Ge and the creation of a suitable template layer by predeposition of a Ge-Si alloy [479].

4.4.2. C quantum fortresses

It was suggested to use carbon both as a surfactant or as a precursor to engineer the self-assembly of Ge islands, and its role on the nucleation of SiGe islands was extensively investigated [480,481,4,219,482,483]. Pre-adsorption of carbon precursors with a typical 0.1 ML coverage can lead to small ($D \sim 10$ nm) Ge islands on Si(001). These islands are randomly distributed, and display a high density of the order of $\sim 10^{11}/\text{cm}^2$ and a relatively narrow size distribution. The growth of Ge on a Si(001) surface precovered with a submonolayer of C generates c(4 × 4) reconstructed domains and proceeds via a Volmer–Weber (VW) mode. However, the microscopic mechanisms linked to the C surfactant which impacts the growth process evolution is still under investigation. It was suggested [484] that the predeposition of a C-submonolayer could create a kinetically limited deposition regime resulting from the decrease in the adatom diffusion length on the C precovered surface. This explanation is consistent with the observation that the average size of the C-induced Ge dots is generally smaller while the island density is larger. Moreover, the strain relaxation allowed by C incorporation in the SiGe layer may also be invoked to

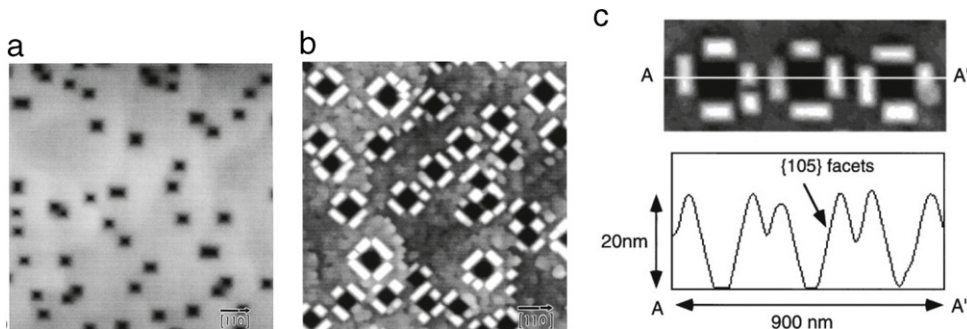


Fig. 197. AFM images of the surface morphology of: (a) the Si buffer layer grown after the deposition of Si and C on the original substrate (scan area is $5 \times 5 \mu\text{m}^2$); (b) the SiGe quantum fortress self-organized around the pits (scan area is $2 \times 2 \mu\text{m}^2$); (c) line profile of the surface showing the prolongation of the (105) facet on the pit walls.

Source: from [486].

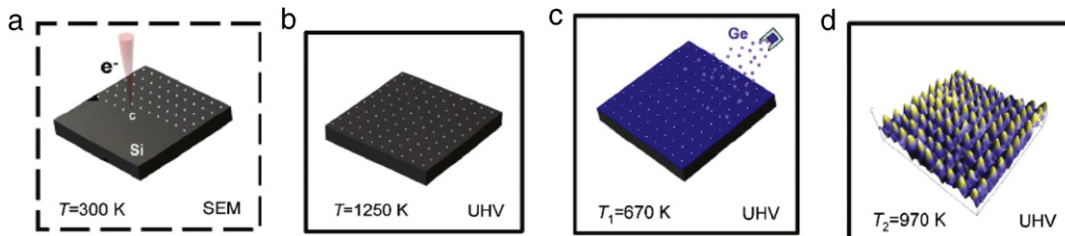


Fig. 198. Schematic representation of the C-based templating process: (a) e-beam induced deposition of carbon dot template; (b) annealing in ultra-high vacuum to form SiC nucleation sites; (c) deposition of Ge at temperature T_1 ; (d) Ge islands that form after annealing at temperature T_2 .

Source: from [407].

explain the change in the growth mode [485]. The origin of the decrease in the Ge diffusion coefficient on C-covered Si(001) substrate was also attributed to the modulation of the activation energy induced by the roughness at the interface and the increased compressive strain within the substrate [484]. These two phenomena, together with the chemical interactions among Si, C, and Ge are the main factors ruling the diffusion modulation and can be described by a linear dependence of the diffusion activation energy on the C coverage [484]. In fact, C atoms predeposited on the substrate can incorporate in the SiGe deposited layer, thus decreasing the epitaxial strain; they can also incorporate into the subsurface of the Si substrate, thus reducing the lattice constant of the C alloyed Si surface (due to their smaller size with respect to Si atoms) and increase the mismatch with the SiGe overlayer. By directly measuring the overlayer critical thickness for nucleation, it was shown that the island growth mode gradually evolves from SK when C is absent, to VW for high C coverage [484].

The use of C was also demonstrated to produce ordered quadruplet arrays of SiGe nanoclusters on the growing surface [486]. Each cluster, typically consisting of four closely spaced SiGe islands, is formed by preferential nucleation around the edges of square pits. Uniform-sized pits are directly formed by controlled deposition of Si and C on the initial Si(001) surface, followed by the growth of a thin Si buffer layer, see Fig. 197(a). After deposition of Ge, the self-organization of SiGe islands around the edges of the pits is clearly visible on the AFM images, see Fig. 197(b). A line profile of three pits with SiGe islands on their edges reveal that the pits walls have {105} orientations in continuation of the island facets (Fig. 197(c)). These results prove that the formation of {105} pit walls as precursors of island formation and elastic relaxation near the pits promotes island nucleation in specific areas [487]. A similar island geometry and self-organization process was observed in SiGe on Si systems when pits are formed by unintentional incorporation of C during the growth of the Si buffer. Sites where pits form provide energetically favorable locations for subsequent island nucleation, creating ordered quadruplet island geometries at the pit boundaries [488,2]. These results show that under kinetically limited conditions, a decrease in the step motion, which can be pinned by SiC impurities can be used to form complex ordered nanoarchitectures.

More recently, an approach based on the conjunction of C-induced Ge islands positioning and high resolution electron beam lithography was developed. The templating process involves the exposure of the Si(001) surface to a high-resolution electron-beam which produces the decomposition of carbon-containing molecules on the surface. The forming “carbon dots” have a diameter $d \sim 4-10 \text{ nm}$ and height $h \sim 1-10 \text{ nm}$ which depend on the electron beam exposure time per dot [489,407]. A schematic representation of the process is given in Fig. 198.

After patterning, the Si wafer suffers various steps to decrease the C-dots size and to form stable SiC nucleation sites by a reaction between the carbon islands and the substrate, see Fig. 199(a) [407]. Fig. 199(a) shows a regular array of C dots spaced by 35 nm and the resulting Ge islands is displayed in Fig. 199(b). Except for isolated defects, no islands are observed in untemplated areas, i.e., outside the array or in interstitial regions. An analysis of the spatial localization of the patterned area proves that the islands form within 2 nm of the initial location of the C dots [407].

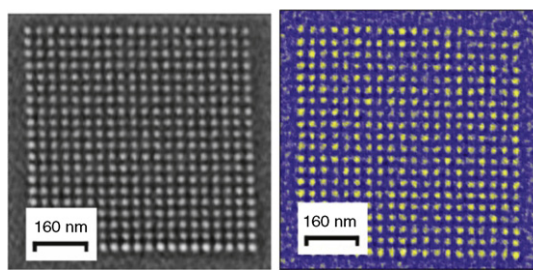


Fig. 199. AFM images of: (left) an array of 20×20 SiC dots; (right) the array 20×20 with Ge islands on SiC template.
Source: from [407].

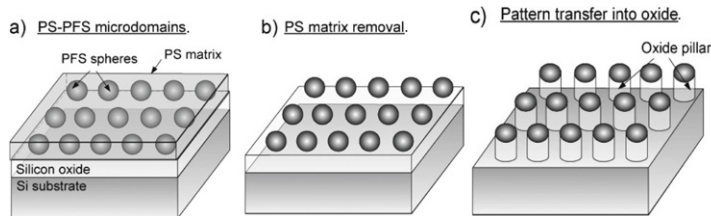


Fig. 200. Schematic representation of the block-copolymer lithography process with (a) the formation of PS-PFS microdomains; (b) the removal of the matrix and (c) the transfer of the patterns to the oxide.
Source: from [490].

4.4.3. Di-block copolymer

A new patterning technique using block-copolymer (BCP) lithography has been developed recently (See Fig. 200.) [490]. The process is based on the separation of block-copolymer microphases which form self-organized patterns with lamellar, cylindrical, or spherical morphologies and a characteristic length scale that depends on the volume ratio and chain length. Block copolymers in which one block is organic while the other one contains Si are appealing for self-assembled lithography because of the high etch contrast between the blocks, the high etch resistance of the Si-containing block, and the high Flory–Huggins interaction parameter which is expected to minimize line edge roughness. The localization and long range order of the microdomains can be controlled using shallow topographical features. BCP lithography has been used to induce self-organized patterns that generally have local close-packed order. Experiments were performed using a polystyrene-block-polyferrocenyldimethylsilane (PS-b-PFS) block copolymer which forms spherical PFS microdomains surrounded by a PS matrix during annealing. The organometallic PFS blocks have a high resistance to etching allowing for a good pattern transfer into the underlying film. Such topographical templating with lithographically defined locations could serve to self-organize various kinds of nanostructures over centimeter-sized substrates [490].

The study of Ge deposition on topographically patterned Si using PS-PMMA diblock copolymer was performed by various teams [491,492]. To make the nano-patterned template for the epitaxial growth, a thermal SiO_2 layer is initially grown on the Si(001) substrate and then polystyrene (PS)-polymethyl methacrylate (PMMA) diblock copolymer is spin coated on top of SiO_2 . Cylinders of PS become spatially separated from PMMA in an hexagonal close-packed configuration during vacuum annealing. After self-organization by phase separation and development in an acetic acid, cylindrical pores with 10 nm diameter are produced in the PS matrix with a 20 nm spacing. The regularly spaced PS patterns can then be transferred into the underlying SiO_2 layer through anisotropic reactive ion etching (RIE). In order to provide a Si nano-patterned template, the Si substrate is further etched and in a last step, the SiO_2 mask is removed by etching [492]. When grown on such nanopatterned substrate, Ge dots nucleate preferentially near the bottom perimeter of individual holes and subsequently grow till the hole is completely filled. Note that the filling of the holes is non-uniform in the experimental conditions used in [491]. During subsequent growth, there appears to be a kinetic barrier to the further increase in the size of individual Ge dots once the hole in the Si substrate is completely filled. In this case, Ge dots appear to be significantly relaxed by dislocations. However, even if the results did not provide defect free dots, they did show the possibility of fabricating high aspect ratio ($\sim 1:1$), high density ($\sim 5 \times 10^{10} \text{ cm}^{-2}$) and ordered (with hexagonal symmetry) Ge dots on Si [491]. Ge deposition may also be carried out on Si substrates designed with a SiO_2 mask patterned using a diblock copolymer, after the SiO_2 mask has been etched away. In this case, the aspect ratio of individual Ge dots remain low ($\sim 1:5$), but the dot size is quite uniform and the island density, quite high ($\sim 5 \times 10^{10} \text{ cm}^{-2}$), see Fig. 201 [491].

4.5. Exotic substrates

Self-organization of SiGe nanostructures on new ‘exotic’ substrates was recently obtained on Si substrates nanostructured by nanomechanical effects. Three different kinds of template materials were used for this purpose: nanowires, nanoribbons

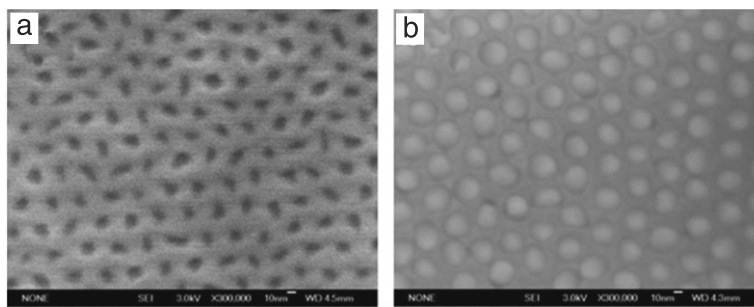


Fig. 201. Plane view SEM images of the SiO_2 nanopatterned Si template before (a) and after (b) the epitaxial Ge growth showing well-controlled Ge selective growth.

Source: from [491].

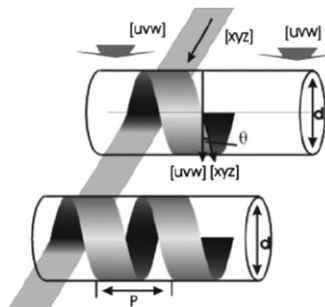


Fig. 202. Schematic drawing of a helix formed by rolling-up of a stripe. The definitions of diameter d , pitch p , and helicity angle θ are presented in the figure where $p = \pi d \tan \theta$. The crystal orientation of the stripe is represented by [xyz], and [uvw] is defined as the scrolling direction. This helix shows a right-handed chirality.

Source: from [493].

and nanomembranes. Such geometrical shapes that have periodic or aperiodic sinusoidal wavy or buckled morphologies enable high levels of mechanical stretchability, bendability and compressibility that exceed, by orders of magnitude, the intrinsic fracture strains of the materials. For instance, ribbons with configurations of coil or helix enable large stretchability. They mechanically behave like spring, according to Hooke's law, $F = k \Delta x$, where F is the force applied to stretch the ribbon along the helix axis, k is a parameter which depends on the helix geometry and on the material of the ribbon, and Δx is the change in the length of the helix [494]. Semiconductor nanoribbons with helix shape were first fabricated on template layers made of strained multilayered films grown on single-crystal wafers and lithographically cut into ribbon shapes, and then released from the substrate for instance by dissolving the sacrificial template layers underneath the ribbons. Upon release, the strained layers in the ribbons cause them to spontaneously bend upward and roll into tubes or helices [493]. The thickness, composition, and longitudinal crystalline orientation of the ribbons determine the shape (tube or helix) and geometrical parameters (diameter, length) of the resulting structures. It was reported that there is a strong correlation between the geometry of the helices and the properties of the template layers. For instance when helical nanobelts are fabricated on $1\text{ }\mu\text{m}$ wide mesas by e-beam evaporation of Cr on Si/SiGe bi-layer structure, the scrolling process is produced by the trilayer structure and the scrolling direction is determined by the orientation of the smallest Young's modulus which results from the combination of the Young's modulus of the two bilayers, Cr/Si and SiGe/Si. A schematic drawing of a helix with right hand chirality formed by rolling-up of a stripe is presented in Fig. 202. The crystal orientation of the stripe is [xyz] while the scrolling direction follows [uvw]. Reducing the mesa line width increases the impact of edge effects on the scrolling process which directly affects the chirality, scrolling direction, and diameter of SiGe/Si nanoscrolls as well as SiGe/Si/Cr helical nanobelts. Fig. 203 gives an example of 3D ring-like structure formed from a Si/amorphous Cr bilayer after selective etching of the undoped Si substrate underneath.

Various nanofabrication approaches were developed for the generic design of nanomechanical architectures based on strained bilayer thin films. They allow the fabrication of a variety of nanostructures, such as nanotubes, nanorings, nanodrills, and nanocoils, using combinations of different materials, see Fig. 204. The process results from the bending of the strained bilayer thin film due to lattice-misfit strain in the two layers. In particular, when the film thickness is reduced to the nanometer scale, its bending magnitude can be so large that it can fold into tubular shapes with multiple turns as the film length becomes longer than $2\pi R_0$, where R_0 is the characteristic radius of curvature of the bending film. Such process was reported for Si thin film deposited on SiGe strained-layer on insulator SGOI [495]. In these conditions the total energy of a nanotube versus a nanocoil, as a function of the film length, width, and thickness has been calculated and a phase diagram defining the thermodynamic limit for nanotube versus nanocoil formation, in terms of film length and width has been

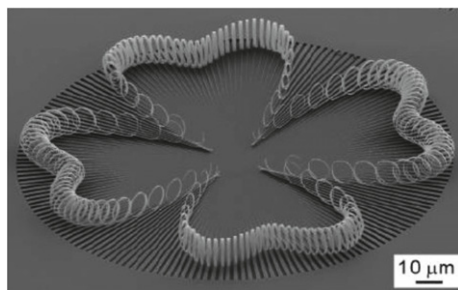


Fig. 203. SEM image of 3D structures formed from a bilayer of p-type crystalline Si coated by amorphous Cr. The ringlike structure is formed after selective etching of the undoped Si substrate underneath.

Source: from [493].

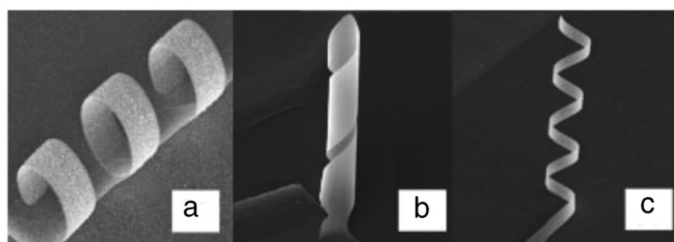


Fig. 204. SEM images of nano-architectures fabricated from strained Si/SiGe bilayer films: (a) Nanoring; (b) nanodrill; and (c) nanocoil. In general, the thickness can be varied from 10 to 200 nm and length and width from 20 nm to 100 μm .

Source: from [495].

deduced. It was shown that there exists a critical film width above which nanotubes form and below which nanocoils form. Conversely, for a given film width, there exists a critical film length. There exists an upper limit of film width for nanocoil formation, above which only nanotubes form. The maximum width for coil formation is only about 3% of L_0 , where L_0 is the minimum length for coil formation. Hence, the nanocoil is generally much harder to form by shearing when the most compliant direction is aligned with the long edge of the film and external force is needed to transform the naturally folded tube into a more stable coiling state [495].

New strategies were also developed to fabricate stretchable wavy structures by bonding patterned ribbons or wrinkled stiff thin films to prestrained elastomeric substrate and then releasing the prestrain [496,497]. The first step of the process involves fabricating semiconductor nanoribbons from a mother wafer by lithographic top-down approaches while holding anchors at the ends of the ribbons to keep them attached to the mother wafer, see Fig. 205. This procedure allows the ribbons to retain the order defined by the lithographic methods used in their fabrication. In the next step, the pre-stretched PDMS substrate is laminated (from a length of L to $L + \Delta L$, resulting in a prestrain of $\epsilon = \Delta L/L$) with an oxidized surface onto the ribbons to ensure a conformal contact between the ribbons and PDMS. During this peeling step, Van der Waals and/or surface chemical bonding between the ribbons and PDMS are sufficiently strong to transfer all the ribbons to the PDMS surface; the relaxation of the pre-stretched PDMS produces rippled geometries with layouts that are determined by the level of prestrain, the mechanical properties of the materials and their geometrical features. Si nanomembranes can be curled into hybrid three-, two-, or one-dimensional structures [498] and they can be designed into wires of any shape or orientation depending on the nanolithography techniques. In these situations, the two surfaces of the membrane are physically close enough to each other to produce a coherency between the processes that occur on each surface. In particular, elastic interactions are completely changed by accessibility to both membrane surfaces and by the ability of the membrane to react by changing shape and dimensions. Free-standing Si nanomembranes have been fabricated by successive oxidation and chemical etching of the underlying SiO_2 to leave a thin Si sheet on a buried layer of SiO_2 .

When a SiGe alloy is deposited simultaneously on both sides of the free-standing nanomembranes, hut strained QDs form on the two surfaces of the membrane and their strain fields interact across the thickness of the membrane [499,500]. Self-ordering of the QDs occurs via through-membrane elastic interactions since the locally distorting thin nanomembrane provides a strong and precise feedback for self-organization of the nanostressors, see Fig. 206 [499]. In these systems, self-assembly of SiGe islands show an anti-correlated alignment on both sides of Si nanomembrane or Si nanowire. The local strain can be made large enough, by using ribbon thicknesses as low as 10 nm and growing nanostressors that produce a high strain. In addition, the SiGe islands can act as nanostressors to periodically strain a Si nanowire, creating a novel type of single-element strain superlattice [501]. A recent procedure used bond-back of a patterned SiGe nanoribbon epitaxial layer onto the host Si substrate upon selective under-etching. The observations evidenced the formation of SiGe nanoribbon bonded to the Si substrate. Following this approach, the SiGe wiggled Hall-bar structure is completely self-assembled with no

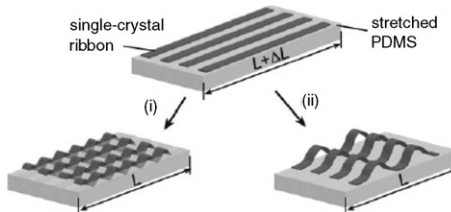


Fig. 205. Schematic illustration of procedures for fabricating rippled semiconductor nanoribbons on elastomeric PDMS substrates. Wavy and buckled profiles on PDMS surfaces that are functionalized for surface chemical bonding uniformly along the lengths of the ribbons (step i) and selectively along only certain portions of the ribbons (step ii) (see [496,497]).

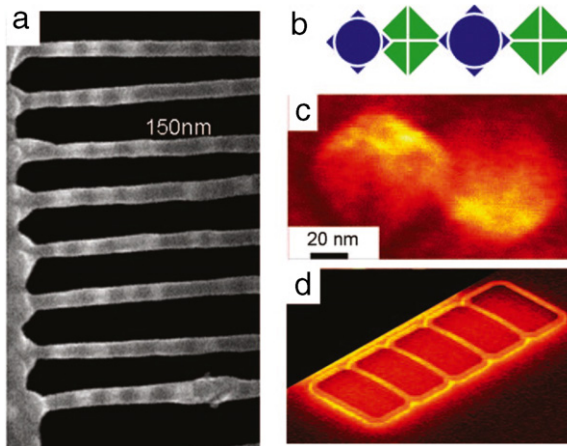


Fig. 206. (a) Scanning electron micrograph of rows of pure Ge QDs ordered and regularly separated by ~ 150 nm on 20 nm thick and 80 nm wide Si(001) nanoribbons cut along [110] and tethered on both ends. (b) Schematic diagram of dot ordering on the two surfaces of the ribbon. (c) Relationship between nucleation on top and bottom of a ribbon; (d) SEM micrograph of a set of nanoribbons showing global bending (see [499]).

predefined bonding. The wrinkled nanomembrane was created by the selective etching in HF vapor of a structure constituted of Si substrate/SiO₂/Si/SiGe [502].

Free-standing two-dimensional semiconductor nanomembranes and helices of several kinds of semiconductors were also grown through chemical synthetic approaches. Surfactant-directed surface assembly processes, where the surfactant serves as a template, were used to form and direct the crystallization of single-crystalline nanomembranes over the entire surface of water. The free-standing nanomembranes are then transferred to an arbitrary substrate and could be integrated with flexible polymer substrates. Such low-cost and large-scale synthesis approach circumvents the need of single-crystalline substrates for making large-area nanomembranes. Moreover, the active functional device elements that can be formed on the surfaces of the wavy or buckled substrates, represent a class of potentially valuable building blocks for stretchable electronics, with applications in flexible thin-film transistors, health monitors, sensory skins, spherically curved optics ... [503,504]. It was shown that by subjecting semiconductor epilayers on sapphire substrates to low-energy/low-dose ion treatment with subsequent photo-electrochemical etching, it is possible to fabricate ultra-thin suspended membranes. Such membranes are transparent to both UV-radiation and keV-energy electrons and their architecture is dependent on the stirring conditions of the electrolyte during electrochemical etching [505].

Finally, another class of SiGe nanostructures that could serve for the self-organization of Ge islands are SiGe nanowires. It was demonstrated that 3D Ge islands grow around Si nanowires by the Stranski–Krastanov mechanism [506]. During the CVD growth of Si–Ge core-shell nanowires, when switching the growth from Si to Ge, as a result of the much higher deposition rate, Ge deposits radially and epitaxially around the initially grown Si nanowires. What is interesting is that instead of coating the Si nanowires as uniform shells, they form 3D island structures around the Si nanowires. When the inlet gas is returned back to SiH₄, the Si regains axial growth. Fig. 207 shows an example of such Si–Ge/Si nanowires with a diameter of about 200 nm. In these conditions, the Ge islands are epitaxial with respect to the Si core. It is also noticeable that the islands are not grown randomly around the Si core, but they appear to be aligned along particular crystallographic facets of the Si nanowire. It is known that Si nanowires tend to facet on low-index crystallographic planes in order to reduce the surface energy. This faceting process can be clearly seen on the Si nanowire shown in Figs. 207 and 208. The Si nanowire with [11-2] axis has facets at (111), (11-0), and {113} planes, forming an octagonal surface while the Ge islands on the outer surface exhibit {113} side facets, which are inclined by 58.5° to the (111) Si facet. Furthermore, the Ge islands appear to grow preferentially on certain Si planes, for example, (111) is more favored compared with (11-0) and {113}, probably because (111) has the lowest surface energy. The diameters of the Si nanowire has been reported to be

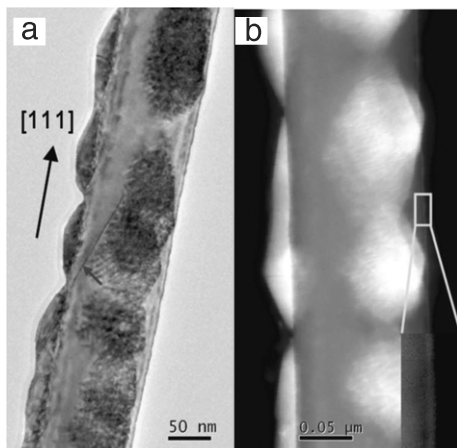


Fig. 207. (a) Bright-field TEM and (b) ADF STEM images of the Ge islands deposited on Si nanowires where Moiré fringes are clearly seen. The inset in (b) shows a thin Ge-rich layer at the surface of Si nanowire (see [506]).

a crucial parameter for the onset of Ge islands growth but a more systematic study is requested to try to understand the underlying factors that control the epitaxial growth of Ge islands around the nanowires. Different continuum approaches have been developed to study the combined effect of mismatch strain and geometrical parameters on the morphology of epitaxial core-shell nanowires [507–509]. The results highlight the importance of geometry in determining the nanowire morphology. The dependence on the core size allows to rationalize the cylindrical (stable) and island (unstable) growth observed experimentally in the Si–Ge system. The variation with shell size shows the importance of the growth rate, relative to surface relaxation kinetics, in controlling the shell morphology. The latter can be changed from stable shells to epitaxial islands solely by adjusting the growth rate, even in regimes of geometric parameters where the theory strictly predicts uniform shells [508]. The development of a more comprehensive understanding of the morphological evolution of core-shell nanowire heterostructures is required especially as regards the account of intermixing, anisotropic surface energies, surface stresses, and kinetics.

5. Conclusion

2011 has seen the SiGe alloys invading most of the microelectronic systems previously dominated by silicon. For example, so-called “smart” energy systems with leading edge performance products such as Power Amplifiers (PAs) and Drivers, Low Noise Amplifiers (LNAs), Switches, Phase Lock Loops (PLLs), Voltage Control Oscillators (VCOs), Synthesizers, Diodes and Front-End Modules (FEMs) are commonly fabricated with SiGe. These systems are used in a wide range of applications such as wireless local area networks (WLAN), automated metering infrastructure (AMI), automated meter reading (AMR), professional mobile radio (PMR), RF and microwave products for security systems, including radio communications, radars, electronic surveillance, electronic countermeasures etc. Moreover, discrete components and multifunction subsystems including packaged, chip and beam PIN diodes, chip attenuators, power amplifiers, mixers, (de)modulators, switches, attenuators, detectors, directional and hybrid couplers, power splitters/combiners, ceramic filters, resonators etc., are also using SiGe active components. However, despite the large industrial activity based on SiGe, the use in industrial applications of SiGe quantum objects is still very limited. This is mainly due to the lack of control and reproducibility of the quantum objects since many fundamental issues concerning their growth and self-organization are still unclear and under debate and need further deep investigations to be fully clarified.

The growth and self-organization of SiGe nanostructures is now a mature field which embodies several communities from crystal growth and surface physics to pattern formation in non-equilibrium systems. It has attracted attention not only for its applications in the microelectronic industry as recalled above, but also as a system which represents, due to its chemical simplicity, a paradigm for coherent hetero-epitaxy in the Stranski–Krastanov mode. Despite its apparent simplicity, it has led to a surprising rich complexity since its discovery more than 30 years ago. The detailed scrutiny of structures such as pre-pyramids, pyramids and domes which arise due to the interplay between the elastic and capillary effects have revealed that not only surface diffusion is at work but that alloying, intermixing and volumic diffusion play a fundamental role during growth. The competition between thermodynamics and kinetics effects rules the different morphological structures that may be found but the coarsening of islands is still a matter of question. The various experimental techniques (AFM, STM, LEEM, TEM, X-ray etc.) which allowed to discover new structures have been pushed to their limits of accuracy in order to obtain an atomic resolution of the strain and composition fields. The theoretical model which range from ab-initio to continuum modeling have permitted for example to investigate the striking appearance of the (105) facets, the evolution and interrupted coarsening of large arrays of islands and alloying in the islands. More recently, substrate patterning using

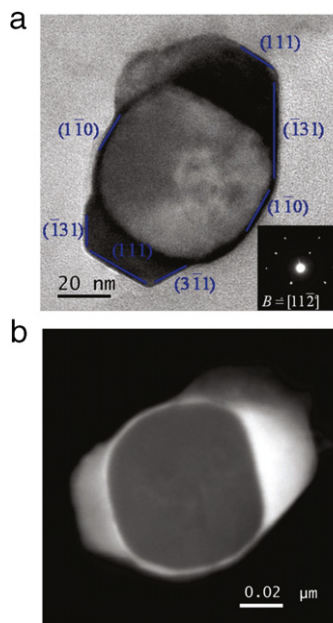


Fig. 208. (a) Bright-field TEM and (b) ADF STEM images of the cross-section of a Ge/Si nanowire, where faceting is clearly seen on the outer surfaces of the Si core and the Ge islands (see [506]).

the most recent nanotechnological tools have allowed to control the position and size of islands and is a natural route for substrate functionalization.

In this review we have given a comprehensive overview of the research work on growth and self-organization of SiGe nanostructures. More precisely, in Section 1, we have given a broad introduction where the basic properties of quantum dots and the challenges for their integration in microelectronic devices are recalled. In Section 2, we have described mainly from an experimental point of view, the morphological, structural and compositional evolution of SiGe nanostructures epitaxially grown on nominal, vicinal and patterned surfaces. We have reviewed the most relevant experimental data concerning island characterization and formation in SiGe films, focusing on the 2D to 3D transformation of SiGe nanostructures. We have emphasized the difference between the nucleation regime in the high-strain regime and the instability regime observed in the low strain case. We have shown the extensive role played by intermixing and its questionable origin. We have also discussed the interplay between strain and composition and emphasized the lack of sufficient information on this interplay at the atomic scale. In Section 3, we described the basic concepts and the mechanisms at the origin of island formation. We presented different theoretical models which describe the formation of islands in interaction with a wetting layer, their unusual coarsening and the alloying phenomena resulting from the growth dynamics. We have discussed the various morphologies corresponding to different levels of strain: 2D undulations for low strain relaxation and 3D islands with different shapes for higher relaxation. Coarsening has been addressed using a combination of energetics and kinetics modeling and compared with the coarsening found in experiments. We have also reviewed the mechanisms for surface and volume diffusion of different atomic species in nanostructures in order to give insights into the redistribution of Ge in the nanostructures. In Section 4, we have put a special focus on the self-organization of SiGe nanostructures on functionalized substrates (bottom-up approach) both theoretically and experimentally. We recalled that there exists a limit to perfect natural self-organization due to fluctuations resulting both from kinetics and energetics effects. This has led the community to investigate the self organization of SiGe islands on various patterned substrates. We have disclosed several ways to control the position of islands using conventional or local nanolithographic techniques. We have also reported some results on the effect of template layers (impurities, surfactants, di-block copolymer) on the spatial position of SiGe nanostructures. We have shown that despite a rich literature on the localization of nanostructures on patterned substrates, the complete understanding of the effect of shape and impurities on self-organization is still controversial and deserves extended efforts.

As a conclusion, we have shown that many fields on growth and self-organization of SiGe nanostructures are still controversial and need further research coupling modeling and experimental results. We have extracted some relevant issues on which we would like to stimulate further research. Among others things, we focus on: (i) the relation at the atomic scale between strain, composition and morphology of SiGe nanostructures; (ii) the understanding of the intermixing using the coupling between atomic scale characterization of unique objects and modeling; (iii) the unusual coarsening at work in strained islands which significantly differs from the usual description of Ostwald ripening; (iv) the effect of patterned substrates on the growth and self-organization of nanostructures which is still under scrutiny both experimentally and theoretically; (v) the quantitative comparison between theory and experiments, e.g. thanks to multi-scale analyses using ab-initio calculations which are still limited to small systems and larger scale modelizations such as Kinetic Monte-Carlo

simulations or dynamical models, which can capture long range phenomena (For example, further investigation is required as regards the quantitative computation of the diffusion coefficient and of the intermixing rate in SiGe systems, which are essential for a quantitative theory which is meant to be confronted to experiments); (vi) the relation between the SiGe nanostructures formation, atomic structure, strain and composition and their local electronic and optical properties. Despite their relative simplicity and now well-grounded basic description, the paradigmatic SiGe systems are still raising puzzling questions and are definitively calling for deeper investigations of both fundamental and applicative issues.

References

- [1] B. Voigtänder, Fundamental processes in Si/Si and Ge/Si epitaxy studied by scanning tunneling microscopy during growth, *Surf. Sci. Rep.* 43 (2001) 127.
- [2] I. Berbezier, A. Ronda, A. Portavoce, SiGe nanostructures: new insights into growth processes, *J. Phys.: Condens. Matter* 14 (2002) 8283.
- [3] K. Brunner, Si/Ge nanostructures, *Rep. Progr. Phys.* 65 (2002) 27.
- [4] J. Stangl, V. Holý, G. Bauer, Structural properties of self-organized semiconductor nanostructures, *Rev. Modern Phys.* 76 (2004) 725.
- [5] J.-M. Baribeau, X. Wu, N.L. Rowell, D.J. Lockwood, Ge dots and nanostructures grown epitaxially on Si, *J. Phys.: Condens. Matter* 18 (2006) R139.
- [6] D.D. Vvedensky, in: A.V. Narlikar, Y.Y. Fu (Eds.), *Oxford Handb Nanosci Technol*, Vol. 3, Oxford University Press, Oxford, England, 2010, p. 205. Ch. Quantum Dots: Self-organized and self-limiting structures.
- [7] I. Berbezier, A. Ronda, SiGe nanostructures, *Surf. Sci. Rep.* 64 (2009) 47.
- [8] D. Nguyen Ngoc, D.A. Sunderland, D.C. Ahlgren, S.J. Jeng, M.M. Gilbert, J.C. Malinowski, K.T. Schonenberg, K.S. Stein, B.S. Meyerson, D.L. Harame, A manufacturable poly-emitter graded-SiGe HBT technology for wireless and mixed-signal applications, *Appl. Surf. Sci.* 102 (1996) 194.
- [9] J. Dick, Recent Innovations in DRAM Manufacturing, in: 2010 IEEE/Semi Adv. Semicond. Manufacturing Conf., Book Series: *Adv. Semicond. Manufacturing Conf. and Workshop-Proc.*, 2010, p. 264.
- [10] C.B. Simmons, T.S. Koh, N. Shaji, M. Thalakulam, L.J. Klein, H. Qin, H. Luo, D.E. Savage, M.G. Lagally, A.J. Rimberg, R. Joynt, R. Blick, M. Friesen, S.N. Coppersmith, M.A. Eriksson, Pauli spin blockade and lifetime-enhanced transport in a Si/SiGe double quantum dot, *Phys. Rev. B* 82 (2010) 245312.
- [11] F. Lippis, F. Pezzoli, M. Stoffel, C. Deneke, J. Thomas, A. Rastelli, V. Kataev, O.G. Schmidt, B. Büchner, Electron spin resonance study of Si/SiGe quantum dots, *Phys. Rev. B* 81 (2010) 125312.
- [12] J.V. Barth, G. Costantini, K. Kern, Engineering atomic and molecular nanostructures at surfaces, *Nature* 437 (2005) 671.
- [13] D.J. Eaglesham, M. Cerullo, Dislocation-free Stranski-Krstanow growth of Ge on Si(100), *Phys. Rev. Lett.* 64 (1990) 1943.
- [14] Y.W. Mo, D.E. Savage, B.S. Swartzentruber, M.G. Lagally, Kinetic pathway in Stranski-Krstanow growth of Ge on Si(001), *Phys. Rev. Lett.* 65 (1990) 1020.
- [15] H. Gao, W. Nix, Surface roughening of heteroepitaxial thin film, *Annu. Rev. Mater. Sci.* 29 (1999) 173.
- [16] P. Politi, G. Grenet, A. Marty, A. Ponchet, J. Villain, Instabilities in crystal growth by atomic or molecular beams, *Phys. Rep.* 324 (2000) 271.
- [17] P. Müller, A. Saúl, Elastic effects on surface physics, *Surf. Sci. Rep.* 54 (2004) 593.
- [18] J.W. Matthews, A.E. Blakeslee, Defects in epitaxial multilayers: I. Misfit dislocations, *J. Cryst. Growth* 27 (1974) 118.
- [19] C. Teichert, Self organization of nanostructures in semiconductor heteroepitaxy, *Phys. Rep.* 365 (2002) 335.
- [20] O. Pierre-Louis, Step bunching with general step kinetics: stability analysis and macroscopic models, *Surf. Sci.* 529 (2003) 114.
- [21] N. Motta, A. Sgarlata, F. Rosei, P.-D. Szkutnik, S. Nufriis, M. Scarselli, A. Balzaretti, Controlling the quantum dot nucleation site, *Mat. Sci. Eng. B* 101 (2003) 77.
- [22] O. Leifeld, E. Müller, D. Grützmacher, B. Müller, K. Kern, In situ scanning tunneling microscopy study of C-induced Ge quantum dot formation on Si(100), *Appl. Phys. Lett.* 74 (1999) 994.
- [23] E.S. Kim, N. Usami, Y. Shiraki, Control of Ge dots in dimension and position by selective epitaxial growth and their optical properties, *Appl. Phys. Lett.* 72 (1998) 1617.
- [24] Y. Homma, Secondary electron imaging of nucleation and growth of semiconductors for nanostructure fabrication, *Thin Solid Films* 332 (1998) 262.
- [25] H. Omi, T. Ogino, Positioning of self-assembling Ge islands on Si(111) mesas by using atomic steps, *Thin Solid Films* 369 (2000) 88.
- [26] O.G. Schmidt, *Lateral Alignment of Epitaxial Quantum Dots*, Springer, 2007.
- [27] F. Hüe, M. Hýtch, H. Bender, F. Houdellier, A. Claverie, Direct mapping of strain in a strained silicon transistor by high-resolution electron microscopy, *Phys. Rev. Lett.* 100 (2008) 156602.
- [28] T.U. Schülli, X-ray in situ observation of semiconductor heteroepitaxy: from surface reconstruction to island growth, *Semicond. Sci. Technol.* 26 (2011) 064003.
- [29] A. Rastelli, M. Stoffel, G. Katsaros, J. Tersoff, U. Denker, T. Merdhanova, G.S. Kar, G. Costantini, K. Kern, H. von Känel, O.G. Schmidt, Reading the footprints of strained islands, *Microelectron. J.* 37 (2006) 1471.
- [30] I.N. Stranski, L. Krstanov, Zur Theorie der orientierten Ausscheidung von Ionenkristallen aufeinander, *Ber. Akad. Wiss. Wien, Mater., Math.-Nat. Kl. IIb* 146 (1938) 797.
- [31] O.P. Pchelyakov, Y.B. Bolkhovityanov, A.V. Dvurechenskii, A.I. Nikiforov, A.I. Yakimov, B. Voigtländer, Molecular beam epitaxy of silicon-germanium nanostructures, *Thin Solid Films* 367 (2000) 75.
- [32] G. Medeiros-Ribeiro, A.M. Bratkowski, T.I. Kamins, D.A.A. Ohlberg, S.R. Williams, Shape transition of germanium nanocrystals on a silicon (001) surface from pyramids to domes, *Science* 279 (1998) 353.
- [33] P. Sutter, M.G. Lagally, Nucleationless three-dimensional island formation in low-misfit heteroepitaxy, *Phys. Rev. Lett.* 84 (2000) 4637.
- [34] J. Tersoff, B.J. Spencer, A. Rastelli, H. von Känel, Barrierless formation and faceting of SiGe Islands on Si(001), *Phys. Rev. Lett.* 89 (2002) 196104.
- [35] J.J. Zhang, G. Katsaros, F. Montalenti, D. Scopece, R.O. Rezaev, C. Mickel, B. Rellinghaus, L. Miglio, S. De Franceschi, A. Rastelli, O.G. Schmidt, Monolithic growth of ultra-thin Ge nanowires on Si(001), *Phys. Rev. Lett.* 109 (2012) 085502.
- [36] F. Wu, X. Chen, Z.Y. Zhang, M.G. Lagally, Reversal of Step Roughness on Ge-Covered Vicinal Si(001), *Phys. Rev. Lett.* 74 (1995) 574.
- [37] O.L. Alerland, D. Vanderbilt, R.D. Meade, J.D. Joannopoulos, Spontaneous formation of stress domains on crystal surfaces, *Phys. Rev. Lett.* 61 (1988) 1973.
- [38] L. Zhong, A. Hojo, Y. Matsushita, Y. Aiba, K. Hayashi, R. Takeda, H. Shirai, H. Saito, J. Matsushita, J. Yoshikawa, Evidence of spontaneous formation of steps on silicon (100), *Phys. Rev. B* 54 (1996) R2304.
- [39] A. Ourmazd, J.C. Bean, Observation of order-disorder transitions in strained-semiconductor systems, *Phys. Rev. Lett.* 55 (1985) 765.
- [40] P. Schwander, C. Kisielowski, M. Seibt, F.H. Baumann, Y. Kim, A. Ourmazd, Mapping projected potential interfacial roughness and composition in general crystalline solids by quantitative transmission electron microscopy, *Phys. Rev. Lett.* 71 (1993) 4150.
- [41] F. Liu, M.G. Lagally, Self-organized nanoscale structures in Si/Ge films, *Surf. Sci.* 386 (1997) 169.
- [42] F.F. Liu, F. Wu, M.G. Lagally, Effect of Strain on Structure and Morphology of Ultrathin Ge Films on Si(001), *Chem. Rev.* 97 (1997) 1045.
- [43] M. Hammar, F.K. Legoues, J. Tersoff, M.C. Reuter, R.M. Tromp, In situ ultrahigh vacuum transmission electron microscopy studies of hetero-epitaxial growth I. Si(001)/Ge, *Surf. Sci.* 349 (1996) 129.
- [44] X. Chen, F. Wu, Z. Zhang, M.G. Lagally, Vacancy-Vacancy Interaction on Ge-Covered Si(001), *Phys. Rev. Lett.* 73 (1994) 850.
- [45] B. Voigtländer, M. Kästner, Evolution of the strain relaxation in a Ge layer on Si(001) by reconstruction and intermixing, *Phys. Rev. B* 60 (1999) R5121.
- [46] A. Malachias, T.U. Schülli, G. Medeiros-Ribeiro, L.G. Cançado, M. Stoffel, O.G. Schmidt, T.H. Metzger, R. Magalhães paniago, X-ray study of atomic ordering in self-assembled Ge islands grown on Si(001), *Phys. Rev. B* 72 (2005) 165315.

- [47] I. Goldfarb, P.T. Hayden, J.H.G. Owen, G.A.D. Briggs, Nucleation of "Hut" pits and clusters during gas-source molecular-beam epitaxy of Ge/Si(001) in *in situ* scanning tunneling microscopy, Phys. Rev. Lett. 78 (1997) 3959.
- [48] K. Li, D.R. Bowler, M.J. Gillan, Tight binding studies of strained Ge/Si(001) growth, Surf. Sci. 526 (2003) 356.
- [49] G.-H. Lu, F. Liu, Towards quantitative understanding of formation and stability of Ge hut islands on Si(001), Phys. Rev. Lett. 94 (2005) 176103.
- [50] P. Sutter, P. Zahn, E. Sutter, Continuous formation and faceting of SiGe islands on Si(100), Appl. Phys. Lett. 82 (2003) 3454.
- [51] A.J. Pidduck, D.J. Robbins, A.G. Cullis, W.Y. Leong, A.M. Pitt, Evolution of surface morphology and strain during SiGe epitaxy, Thin Solid Films 222 (1992) 78.
- [52] J.-N. Aqua, A. Gouyé, T. Auphan, T. Frisch, A. Ronda, I. Berbezier, Orientation dependence of the elastic instability on strained SiGe films, Appl. Phys. Lett. 98 (2011) 161909.
- [53] A.G. Cullis, D.J. Robbins, A.J. Pidduck, P.W. Smith, The characteristics of strain-modulated surface undulations formed upon epitaxial $\text{Si}_{1-x}\text{Ge}_x$ alloy layers on Si, J. Cryst. Growth 123 (1992) 333.
- [54] D.E. Jesson, S.J. Pennycook, J.-M. Baribeau, D.C. Houghton, Direct imaging of surface cusp evolution during strained-layer epitaxy and implications for strain relaxation, Phys. Rev. Lett. 71 (1993) 1744.
- [55] C.S. Ozkan, W.D. Nix, H. Gao, Strain relaxation and defect formation in heteroepitaxial $\text{Si}_{1-x}\text{Ge}_x$ films via surface roughening induced by controlled annealing experiments, Appl. Phys. Lett. 70 (1997) 2247.
- [56] I. Berbezier, B. Gallas, A. Ronda, J. Derrien, Dependence of SiGe growth instability on Si substrate orientation, Surf. Sci. 412 (1998) 415.
- [57] J.A. Floro, E. Chason, L.B. Freund, R.D. Tweten, R.Q. Hwang, G.A. Lucadamo, Evolution of coherent islands in $\text{Si}_{1-x}\text{Ge}_x/\text{Si}(001)$, Phys. Rev. B 59 (1999) 1990.
- [58] R.M. Tromp, F.M. Ross, M.C. Reuter, Instability-driven SiGe island growth, Phys. Rev. Lett. 84 (2000) 4641.
- [59] R.J. Asaro, W.A. Tiller, Interface morphology development during stress-corrosion cracking: Part 1. Via surface diffusion, Metall. Trans. 3 (1972) 1789.
- [60] M.A. Grinfeld, Instability of the separation boundary between a nonhydrostatically stressed elastic body and a melt, Sov. Phys. Dokl. 31 (1986) 831.
- [61] M. Thiel, A. Willibald, P. Evers, A. Levchenko, P. Leiderer, S. Balibar, Stress-induced melting and surface instability of ${}^4\text{He}$ crystals, EuroPhys. Lett. 20 (1992) 707.
- [62] S. Balibar, H. Alles, A.Y. Parshin, Helium crystals under stress: the Grinfeld instability, Rev. Modern Phys. 77 (2005) 317.
- [63] J. Bodensohn, K. Nicolai, P. Leiderer, The Growth of Atomically Rough ${}^4\text{He}$ Crystals, Z. Phys. B: Condens. Matter 64 (1986) 55.
- [64] J. Berréhar, C. Caroli, C. Lapersonne-Meyer, M. Schott, Surface patterns on single-crystal films under uniaxial stress: experimental evidence for the Grinfeld instability, Phys. Rev. B 46 (1992) 13487.
- [65] I. Cantat, K. Kassner, C. Misbah, H. Müller-Krumbhaar, Directional solidification under stress, Phys. Rev. E 58 (1998) 6027.
- [66] K.Y. Suh, H.H. Lee, Dynamic instability of strongly confined thin polymer films in spinodal dewetting, Phys. Rev. Lett. 87 (2001) 135502.
- [67] J.E. Guyer, P.W. Voorhees, Morphological stability of alloy thin films, Phys. Rev. Lett. 74 (1995) 4031.
- [68] Y.H. Xie, G.H. Gilmer, C. Roland, P.J. Silverman, S.K. Buratto, J.Y. Cheng, E.A. Fitzgerald, A.R. Kortan, S. Schuppler, M.A. Marcus, P.H. Citrin, Semiconductor surface roughness: dependence on sign and magnitude of bulk strain, Phys. Rev. Lett. 73 (1994) 3006.
- [69] J.Y. Yao, T.G. Andersson, G.L. Dunlop, Structure of lattice-strained $\text{In}_x\text{Ga}_{1-x}\text{As}/\text{GaAs}$ layers studied by transmission electron microscopy, Appl. Phys. Lett. 53 (1988) 1420.
- [70] V.M. Kaganer, K.H. Ploog, Energies of strained vicinal surfaces and strained islands, Phys. Rev. B 64 (2001) 205301.
- [71] A. Oral, R. Ellialtıoglu, Initial stages of SiGe epitaxy on Si(001) studied by scanning tunneling microscopy, Surf. Rev. 323 (1995) 295.
- [72] A. Videcoq, M. Vladimirova, A. Pimpinelli, Kinetic surface structuring during homoepitaxy of GaAs (110): a model study, Appl. Surf. Sci. 175 (2001) 140.
- [73] J. Mysliveček, C. Schelling, G. Springholz, F. Schäffler, B. Voigtländer, J. Krug, P. Šmilauer, On the microscopic origin of the kinetic growth instability of homoepitaxy on Si(001), Surf. Sci. 520 (2002) 193.
- [74] A. Rastelli, H. von Känel, Island formation and faceting in the SiGe/Si(001) system, Surf. Sci. 532 (2003) 769.
- [75] S. Balibar, D.O. Edwards, W.F. Saam, The effect of heat flow and nonhydrostatic strain on the surface of helium crystals, J. Low Temp. Phys. 82 (1991) 119.
- [76] A. Rastelli, H. von Känel, B.J. Spencer, J. Tersoff, Prepyramid-to-pyramid transition of SiGe islands on Si(001), Phys. Rev. B 68 (2003) 115301.
- [77] A. Carlsson, L.R. Wallenberg, C. Persson, W. Seifert, Strain state in semiconductor quantum dots on surfaces: a comparison of electron microscopy and finite element calculations, Surf. Sci. 406 (1998) 48.
- [78] T. Wiebach, M. Schmidbauer, M. Hanke, H. Raidt, R. Köhler, H. Wawra, Strain and composition in SiGe nanoscale islands studied by X-ray scattering, Phys. Rev. B 61 (2000) 5571.
- [79] N.I. Muskhelishvili, Some basic problems of the theory of elasticity, JRM Radok, P. Noordhoff, Groningen, Netherlands, 1963.
- [80] B.J. Spencer, J. Tersoff, Stresses and first-order dislocation energetics in equilibrium Stranski-Krastanow islands, Phys. Rev. B 63 (2001) 205424.
- [81] J. Tersoff, F.K. Legoues, Competing relaxation mechanisms in strained layers, Phys. Rev. Lett. 72 (1994) 3570.
- [82] D.E. Jesson, M. Kästner, B. Voigtländer, Direct observation of subcritical fluctuations during the formation of strained semiconductor islands, Phys. Rev. Lett. 84 (2000) 330.
- [83] U. Köhler, O. Jusko, G. Pietsch, B. Müller, M. Henzler, Strained-layer growth and islanding of germanium on Si(111)-(7 \times 7) studied with STM, Surf. Sci. 248 (1991) 321.
- [84] D. Pachinger, H. Groiss, H. Lichtenberger, J. Stangl, G. Hesser, F. Schaffler, Stranski-Krastanow growth of tensile strained Si islands on Ge (001), Appl. Phys. Lett. 91 (2007) 233106.
- [85] C. Priester, M. Lannoo, Origin of self-assembled quantum dots in highly mismatched heteroepitaxy, Phys. Rev. Lett. 75 (1995) 93.
- [86] C. Ratsch, P. Smilauer, D.D. Vvedensky, A. Zangwill, Mechanism for coherent island formation during heteroepitaxy, J. Phys. I France 6 (1996) 575.
- [87] P. Müller, R. Kern, The physical origin of the two-dimensional towards three-dimensional coherent epitaxial Stranski-Krastanow transition, Appl. Surf. Sci. 102 (1996) 6.
- [88] Y. Chen, J. Washburn, Structural transition in large-lattice-mismatch heteroepitaxy, Phys. Rev. Lett. 77 (1996) 4046.
- [89] A. Vailionis, B. Cho, G. Glass, P. Desjardins, D.G. Cahill, J.E. Greene, Pathway for the strain-driven two-dimensional to three-dimensional transition during growth of Ge on Si(001), Phys. Rev. Lett. 85 (2000) 3672.
- [90] I. Goldfarb, Effect of strain on the appearance of subcritical nuclei of Ge nanohuts on Si(001), Phys. Rev. Lett. 95 (2005) 025501.
- [91] K.M. Chen, D.E. Jesson, S.J. Pennycook, M. Mostoller, T. Kaplan, T. Thundat, R.J. Warmack, Step Instabilities: a New Kinetic Route to 3D Growth, Phys. Rev. Lett. 75 (1995) 1582.
- [92] P. Raiteri, D.B. Migas, L. Miglio, A. Rastelli, H. von Känel, Critical role of the surface reconstruction in the thermodynamic stability of {105} Ge pyramids on Si(001), Phys. Rev. Lett. 88 (2002) 256103.
- [93] Y. Fujikawa, K. Akiyama, T. Nagao, T. Sakurai, M.G. Lagally, T. Hashimoto, Y. Morikawa, K. Terakura, Origin of the stability of Ge(105) on Si: a new structure model and surface strain relaxation, Phys. Rev. Lett. 88 (2002) 176101.
- [94] T. Hashimoto, Y. Morikawa, Y. Fujikawa, T. Sakurai, M.G. Lagally, K. Terakura, Rebonded SB step model of Ge/Si(105)1 \times 2: a first-principles theoretical study, Surf. Sci. 513 (2002) L445.
- [95] D.B. Migas, S. Cereda, F. Montalenti, L. Miglio, Electronic and elastic contributions in the enhanced stability of Ge(105) under compressive strain, Surf. Sci. 556 (2004) 121.
- [96] G.-H. Lu, M. Cuma, F. Liu, First-principles study of strain stabilization of Ge(105) facet on Si(001), Phys. Rev. B 72 (2005) 125415.
- [97] D.E. Jesson, G. Chen, K.M. Chen, S.J. Pennycook, Self-limiting growth of strained faceted islands, Phys. Rev. Lett. 80 (1998) 5156.
- [98] J. Tersoff, R.M. Tromp, Shape transition in growth of strained islands: spontaneous formation of quantum wires, Phys. Rev. Lett. 70 (1993) 2782.

- [99] B. Voigtlander, A. Zinner, Simultaneous molecular beam epitaxy growth and scanning tunneling microscopy imaging during Ge/Si epitaxy, *Appl. Phys. Lett.* 63 (1993) 3055.
- [100] P.O. Hansson, M. Albrecht, W. Dorsch, H.P. Strunk, E. Bauser, Interfacial energies providing a driving force for Ge/Si heteroepitaxy, *Phys. Rev. Lett.* 73 (1994) 444.
- [101] M. Meixner, E. Schöll, M. Schmidbauer, H. Raidt, R. Köhler, Formation of island chains in SiGe/Si heteroepitaxy by elastic anisotropy, *Phys. Rev. B* 64 (2001) 245307.
- [102] M. Tomitori, K. Watanabe, M. Kobayashi, F. Iwasaki, Layered heteroepitaxial growth of germanium on Si(015) observed by scanning tunneling microscopy, *Surf. Sci.* 301 (1994) 214.
- [103] I. Goldfarb, J.H.G. Owen, D.R. Bowler, C.M. Goringe, P.T. Hayden, K. Miki, D.G. Pettifor, G.A.D. Briggs, In situ observation of gas-source molecular beam epitaxy of silicon and germanium on Si(001), *J. Vac. Sci. Technol. A* 16 (1998) 1938.
- [104] L.V. Arapkin, V.A. Yuryev, Nucleation of Ge quantum dots on the Si(001) surface, *Phys. Rev. B* 82 (2010) 045315.
- [105] I. Berbezier, A. Ronda, F. Volpi, A. Portavoce, Morphological evolution of SiGe layers, *Surf. Sci.* 531 (2003) 231.
- [106] A. Ronda, M. Abdallah, J.M. Gay, J. Stettner, I. Berbezier, Kinetic evolution of self-organised SiGe nanostructures, *Appl. Surf. Sci.* 162–163 (2000) 576.
- [107] J.A. Floro, E. Chason, R.D. Tweten, R.Q. Hwang, L.B. Freund, SiGe coherent islanding and stress relaxation in the high mobility regime, *Phys. Rev. Lett.* 79 (1997) 3946.
- [108] J. Stangl, A. Daniel, V. Holy, T. Roch, G. Bauer, I. Kegel, T.H. Metzger, T. Wiebach, O.G. Schmidt, K. Eberl, Strain and composition distribution in uncapped SiGe islands from X-ray diffraction, *Appl. Phys. Lett.* 79 (2001) 1474.
- [109] A.J. Steinfort, P.M.L.O. Scholte, A. Ettema, F. Tuinstra, M. Nielsen, E. Landemark, D.M. Smilgies, R. Feidenhans'l, G. Falkenberg, L. Seehofer, R.L. Johnson, Strain in nanoscale Germanium hut clusters on Si(001) studied by X-Ray diffraction, *Phys. Rev. Lett.* 77 (1996) 2009.
- [110] I. Kegel, T.H. Metzger, A. Lorké, J. Peisl, J. Stangl, G. Bauer, J.M. García, P.M. Petroff, Nanometer-scale resolution of strain and interdiffusion in self-assembled InAs/GaAs quantum dots, *Phys. Rev. Lett.* 85 (2000) 1694.
- [111] M. Cazayous, J. Groenen, F. Demangeot, R. Sirvin, M. Caumont, T. Remmelle, M. Albrecht, S. Christiansen, M. Becker, H.P. Strunk, H. Wawra, Strain and composition in self-assembled SiGe islands by Raman spectroscopy, *J. Appl. Phys.* 91 (2002) 6772.
- [112] M. Hanke, M. Dubslaff, M. Schmidbauer, T. Boeck, S. Schoder, M. Burghammer, C. Riekel, J. Patommel, C.G. Schroer, Scanning X-ray diffraction with 200 nm spatial resolution, *Appl. Phys. Lett.* 92 (2008) 193109.
- [113] C. Mocuta, J. Stangl, K. Mundboth, T.H. Metzger, G. Bauer, I.A. Vartanyants, M. Schmidbauer, T. Boeck, Beyond the ensemble average: X-ray microdiffraction analysis of single SiGe islands, *Phys. Rev. B* 77 (2008) 245425.
- [114] A. Diaz, C. Mocuta, J. Stangl, J. Vila-Comamala, C. David, T.H. Metzger, G. Bauer, Spatially resolved strain within a single SiGe island investigated by X-ray scanning microdiffraction, *Phys. Status Solidi (a)* 206 (2009) 1829.
- [115] L. Reimer, *Transmission electron microscopy*, 2nd edition, Springer Verlag, Berlin, 1989.
- [116] P. Donnadieu, T. Neisiaus, A. Gouyé, G. Amiard, A. Ronda, I. Berbezier, On morphology and strain field of Ge/Si(001) islands according to TEM phase imaging method, *J. Nanosc. Nanotech.* 10 (2011) 9208.
- [117] F. Patella, A. Sgarlata, F. Arciprete, S. Nufriš, P.-D. Szkutnik, E. Placidi, M. Fanfoni, N. Motta, A. Balzarotti, Self-assembly of InAs and Si/Ge quantum dots on structured surfaces, *J. Phys.: Condens. Matter* 16 (2004) S1503.
- [118] L. Persichetti, A. Sgarlata, M. Fanfoni, A. Balzarotti, Shaping Ge islands on Si(001) surfaces with misorientation angle, *Phys. Rev. Lett.* 104 (2010) 036104.
- [119] P.D. Szkutnik, A. Sgarlata, A. Balzarotti, N. Motta, A. Ronda, I. Berbezier, Early stage of Ge growth on Si(001) vicinal surfaces with an 8° miscut along [110], *Phys. Rev. B* 75 (2007) 033305.
- [120] G. Chen, B. Sandujav, D. Matei, G. Springholz, D. Scopece, M.J. Beck, F. Montalenti, L. Miglio, Formation of Ge nanoripples on vicinal Si(1110): from Stranski-Krastanow seeds to a perfectly faceted wetting layer, *Phys. Rev. Lett.* 108 (2012) 055503.
- [121] A. Ronda, I. Berbezier, Self-patterned Si surfaces as templates for Ge islands ordering, *Physica E* 23 (2004) 370.
- [122] L. Persichetti, A. Sgarlata, M. Fanfoni, A. Balzarotti, Breaking elastic field symmetry with substrate vicinality, *Phys. Rev. Lett.* 106 (2011) 055503.
- [123] T. Sekiguchi, S. Yoshida, K.M. Itoh, J. Mysliveček, B. Voigtländer, One-dimensional ordering of Ge nanoclusters along atomically straight steps of Si(111), *Appl. Phys. Lett.* 90 (2007) 013108.
- [124] N. Motta, Self-assembling and ordering of Ge/Si(111) quantum dots: scanning microscopy probe studies, *J. Phys.: Condens. Matter* 14 (2002) 8353.
- [125] C. Schelling, G. Springholz, F. Schäffler, Kinetic growth instabilities on vicinal Si(001) surfaces, *Phys. Rev. Lett.* 83 (1999) 995.
- [126] A.M. Pascale, Evolution morphologique des nanostructures Si-Ge pendant la croissance par ejm, Ph.D. thesis, Université de la Méditerranée, 2003.
- [127] T. Frisch, A. Verga, Kinetic step bunching instability during surface growth, *Phys. Rev. Lett.* 94 (2005) 226102.
- [128] T. Frisch, A. Verga, Effect of step stiffness and diffusion anisotropy on the meandering of a growing vicinal surface, *Phys. Rev. Lett.* 96 (2006) 166104.
- [129] M. Tomitori, K. Watanabe, M. Kobayashi, O. Nishikawa, STM study of the Ge growth mode on Si(001) substrates, *Appl. Surf. Sci.* 76–77 (1994) 322.
- [130] M.A. Lutz, R.M. Feenstra, P.M. Mooney, J. Tersoff, J.O. Chu, Facet formation in strained Si_{1-x}Ge_x films, *Surf. Sci.* 316 (1994) L1075.
- [131] J.A. Floro, G.A. Lucadamo, E. Chason, L.B. Freund, M. Sinclair, R.D. Tweten, R.Q. Hwang, SiGe island shape transitions induced by elastic repulsion, *Phys. Rev. Lett.* 80 (1998) 4717.
- [132] F.M. Ross, R.M. Tromp, M.C. Reuter, Transition states between pyramids and domes during Ge/Si island growth, *Science* 286 (1999) 1931.
- [133] T.I. Kamins, G. Medeiros-Ribeiro, D.A.A. Ohlberg, R.S. Williams, Evolution of Ge islands on Si(001) during annealing, *J. Appl. Phys.* 85 (1999) 1159.
- [134] S.A. Chaparro, Y. Zhang, J. Drucker, D. Chandrasekhar, D.J. Smith, Evolution of Ge/Si(100) islands: island size and temperature dependence, *J. Appl. Phys.* 87 (2000) 2245.
- [135] V. Zela, I. Pietzonka, T. Sass, C. Thelander, S. Jeppesen, W. Seifert, Unimodal dome-shaped island population of Ge/Si (0 0 1) by step-wise growth in UHV-CVD, *Physica E* (Amsterdam) 13 (2002) 1013.
- [136] F. Montalenti, P. Raiteri, D.B. Migas, H. von Känel, A. Rastelli, C. Manzano, G. Costantini, U. Denker, O.G. Schmidt, K. Kern, L. Miglio, Atomic-scale pathway of the pyramid-to-dome transition during Ge growth on Si(001), *Phys. Rev. Lett.* 93 (2004) 216102.
- [137] J. Johansson, W. Seifert, Kinetics of self-assembled island formation: part II—Island size, *J. Cryst. Growth* 234 (2002) 139.
- [138] V.A. Shchukin, N.N. Ledentsov, P.S. Kop'ev, D. Bimberg, Spontaneous ordering of arrays of coherent strained islands, *Phys. Rev. Lett.* 75 (1995) 2968.
- [139] G. Medeiros-Ribeiro, T.I. Kamins, D.A.A. Ohlberg, R.S. Williams, Annealing of Ge nanocrystals on Si(001) at 550°C: metastability of huts and the stability of pyramids and domes, *Phys. Rev. B* 58 (1998) 3533.
- [140] F.M. Ross, J. Tersoff, R.M. Tromp, Coarsening of self-assembled Ge quantum dots on Si(001), *Phys. Rev. Lett.* 80 (1998) 984.
- [141] I. Daruka, J. Tersoff, A.L. Barabási, Shape transition in growth of strained islands, *Phys. Rev. Lett.* 82 (1999) 2753.
- [142] M. Goryll, L. Vescan, K. Schmidt, S. Mesters, H. Luth, K. Szot, Size distribution of Ge islands grown on Si(001), *Appl. Phys. Lett.* 71 (1997) 410.
- [143] G. Medeiros-Ribeiro, T.I. Kamins, D.A.A. Ohlberg, R.S. Williams, Equilibrium size distributions of clusters during strained epitaxial growth, *Mater. Sci. Eng. B* 67 (1999) 31.
- [144] M. Stoffel, A. Rastelli, J. Tersoff, T. Merdhanova, O.G. Schmidt, Local equilibrium and global relaxation of strained SiGe/Si(001) layers, *Phys. Rev. B* 74 (2006) 155326.
- [145] E. Sutter, P. Sutter, J.E. Bernard, Extended shape evolution of low mismatch Si_{1-x}Ge_x alloy islands on Si(100), *Appl. Phys. Lett.* 84 (2004) 2262.
- [146] D.J. Eaglesham, R. Hull, Island formation in Ge/Si epitaxy, in: M.S.E.B.-S.S.M.A. Technol (Ed.), *Workshop on critical issues in epitaxy/electronic materials*, vol. 30, 1994, p. 197.
- [147] M. Stoffel, A. Rastelli, J. Stangl, T. Merdhanova, G. Bauer, O.G. Schmidt, Shape oscillations: a walk through the phase diagram of strained islands, *Phys. Rev. B* 75 (2007) 113307.
- [148] M. Brehm, F. Montalenti, M. Grydlik, G. Vastola, H. Lichtenberger, N. Hrauda, M.J. Beck, T. Fromherz, F. Schäffler, L. Miglio, G. Bauer, Key role of the wetting layer in revealing the hidden path of Ge/Si(001) Stranski-Krastanow growth onset, *Phys. Rev. B* 80 (2009) 205321.

- [149] Z.M. Jiang, X.M. Jiang, W.R. Jiang, Q.J. Jia, W.L. Zheng, D.C. Qian, Lattice strains and composition of self-organized Ge dots grown on Si(001), *Appl. Phys. Lett.* 76 (2000) 3397.
- [150] C.-P. Liu, J.M. Gibson, D.G. Cahill, T.I. Kamins, D.P. Basile, R.S. Williams, Strain evolution in coherent Ge/Si islands, *Phys. Rev. Lett.* 84 (2000) 1958.
- [151] B.V. Kamenev, H. Grebel, L. Tsybeskov, T.I. Kamins, R. Stanley williams, J.-M. Baribeau, D.J. Lockwood, Polarized Raman scattering and localized embedded strain in self-organized Si/Ge nanostructures, *Appl. Phys. Lett.* 83 (2003) 5035.
- [152] W. Neumann, H. Kirmse, I. Häusler, R. Otto, I. Hähnert, Quantitative TEM analysis of quantum structures, *J. Alloys Compd.* 382 (2004) 2.
- [153] R.V. Kukta, L.B. Freund, Minimum energy configuration of epitaxial material clusters on a lattice-mismatched substrate, *J. Mech. Phys. Solids* 45 (1997) 1835.
- [154] R.K. Singha, S. Das, S. Majumdar, K. Das, A. Dhar, S.K. Ray, Evolution of strain and composition of Ge islands on Si (001) grown by molecular beam epitaxy during postgrowth annealing, *J. Appl. Phys.* 103 (2008) 114301.
- [155] R. Magalhães paniago, G. Medeiros-Ribeiro, A. Malachias, S. Kycia, T.I. Kamins, R.S. Williams, Direct evaluation of composition profile, strain relaxation, and elastic energy of Ge:Si(001) self-assembled islands by anomalous X-ray scattering, *Phys. Rev. B* 66 (2002) 245312.
- [156] A. Malachias, M. Stoffel, M. Schmidbauer, T.U. Schülli, G. Medeiros-Ribeiro, O.G. Schmidt, R. Magalhães paniago, T.H. Metzger, Atomic ordering dependence on growth method in Ge:Si(001) islands: influence of surface kinetic and thermodynamic interdiffusion mechanisms, *Phys. Rev. B* 82 (2010) 035307.
- [157] L.A. Montoro, M.S. Leite, D. Biggemann, F.G. Peterella, K.J. Batenburg, G. Medeiros-Ribeiro, A.J. Ramirez, Revealing quantitative 3D chemical arrangement on Ge-Si nanostructures, *J. Phys. Chem. C* 113 (2009) 9018.
- [158] B.P. Uberuaga, M. Leskovar, A.P. Smith, H. Jónsson, M. Olmstead, Diffusion of Ge below the Si(100) surface: theory and experiment, *Phys. Rev. Lett.* 84 (2000) 2441.
- [159] D. Aubertine, M. Mander, N. Ozguen, A. Marshall, P. McIntyre, J. Chu, P. Mooney, Observation and modeling of the initial fast interdiffusion regime in Si/SiGe multilayers, *J. Appl. Phys.* 92 (2002) 5027.
- [160] P. Castrillo, R. Pinacho, M. Jaraiz, J.E. Rubio, Physical modeling and implementation scheme of native defect diffusion and interdiffusion in SiGe heterostructures for atomistic process simulation, *J. Appl. Phys.* 109 (2011) 103502.
- [161] N. Sugii, Thermal stability of the strained-Si/Si_{0.7}Ge_{0.3} heterostructure, *J. Appl. Phys.* 89 (2001) 6459.
- [162] T.F. Kelly, D.J. Larson, K. Thompson, R.L. Alvis, J.H. Bunton, J.D. Olson, B.P. Gorman, Atom probe tomography of electronic materials, *Annu. Rev. Mater. Res.* 37 (2007) 681.
- [163] M. Brehm, L. Grydlík, H. Lichtenberger, T. Fromherz, N. Hrauda, W. Jantsch, F. Schaffler, G. Bauer, Quantitative determination of Ge profiles across SiGe wetting layers on Si (001), *Appl. Phys. Lett.* 93 (2008) 121901.
- [164] F. Ratto, F. Rosei, A. Locatelli, S. Cherifi, S. Fontana, S. Heun, P.-D. Szkutnik, A. Sgarlata, M. De crescenzi, N. Motta, Composition of Ge(Si) islands in the growth of Ge on Si(111), *Appl. Phys. Lett.* 84 (2004) 4526.
- [165] G. Katsaros, G. Costantini, M. Stoffel, R. Esteban, A.M. Bittner, A. Rastelli, U. Denker, O.G. Schmidt, K. Kern, Kinetic origin of island intermixing during the growth of Ge on Si(001), *Phys. Rev. B* 72 (2005) 195320.
- [166] F. Ratto, F. Rosei, A. Locatelli, S. Cherifi, S. Fontana, S. Heun, P. Szutnik, A. Sgarlata, M. De crescenzi, N. Motta, Composition of Ge(Si) islands in the growth of Ge on Si(111) by X-ray spectromicroscopy, *J. Appl. Phys.* 97 (2005) 043516.
- [167] F.F. Ratto, A. Locatelli, S. Fontana, S. Kharrazi, S. Ashtaputre, S.K. Kulkarni, S. Heun, F. Rosei, Chemical mapping of individual semiconductor nanostructures, *Small* 2 (2006) 401.
- [168] F. Ratto, A. Locatelli, S. Fontana, S. Kharrazi, S. Ashtaputre, S.K. Kulkarni, S. Heun, F. Rosei, Diffusion dynamics during the nucleation and growth of Ge/Si nanostructures on Si(111), *Phys. Rev. Lett.* 96 (2006) 096103.
- [169] X. Liao, J. Zou, D. Cockayne, Z. Jiang, X. Wang, Extracting composition and alloying information of coherent Ge(Si)/Si(001) islands from [001] on-zone bright-field diffraction contrast images, *J. Appl. Phys.* 90 (2001) 2725.
- [170] N.A. Katcho, M.-I. Richard, M.G. Proietti, H. Renevier, C. Leclerc, V. Favre-Nicolin, J.J. Zhang, G. Bauer, Composition and strain of Ge domes on Si(001) close to the dome/substrate interface, *Europhys. Lett.* 93 (2011) 66004.
- [171] J. Baribeau, X. Wu, D.J. Lockwood, Probing the composition of Ge dots and Si/Si_{1-x}Ge_x island superlattices, *J. Vac. Sci. Technol. A* 24 (2006) 663.
- [172] A. Malachias, S. Kycia, G. Medeiros-Ribeiro, R. Magalhães paniago, T.I. Kamins, R.S. Williams, 3D composition of epitaxial nanocrystals by anomalous X-Ray diffraction: observation of a Si-rich core in Ge domes on Si(100), *Phys. Rev. Lett.* 91 (2003) 176101.
- [173] Y. Ogawa, T. Toizumi, F. Minami, A.V. Baranov, Nanometer-scale mapping of the strain and Ge content of Ge/Si quantum dots using enhanced Raman scattering by the tip of an atomic force microscope, *Phys. Rev. B* 83 (2011) 081302.
- [174] G. Medeiros-Ribeiro, A. Malachias, S. Kycia, R. Magalhães-Paniago, T.I. Kamins, R.S. Williams, Elastic energy mapping of epitaxial nanocrystals, *Appl. Phys. A* 80 (2005) 1211.
- [175] T.U. Schülli, G. Vastola, M.I. Richard, A. Malachias, G. Renaud, F. Uhlik, F. Montalenti, G. Chen, L. Miglio, F. Schäffler, G. Bauer, Enhanced relaxation and intermixing in Ge islands grown on pit-patterned Si(001) substrates, *Phys. Rev. Lett.* 102 (2009) 025502.
- [176] M.-I. Richard, Étude *in situ* et *ex situ* par rayonnement synchrotron de la croissance d'îlots de Ge sur substrats de Si(001) nominaux et pré-structurés, Ph.D. Thesis, Université Joseph Fourier-Grenoble I, 2007.
- [177] M.S. Leite, A. Malachias, S.W. Kycia, T.I. Kamins, R.S. Williams, G. Medeiros-Ribeiro, Evolution of thermodynamic potentials in closed and open nanocrystalline systems: Ge-Si/Si(001) islands, *Phys. Rev. Lett.* 100 (2008) 226101.
- [178] G. Capellini, M. De seta, F. Evangelisti, SiGe intermixing in Ge/Si(100) islands, *Appl. Phys. Lett.* 78 (2001) 303.
- [179] T.U. Schülli, M. Stoffel, A. Hesse, J. Stangl, R.T. Lechner, E. Wintersberger, M. Sztucki, T.H. Metzger, O.G. Schmidt, G. Bauer, Influence of growth temperature on interdiffusion in uncapped SiGe-islands on Si(001) determined by anomalous X-ray diffraction and reciprocal space mapping, *Phys. Rev. B* 71 (2005) 035326.
- [180] M. Floyd, Y. Zhang, K. Driver, J. Drucker, P. Crozier, D. Smith, Nanometer-scale composition measurements of Ge/Si(100) islands, *Appl. Phys. Lett.* 82 (9) (2003).
- [181] R.R. Vanfleet, D.P. Basile, T.I. Kamins, J. Silcox, R. Stanley williams, Silicon-germanium interdiffusion and interfaces in self-assembled quantum dots, *Appl. Phys. A* 86 (2007) 1.
- [182] S.A. Chaparro, J. Drucker, Y. Zhang, D. Chandrasekhar, M.R. Mccartney, D.J. Smith, Strain-driven alloying in Ge/Si(100) coherent islands, *Phys. Rev. Lett.* 83 (1999) 1199.
- [183] T. Ide, A. Sakai, K. Shimizu, Nanometer-scale imaging of strain in Ge island on Si(001) surface, *Thin Solid Films* 357 (1999) 22.
- [184] P. Raiteri, L. Miglio, F. Valentiniotti, M. Celino, Strain maps at the atomic scale below Ge pyramids and domes on a Si substrate, *Appl. Phys. Lett.* 80 (2002) 3736.
- [185] U. Denker, M. Stoffel, O.G. Schmidt, H. Sigg, Ge hut cluster luminescence below bulk Ge band gap, *Appl. Phys. Lett.* 82 (2003) 454.
- [186] C. Huang, Y. Zuo, D. Li, B. Cheng, L. Luo, J. Yu, Q. Wang, Shape evolution of Ge/Si(001) islands induced by strain-driven alloying, *Appl. Phys. Lett.* 78 (2001) 3881.
- [187] A. Rastelli, M. Stoffel, A. Malachias, T. Merdzhanova, G. Katsaros, K. Kern, T.H. Metzger, O.G. Schmidt, Three-dimensional composition profiles of single quantum dots determined by scanning-probe-microscopy-based nanotomography, *Nano Lett.* 8 (2008) 1405.
- [188] O. Moutanabbir, S. Miyamoto, E.E. Haller, K.M. Itoh, Transport of deposited atoms throughout strain-mediated self-assembly, *Phys. Rev. Lett.* 105 (2010) 026101.
- [189] G. Biasiol, S. Heun, Compositional mapping of semiconductor quantum dots and rings, *Phys. Rep.* 500 (2011) 117.
- [190] S. Lee, L. Chen, P. Chen, M. Tsai, C. Liu, T. Chien, C. Chia, Self-assembled nanorings in Si-capped Ge quantum dots on (001)Si, *Appl. Phys. Lett.* 83 (2003) 5283.
- [191] M. Copel, M.C. Reuter, E. Kaxiras, R.M. Tromp, Surfactants in epitaxial growth, *Phys. Rev. Lett.* 63 (1989) 632.

- [192] N. Ohtani, S.M. Mokler, M.H. Xie, J. Zhang, B.A. Joyce, Rheed investigation of Ge surface segregation during gas source mbe of $\text{SiSi}_{1-x}\text{Ge}_x$ heterostructures, *Surf. Sci.* 284 (1993) 305.
- [193] K. Fujita, S. Fukatsu, H. Yaguchi, Y. Shiraki, R. Ito, Involvement of the topmost Ge layer in the Ge surface segregation during Si/Ge heterostructure formation, *Appl. Phys. Lett.* 59 (1991) 2240.
- [194] R. Butz, S. Kampers, $2 \times n$ surface structure of SiGe layers deposited on Si(100), *Appl. Phys. Lett.* 61 (1992) 1307.
- [195] Y. Li, G. Hembree, J. Venables, Quantitative Auger electron spectroscopic analysis of Ge surface segregation in Si/Ge/Si(100) heterostructures, *Appl. Phys. Lett.* 67 (1995) 276.
- [196] A. Rastelli, M. Kummer, H. Von känel, Reversible shape evolution of Ge islands on Si(001), *Phys. Rev. Lett.* 87 (2001) 256101.
- [197] S.W. Lee, C.H. Lee, H.T. Chang, S.L. Cheng, C.W. Liu, Evolution of composition distribution of Si-capped Ge islands on Si(001), *Thin Solid Films* 517 (2009) 5029.
- [198] O. Kirlfel, E. Müller, D. Grützmacher, K. Kern, A. Hesse, J. Stangl, V. Holý, G. Bauer, Shape and composition change of Ge dots due to Si capping, *Appl. Surf. Sci.* 224 (2004) 139.
- [199] A. Hesse, J. Stangl, V. Holý, T. Roch, G. Bauer, O.G. Schmidt, U. Denker, B. Struth, Effect of overgrowth on shape, composition, and strain of SiGe islands on Si(001), *Phys. Rev. B* 66 (2002) 085321.
- [200] J. Stangl, A. Hesse, V. Holý, Z. Zhong, G. Bauer, U. Denker, O.G. Schmidt, Effect of overgrowth temperature on shape, strain, and composition of buried Ge islands deduced from X-ray diffraction, *Appl. Phys. Lett.* 82 (2003) 2251.
- [201] N. Ohtani, S.M. Mokler, B.A. Joyce, Simulation studies of Ge surface segregation during gas source MBE growth of Si/Si_{1-x}Ge_x heterostructures, *Surf. Sci.* 295 (1993) 325.
- [202] T. Walther, C.J. Humphreys, A quantitative study of compositional profiles of chemical vapour-deposited strained silicon-germanium/silicon layers by transmission electron microscopy, *J. Cryst. Growth* 197 (1999) 113.
- [203] A. Dunbar, U. Bangert, P. Dawson, M. Halsall, Y. Shiraki, M. Miura, I. Berbezier, B.A. Joyce, J. Zhang, Structural, compositional and optical properties of self-organised ge quantum dots, *Phys. Status Solidi (b)* 224 (2001) 265.
- [204] O. Schmidt, U. Denker, S. Christiansen, F. Ernst, Composition of self-assembled Ge/Si islands in single and multiple layers, *Appl. Phys. Lett.* 81 (2002) 2614.
- [205] T. Ruf, Phonon Raman Scattering in Semiconductors, *Quantum Wells and Superlattices*, Springer, Berlin, 1998.
- [206] J. Menéndez, in: W.H. Weber, R. Merlin (Eds.), *Raman Scattering in Materials Science*, Springer-Verlag, Berlin, Heidelberg, 2000, p. 55. (Chapter 3).
- [207] H.K. Shin, D.J. Lockwood, J.-M. Baribeau, Strain in coherent-wave SiGe/Si superlattices, *Solid State Commun.* 114 (2000) 505.
- [208] D.J. Lockwood, R. Radomski, Z. Wasilewski, Raman study of phonons in Ga_{1-x}Al_xAs, *J. Raman Spectrosc.* 33 (2002) 202.
- [209] B. Ismail, M. Descoins, A. Ronda, F. Bassani, G. Brémont, H. Maeref, I. Berbezier, Effect of self-patterned Si_{1-x}Ge_x template layer on the structural and optical properties of Ge dots, *J. Vac. Sci. Technol. B* 23 (2005) 242.
- [210] J.M. Baribeau, D.J. Lockwood, et al., in: W.D. Nix (Ed.), *Thin films: Stresses and Mechanical Properties III*, vol. 239, Materials Research Society, Boston, 1992, p. 449.
- [211] D.J. Lockwood, J.M. Baribeau, Strain-shift coefficients for phonons in Si_{1-x}Ge_x epilayers on silicon, *Phys. Rev. B* 45 (1992) 8565.
- [212] J.P. Dismukes, L. Ekstrom, R.J. Paff, Lattice parameter and density in Germanium-Silicon alloys, *J. Phys. Chem.* 68 (1964) 3021.
- [213] A. Kolobov, K. Morita, K. Itoh, E. Haller, A Raman scattering study of self-assembled pure isotope Ge/Si(100) quantum dots, *Appl. Phys. Lett.* 81 (2002) 3855.
- [214] B. Kamenev, L. Tsybeskov, J. Baribeau, D. Lockwood, Photoluminescence and Raman scattering in three-dimensional Si/Si_{1-x}Ge_x nanostructures, *Appl. Phys. Lett.* 84 (2004) 1293.
- [215] P. Tan, D. Bougeard, G. Abstreiter, K. Brunner, Raman scattering of folded acoustic phonons in self-assembled Si/Ge dot superlattices, *Appl. Phys. Lett.* 84 (2004) 2632.
- [216] J. Liu, G. Jin, Y. Tang, Y. Luo, K. Wang, D. Yu, Optical and acoustic phonon modes in self-organized Ge quantum dot superlattices, *Appl. Phys. Lett.* 76 (2000) 586.
- [217] F.H. Li, Y.L. Fan, X.J. Yang, Z.M. Jiang, Y.Q. Wu, J. Zou, Atomic composition profile change of SiGe islands during Si capping, *Appl. Phys. Lett.* 89 (2006) 103108.
- [218] O. Schmidt, K. Eberl, Photoluminescence and band edge alignment of C-induced Ge islands and related SiGeC structures, *Appl. Phys. Lett.* 73 (1998) 2790.
- [219] O. Leifeld, A. Beyer, D. Grützmacher, K. Kern, Nucleation of Ge dots on the C-alloyed Si(001) surface, *Phys. Rev. B* 66 (2002) 125312.
- [220] G. Hadjisavvas, P. Sonnet, P.C. Kelires, Stress and composition of C-induced Ge dots on Si(100), *Phys. Rev. B* 67 (2003) 241302R.
- [221] A. Portavoce, I. Berbezier, A. Ronda, Sb-surfactant-mediated growth of Si and Ge nanostructures, *Phys. Rev. B* 69 (2004) 155416.
- [222] M.S. Leite, G. Medeiros-Ribeiro, T.I. Kamins, R.S. Williams, Alloying mechanisms for epitaxial nanocrystals, *Phys. Rev. Lett.* 98 (2007) 165901.
- [223] M.S. Leite, T.I. Kamins, G. Medeiros-Ribeiro, Control of Ge/Si intermixing during Ge island growth, *Appl. Phys. Lett.* 94 (2009) 053118.
- [224] D.J. Srolovitz, On the stability of surfaces of stressed solids, *Acta Metall.* 37 (1989) 621.
- [225] W.W. Mullins, Theory of thermal grooving, *J. Appl. Phys.* 28 (1957) 333.
- [226] B.J. Spencer, P.W. Voorhees, S.H. Davies, Morphological instability in epitaxially strained dislocation-free solid films: linear stability theory, *J. Appl. Phys.* 73 (1993) 4955.
- [227] J.R. Rice, T.-J. Chuang, Energy variations in diffusive cavity growth, *J. Am. Ceram. Soc.* 64 (1981) 46.
- [228] B.J. Spencer, P.W. Voorhees, S.H. Davis, Morphological instability in epitaxially strained dislocation-free solid films, *Phys. Rev. Lett.* 67 (1991) 3696.
- [229] E. Chason, J.Y. Tsao, K.M. Horn, S.T. Picraux, H.A. Atwater, Surface roughening of Ge(001) during 200 eV Xe ion bombardment and Ge molecular beam epitaxy, *J. Vac. Sci. Technol. A* 8 (1990) 2507.
- [230] J.-N. Aqua, T. Frisch, Influence of surface energy anisotropy on the dynamics of quantum dot growth, *Phys. Rev. B* 82 (2010) 085322.
- [231] M.S. Levine, A.A. Golovin, S.H. Davis, Self-assembly of quantum dots in a thin epitaxial film wetting an elastic substrate, *Phys. Rev. B* 75 (2007) 205312.
- [232] C.-H. Chiu, H. Gao, A numerical study of stress controlled surface diffusion during epitaxial film growth, in: S.P. Baker, et al. (Eds.), *Thin Films: Stresses and Mechanical Properties V*, MRS Symposia Proceedings No. 356, Materials Research Society, Pittsburgh, 1995, p. 33.
- [233] B.J. Spencer, J. Tersoff, Equilibrium shapes and properties of epitaxially strained islands, *Phys. Rev. Lett.* 79 (1997) 4858.
- [234] J. Tersoff, Stress-induced layer-by-layer growth of Ge on Si(100), *Phys. Rev. B* 43 (1991) 9377.
- [235] M.J. Beck, A.de. Van walle, M. Asta, Surface energetics and structure of the Ge wetting layer on Si(100), *Phys. Rev. B* 70 (2004) 205337.
- [236] J.-N. Aqua, T. Frisch, A. Verga, Nonlinear evolution of a morphological instability in a strained epitaxial film, *Phys. Rev. B* 76 (2007) 165319.
- [237] Y. Tu, J. Tersoff, Origin of apparent critical thickness for island formation in heteroepitaxy, *Phys. Rev. Lett.* 93 (2004) 216101.
- [238] W.T. Tekalign, B.J. Spencer, Evolution equation for a thine epitaxial film on a deformable substrate, *J. Appl. Phys.* 96 (2004) 5505.
- [239] Z.-F. Huang, R.C. Desai, Epitaxial growth in dislocation-free strained alloy films: morphological and compositional instabilities, *Phys. Rev. B* 65 (2002) 205419.
- [240] H. Wang, Y. Zhang, F. Liu, Enhanced growth instability of strained film on wavy substrate, *J. Appl. Phys.* 104 (2008) 054301.
- [241] X. Xu, J. Aqua, T. Frisch, Growth kinetics in a strained crystal film on a wavy patterned substrate, *J. Phys.: Condens. Matter* 24 (2012) 045002.
- [242] G. Wulff, Zur frage der geschwindigkeit des wachstums und der auflösung der kristallflächen, *Z. Kristallogr.* 34 (1901) 449.
- [243] P. Nozières, Shape and growth of crystals, in: C. Godrèche (Ed.), *Solids Far from Equilibrium*, Cambridge University Press, Cambridge, 1991, p. 1.
- [244] A. Pimpinelli, J. Villain, *Physics of Crystal Growth*, Cambridge University Press, 1998.
- [245] I. Berbezier, B. Gallas, J. Derrien, Elastic strain relaxation in Si_{1-x}Ge_x layers epitaxially grown on Si substrates, *Surf. Rev. Lett.* 5 (1998) 133.
- [246] Y.W. Zhang, Self-organization, shape transition, and stability of epitaxially strained islands, *Phys. Rev. B* 61 (2000) 10388.

- [247] A. Ramasubramaniam, V.B. Shenoy, Three-dimensional simulations of self-assembly of hut-shaped Si–Ge quantum dots, *J. Appl. Phys.* 95 (2004) 7813.
- [248] C.-H. Chiu, Z. Huang, Numerical simulation for the formation of nanostructures on the Stranski–Krasanow systems by surface undulation, *J. Appl. Phys.* 101 (2007) 113540.
- [249] D.J. Eaglesham, A.E. White, L.C. Feldman, N. Moriya, D.C. Jacobson, Equilibrium shape of Si, *Phys. Rev. Lett.* 70 (1993) 1643.
- [250] J.M. Bermond, J.J. Métois, X. Egéa, F. Floret, The equilibrium shape of silicon, *Surf. Sci.* 330 (1995) 48.
- [251] C.J. Moore, C.M. Retford, M.J. Beck, M. Asta, M.J. Miksis, P.W. Voorhees, Orientation dependence of strained-Ge surface energies near (001): role of dimer-vacancy lines and their interactions with steps, *Phys. Rev. Lett.* 96 (2006) 126101.
- [252] S.P.A. Gill, T. Wang, On the existence of a critical perturbation amplitude for the Stranski–Krasanow transition, *Surf. Sci.* 602 (2008) 3560.
- [253] P. Berger, P. Kohlert, K. Kassner, C. Misbah, Pattern selection in biaxially stressed solids, *Phys. Rev. Lett.* 90 (2003) 176103.
- [254] S.P.A. Gill, Self-organised growth on strained substrates: the influence of anisotropic strain, surface energy and surface diffusivity, *Thin Solid Films* 423 (2003) 136.
- [255] P. Liu, Y.W. Zhang, C. Lu, Formation of self-assembled heteroepitaxial islands in elastically anisotropic films, *Phys. Rev. B* 67 (2003) 165414.
- [256] P. Liu, Y.W. Zhang, C. Lu, Anisotropy effect on heteroepitaxial growth of self-assembled islands, *Appl. Phys. Lett.* 88 (2006) 041922.
- [257] Y.W. Zhang, Surface stability and evolution of biaxially strained epitaxial thin films, *Appl. Phys. Lett.* 87 (2005) 121916.
- [258] Y. Pang, R. Huang, Bifurcation of surface pattern in epitaxial thin films under anisotropic stresses, *J. Appl. Phys.* 101 (2007) 023519.
- [259] W.H. Yang, D.J. Srolovitz, Cracklike surface instabilities in stressed solids, *Phys. Rev. Lett.* 71 (1993) 1593.
- [260] B.J. Spencer, D.I. Meiron, Nonlinear evolution of the stress-driven morphological instability in a two-dimensional semi-infinite solid, *Acta Metall. Mater.* 42 (1994) 3629.
- [261] Y. Xiang, W.E., Nonlinear evolution equation for the stress-driven morphological instability, *J. Appl. Phys.* 91 (2002) 9414.
- [262] P. Kohlert, K. Kassner, C. Misbah, Large-amplitude behavior of the Grinfeld instability: a variational approach, *Eur. Phys. J. B* 35 (2003) 493.
- [263] A.A. Golovin, S.H. Davis, P.W. Voorhees, Self-organization of quantum dots in epitaxially strained solid films, *Phys. Rev. E* 68 (2003) 056203.
- [264] Y. Pang, R. Huang, Nonlinear effect of stress and wetting on surface evolution of epitaxial thin films, *Phys. Rev. B* 74 (2006) 075413.
- [265] C.-H. Chiu, H. Gao, Stress singularities along a cycloid rough surface, *Int. J. Solids Structures* 30 (1993) 2983.
- [266] P. Nozières, Amplitude expansion for the Grinfeld instability due to uniaxial stress at a solid surface, *J. Phys. I France* 3 (1993) 681–686.
- [267] K. Kassner, C. Misbah, Non-linear evolution of a uniaxially stressed solid—a route to fracture, *Europhys. Lett.* 28 (1994) 245.
- [268] L. Ratke, P.W. Voorhees, Growth and Coarsening: Ostwald Ripening in Material Processing, Springer, 2002.
- [269] T. Aqua, J.-N. Frisch, A. Verga, Ordering of strained islands during surface growth, *Phys. Rev. E* 81 (2010) 021605.
- [270] B. Cho, T. Schwarz-Selinger, K. Ohmori, D.G. Cahill, J.E. Greene, Effect of growth rate on the spatial distributions of dome-shaped Ge islands on Si(001), *Phys. Rev. B* 66 (2002) 195407.
- [271] F.K. Legoues, M. Copel, R.M. Tromp, Microstructure and strain relief of Ge films grown layer by layer on Si(001), *Phys. Rev. B* 42 (1990) 11690.
- [272] H.T. Johnson, L.B. Freund, Mechanics of coherent and dislocated island morphologies in strained epitaxial material systems, *J. Appl. Phys.* 81 (1997) 6081.
- [273] J.W. Evans, P.A. Thiel, M.C. Bartelt, Morphological evolution during epitaxial thin film growth: formation of 2D islands and 3D mounds, *Surf. Sci. Rep.* 61 (2006) 1.
- [274] Y.W. Mo, J. Kleiner, M.B. Webb, M.G. Lagally, Activation energy for surface diffusion of Si on Si(001): a scanning-tunneling-microscopy study, *Phys. Rev. Lett.* 66 (1991) 1998.
- [275] V. Cherepanov, B. Voigtländer, Influence of material, surface reconstruction, and strain on diffusion at the Ge(111) surface, *Phys. Rev. B* 69 (2004) 125331.
- [276] A.-L. Barabasi, H.E. Stanley, Fractal Concepts in Surface Growth, Cambridge University Press, 1995.
- [277] T. Vicsek, F. Family, Dynamic scaling for aggregation of clusters, *Phys. Rev. Lett.* 52 (1984) 1669.
- [278] M.C. Bartelt, J.W. Evans, Scaling analysis of diffusion-mediated island growth in surface adsorption processes, *Phys. Rev. B* 46 (1992) 12675.
- [279] J.A. Venables, G.D.T. Spiller, M. Hanbucken, Nucleation and growth of thin-films, *Rep. Progr. Phys.* 47 (1984) 399.
- [280] S. Stoyanov, D. Kashchiev, in: E. Kaldis (Ed.), Current Topics in Materials Science, vol. 7, North-Holland, Amsterdam, 1981.
- [281] J.A. Blackman, A. Wilding, Scaling theory of island growth in thin films, *EuroPhys. Lett.* 16 (1991) 115.
- [282] J. Villain, A. Pimpinelli, L. Tang, D. Wolf, Terrace sizes in molecular beam epitaxy, *J. Phys. I France* 2 (1992) 2107.
- [283] C. Ratsch, A. Zangwill, P. Smilauer, Scaling of heteroepitaxial island sizes, *Surf. Sci. Lett.* 314 (1994) L937.
- [284] J.G. Amar, F. Family, Critical cluster size: island morphology and size distribution in submonolayer epitaxial growth, *Phys. Rev. Lett.* 74 (1995) 2066.
- [285] B. Croset, H. Guesmi, G. Prévot, Role of anisotropies on the self organization of stressed domains on (001) surfaces of cubic crystals, *Phys. Rev. B* 76 (2007) 073405.
- [286] F. Gutheim, H. Müller-Krumbhaar, E. Brener, Epitaxial growth with elastic interaction: submonolayer island formation, *Phys. Rev. E* 63 (2001) 041603.
- [287] G. Nandipati, J.G. Amar, Effects of strain on island morphology and size distribution in irreversible submonolayer growth, *Phys. Rev. B* 73 (2006) 045409.
- [288] R. Grima, J. Degraffenreid, J.A. Venables, Mean-field theory of nucleation and growth on strained surfaces, *Phys. Rev. B* 76 (2007) 233405.
- [289] C.-H. Lam, C.-K. Lee, L.M. Sander, Competing roughening mechanisms in strained heteroepitaxy: a fast kinetic Monte Carlo study, *Phys. Rev. Lett.* 89 (2002) 216102.
- [290] J.-N. Aqua, T. Frisch, Elastic interactions and kinetics during reversible submonolayer growth: Monte Carlo simulations, *Phys. Rev. B* 78 (2008) 121305(R).
- [291] M. Rangathan, Private communication.
- [292] C. Ratsch, J. Devita, P. Smereka, Level-set simulation for the strain-driven sharpening of the island-size distribution during submonolayer heteroepitaxial growth, *Phys. Rev. B* 80 (2009) 155309.
- [293] C. Ratsch, A. Zangwill, Equilibrium theory of the Stranski–Krasanow epitaxial morphology, *Surf. Sci.* 293 (1993) 123.
- [294] O.E. Shklyarev, M.J. Beck, M. Asta, M.J. Miksis, P.W. Voorhees, Role of strain-dependent surface energies in Ge/Si(100) island formation, *Phys. Rev. Lett.* 94 (2005) 176102.
- [295] T. Miyazaki, D.R. Bowler, M.J. Gillan, T. Ohno, The energetics of hut-cluster self-assembly in Ge/Si(001) from linear-scaling dft calculations, *J. Phys. Soc. Japan* 77 (2008) 123706.
- [296] H.T. Dobbs, D.D. Vvedensky, A. Zangwill, J. Johansson, N. Carlsson, W. Seifert, Mean-field theory of quantum dot formation, *Phys. Rev. Lett.* 79 (1997) 897.
- [297] T.J. Krzyzewski, P.B. Joyce, G.R. Bell, T.S. Jones, Scaling behavior in InAs/GaAs(001) quantum-dot formation, *Phys. Rev. B* 66 (2002) 201302.
- [298] H.M. Koduvely, A. Zangwill, Epitaxial growth kinetics with interacting coherent islands, *Phys. Rev. B* 60 (1999) R2204.
- [299] S. Miyamoto, O. Moutanabbir, E.E. Haller, K.M. Itoh, Spatial correlation of self-assembled isotopically pure Ge/Si(001) nanoislands, *Phys. Rev. B* 79 (2009) 165415.
- [300] B.G. Orr, D. Kessler, C.W. Snyder, L. Sander, A model for strain-induced roughening and coherent island growth, *Europhys. Lett.* 19 (1) (1992) 33.
- [301] A.-L. Barabasi, Self-assembled island formation in heteroepitaxial growth, *Appl. Phys. Lett.* 70 (1997) 2565.
- [302] K.E. Khor, S. Das Sarma, Quantum dot self-assembly in growth of strained-layer thin films: a kinetic Monte Carlo study, *Phys. Rev. B* 62 (2000) 16657.
- [303] G. Russo, P. Smereka, Computation of strained epitaxial growth in three dimensions by kinetic Monte Carlo, *J. Comput. Phys.* 214 (2006) 809.
- [304] M. Meixner, E. Schöll, V.A. Shchukin, D. Bimberg, Self-assembled quantum dots: Crossover from kinetically controlled to thermodynamically limited growth, *Phys. Rev. Lett.* 87 (23) (2001) 236101.
- [305] B.M.T. Gonçalves, J.F.F. Mendes, Monte Carlo study of the elastic interaction in heteroepitaxial growth, *Phys. Rev. E* 65 (2002) 061602.
- [306] R. Zhu, E. Pan, P.W. Chung, Fast multiscale kinetic Monte Carlo simulations of three-dimensional self-assembled quantum dot islands, *Phys. Rev. B* 75 (2007) 205339.

- [307] M.T. Lung, C.-H. Lam, L.M. Sander, Island, pit, and groove formation in strained heteroepitaxy, *Phys. Rev. Lett.* 95 (2005) 086102.
- [308] R. Xiang, M.T. Lung, C.-H. Lam, Layer-by-layer nucleation mechanism for quantum dot formation in strained heteroepitaxy, *Phys. Rev. E* 82 (2010) 021601.
- [309] T. Miyazaki, D.R. Bowler, R. Choudhury, M.J. Gillan, Density functional calculations of Ge(105): local basis sets and O(N) methods, *Phys. Rev. B* 76 (2007) 115327.
- [310] T. Eguchi, Y. Fujikawa, K. Akiyama, T. An, M. Ono, T. Hashimoto, Y. Morikawa, K. Terakura, T. Sakurai, M.G. Lagally, Y. Hasegawa, imaging of all dangling bonds and their potential on the Ge/Si(105) surface by noncontact atomic force microscopy, *Phys. Rev. Lett.* 93 (2004) 266102.
- [311] V.B. Shenoy, C.V. Ciobanu, L.B. Freund, Strain induced stabilization of stepped Si and Ge surfaces near (001), *Appl. Phys. Lett.* 81 (2002) 364.
- [312] V.B. Shenoy, L.B. Freund, A continuum description of the energetics and evolution of stepped surfaces in strained nanostructures, *J. Mech. Phys. Solids* 50 (2002) 1817.
- [313] T. Hashimoto, Y. Morikawa, K. Terakura, Stability and electronic structure of Ge (105)1 × 2: a first-principles theoretical study, *Surf. Sci.* 576 (2005) 61.
- [314] C.-H. Chiu, Stable and uniform arrays of self-assembled nanocrystalline islands, *Phys. Rev. B* 69 (2004) 165413.
- [315] C.H. Chiu, Z. Huang, Common features of nanostructure formation induced by the surface undulation on the Stranski–Krastanow systems, *Appl. Phys. Lett.* 89 (2006) 171904.
- [316] C.-H. Chiu, The self-assembly of uniform heteroepitaxial islands, *Appl. Phys. Lett.* 75 (1999) 3473.
- [317] see www.insp.upmc.fr/filmsATG.html.
- [318] T. Takaki, T. Hirouchi, Y. Tomita, Phase-field study of interface energy effect on quantum dot morphology, *J. Cryst. Growth* 310 (2008) 2248.
- [319] R.E. Rudd, G.A.D. Briggs, A.P. Sutton, G. Medeiros-Ribeiro, R.S. Williams, Equilibrium model of bimodal distributions of epitaxial island growth, *Phys. Rev. Lett.* 90 (2003) 146101.
- [320] A. Rastelli, M. Stoffel, J. Tersoff, G.S. Kar, O.G. Schmidt, Kinetic evolution and equilibrium morphology of strained islands, *Phys. Rev. Lett.* 95 (2005) 026103.
- [321] W.L. Henstrom, C.-P. Liu, J.M. Gibson, T.I. Kamins, S.R. Williams, Dome-to-pyramid shape transition in Ge/Si islands due to strain relaxation by interdiffusion, *Appl. Phys. Lett.* 77 (2000) 1623.
- [322] B.J. Spencer, J. Tersoff, Asymmetry and shape transitions of epitaxially strained islands on vicinal surfaces, *Appl. Phys. Lett.* 96 (2010) 073114.
- [323] C.H. Lam, Kinetic Monte Carlo simulation of shape transition of strained quantum dots, *J. Appl. Phys.* 108 (2010) 064328.
- [324] C.-H. Lam, Kinetic monte carlo simulation of faceted islands in heteroepitaxy using a multistate lattice model, *Phys. Rev. E* 81 (2010) 021607.
- [325] V. Shchukin, N. Ledentsov, D. Bimberg, *Epitaxy of Nanostructures*, Springer, 2003; V.A. Shchukin, D. Bimberg, *Rev. Modern Phys.* 71 (1999) 1125.
- [326] V.A. Shchukin, N.N. Ledentsov, D. Bimberg, *Epitaxy of Nanostructures*, Springer, 2003.
- [327] P. Fratzl, O. Penrose, J.L. Lebowitz, Modeling of phase separation in alloys with coherent elastic misfit, *J. Stat. Phys.* 95 (1999) 1429.
- [328] J.E. Guyer, P.W. Voorhees, Morphological stability of alloy thin films, *Phys. Rev. B* 54 (1996) 11710.
- [329] F. Glas, Thermodynamics of a stressed alloy with a free surface: coupling between the morphological and compositional instabilities, *Phys. Rev. B* 55 (1997) 11277.
- [330] F. Léonard, R.C. Desai, Alloy decomposition and surface instabilities in thin films, *Phys. Rev. B* 57 (1998) 4805.
- [331] F. Glas, Thermodynamic and kinetic instabilities of lattice-matched alloy layers: compositional and morphological perturbations, *Phys. Rev. B* 62 (2000) 7393.
- [332] B.J. Spencer, P.W. Voorhees, Enhanced instability of strained alloy films due to compositional stresses, *Phys. Rev. Lett.* 84 (2000) 2449.
- [333] B.J. Spencer, P.W. Voorhees, J. Tersoff, Morphological instability theory for strained alloy film growth: the effect of compositional stresses and species-dependent surface mobilities on ripple formation during epitaxial film deposition, *Phys. Rev. B* 64 (2001) 235318.
- [334] Z.-F. Huang, R.C. Desai, Instability and decomposition on the surface of strained alloy films, *Phys. Rev. B* 65 (2002) 195421.
- [335] Z.-F. Huang, K.R. Elder, Mesoscopic and microscopic modeling of island formation in strained film epitaxy, *Phys. Rev. Lett.* 101 (2008) 158701.
- [336] R.C. Desai, H.K. Kim, A. Chatterji, D. Ngai, S. Chen, N. Yang, Epitaxial growth in dislocation-free strained asymmetric alloy films, *Phys. Rev. B* 81 (23) (2010) 235301.
- [337] T. Walther, C.J. Humphreys, A.G. Cullis, D.J. Robbins, A correlation between compositional fluctuations and surface undulations in strained layer epitaxy, *Mater. Sci. Forum* 196 (1995) 505.
- [338] B.J. Spencer, M. Blanariu, Shape and composition map of a prepyramid quantum dot, *Phys. Rev. Lett.* 95 (2005) 206101.
- [339] Y. Tu, J. Tersoff, Coarsening, mixing, and motion: the complex evolution of epitaxial islands, *Phys. Rev. Lett.* 98 (2007) 096103.
- [340] P.M. Petroff, S.P. Denbaars, MBE and MOCVD growth and properties of self-assembling quantum dot arrays in III-V semiconductor structures, *Superlattices Microstruct.* 15 (1994) 15.
- [341] T. Walther, A.G. Cullis, D.J. Norris, M. Hopkinson, Nature of the Stranski–Krastanow transition during epitaxy of InGaAs on GaAs, *Phys. Rev. Lett.* 86 (2001) 2381.
- [342] A.G. Cullis, D.J. Norris, T. Walther, M.A. Migliorato, M. Hopkinson, Stranski–Krastanow transition and epitaxial island growth, *Phys. Rev. B* 66 (2002) 081305(R).
- [343] M. Blanariu, B.J. Spencer, Weakly non-linear bifurcation analysis of pattern formation in strained alloy film growth, *IMA J. Appl. Math.* 72 (2007) 9.
- [344] J. Tersoff, Enhanced nucleation and enrichment of strained-alloy quantum dots, *Phys. Rev. Lett.* 81 (1998) 3183.
- [345] X. Liang, Y. Ni, L. He, Shape-dependent composition profile in epitaxial alloy quantum dots: a phase-field simulation, *Computat. Mat. Sci.* 48 (2010) 871.
- [346] N.V. Medhekar, V. Hegadekatte, V.B. Shenoy, Composition maps in self-assembled alloy quantum dots, *Phys. Rev. Lett.* 100 (2008) 106104.
- [347] D. Digiuni, R. Gatti, F. Montalenti, Aspect-ratio-dependent driving force for nonuniform alloying in Stranski–Krastanow islands, *Phys. Rev. B* 80 (2009) 155436.
- [348] N.V. Medhekar, V. Hegadekatte, V.B. Shenoy, Compositional patterning in coherent and dislocated alloy nanocrystals, *Solid State Commun.* 149 (2009) 1395.
- [349] G. Vastola, V.B. Shenoy, J. Guo, Y.-W. Zhang, Coupled evolution of composition and morphology in a faceted three-dimensional quantum dot, *Phys. Rev. B* 84 (2011) 035432.
- [350] C. Lang, D.J.H. Cockayne, D. Nguyen-Manh, Alloyed Ge(Si)/Si(001) islands: the composition profile and the shape transformation, *Phys. Rev. B* 72 (2005) 155328.
- [351] G. Hadjisavvas, P.C. Kelires, Critical aspects of alloying and stress relaxation in Ge/Si(100) islands, *Phys. Rev. B* 72 (2005) 075334.
- [352] T. Leontiou, J. Tersoff, P.C. Kelires, Suppression of intermixing in strain-relaxed epitaxial layers, *Phys. Rev. Lett.* 105 (2010) 236104.
- [353] X.B. Niu, G.B. Stringfellow, F. Liu, Nonequilibrium composition profiles of alloy quantum dots and their correlation with the growth mode, *Phys. Rev. Lett.* 107 (2011) 076101.
- [354] A. Baskaran, J. Devita, P. Smereka, Kinetic Monte Carlo simulation of strained heteroepitaxial growth with intermixing, *Continuum Mech. Thermodyn.* 22 (2009) 1.
- [355] P. Venezuela, J. Tersoff, J.A. Floro, E. Chason, D.M. Follstaedt, F. Liu, M.G. Lagally, Self-organized growth of alloy superlattices, *Nature* 397 (1999) 678.
- [356] F. Liu, J. Tersoff, M.G. Lagally, Self-organization of steps in growth of strained films on vicinal substrates, *Phys. Rev. Lett.* 80 (1998) 1268.
- [357] J. Tersoff, Stress-driven alloy decomposition during step-flow growth, *Phys. Rev. Lett.* 77 (1996) 2017.
- [358] B. Rangelov, I. Markov, Adatom diffusion on vicinal surfaces with permeable steps, *Centr. Eur. J. Phys.* 7 (2009) 350.
- [359] M.H. Xie, J. Zhang, A. Lees, J.M. Fernandez, B.A. Joyce, Surface segregation during molecular beam epitaxy: the site-blocking effects of surfactant atoms, *Surf. Sci.* 367 (1996) 231.

- [360] S. Fukatsu, K. Fujita, H. Yaguchi, Y. Shiraki, R. Ito, Self-limitation in the surface segregation of Ge atoms during Si molecular beam epitaxial growth, *Appl. Phys. Lett.* 59 (1991) 2103.
- [361] T. Walther, C. Humphreys, A. Cullis, Observation of vertical and lateral Ge segregation in thin undulating SiGe layers on Si by electron energy-loss spectroscopy, *Appl. Phys. Lett.* 71 (1997) 809.
- [362] L. Huang, F. Liu, G.-H. Lu, X.G. Gong, Surface mobility difference between si and ge and its effect on growth of sige alloy films and islands, *Phys. Rev. Lett.* 96 (2006) 016103.
- [363] L. Huang, F. Liu, X.G. Gong, Strain effect on adatom binding and diffusion in homo- and heteroepitaxies of Si and Ge on (001) Surfaces, *Phys. Rev. B* 70 (2004) 155320.
- [364] R. Pala, F. Liu, Determining the adsorptive and catalytic properties of strained metal surfaces using adsorption-induced stress, *J. Chem. Phys.* 120 (2004) 7720.
- [365] I.M. Lifshitz, V.V. Slyozov, The kinetics of precipitation from supersaturated solid solutions, *J. Phys. Chem. Solids* 19 (1961) 35.
- [366] B.K. Chakraverty, Grain size distribution in thin films-1. Conservative systems, *J. Phys. Chem. Solids* 28 (1967) 2401.
- [367] B.K. Chakraverty, Grain size distribution in thin films-2. Non-conservative systems, *J. Phys. Chem. Solids* 28 (1967) 2413.
- [368] M. Kästner, B. Voigtländer, Kinetically self-limiting growth of ge islands on Si(001), *Phys. Rev. Lett.* 82 (1999) 2745.
- [369] M.R. McKay, J.A. Venables, J. Drucker, Kinetically suppressed ostwald ripening of Ge/Si(100) hut clusters, *Phys. Rev. Lett.* 101 (2008) 216104.
- [370] D.E. Jesson, T.P. Munt, V.A. Shchukin, D. Bimberg, Suppression of coalescence during the coarsening of quantum dot arrays, *Phys. Rev. B* 69 (2004) 041302(R).
- [371] J.A. Floro, M.B. Sinclair, E. Chason, L.B. Freund, R.D. Tweten, R.Q. Hwang, G.A. Lucadamo, Novel SiGe island coarsening kinetics: ostwald ripening and elastic interactions, *Phys. Rev. Lett.* 84 (2000) 701.
- [372] I. Daruka, A.L. Barabási, Dislocation-free island formation in heteroepitaxial growth: a study at equilibrium, *Phys. Rev. Lett.* 79 (1997) 3708.
- [373] V.A. Shchukin, D. Bimberg, Spontaneous ordering of nanostructures on crystal surfaces, *Rev. Modern Phys.* 71 (4) (1999) 1125–1171.
- [374] T.P. Munt, D.E. Jesson, V.A. Shchukin, D. Bimberg, Metastable states of surface nanostructure arrays studied using a Fokker–Planck equation, *Phys. Rev. B* 75 (2007) 085422.
- [375] V.A. Shchukin, D. Bimberg, T.P. Munt, D.E. Jesson, Metastability of ultradense arrays of quantum dots, *Phys. Rev. Lett.* 90 (2003) 076102.
- [376] M.R. McKay, J.A. Venables, J. Drucker, Kinetic frustration of Ostwald ripening in Ge/Si(100) hut ensembles, *Solid State Commun.* 149 (2009) 1403.
- [377] M.D. Korzec, P.L. Evans, From bell shapes to pyramids: a reduced continuum model for self-assembled quantum dot growth, *Physica D* 239 (2010) 465.
- [378] L.G. Wang, P. Kratzer, M. Scheffler, N. Moll, Formation and stability of self-assembled coherent islands in highly mismatched heteroepitaxy, *Phys. Rev. Lett.* 82 (1999) 4042.
- [379] X.L. Li, G. Ouyang, G.W. Yang, A thermodynamic theory of the self-assembly of quantum dots, *New J. Phys.* 10 (2008) 043007.
- [380] Y.W. Zhang, A.F. Bower, Three-dimensional analysis of shape transitions in strained-heteroepitaxial islands, *Appl. Phys. Lett.* 78 (2001) 2706.
- [381] A. Rastelli, H. von Känel, Surface evolution of faceted islands, *Surf. Sci. Lett.* 515 (2002) L493.
- [382] D.S.L. Mui, D. Leonard, L.A. Coldren, P.M. Petroff, Surface migration induced self-aligned InAs islands grown by molecular beam epitaxy, *Appl. Phys. Lett.* 66 (1995) 1620.
- [383] W. Seifert, N. Carlsson, A. Petersson, L.E. Wernersson, L. Samuelson, Alignment of InP Stranski–Krastanow dots by growth on patterned GaAs/GaInP surfaces, *Appl. Phys. Lett.* 68 (1996) 1684.
- [384] T. Ishikawa, S. Kohmoto, K. Asakawa, Site control of self-organized InAs dots on GaAs substrates by in situ electron-beam lithography and molecular-beam epitaxy, *Appl. Phys. Lett.* 73 (1998) 1712.
- [385] A. Konkar, A. Madhukar, P. Chen, Stress-engineered spatially selective self-assembly of strained InAs quantum dots on nonplanar patterned GaAs(001) substrates, *Appl. Phys. Lett.* 72 (1998) 220.
- [386] E.S. Kim, N. Usami, Y. Shiraki, Selective epitaxial growth of dot structures on patterned Si substrates by gas source molecular beam epitaxy, *Semicond. Sci. Technol.* 14 (1999) 257.
- [387] G. Jin, J.L. Liu, S.G. Thomas, Y.H. Luo, K.L. Wang, B.-Y. Nguyen, Controlled arrangement of self-organized Ge islands on patterned Si (001) substrates, *Appl. Phys. Lett.* 75 (1999) 2752.
- [388] M. Borgström, V. Zela, W. Seifert, Arrays of Ge islands on Si(001) grown by means of electron-beam pre-patterning, *Nanotechn.* 14 (2003) 264.
- [389] M. Bavencoffe, E. Houdart, C. Priester, Strained heteroepitaxy on nanomesas: a way toward perfect lateral organization of quantum dots, *J. Cryst. Growth* 275 (2005) 305.
- [390] A. Pascale, I. Berbezier, A. Ronda, P.C. Kelires, Self-assembly and ordering mechanisms of Ge islands on prepatterned Si(001), *Phys. Rev. B* 77 (2008) 075311.
- [391] P.C. Kelires, J. Tersoff, Equilibrium Alloy Properties by Direct Simulation: Oscillatory Segregation at the Si–Ge(100) (2 × 1) Surface, *Phys. Rev. Lett.* 63 (1989) 1164.
- [392] I. Berbezier, B. Gallas, L. Lapena, J. Fernandez, J. Derrien, B. Joyce, New insights on SiGe growth instabilities, *J. Vac. Sci. Technol. B* 16 (1998) 1582.
- [393] H. Hu, H.J. Gao, F. Liu, Theory of directed nucleation of strained islands on patterned substrates, *Phys. Rev. Lett.* 101 (2008) 216102.
- [394] T. Kitajima, B. Liu, S.R. Leone, Two-dimensional periodic alignment of self-assembled Ge islands on patterned Si(001) surfaces, *Appl. Phys. Lett.* 80 (2002) 497.
- [395] T.I. Kamins, R.S. Williams, Lithographic positioning of self-assembled Ge islands on Si(001), *Appl. Phys. Lett.* 71 (1997) 1201.
- [396] B. Yang, F. Liu, M.G. Lagally, Local strain-mediated chemical potential control of quantum dot self-organization in heteroepitaxy, *Phys. Rev. Lett.* 92 (2004) 025502.
- [397] G. Jin, J.L. Liu, K.L. Wang, Regimented placement of self-assembled Ge dots on selectively grown Si mesas, *Appl. Phys. Lett.* 76 (2000) 3591.
- [398] L. Nurminen, A. Kuronen, K. Kaski, Kinetic Monte Carlo simulation of nucleation on patterned substrates, *Phys. Rev. B* 63 (2000) 035407.
- [399] J.T. Robinson, J.A. Liddle, A. Minor, V. Radmilovic, D.O. Yi, P.A. Greaney, K.N. Long, D.C. Chrzan, O.D. Dubon, Metal-induced assembly of a semiconductor island lattice: Ge truncated pyramids on Au-patterned Si, *Nano Lett.* 5 (2005) 2070.
- [400] R. Bergamaschini, F. Montalenti, L. Miglio, Optimal growth conditions for selective Ge islands positioning on pit-patterned Si(001), *Nanoscale Res. Lett.* 5 (2010) 1873.
- [401] L. Vescan, K. Grimm, M. Goryll, B. Holländer, Ordered nucleation of Ge islands along high index planes on Si, *Mat. Sci. Engi. B* 69 (2000) 324.
- [402] Z. Zhong, W. Schwinger, F. Schäffler, G. Bauer, G. Vastola, F. Montalenti, L. Miglio, Delayed Plastic relaxation on patterned Si substrates: coherent SiGe pyramids with dominant {111} facets, *Phys. Rev. Lett.* 98 (2007) 176102.
- [403] G. Chen, G. Vastola, H. Lichtenberger, D. Pachinger, G. Bauer, W. Jantsch, F. Schäffler, L. Miglio, Ordering of ge islands on hill-patterned si (001) templates, *Appl. Phys. Lett.* 92 (2008) 113106.
- [404] G. Katsaros, J. Tersoff, M. Stoffel, A. Rastelli, P. Acosta-Diaz, G.S. Kar, G. Costantini, O.G. Schmidt, K. Kern, Positioning of strained islands by interaction with surface nanogrooves, *Phys. Rev. Lett.* 101 (2008) 096103.
- [405] T. Stoica, V. Shushunova, C. Dais, H. Solak, D. Grützmacher, Two-dimensional arrays of self-organized Ge islands obtained by chemical vapor deposition on pre-patterned silicon substrates, *Nanotechn.* 18 (2007) 455307.
- [406] M. Bollani, D. Chrustina, A. Federov, R. Sordan, A. Picco, E. Bonera, Ge-rich islands grown on patterned Si substrates by low-energy plasma-enhanced chemical vapour deposition, *Nanotechn.* 21 (2010) 475302.
- [407] O. Guise, J.T. Yates, J. Levy, J. Ahner, V. Vaithyanathan, D.G. Schlom, Patterning of sub-10-nm Ge islands on Si(100) by directed self-assembly, *Appl. Phys. Lett.* 87 (2005) 171902.
- [408] G. Chen, H. Lichtenberger, G. Bauer, W. Jantsch, F. Schäffler, Initial stage of the two-dimensional to three-dimensional transition of a strained SiGe layer on a pit-patterned Si(001) template, *Phys. Rev. B* 74 (2006) 035302.

- [409] H.N. Lam, V. Le thanh, V. Yam, D. Débarre, M. Halbwax, D. Bouchier, You have full text access to this content Formation and optical properties of Ge quantum dots selectively grown on patterned Si(001) substrates, *Phys. Status Solidi (a)* 201 (2004) 353.
- [410] A. Karmous, A. Cuenat, A. Ronda, I. Berbezier, S. Atha, R. Hull, Ge dot organization on Si substrates patterned by focused ion beam, *Appl. Phys. Lett.* 85 (2004) 6401.
- [411] I. Berbezier, A. Karmous, A. Ronda, in: O. Schmidt (Ed.), *Nanoscience and Technology*, Springer Verlag, Berlin Heidelberg, 2007, p. 429. (Chapter 15).
- [412] R. Hull, J.A. Floro, J. Graham, J.L. Gray, M. Gherasimova, A. Portavoce, F.M. Ross, Synthesis and functionalization of epitaxial quantum dot nanostructures for nanoelectronic architectures, *Mater. Sci. Semicond. Process.* 11 (2008) 160.
- [413] A. Portavoce, M. Kammler, R. Hull, M.C. Reuter, F.M. Ross, Mechanism of the nanoscale localization of Ge quantum dot nucleation on focused ion beam templated Si(001) surfaces, *Nanotechnology* 17 (2005) 4451.
- [414] I. Berbezier, A. Ronda, Self-assembling of Ge dots on nanopatterns: experimental investigation of their formation, evolution and control, *Phys. Rev. B* 75 (2007) 195407.
- [415] C. Misbah, O. Pierre-Louis, Y. Saito, Crystal surfaces in and out of equilibrium: a modern view, *Rev. Modern Phys.* 82 (2010) 981.
- [416] T. Maroutian, L. Douillard, H.-J. Ernst, Wavelength selection in unstable homoepitaxial step flow growth, *Phys. Rev. Lett.* 83 (1999) 4353.
- [417] P. Tejedor, P. Smilauer, C. Roberts, B.A. Joyce, Surface-morphology evolution during unstable homoepitaxial growth of GaAs(110), *Phys. Rev. B* 59 (1999) 2341.
- [418] A.V. Latyshev, L.V. Litvin, A.I. Aseev, Peculiarities of step bunching on Si(001) surface induced by DC heating, *Appl. Surf. Sci.* 130–132 (1998) 139.
- [419] J.E. Van nostrand, S.J. Chey, D.G. Cahill, Low-temperature growth morphology of singular and vicinal Ge(001), *Phys. Rev. B* 57 (1998) 12536.
- [420] M.V. Ramana murty, P. Fini, G.B. Stephenson, C. Thompson, J.A. Eastman, A. Munkholm, O. Auciello, R. Jothilingam, S.P. Denbaars, J.S. Speck, Step bunching on the vicinal GaN(0001) surface, *Phys. Rev. B* 62 (2000) R10661.
- [421] S.N. Filimonov, B. Voigtlander, “Rotating” steps in Si(0 0 1) homoepitaxy, *Surf. Sci.* 549 (2004) 31.
- [422] M. Esser, E. Zoethout, H.J.W. Zandvliet, H. Wormeester, B. Poelsema, Kinetic growth manipulation of Si(0 0 1) homoepitaxy, *Surf. Sci.* 552 (2004) 35.
- [423] M. Ono, A. Kamoshida, N. Matsuura, E. Ishikawa, T. Eguchi, Y. Hasegawa, Dimer buckling of the Si(001)2 × 1 surface below 10 K observed by low-temperature scanning tunneling microscopy, *Phys. Rev. B* 67 (2003) 201306(R).
- [424] V. Zielasek, F. Liu, Y. Zhao, J.B. Maxson, M.G. Lagally, Surface stress-induced island shape transition in Si(001) homoepitaxy, *Phys. Rev. B* 64 (2001) 201320.
- [425] J.M. Blakely, S. Tanaka, R.M. Tromp, Atomic step dynamics on periodic semiconductor surface structures, *J. Electron Microsc.* 48 (1999) 747.
- [426] R.L. Schwoebel, E.J. Shipsey, Step motion on crystal surfaces, *J. Appl. Phys.* 37 (1967) 3682.
- [427] G. Ehrlich, F.G. Hudda, Atomic view of surface self-diffusion: tungsten on tungsten, *J. Chem. Phys.* 44 (1966) 1039.
- [428] C. Duport, P. Nozières, J. Villain, New instability in molecular beam epitaxy, *Phys. Rev. Lett.* 74 (1995) 134.
- [429] F.K. Men, F. Liu, P.J. Wang, C.H. Chen, D.L. Cheng, J.L. Lin, F.J. Himpsel, Self-organized nanoscale pattern formation on vicinal Si(111) surfaces via a two-stage faceting transition, *Phys. Rev. Lett.* 88 (2002) 096105.
- [430] J.P. Van der eerden, H. Müller-Krumbhaar, Dynamic coarsening of crystal surfaces by formation of macrosteps, *Phys. Rev. Lett.* 57 (1986) 2431.
- [431] S. Stoyanov, V. Tonchev, Properties and dynamic interaction of step density waves at a crystal surface during electromigration affected sublimation, *Phys. Rev. B* 58 (1998) 1590.
- [432] A.V. Latyshev, A.L. Aseev, A.B. Krasilnikov, S.I. Stenin, Transformation on clean Si (111) stepped surface during sublimation, *Surf. Sci.* 213 (1989) 157.
- [433] A. Pascale, I. Berbezier, A. Ronda, A. Videcoq, A. Pimpinelli, Self-organization of step bunching instability on vicinal substrate, *Appl. Phys. Lett.* 89 (2006) 104108.
- [434] P. Politi, J. Krug, Crystal symmetry, step-edge diffusion, and unstable growth, *Surf. Sci.* 446 (2000) 89.
- [435] A. Pimpinelli, A. Videcoq, Iodobenzene on Pd(111) studied by thermal desorption spectroscopy and laser-induced thermal desorption–Fourier transform mass spectrometry, *Surf. Sci.* 445 (2000) L23.
- [436] B. Voigtänder, T. Weber, P. Smilauer, D.E. Wolf, Transition from island growth to step-flow growth for Si/Si(100) epitaxy, *Phys. Rev. Lett.* 78 (1997) 2164.
- [437] B. Gallas, I. Berbezier, J. Derrien, D. Gandolfo, J. Ruiz, V.A. Zagrebnev, Defect-mediated kinetic roughening in low-temperature MBE growth of Si/Si (111), *EuroPhys. Lett.* 41 (1998) 519.
- [438] A. Ronda, I. Berbezier, A. Pascale, A. Portavoce, F. Volpi, Experimental insights into Si and SiGe growth instabilities: influence of kinetic growth parameters and substrate orientation, *Mat. Sci. Engi. B* 101 (2003) 95.
- [439] A. Barabasi, H.E. Stanley, *Fractal concepts in surface growth*, Cambridge University Press, 1995.
- [440] A.F. Andreev, Faceting phase transitions of crystals, *Sov. Phys. JETP* 53 (1981) 1063.
- [441] V. Marchenko, Possible structures and phase transitions on the surface of crystals, *JETP Lett.* 33 (1981) 381.
- [442] H. Hibino, T. Fukuda, M. Suzuki, Y. Hommo, T. Sato, M. Iwatsuki, K. Miki, H. Tokumoto, High-temperature scanning-tunneling-microscopy observation of phase transitions and reconstruction on a vicinal Si(111) surface, *Phys. Rev. B* 47 (1993) 13027.
- [443] E.D. Williams, R.J. Phaneuf, J. Wei, N.C. Bartelt, T.L. Einstein, Thermodynamics and statistical mechanics of the faceting of stepped Si(111), *Surf. Sci.* 294 (1993) 219.
- [444] A.A. Baski, L.J. Whitman, Quasiperiodic nanoscale faceting of high-index Si surfaces, *Phys. Rev. Lett.* 74 (1995) 956.
- [445] R.J. Phaneuf, E.D. Williams, N.C. Bartelt, Temperature dependence of vicinal Si(111) surfaces, *Phys. Rev. B* 38 (1988) 1984.
- [446] R.J. Phaneuf, N.C. Bartelt, E.D. Williams, W. Świech, E. Bauer, Low-energy electron-microscopy investigations of orientational phase separation on vicinal Si(111) surfaces, *Phys. Rev. Lett.* 67 (1991) 2986.
- [447] J. Viernow, J.-L. Lin, F.M. Petrovykh, D.Y. Leibscale, F.K. Men, F.J. Himpsel, Regular step arrays on silicon, *Appl. Phys. Lett.* 72 (1998) 948.
- [448] A.A. Golovin, M.S. Levine, T.V. Savina, S.H. Davies, Faceting instability in the presence of wetting interactions: A mechanism for the formation of quantum dots, *Phys. Rev. B* 70 (2004) 235342.
- [449] V.A. Shchukin, A.I. Borovkov, N.N. Ledentsov, P.S. Kop'ev, Theory of quantum-wire formation on corrugated surfaces, *Phys. Rev. B* 51 (1995) 17767.
- [450] K. Brunner, J. Zhu, G. Abstreiter, O. Kienzle, F. Ernst, You have full text access to this content self-ordering of Ge islands on Si substrates mediated by local strain fields, *Phys. Status Solidi (b)* 224 (2001) 531.
- [451] S. Christiansen, M. Albrecht, H.P. Strunk, H.J. Maier, Strained state of Ge(Si) islands on Si: finite element calculations and comparison to convergent beam electron-diffraction measurements, *Appl. Phys. Lett.* 64 (1994) 3617.
- [452] H. Kim, H. Li, J.M. Seo, Nucleation, growth, and deformation of one-dimensional Ge nanostructures on the Si(5 5 12)-2 × 1 surface, *Surf. Sci.* 602 (2008) 2563.
- [453] F. Lin, K. Sumimoto, Y. Homma, T. Ogino, STM observations of three-dimensional Ge islands on Si(1 1 1) surfaces with different step orientations and step-bunching conditions, *Surf. Sci.* 562 (2004) 15.
- [454] D.J. Eaglesham, F.C. Unterwald, D.C. Jacobson, Growth morphology and the equilibrium shape: the role of “surfactants” in Ge/Si island formation, *Phys. Rev. Lett.* 70 (1993) 966.
- [455] I. Berbezier, A. Ronda, A. Portavoce, N. Motta, Ge dots self-assembling: surfactant mediated growth of Ge on SiGe (118) stress-induced kinetic instabilities, *Appl. Phys. Lett.* 83 (2003) 4833.
- [456] M. Copel, M.C. Reuter, M. Horn von hoegen, R.M. Tromp, Influence of surfactants in Ge and Si epitaxy on Si(001), *Phys. Rev. B* 42 (1990) 11682.
- [457] R.D. Bringans, R.I.G. Uhrberg, M.A. Olmstead, R.Z. Bachrach, Surface bands for single-domain 2 × 1 reconstructed Si(100) and Si(100): as. Photoemission results for off-axis crystals, *Phys. Rev. B* 34 (1986) 7447.
- [458] R.M. Tromp, M.C. Reuter, Local dimer exchange in surfactant-mediated epitaxial growth, *Phys. Rev. Lett.* 68 (1992) 954.
- [459] W.H. Shi, C.B. Li, L.P. Luo, B.W. Cheng, Q.M. Wang, Growth of Ge quantum dot mediated by boron on Ge wetting layer, *J. Cryst. Growth* 279 (2005) 329.

- [460] T. Schmidt, J.I. Flege, S. Gangopadhyay, T. Clausen, A. Locatelli, S. Heun, J. Falta, Alignment of Ge nanoislands on Si(111) by Ga-induced substrate self-patterning, *Phys. Rev. Lett.* 98 (2007) 066104.
- [461] T. Schmidt, T. Clausen, J.I. Flege, S. Gangopadhyay, A. Locatelli, T.O. Mentes, F.Z. Guo, S. Heun, J. Falta, Adsorbate induced self-ordering of germanium nanoislands on Si(113), *New J. Phys.* 9 (2007) 392.
- [462] K. Romanyuk, J. Brona, B. Voigtlander, Nanoscale pit formation at 2D ge layers on Si: influence of energy and entropy, *Phys. Rev. Lett.* 103 (2009) 096101.
- [463] I. Berbezier, A. Ronda, A. Karmous, in: O. Schmidt (Ed.), *Ge quantum dot self-alignment on vicinal substrates*, Nanosci. and Technol., Springer-Verlag, Berlin Heidelberg, 2007, (Chapter 6).
- [464] C. Teichert, L.J. Petricolas, J.C. Bean, J. Tersoff, M.G. Lagally, Stress-induced self-organization of nanoscale structures in SiGe/Si multilayer films, *Phys. Rev. B* 53 (1996) 16334.
- [465] J. Tersoff, C. Teichert, M.G. Lagally, Self-organization in growth of quantum dot superlattices, *Phys. Rev. Lett.* 76 (1996) 1675.
- [466] D.J. Omi, H. Bottomley, Y. Homma, T. Ogino, Wafer-scale strain engineering on silicon for fabrication of ultimately controlled nanostructures, *Phys. Rev. B* 67 (2003) 115302.
- [467] A. Dunbar, M. Halsall, P. Dawson, U. Bangert, M. Miura, Y. Shiraki, The effect of strain field seeding on the epitaxial growth of Ge islands on Si(001), *Appl. Phys. Lett.* 78 (2001) 1658.
- [468] N. Usami, Y. Araki, Y. Ito, M. Miura, Y. Shiraki, Modification of the growth mode of Ge on Si by buried Ge islands, *Appl. Phys. Lett.* 76 (2000) 3723.
- [469] G. De seta, M. Capellini, F. Evangelisti, C. Ferrari, L. Lazzarini, G. Salviati, R.W. Peng, S.S. Jiang, Effect of interlayer strain interaction on the island composition and ordering in Ge/Si(001) island superlattices, *J. Appl. Phys.* 102 (2007) 043518.
- [470] H.J. Kim, Z.M. Zhao, Y.H. Xie, Three-stage nucleation and growth of Ge self-assembled quantum dots grown on partially relaxed SiGe buffer layers, *Phys. Rev. B* 68 (2003) 205312.
- [471] C. Shin, H. Jin, J. Chang, H. Kim, W.W. Kim, Computation of the preferential nucleation sites for Ge quantum dots on a relaxed SiGe layer, *Acta Mater.* 55 (2007) 225.
- [472] F. Leroy, J. Eymery, P. Gentile, F. Fournel, Controlled surface nanopatterning with buried dislocation arrays, *Surf. Sci.* 545 (2003) 211.
- [473] C.I. Marcus, I. Berbezier, M.I. Alonso, A. Ronda, M. Garriga, R. Goñi, E. Gomes, L. Favre, A. Delobbe, P. Sudraud, How FIB patterning can change the position of Ge islands?, private communication.
- [474] A. Portavoce, M. Kammler, R. Hull, M.C. Reuter, M. Copel, F.M. Ross, Growth kinetics of Ge islands during Ga-surfactant-mediated ultrahigh vacuum chemical vapor deposition on Si(001), *Phys. Rev. B* 70 (2004) 195306.
- [475] B. Liu, C.L. Berrie, T. Kitajima, S.R. Leone, Arsenic-induced Ge island morphology changes during molecular beam epitaxy of Ge on Si(001), *J. Cryst. Growth* 241 (2002) 271.
- [476] P.I. Gaiduk, A. Nylandsted Larsen, J. Hansen Lundsgaard, Self-organization of GeAs nanodots in relaxed $\text{Si}_{0.5}\text{Ge}_{0.5}$ alloys, *Appl. Phys. Lett.* 79 (2001) 3494.
- [477] A. Portavoce, A. Ronda, I. Berbezier, Sb-surfactant mediated growth of Ge nanostructures, *Mat. Sci. Engi. B* 89 (2002) 205.
- [478] M. Abdallah, I. Berbezier, P. Dawson, M. Serpentini, G. Bremond, B. Joyce, Self organization of Ge dots on Si substrates: influence of misorientation, *Thin Solid Films* 336 (1998) 256.
- [479] N. Motta, P.D. Szkutnik, M. Tomellini, A. Sgarlata, M. Fanfoni, F. Patella, A. Balzarotti, Role of patterning in islands nucleation on semiconductor surfaces, *C. R. Phys.* 7 (2006) 1046.
- [480] O.G. Schmidt, S. Schieker, K. Eberl, O. Kienzle, F. Ernst, Carbon-induced germanium dots: Kinetically-limited islanding process prevents coherent vertical alignment, *Appl. Phys. Lett.* 73 (1998) 659.
- [481] D. Dentel, J.L. Bischoff, L. Kubler, M. Stoffel, G. Castellein, Influence of a pre-deposited carbon submonolayer on the Ge island nucleation on Si(001), *J. Appl. Phys.* 93 (2003) 5069.
- [482] A. Bernardi, M.I. Alonso, A.R. Goñi, J.O. Ossó, M. Garriga, Growth dynamics of C-induced Ge dots on $\text{Si}_{1-x}\text{Ge}_x$ strained layers, *Surf. Sci.* 601 (2007) 2783.
- [483] A. Bernardi, M.I. Alonso, A.R. Goni, J.O. Osso, M. Garriga, Density control on self-assembling of Ge islands using carbon-alloyed strained SiGe layers, *Appl. Phys. Lett.* 89 (2006) 101921.
- [484] G. Vanacore, M. Zani, M. Bollani, D. Colombo, G. Isella, J. Osmond, R. Sordan, A. Tagliaferri, Size evolution of ordered SiGe islands grown by surface thermal diffusion on pit-patterned Si(100) surface, *Nano. Res. Lett.* 5 (2010) 1921.
- [485] V. Loup, J.M. Hartmann, G. Rolland, P. Holliger, F. Laugier, D. Lafond, M.N. Sémeria, P. Besson, P. Gentille, Reduced pressure chemical vapour deposition of Si/ $\text{Si}_{1-x}\text{Ge}_x$ heterostructures using a chlorinated chemistry, *Semicond. Sci. Technol.* 18 (2003) 352.
- [486] X. Deng, M. Krishnamurthy, Self-assembly of quantum-dot molecules: heterogeneous nucleation of SiGe islands on Si(100), *Phys. Rev. Lett.* 81 (1998) 1473.
- [487] D.E. Jesson, K.M. Chen, S.J. Pennycook, T. Thundat, R.J. Warmack, Morphological evolution of strained films by cooperative nucleation, *Phys. Rev. Lett.* 77 (1996) 1330.
- [488] J.L. Gray, R. Hull, J.A. Floro, Control of surface morphology through variation of growth rate in SiGe/Si(100) epitaxial films: nucleation of "quantum fortresses", *Appl. Phys. Lett.* 81 (2002) 2445.
- [489] O. Guise, J. Ahner, J. Yates, J. Levy, Formation and thermal stability of sub-10-nm carbon templates on Si(100), *Appl. Phys. Lett.* 85 (2004) 2352.
- [490] S.-W. Chang, V.P. Chuan, S.T. Boles, C.A. Ross, C.V. Thompson, You have full text access to this content densely packed arrays of ultra-high-aspect-ratio silicon nanowires fabricated using Block-Copolymer lithography and metal-assisted etching, *Adv. Funct. Mater.* 19 (2009) 2495.
- [491] Z.M. Zhao, T.S. Yoon, W. Feng, B.Y. Li, J.H. Kim, J. Liu, O. Hulkó, Y.H. Xie, H.M. Kim, K.B. Kim, H.J. Kim, K.L. Wang, C. Ratsch, R. Caflisch, D.Y. Ryu, T.P. Russell, The challenges in guided self-assembly of Ge and InAs quantum dots on Si, *Thin Solid Films* 508 (2006) 195.
- [492] J. Lee, K.L. Wang, H.-T. Chen, L.-J. Chen, High-quality heteroepitaxial Ge growth on nano-patterned Si templates using diblock copolymer patterning, *J. Cryst. Growth* 301 (2007) 330.
- [493] L. Zhang, E. Ruh, D. Grützmacher, L. Dong, D.J. Bell, B.J. Nelson, C. Schönenberger, Anomalous coiling of sige/si and sige/si/cr helical nanobelts, *Nano Lett.* 6 (2006) 1311.
- [494] Y. Sun, J.A. Rogers, Structural forms of single crystal semiconductor nanoribbons for high-performance stretchable electronics, *J. Mat. Chem.* 17 (2007) 832.
- [495] M. Huang, C. Boone, M. Roberts, D. Savage, M. Lagally, N. Shaji, H. Qin, R. Blick, J. Nairn, F. Liu, Nanomechanical architecture of strained bilayer thin films: from design principles to experimental fabrication, *Adv. Mater.* 17 (2005) 2860.
- [496] C. Yu, H. Jiang, Forming wrinkled stiff films on polymeric substrates at room temperature for stretchable interconnects applications, *Thin Solid Films* 519 (2010) 818.
- [497] D.-Y. Khang, H. Jiang, Y. Huang, J.A. Rogers, A stretchable form of single-crystal silicon for high-performance electronics on rubber substrates, *Science* 311 (2006) 208.
- [498] M.M. Roberts, L.J. Klein, D.E. Savage, K.A. Slinker, M. Friesen, G. Celler, M.A. Eriksson, M.G. Lagally, Elastically relaxed free-standing strained-silicon nanomembranes, *Nature Mater.* 5 (2006) 388.
- [499] M. Huang, C.S. Ritz, B. Novakovic, D. Yu, Y. Zhang, F. Flack, D.E. Savage, P.G. Evans, I. Knezevic, F. Liu, M.G. Lagally, Mechano-electronic superlattices in silicon nanoribbons, *ACS Nano* 3 (2009) 721.
- [500] Y. Ni, L.H. He, Spontaneous formation of vertically anticorrelated epitaxial islands on ultrathin substrates, *Appl. Phys. Lett.* 97 (2010) 261911.
- [501] Z. Liu, J. Wu, W. Duan, M.G. Lagally, F. Liu, Electronic phase diagram of single-element silicon "strain" superlattices, *Phys. Rev. Lett.* 105 (2010) 016802.
- [502] A. Malachias, Y. Mei, R.K. Annabattula, C. Deneke, P.R. Onck, O.G. Schmidt, Wrinkled-up nanochannel networks: long-range ordering, scalability, and X-ray investigation, *ACS Nano* 2 (2008) 1715.

- [503] H.-J. Chung, T.-I. Kim, H.-S. Kim, S.A. Wells, S. Jo, N. Ahmed, Y.H. Jung, S.M. Won, C.A. Bower, J.A. Rogers, Fabrication of releasable single-crystal silicon–metal oxide field-effect devices and their deterministic assembly on foreign substrates, *Adv. Funct. Mater.* 21 (2011) 3029.
- [504] F. Wang, J.-H. Seo, Z. Ma, X. Wang, Substrate-free self-assembly approach toward large-area nanomembranes, *ACS Nano* 6 (2012) 2602.
- [505] I. Tiginyanu, V. Popa, M.A. Stevens-Kalceff, Bioelectronics, biomedical and bioinspired systems and nanotechnology, in: A.B. Rodriguez Vazquez, R.A. Carmona Galan, G. Linares Cembrano, A. Adelung, C. Ronning (Eds.), *Proceedings of SPIE*, vol. 8068, 2011.
- [506] L. Pan, K.-K. Lew, J.M. Redwing, E.C. Dickey, Stranski–Krastanow growth of germanium on silicon nanowires, *Nano Lett.* 5 (2005) 1081.
- [507] V. Schmidt, P.C. McIntyre, U. Gösele, Morphological instability of misfit-strained core-shell nanowires, *Phys. Rev. B* 77 (2008) 235302.
- [508] H. Wang, M. Upmanyu, C.V. Ciobanu, Morphology of epitaxial core-shell nanowires, *Nano Lett.* 8 (2008) 4305.
- [509] J.-Y. Guo, Y.-W. Zhang, V.B. Shenoy, Morphological evolution and ordered quantum structure formation in heteroepitaxial core-shell nanowires, *ACS Nano* 4 (2010) 4455.